THE UNIVERSITY *of* EDINBURGH

Characterisation of a novel *Rab18* mouse model for Warburg Micro syndrome

Sarah Marie Carpanini

Thesis submitted for the degree of Doctor of Philosophy

The University of Edinburgh

2013

This thesis is composed of original research undertaken by myself, and where the work of others is included their contributions have been duly acknowledged.

Sarah Marie Carpanini

November 2013

Acknowledgements

Firstly, I wish to thank Irene for taking me on as a student and starting the project. You have had a very difficult few years but have still always been there to provide support and guidance whenever needed. It has been an honour to work with you and continue this project.

Thank you to Ian for allowing me to become part of your lab; it has been a fantastic group to work for. Thank you for your support and enthusiasm in the project and interesting discussions and ideas after every new result.

Thank you to Mark for your help and guidance and answering questions and queries; including those starting with “I know this is a stupid question but...” Thank you for your passion in the RAB protein field and science in general, you have showed me how great work in this field can be.

Thank you to the Jackon lab for adopting me and making me feel like part of the family. Thanks for all your help and support and sharing reagents and antibodies. In particular, thanks to Lisa for all your help with phenotyping and maintenance of the mouse colony. Thanks to Lisa and Shalini for all your help with sectioning and characterisation of the mouse eye phenotype. Thanks to everyone in C204 office, thanks for all the gossips and chats over the last few years, and for being a great distraction exactly when needed.

Thank you to Tom Gillingwater for also taking me in and making me part of your lab. Thank you for your interest, enthusiasm and ideas for taking this project forward and always making time for me either for brainstorming sessions, paper writing meetings or just general discussions. Thank you to Tom Wishart for help with analysis of the proteomics and IPA. Thanks to all members of the Gillingwater lab, in particular, thank you to Eilidh, Sarah and Sophie for teaching the nerve and muscle dissections. Thanks to Derek for coming across to perform the sciatic nerve ligation surgery, twice! Thanks to Sarah and Ann for processing the nerves and sectioning for EM.

Thank you to Mike Cousin and Sarah Gordon for your help with the synaptic vesicle recycling experiments.

Thank you to Paul Perry and Matt Pearson for microscope help and support. Thanks to Allyson Ross for help with histology. Thank you to Ian McCall and all technical staff at the BRF for managing the mouse colony. Thank you to Professor Francis Barr for the GFP-RAB18 and GFP-TBC1D20-RA constructs. Thanks also to Harris Morrison for performing the OPT processing and imaging.

Thank you to Dad, Mum, Helen, Bex and Grandma for your continued support and patience throughout my studies, you can all breathe a sigh of relief the studies are almost over! Thank you for listening to me rant and stress and I hope to spend more weekends at home with you all, when this is all completed.

And last but by no means least, I wish to thank Mike. Thanks for your help with illustrator. Thanks for your support and patience over the last eight years, it has meant more to me than you could ever know. Thank you for knowing exactly when I needed you there and when I needed peace, and for trying to keep quiet when Cardiff City were playing. And most of all, thank you that after all this you still want to marry me!

Dedications

I dedicate this thesis in loving memory of Nonno, who was so proud that there could one day be a Dr Carpanini but never lived to see it happen. And to Mike, my fiancé, my best friend and my rock, I love you.

Abstract

Warburg Micro syndrome is a severe autosomal recessive condition characterised by abnormalities affecting the ocular, neurological and endocrine systems. Previous studies have identified causative loss-of-function mutations in four members of the RAB protein network; *RAB3GAP1, RAB3GAP2, RAB18* and *TBC1D20,* causing clinically indistinguishable phenotypes. RAB3GAP1 and RAB3GAP2 form a heterodimeric complex specifically regulating the RAB3 family of proteins in calcium mediated exocytosis of hormones and neurotransmitters. *Rab3gap1* deficient mice have previously been generated and showed altered short term plasticity in the hippocampus and inhibition of Ca^{2+} mediated exocytosis of glutamate from cortical synaptosomes, but failed to recapitulate the characteristic ocular or neurological features of Warburg Micro syndrome. Mutations in *TBC1D20*, a GTPase activating protein (GAP) for the RAB1 family, have recently been identified in Warburg Micro syndrome patients and the *bs* (blind sterile) mouse model; although this model recapitulated many ocular and endocrine abnormalities of the disease any neurological abnormalities have yet to be reported.

The function and localisation of RAB18 remains to be fully elucidated and its role in disease pathogenesis is still unclear. Initially, I have confirmed previous reports co-localising RAB18 with the *cis*-Golgi, ER and lipid droplets in mouse embryonic fibroblasts and identified a novel localisation in neuronal processes of primary hippocampal neurons. To examine the role of RAB18 *in vivo* a novel *Rab18* genetrap mouse was generated by MRC Harwell as part of the EUMODIC screen. In this study I describe detailed histopathological and neurological characterisation of the *Rab18*$^{-/-}$ mouse model. *Rab18*$^{-/-}$ mice were viable and fertile. At eye opening they presented with dense nuclear congenital cataracts and atonic pupils recapitulating major ocular features of Warburg Micro syndrome. Analysis of embryonic eye development revealed a delay in lens development in *Rab18*$^{-/-}$ mice as early as embryonic day 12.5. From three weeks of age *Rab18*$^{-/-}$ mice developed progressive hind limb weakness indicative of neurological dysfunction. I have undertaken

detailed neuropathological analysis of the observed hind limb weakness and identified no abnormalities in synaptic vesicle recycling and no atrophy of peripheral muscles or aberrant development or stability of neuromuscular connectivity. However, loss of RAB18 resulted in gross accumulations of neurofilament and microtubule proteins at the neuromuscular junction and disorganisation of the cytoskeleton in peripheral nerves. Investigation of global proteomic profiling in peripheral nerve of *Rab18*$^{-/-}$ mice identified alterations in core pathways regulating the axonal cytoskeleton in neurons.

In summary this thesis describes a novel *Rab18*$^{-/-}$ mouse model recapitulating the characteristic ocular and neurological features of Warburg Micro syndrome. I highlight a novel mechanistic insight into Warburg Micro syndrome disease pathogenesis and a role for RAB18 in regulating cytoskeletal dynamics in neurons.

Publications

Sarah M. Carpanini, Lisa McKie, Derek Thomson, Ann K. Wright, Sarah L. Gordon, Sarah L. Roche, Mark T. Handley, Harris Morrison, David Brownstein, Thomas M. Wishart, Michael A. Cousin, Thomas H. Gillingwater, Irene A. Aligianis and Ian J. Jackson. A mouse model of Warburg Micro syndrome reveals roles for RAB18 in eye development and regulation of the neuronal cytoskeleton. Submitted Human Molecular Genetics August 2013.

Ryan P. Liegel, Mark Handley, Adam Ronchetti, Stephen Brown, Lars Langemeyer, Andrea Linford, Bo Chang, Deborah Morris-Rosendahl, **Sarah Carpanini**, Verity Harthill, Eamonn Sheridan, Ghada M. H. Abdel-Salam, Paulien A. Terhal, Francesca Faravelli, Patrizia Accorsi, Lucio Giordano, Lorenzo Pinelli, Britta Hartmann, Alison Ebert, Francis A. Barr, Irene Aligianis and Duska J. Sidjanin. Loss-of-Function mutations in *TBC1D20* Cause Cataracts and Male Infertility in *blind sterile* Mice and Warburg Micro syndrome in Humans. American Journal of Human Genetics, in press, corrected proof, available online 14 November 2013.

Handley MT, Morris-Rosendahl DJ, Brown S, Macdonald F, Hardy C, Bem D, **Carpanini SM**, Borck G, Martorell L, Izzi C, Faravelli F, Accorsi P, Pinelli L, Basel-Vanagaite L, Peretz G, Abdel-Salam GM, Zaki MS, Jansen A, Mowat D, Glass I, Stewart H, Mancini G, Lederer D, Roscioli T, Giuliano F, Plomp AS, Rolfs A, Graham JM, Seemanova E, Poo P, García-Cazorla A, Edery P, Jackson IJ, Maher ER, Aligianis IA. Muation Spectrum in RAB3GAP1, RAB3GAP2 and RAB18 and Genotype-Phenotype Correlations in Warburg Micro syndrome and Martsolf syndrome. Human Mutation 2013 May;34(5):686-96.

Gakovic M, Shu X, Kasioulis I, **Carpanini S**, Moraga I, Wright AF. The role of RPGR in cilia formation and actin stability. Human Molecular Genetics. 2011 Dec 15;20(24):4840-50.

Abbreviations

%	Percent
ºC	Degrees Celsius
ACh	Acetylcholine
AChE	Acetylcholinesterase
AChR	Acetylcholine receptor
ALS	Amyotrophic lateral sclerosis
APOD	Apolipoprotein D
APP	Amyloid Precursor Protein
β-ME	β-mercaptoethanol
β-geo	β-galactosidase/neomycin phosphotransferase fusion gene
aa	Amino acid
bs	blind sterile
BSA	Bovine serum albumin
BTX	Bungarotoxin
C57BL/6J	C57 Black 6J mouse line
Ca^{2+}	Calcium
CDR	Complementary Determining Region
cDNA	Complementary DNA
CNS	Central Nervous System
CMT	Charcot Marie Tooth
DAPI	4',6-diamidino-2-phenylindole
DIV	Days *in vitro*
DNA	Deoxyribonucleic acid
DMEM	Dulbecco's Modified Eagles Medium
dNTP	Deoxyribonucleotide triphosphate
E	Embryonic day
eGFP	Enhanced green fluorescent protein
EM	Electron microscopy
ENU	N-ethyl-*N*-nitrosourea

EPP	Endplate potential
EPSC	Excitatory Postsynaptic Potential
ER	Endoplasmic Reticulum
ES	Embryonic stem cells
EUCOMM	European Conditional Mouse Mutagenesis Program
FBS	Foetal bovine serum
FCS	Fetal calf serum
FDB	Flexor digitorum brevis
FITC	Fluorescein isothiocyanate
Frt	Flip-recombinase targets
GalT	*trans*/TGN enzyme β1,4-galactosyltransferase
GAP	GTPase activating protein
GDI	GDP dissociation inhibitor
GDF	GDP dissociation factor
GDP	Guanosine diphosphate
GEF	Guanine nucleotide exchange factor
GEP	GDP/GTP Exchange protein
GFP	Green fluorescent protein
GTP	Gaunosine triphosphate
GWAS	Genome wide association study
H&E	Haemotoxylin and eosin
HET	Heterozygote
HSP	Hereditary spastic paraplegia
HOM	Homozygote
Hpf	hours post fertilisation
IHC	Immunohistochemistry
IF	Immunofluorescence
IGMM	Institute of Genetics and Molecular Medicine
iTRAQ	Isobaric tag for relative and absolute quantitation
K+	Potassium
KO	Knock out

KIF5A	Kinesin Family Member 5A
LTP	Long Term Potentiation
MAP	Microtubule associated proteins
MEFs	Mouse embryonic fibroblasts
MeOH	Methanol
min	Minutes
MLPA	Multiplex ligation-dependent probe amplification
MRC HGU	Medical Research Council, Human Genetics Unit
mRNA	Messenger RNA
ms	Milliseconds
MPZ	Myelin Protein Zero
NER	Nucleotide Excision Repair
NF	Neurofilament
NEFH	200kDa Neurofilament Heavy Chain
NEFL	68kDa Neurofilament Light Chain
NEFM	165kDa Neurofilament Medium Chain
NMJ	Neuromuscular junction
nt	Nucleotide
OCRL	Oculocerebrorenal syndrome of Lowe
OFZ	Organelle Free Zone
OPT	Optical Projection Tomography
p	Phospho
P	Days post-partum
pA	Poly adenylation sequence
P/S	Penicillin/streptomycin
PBS	Phosphate buffered solution
PCR	Polymerase chain reaction
PFA	Paraformaldehyde
pH	Potential hydrogen
PMP	Peripheral Myelin Protein
PNS	Peripheral Nervous System

PPF	Paired Pulse Facilitation
PVDF	Polyvinylidene difluoride
PRX	Periaxin
qRT-PCR	Quantitative reverse transcription PCR
RAB	Member of Ras oncogene family
RABF	RAB specific sequence motif
RABGGTase	RAB geranylgeranyltransferase
RABSF	RAB subfamily specific region
RAS	Rat sarcoma virus oncogene
REP	RAB Escort Protein
RNA	Ribonucleic acid
RPE	Retinal Pigment Epithelium
RT	Reverse transcriptase
RT-PCR	Reverse transcription-PCR
SA	Splice acceptor
SMA	Spinal Muscular Atrophy
SEM	Standard Error of the Mean
SDS	Sodium dodecyl sulfate
SDS-PAGE	Sodium dodecyl sulfate polyacrylamide gel electrophoresis
SNARE	Soluble NSF Attachment Protein Receptor
SNP	Single nucleotide polymorphism
SypHy	synaptophysin-pHluorin
TBC	Tre-2/Bub2/Cdc16
TBE	Tris/Borate/EDTA buffer
TBS	Tris Buffered Solution
TBST	TBS with 0.1% Triton X
TBP	TATA Binding Protein
TEM	Transmission electron microscopy
TGN	*Trans*-Golgi Network
TRITC	Tetramethylrhodamine iso-thiocynanate
TRITC-α-BTX	Tetramethylrhodamine iso-thiocynanate- conjugated- alpha-bungarotoxin

t-SNARE	target-SNARE
TVA	Transverse abdominus
UV	Ultraviolet
v/v	Volume to volume
v-SNARE	vesicle-SNARE
WB	Western blot
WT	Wildtype
w/v	Weight to volume
X-gal	(5-bromo-4-chloro-3-indolyl-β-D- galactopyranoside)

Table of Contents

List of Figures

List of Tables

Chapter 1 Introduction

1.1 Warburg Micro syndrome

1.1.1 Clinical features

Warburg Micro syndrome (MIM:600118, 614222, 614225) is a severe neurodevelopmental disorder of autosomal recessive inheritance. It was initially reported in 1993 by Mette Warburg in two siblings and a male cousin from a consanguineous family of Pakistani origin (Warburg et al., 1993). All three affected individuals presented with microcornea, congenital cataracts, pinpoint pupils, retinal dystrophy and atrophy of the optic nerve. They also displayed hypotonic spastic diplegia, agenesis of the corpus callosum, microcephaly and severe developmental delay. All three had similar facial features including hypertrichosis, anteverted ears and a prominent root of the nose. Additionally the two male subjects had microgenitalia with penile hypoplasia, crytorchidism and hypospadius, while the female subject exhibited delayed onset of puberty suggestive of hypothalamic hypogonadism.

Over the past two decades multiple case reports and the subsequent gene identification of causative mutations in four members of the RAB protein network have helped to clearly delineate the clinical features associated with Warburg Micro syndrome (Aligianis et al., 2005, Abdel-Salam et al., 2007, Ainsworth et al., 2001, Bem et al., 2011, Borck et al., 2010, Derbent et al., 2004, Dursun et al., 2012, Graham et al., 2004, Megarbane et al., 1999, Morris-Rosendahl et al., 2010, Yildirim et al., 2012, Yuksel et al., 2007).

Characteristic ocular abnormalities associated with Warburg Micro syndrome include bilateral congenital cataracts, microphthalmia, microcornea (<10mm diameter), pinpoint atonic pupils that do not respond to dark or mydriatic agents and atrophy of the optic nerve. Additionally, congenital ptosis, nystagmus and microphakia are occasionally observed. In initial cases patients were subjected to

cataract surgery (phacoemulsification) but only minimal light perception was achieved, with normal electroretinogram (ERG) and absent visually evoked potentials (VEPs) recorded.

Postnatally, patients go on to develop growth retardation and neurological abnormalities including microcephaly (-4 to -6 standard deviations below the mean) and severe global developmental delay. While patients may develop early milestones such as smiling, most achieve no developmental milestones beyond those associated with normal development at 4 months of age: they do not learn to crawl, pull up to a standing position, walk or talk.

Characteristically, patients show congenital hypotonia and lower-limb spasticity which progresses to the upper limbs leading to spastic quadriplegia later in life. Evidence of a peripheral neuropathy has also been reported. Computerised tomography (CT) scans and magnetic resonance imaging (MRI) imaging have proven invaluable in characterising the neurological abnormalities of Warburg Micro syndrome. Ainsworth *et al.,* 2001 reported 10 affected individuals with pachygyria and variable abnormalities of the corpus callosum. Graham *et al.,* (2004) further examined 6 Warburg Micro syndrome patients showing a simplified gyral pattern with shallow sulci, thickening of the cortex and microgyri and a thin corpus callosum. Further analysis of the brain phenotype further delineated the characteristic neurodevelopmental abnormalities including: frontal and parietal lobal polymicrogyria, hypogenesis of the corpus callosum and broad sylvian fissures. Handley *et al.,* 2013 reported a detailed analysis of brain MRI scans from 17 Warburg Micro or Martsolf syndrome patients and identified bilateral polymicrogyria, predominantly within the frontal lobe and extending into Sylvian fissures but occasionally within the temporal lobe, partial formation of the corpus callosum, enlargement of subdural spaces and hypoplasia of the cerebellum and particularly cerebellar vermis (Handley *et al.,* 2013). Patients occasionally suffer from seizures and this could be attributable to the array of cerebral anomalies observed.

A characteristic facial appearance of Warburg Micro syndrome patients has also been noted with low set ears that are posteriorly angulated, a beaked nose and prominent

broad nasal root, deep set eyes, lengthened philtrum, undersized or under developed jaw and a high arched palate.

Bone and joint abnormalities have also been reported in some patients, including; micrognathia, scoliosis, congenital hip dislocations and finger anomalies including achromachia and clinodactyly. Affected children can additionally show hypogonadism, thought to be hypothalamic in origin, with micropenis and cryptorchidism in boys and clitoral hypoplasia in girls. However, micropenis is not reported in all cases (Warburg et al., 1993, Abdel-Salam et al., 2007, Bem et al., 2011).

1.1.2 Differential diagnosis of Warburg Micro syndrome

To date, there is no accurate information regarding the incidence of Warburg Micro syndrome as cases are often misdiagnosed with similar disorders characterised by many if not all of the following features; congenital cataracts, microcephaly, growth retardation and developmental delay with autosomal recessive inheritance (Graham et al., 2004). As a result, detailed phenotypic reports and genetic analysis are essential to delineate characteristic Warburg Micro syndrome cases from similar disorders, including; Cockayne syndrome, Cerebro-Oculo-Facio-Skeletal syndrome, Martsolf syndrome, Congenital Cataracts-Facial Dysmorphism-Neuropathy syndrome and Marinesco Schjogren syndrome. Cockayne syndrome (Cockayne syndrome A MIM: 216400 and Cockayne syndrome B MIM:133540) is characterised by postnatal growth retardation, mental retardation, photosensitivity, progressive pigmentary retinopathy, hearing loss and joint contractures, with cataracts occasionally observed. Cerebro-Oculo-Facio-Skeletal syndrome (MIM: 214150) is associated with microcephaly, mental retardation, congenital cataracts, joint contractures and facial anomalies. Cogenital Cataracts-Facial Dysmorphism-Neuropathy syndrome (MIM:604168) is characteristically associated with severe developmental delay, skeletal anomalies, hypogonadism, congenital cataracts and progressive motor neuropathy. Marinesco Schjogren syndrome (MIM:248800) is characterised by infantile cataracts, cerebellar ataxia, progressive muscle weakness, developmental delay, growth retardation, hypogonadism and skeletal abnormalities.

However, COFs and Cockayne syndrome patients have a worse prognosis that those of Warburg Micro syndrome patients and examination of patient cell lines identified hypersensitivity to UV irradiation due to defective Nucleotide Excision Repair (NER). Whereas, Warburg Micro syndrome patient cell lines do not show hypersensitivity to UV or impairment of NER (Graham et al., 2004). Additionally, while cataracts are a characteristic feature of Marinesco Schjogren syndrome reports have suggested that they can develop postnatally in some patients rather than congenital as observed for Warburg Micro syndrome patients. It should also be noted that although the Warburg Micro syndrome phenotype overlaps that of many other disorders, its presentation is characteristic irrespective of which gene is mutated.

1.2 Martsolf syndrome

Warburg Micro and Martsolf syndromes share a high degree of clinical similarity with congenital cataracts, microgenitalia and developmental delay observed in both. However, Martsolf syndrome is much rarer in incidence than Warburg Micro syndrome. Martsolf syndrome (MIM: 212720) is an autosomal recessive disorder that was originally reported in 1978 in two brothers of consanguineous Polish-Jewish decent (Martsolf et al., 1978). Patients with Martsolf syndrome present with bilateral cataracts (and no other ocular malformations), prominent facial dysmorphism (including high forehead, undersized jaw, high palate, and low set and rotated ears), microcephaly, microgenitalia, developmental delay, occasional bone/joint abnormalities (including scoliosis and contractures) (Sanchez et al., 1985, Hennekam et al., 1988, Ehara et al., 2007). Cranial CT and Brain MRI studies of Martsolf syndrome patients (Ehara et al., 2007, Handley et al., 2013) identified mild to moderate polymicrogyria restricted to Sylvian fissures and frontal lobe. However, unlike Warburg Micro syndrome no cerebellar hypoplasias or increase in subdural spaces was observed.

Additionally, patients with Martsolf syndrome are able to support their own heads, walk with aids and may speak one or a few words. Thus, the ocular and neurodevelopmental features of Martsolf syndrome are milder than those observed in Warburg Micro syndrome.

1.3 Molecular genetics

Through linkage analysis, positional cloning and very recently advancements in whole exome sequencing causative loss-of-function mutations for Warburg Micro syndrome have been identified within approximately 50% of our cohort in one of four genes; *RAB3GAP1, RAB3GAP2, RAB18* or *TBC1D20*.

Aligianis *et al.*, 2005 carried out a 10cM genome wide scan in 12 Warburg Micro syndrome individuals and unaffected family members from 8 consanguineous families and identified homozygosity between microsatellite markers D2S410 and D2S1399. Inactivating mutations were identified in *RAB3GAP1* in 5 families. Further analysis of both Warburg Micro and Martsolf syndrome cases identified mutations in 41% of the cohort, with 18 frameshift, 20 nonsense and 5 splicing mutations now reported (Handley et al., 2013). Most of these mutations are predicted to affect protein function and/or be a target for nonsense mediated decay (Aligianis et al., 2005, Morris-Rosendahl et al., 2010, Dursun et al., 2012, Yuksel et al., 2007, Abdel-Salam et al., 2007, Handley et al., 2013). A *RAB3GAP1* mutation in two siblings with Martsolf syndrome has also recently been reported, and it is suggested that residual protein expression is probably responsible for avoiding the more severe Warburg Micro syndrome phenotype (Handley et al., 2013).

An additional 10cM genome wide scan was carried out on 3 affected Martsolf individuals and identified homozygosity between GATA124F08 and D1S549 (Aligianis et al., 2006). All three individuals were found to be homozygous for the p.Gly1051Cys mutation in *RAB3GAP2*. However, RNA obtained from patient lymphocytes identified two transcripts, a wild type transcript of reduced intensity compared to wild type and a stronger additional transcript skipping exon 28 and resulting in a frameshift mutation, thus suggesting some wild type transcript is probably produced. An additional p.Arg426Cys missense mutation has also been reported that is predicted to disturb protein function (Handley et al., 2013). Borck *et al.*, 2011 sequenced Warburg Micro syndrome patients and identified an inframe deletion of 9 evolutionary conserved base pairs in exon 6, resulting in loss of function and the more severe prognosis (Borck et al., 2010). A further 9 cases of Warburg Micro syndrome with *RAB3GAP2* mutations have since been reported with

RAB3GAP2 mutations now accounting for 7% of Warburg Micro or Martsolf syndrome cases (Handley et al., 2013). Warburg Micro and Martsolf syndromes therefore appear to represent a phenotypic continuum, whereby mutations in *RAB3GAP1* and *RAB3GAP2* resulting in residual expression and/or function cause the milder Martsolf syndrome, and loss-of-function mutations cause Warburg Micro syndrome. The outcome (Warburg Micro or Martsolf) therefore appears to be related to the nature and severity of the mutation.

To identify the cause of further genetic heterogeneity, Bem *et al.,* 2011 carried out a genome wide linkage scan using the 250K SNP array in 5 consanguineous families and identified several homozygous regions. Microsatellite analysis narrowed this to a 10Mb region between rs943124 to rs3847396. Genetic sequencing and MLPA (multiplex ligation-dependent probe amplification) of *RAB18* identified a homozygous missense mutation c.71T>A, a compound heterozygote inframe arginine deletion (p.93Argdel) or an antitermination mutation (p.X207GlnextX20) in 5 families, all predicted to result in loss of function (Bem et al., 2011). Since this, Handley *et al.,* have reported an additional novel p.Thr95Arg mutation in *RAB18. RAB18* mutations in now been identified in 5% of Warburg Micro syndrome cases (Handley et al., 2013).

Very recently, causative mutations in *Tbc1d20* have been identified through linkage analysis and positional cloning of the *blindsterile (bs)* locus and revealed a 416 kb region of homogeneity on chromosome 2 between microsatellite markers *rs27385663* and *rs27343710* (Leigel *et al.,* 2013, in press). Sequencing of the 16 genes encompassing this region identified a c.692_703 deletion in exon 6 of *Tbc1d20*. Given the high degree of similarity between the *bs* mouse and the Warburg Micro syndrome patient phenotype (see below) a cohort of 77 Warburg Micro syndrome families negative for mutations in *RAB3GAP1, RAB3GAP2* or *RAB18* were screened and five different causative loss-of-function mutations in *TBC1D20* were identified in seven Warburg Micro syndrome patients: c.199C>T, c.292C>T, c.352_353delCA, c.672G>A and in one individual a microdeletion of exons 2-8 (Leigel *et al.,* 2013, in press).

To date causative mutations for Martsolf syndrome have not been identified in *RAB18* or *TBC1D20.*

1.4 RAB18

Mouse models for *Rab3gap1* (Sakane et al., 2006) and *Tbc120* (Leigel *et al.*, 2013, in press) have previously been generated and will be discussed in further detail in section 1.9. In this thesis I describe the generation and characterisation of a novel *Rab18*$^{-/-}$mouse model, I will therefore primarily focus on RAB18. *Rab18* was cloned in 1993 from mouse pituitary AT-t20 cells and adult mouse kidney (Lutcke et al., 1994, Yu et al., 1993). RAB18 is a 23 kDa protein encoded by seven exons. An additional novel splice variant of 235 aa was reported in 2005, although this is predominantly expressed in the testis (Dou et al., 2005). Northern blot analysis on adult mouse tissues identified *Rab18* mRNA in all tissues examined albeit at different levels of intensity with highest levels observed in brain and heart (Lutcke et al., 1994).

RAB18's cellular localisation and hence function has been the basis of multiple reports over the past two decades, with various roles reported in different cell types. Following its cloning, initial studies examining RAB18 localisation were undertaken on mouse kidney cryosections and identified labelling throughout the cortex, with enrichment in proximal tubules (Lutcke et al., 1994). At the subcellular level RAB18 localised to both vesicles and clathrin positive invaginations, prompting the proposal of a role for RAB18 in endocytosis. Further analysis on paraffin intestinal sections localised RAB18 to the apical and basolateral portions of intestinal epithelial cells (Lutcke et al., 1994). This provided the first insight into RAB18 serving a tissue or cell type specific function. In a macrophage cell line (mannose receptor positive) RAB18 localised to a distinct vesicular compartment also containing RAB5 where it appeared to play a role in the immune evasion of *Salmonella* phagocytosis (Hashim et al., 2000). The most reproducible localisation of RAB18 in variable cell lines is to lipid droplets (Vero, 3T3-L1 fibroblasts and differentiated adipocytes and HepG2 cells) where it is reported to play a role in both lipolysis and lipogenesis (Martin et al., 2005, Ozeki et al., 2005, Pulido et al., 2011). One study in these same cell lines also reported the localisation of RAB18 to the endoplasmic reticulum and variably to

the Golgi apparatus where they reported a role for RAB18 in Golgi to ER trafficking via the COPI-independent transport pathway (Dejgaard et al., 2008). However, screens of multiple RAB proteins have failed to identify RAB18 within this pathway. For example, analysis of Shiga toxin uptake from the cell surface and trafficking to the Golgi is dependent on a minimum of 6 RAB-GAPs, none of which show activity towards RAB18 (Fuchs et al., 2007). Furthermore, analysis of GTPase activating proteins implicated in ER to Golgi trafficking and maintenance of Golgi morphology failed to identify RAB18 (Haas et al., 2007).

RAB18 has also been reported to localise to peroxisomes, preferentially in its GDP-bound state (Gronemeyer et al., 2013). Studies in both neuroendocrine cells and pituitary melanotropes have also identified an interaction of RAB18 with secretory granules where it seemingly functions to inhibit their exocytosis (Vazquez-Martinez et al., 2007). A similar role has also been reported for RAB3, localising to synaptic vesicles and inhibiting calcium mediated exocytosis of hormones and neurotransmitters (Fischer von Mollard et al., 1991, Schluter et al., 2002). However, examination of RAB18 and RAB3A localisation in PC12 cells failed to identify any colocalisation under either basal conditions or stimulation of the secretory pathway with potassium, suggesting that RAB18 and RAB3A associate with distinct populations and function in different processes of the secretory pathway (Vazquez-Martinez et al., 2007). Reduced RAB18 levels have been reported in growth hormone hypersecretory pituitary adenomas in patients with acromegaly. Furthermore, this hypersecretory activity could be reversed upon overexpression of RAB18 (Vazquez-Martinez et al., 2008). These studies all point towards a role for RAB18 in negative regulation of exocytosis. Interestingly, many studies have reported that RAB18 localisation is enhanced upon cellular stimulation. For example, in PC12 and AtT20 cell lines RAB18 is found localised to the cytosol but redistributes to secretory granules after stimulation with a depolarising K+ pulse to activate the secretory pathway (Vazquez-Martinez et al., 2007). Furthermore, in 3T3-L1 adipocytes RAB18 localises to lipid droplets. This localisation is enhanced upon stimulation of lipolysis by isoproterenol activation of β-adrenergic receptor or forskolin. Additionally, blockage of stimulation by propranolol prevented this

association (Martin et al., 2005). Pulido *et al.*, also reported an increased association of RAB18 to the lipid droplet surface upon insulin treatment (Pulido et al., 2011).

RAB18 has been implicated in disease pathogenesis of various conditions including Warburg Micro syndrome and acromegaly (Bem et al., 2011, Vazquez-Martinez et al., 2008). In addition, its increased expression was reported in microarray studies of high grade prostate adenocarcinoma (True et al., 2006). *RAB18* was also identified as one of the top hits for genes implicated in pathophysiology of Schizophrenia by GWAS (Ayalew et al., 2012) and *RAB18* has been identified as being downregulated in neuroendocrine gastrointestinal tumour cells upon growth factor treatment to induce proliferation (Hofsli et al., 2005). RAB18 has also been found to be dysregulated in PaCa 5061- a human pancreatic adenocarcinoma cell line (Kalinina et al., 2010).

1.5 RAB protein activation and function

RAB3GAP1, RAB3GAP2, RAB18 and TBC1D20 are all members to the RAB protein network. RAB18 is a small GTPase of the RAB subfamily, whereas the other three proteins have been characterised as regulators of RAB protein function. RAB3GAP1 and RAB3GAP2 form a heterodimeric enzyme complex regulating the RAB3 cycle (Nagano et al., 1998, Fukui et al., 1997, Sudhof, 2004), and TBC1D20 functions as a GAP with activity towards the RAB1 and RAB2 subfamilies (Haas et al., 2007). It is therefore believed that RAB protein dysfunction underlies Warburg Micro syndrome pathogenesis. RAB proteins are small G-proteins of the RAS superfamily functioning as master regulators of vesicular trafficking between membranous organelles, including the endoplasmic reticulum (ER), Golgi, plasma membrane, endosomes and lysosomes. Membrane organelles enclose distinct environments serving specific cellular functions that rely on bidirectional membrane transport to transfer materials between phospholipid membranes. Membrane trafficking can be divided into a series of distinct stages (Grosshans et al., 2006). Primarily proteins and protein constituents to be trafficked are selected and bud from donor membranes into intermediate vesicles. These vesicles are transported along cytoskeletal tracks composed of actin or microtubule filaments responsible for short and long range transport respectively to target membranes. When the intermediate

vesicle reaches the target membrane of the recipient organelle it is then tethered or docked and the intermediate vesicle and target membrane fuse their lipid bilayers to transfer material (Stenmark, 2009, Grosshans et al., 2006).

The two major routes of trafficking in secretory organelles are the exocytotic pathway, which ends at the plasma membrane, and the endocytotic pathway, which begins there. Initially, protein constituents for exocytotic trafficking are formed in ribosomes on the surface of the endoplasmic recitulum (ER) where protein components for trafficking are synthesised and imported into the ER lumen (Grosshans et al., 2006, Brighouse et al., 2010). Within the ER, proteins are post-translationally modified and folded into correct nascent peptides. Modified and folded proteins can then exit the ER at ER exit sites in COPII coated vesicles and are transported along microtubules to the *cis*-face of the Golgi apparatus. Proteins pass through the Golgi, where they can be further modified and emerge at the *trans*-interface, *trans*-Golgi network (TGN). Following release from the Golgi, proteins are transported in vesicles to the cell surface where they release into the external environment (Brighouse et al., 2010). Endocytosis refers to the uptake of cellular components from the external environment. Endocytosed molecules are primarily transported to early endosomes where they are sorted for either recycling or degradation. Those molecules to be recycled are thus transported to recycling endosomes and released into the plasma membrane, whereas those for degradation are transported to late endosomes and subsequently lysosomes (Grosshans et al., 2006).

RAB proteins regulate vesicular trafficking through their function as molecular switches cycling between GDP bound ‘inactive’ and GTP bound ‘active’ conformations (Stenmark, 2009). This reversible activation and the association and dissociation of RAB proteins on and off membranes, enables regulation in both a temporally and spatially restricted manner. In brief, GDP bound RAB proteins are delivered to target membranes. Once attached at the membrane, GDP is exchanged for GTP by guanine nucleotide exchange factors (GEFs). GTP bound RAB proteins can then interact with multiple effector molecules in vesicular budding, transport,

tethering and fusion. Following function, GTPase activating proteins (GAPs) accelerate the RAB proteins GTP hydrolysis activity mediating GTP hydrolysis to GDP at the nucleotide binding site. The GDP bound RAB protein once again comes into contact with GDI and is extracted from the membrane and sequestered in the cytosol until the next round of activation (Corbeel and Freson, 2008, Stenmark, 2009). The RAB protein cycle is depicted in figure 1.1 and will be discussed in further detail below.

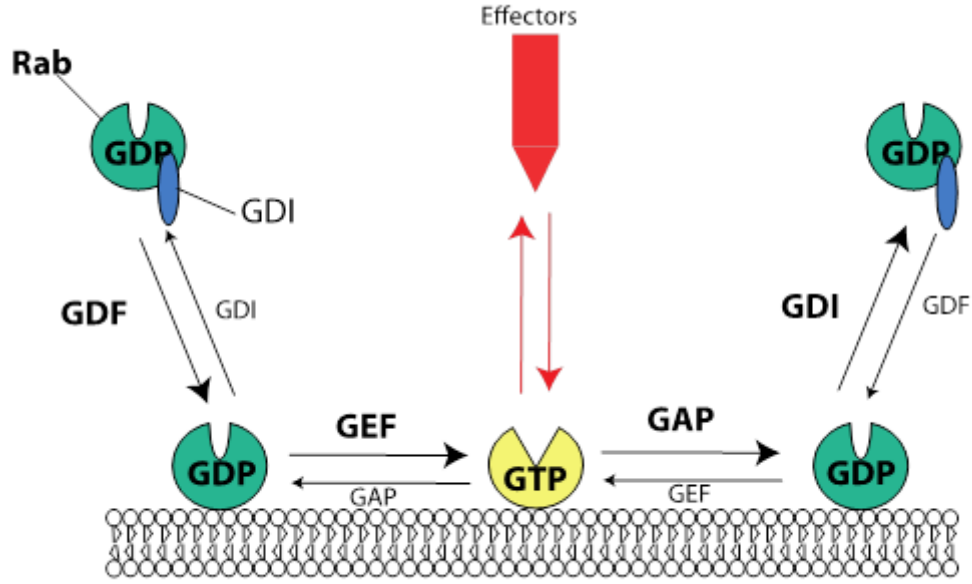

Figure 1.1: The RAB protein cycle

RAB proteins cycle from GDP to GTP bound on and off target membranes. In brief GDP bound RAB proteins are sequestered in the cytosol by GDI and targeted to the membrane by GDF. GDP is then exchanged for GTP through the action of GEFs. It is typically thought to be a GTP bound RAB protein that is 'active' and interacts with effector molecules. GTP bound RAB is then converted to GDP through the action of RAB GAPS that function to stimulate the intrinsic GTPase hydrolysis of the RAB. GDP bound RABs are then extracted from the membrane and sequestered in the cytosol once more by GDI.

1.5.1 RAB protein structure

The first report of RAB protein involvement in membrane trafficking came from studies in yeast (Salminen and Novick, 1987). Since this study eleven RAB homologues have now been identified in yeast (Zerial and McBride, 2001). Throughout evolution great expansion of the RAB protein family occurred with duplication and diversification of specific RAB protein functions, resulting in more than 60 RAB proteins identified in the human genome localising to multiple cellular compartments and functioning in diverse steps of membrane trafficking (Pereira-Leal and Seabra, 2001). For example, RAB18 has been reported to function in calcium mediated exocytosis, lipolysis and lipogenesis (Vazquez-Martinez et al., 2007, Martin et al., 2005, Ozeki et al., 2005).

Phylogenetic analysis of RAB proteins in human, nematode, fly and fission yeast have made it possible to track the expansion of the gene family and enabled some RABs to be separated into 8 distinct subgroups, labelled I-VIII (Table 1.1) dependent on similar reported localisation and/or function (Pereira-Leal and Seabra, 2001). This suggests that these 8 subgroups may share a related ancestry or be related in terms of function or potentially both. However, it must be noted that a minority of RAB proteins, including RAB18, are excluded from these phylogenetic groups suggesting they serve more divergent roles (Pereira-Leal and Seabra, 2001).

Table 1.1: Analysis of RAB phylogenetic function has enabled subdivision of the RAB family into 8 distinct domains based on localisation and/or function (Pereira-Leal and Seabra, 2001).

RAB subgroup	Contained RABs
I	RAB1A, RAB1B & RAB35
II	RAB2A, RAB2B, RAB4, RAB4B, RAB11a, RAB11B & RAB25
III	RAB3A, RAB3B, RAB3C, RAB3D, RAB27A, RAB27B, RAB37 & RAB36
IV	RAB19 & RAB30
V	RAB21, RAB5A, RAB5B, RAB5C & RAB22A, RAB22B & RAB22C
VI	RAB41, RAB6, RAB6B & RAB6C
VII	RAB7, RAB9 & RAB9B
VIII	RAB13, RAB8, RAB8B & RAB10

Despite their various functions and cellular localisations, all RAB proteins including RAB18 share a high degree of structural morphology, sharing a folded structure common to members of the RAS superfamily; a core of five parallel and one anti-parallel beta-sheet flanked by five alpha-helices. The beta-sheets and alpha-helices are connected by 5 loops, where the elements responsible for guanine nucleotide binding, magnesium binding and GTP hydrolysis are located (Stenmark and Olkkonen, 2001, Liu and Storrie, 2012, Dumas et al., 1999). All RABs have two switch regions (switch I and switch II) located in loop2 and loop4-α2-loop5 regions respectively, that are responsible for binding the gamma phosphate group of GTP and alter depending on nucleotide bound state. As a result they are thought to be the principle site of RAB effector protein interactions (Stenmark and Olkkonen, 2001). The switch regions of GDP bound 'inactive' RAB proteins are highly disordered and natively unfolded, whereas in GTP bound 'active' RABs switch regions show highly organised conformations (Lee et al., 2009). Nucleotide binding and the resultant conformational change are thus intrinsic to RAB protein function. Additionally, the

p.Arg93del and p.Leu24Gln *RAB18* mutations abolish nucleotide binding and hence lead to a complete loss of protein function (Bem et al., 2011).

Pereira-Leal & Seabra performed in depth phylogenetic analysis through ClustalW alignment of all reported RAB isoforms from mammals and identified five RAB specific sequence motifs (RABF) that distinguish RAB proteins from other small GTPases (Pereira-Leal and Seabra, 2000). These conserved motifs all localise to switch I and switch II regions and to surrounding areas. Furthermore, through analysis of the complete mammalian RAB genome they also identified 4 RAB subfamily specific regions (RABSF) shared between 'related' RAB proteins (see table 1.1). These RABSF regions are found throughout the RAB sequence, in both loops and the hypervariable domains (Pereira-Leal and Seabra, 2000). Furthermore, the crystal structure of RAB3A in complex with rabphilin-3A was reported in 1999 and identified two interaction sites between the two proteins; one within the switch I and switch II regions and the other within a deep pocket which they referred to as RAB CDRs (Complementary Determining Region) (Ostermeier and Brunger, 1999). These regions of CDR are thought to be composed of highly variable sequences within the conserved structural motif of RAB GTPases and are thought to provide structural specificity for RAB-effector protein binding. This suggests that other components of the RAB protein structure are implicated in effector binding and not just the switch domains as previously thought.

1.5.2 RAB protein post-translational modification

Despite the highly similar core structure, all RAB proteins including RAB18 contain a hypervariable C-terminal domain, with great variations in composition and length observed between RABs. This C-terminal domain is the site of post-translational modification by RAB geranylgeranyltransferase (RABGGTase) which is essential for RAB-membrane targeting. The majority of RAB proteins are prenylated at two C-terminal cysteine residues by the covalent attachment of a 20 carbon geranylgeranyl isoprenoid through thioether linkages (Pereira-Leal et al., 2001, Goody et al., 2005). However, a small subset of RAB proteins (including RAB18) instead contain a CAAX box motif (C= cysteine, A= aliphatic residue, X= any amino acid) and as a result are geranylgeranylated at only one C-terminal cysteine residue

by protein geranylgeranyltransferase type I (CAAX-GGT). Leung *et al.,* showed that this small subset of CAAX containing RAB proteins are also modified post-prenylation by methylation. This methylation has no major impact on membrane targeting but RAB mutants that are geranylgeranylated but not methylated show abnormalities in membrane/cytosol cycling, thus pointing towards a direct or indirect role for RAB methylation in their association with membranes (Leung et al., 2007). A *RAB18* antitermination mutation has also been reported in Warburg Micro syndrome (Bem et al., 2011). The p.X207GlnextX20 mutation extends the C-terminus of RAB18 by 20 amino acids and thus disrupts geranylgeranylation and membrane targeting and hence protein function.

1.5.3 RAB protein targeting to membranes

All RABs including RAB18 localise to specific subcellular compartments where they function in a diverse array of membrane trafficking steps. Targeting of RAB proteins to membranes is coordinated by both REP (RAB Escort Protein) and RAB GDI (GDP Dissociation Inhibitor). Immediately following synthesis, newly synthesised RAB proteins are recognized and bound by REP and presented to the RAB geranylgeranyltransferse (RABGGTase) enzyme for post-translational modification. The prenylated RAB protein in contact with REP is then targeted to the membrane. The REP protein thus recognizes both prenylated and unprenylated RAB proteins. However, REP is only required for initial membrane localisation following prenylation, after this the function of membrane targeting and dissociation is taken over by GDI proteins (Goody et al., 2005, Pereira-Leal et al., 2001).

GDI thus functions to bind to GDP-bound RAB proteins and sequester them within the cytosol but also target RAB proteins to membranes. The first RAB GDI was reported in 1990 by Sasaki *et al.,* as a protein that inhibits GDP dissociation and GTP binding (Sasaki et al., 1990). Since this study only three GDI isoforms have been identified in the mammalian genome (GDIα, GDIβ and GDIγ) (Alory and Balch, 2001). Due to the large number of identified RAB proteins functioning in diverse intracellular processes, this suggests that RAB GDI proteins serve a general role rather than a specific function in RAB protein localisation (Ullrich et al., 1993). Additionally, studies of endosomal RABs binding GDI with high affinity, have

proposed the involvement of a novel RAB effector called GDF (GDP displacement factor) (Dirac-Svejstrup et al., 1997). GDF may function to dissociate the highly stable GDI:GDP RAB complex and mediate the association of RAB proteins to particular target membranes (Pfeffer and Aivazian, 2004), however it is not yet clear whether GDFs participate in the targeting of all RAB isoforms.

Studies have also suggested that other components in addition to the prenylation motif may be implicated in RAB protein localisation. For example exchanging the prenylation motif between RAB5 with that of RAB7 and RAB2 with either RAB5 or RAB7 showed endosomal localisation reminiscent of the acceptor RAB protein, whereas exchange of the C-terminal 34 amino acids, including the cysteine for prenylation observed localisation to the donor protein (Chavrier et al., 1991).

1.5.4 RAB protein activation by GEFs

Following membrane targeting, all RAB proteins including RAB18 interact with an alternative RAB regulatory protein; RAB GEF (Guanine Nucleotide Exchange Factor). GEF proteins function by displacing the switch I region implicated in nucleotide binding and dislodging the phenylalanine/tyrosine residue that caps guanine, thus promoting GDP nucleotide release and exchange for GTP (Barr and Lambright, 2010). Stable membrane-association and the majority of reported RAB protein interactions mediating downstream events in membrane trafficking occur in a GTP bound state. Therefore, RAB GEFs play critical roles in activating RAB proteins to mediate membrane traffic.

The GEFs for RAB18 remains to be identified. GEFs can function as small individual proteins or as components of large multimolecular complexes. For example the TRAPPI (Transport Protein Particle I) complex is composed of seven subunits (Bet3p, Bet5p, Trs20p, Trs23p, Trs31p, Trs33p and Trs85p), and functions as a GEF for Ypt1 and Ypt31/32 controlling ER to Golgi transport (Jones et al., 2000). TRAPP II contains the seven TRAPPI subunits and a further three (Trs65p, Trs120p and Trs130p). Delineation of TRAPPI and TRAPPII identified that TRAPPI specifically functions as a GEF for Ypt1 functioning in ER to *cis*-Golgi transport whereas the addition of TRAPPII specific subunits (in particular Trs120p and

Trs130p) directs GEF activity towards Ypt31/32p in transport mechanisms exiting the Golgi (Morozova et al., 2006), thus linking different stages of membrane transport. This phenomenon of RAB GEFs mediating links between different stages of membrane transport is also observed in the case of RAB5 and RAB7 trafficking through early to late endosomes (Rink et al., 2005). Through live cell imaging they observed that loss of RAB5 signal (a marker of early endosomes) occurred in coordination with the gain of RAB7 (a marker for late endosomes). The authors also identified through mass spectrometry that active RAB5 interacted with hVps11, a component of the class C VPS/HOPS complex, and an additional subunit Vsp39p has GEF activity towards the yeast RAB7 ortholog, Ypt7p. They thus reported an essential role of the VPS/HOPs complex on the RAB5 dependent recruitment of RAB7 during early to late endosome transport (Rink et al., 2005). Interestingly, a recent study has reported a function of RAB GEFs (in particular RABEX-5, DRRA and RABIN-8) as a major factor in determining the localisation of specific RAB proteins (RAB5A, RAB1A and RAB8A respectively) to correct membrane localisations (Blumer et al., 2013). However, to this date they cannot rule out the possibility that other RAB regulators and effectors may also mediate membrane localisation.

With regards to the case of RAB18, immunoprecipitation studies performed during my masters project identified an interaction specifically between GDP bound RAB18 and RAB3GAP2 (unpublished data). This suggests that RAB3GAP2 may stabilise RAB18 in its GDP bound state and thus could potentially serve as a RAB18 GEF. Studies are currently underway with Dr Mark Handley and Prof Francis Barr (Oxford) to investigate this potential link and novel function of RAB3GAP2 as a RAB18 GEF.

1.5.5 RAB effector proteins

RAB protein function is mediated through interactions with specific ‘effector’ proteins. Except for a small subset, the majority of these effectors preferentially bind GTP-bound ‘active’ RABs. Effector proteins are generally thus recruited from the cytosol by activated GTP bound RABs and function to regulate multiple aspects of vesicular trafficking including budding, transport, tethering and fusion (Zerial and

McBride, 2001). However, despite extensive research aiming to elucidate RAB protein effectors, effector proteins for the majority of RAB isoforms are still to be reported. This is hindered by the fact that no obvious conservation of structure has been identified in the majority of RAB effectors, suggesting that individual effector molecules target specific transport mechanisms (Zerial and McBride, 2001). No specific effector molecules for RAB18 have been reported.

The majority of RAB effectors are thought to show specificity for a distinct RAB isoform, whereas a small minority show less specificity and interact with a multitude of RAB proteins in multiple locations. A recent study performed by Fukuda *et al.,* undertook a large scale yeast-2-hybrid screen for novel effectors of 28 RABs and identified 27 GTP specific effector proteins. However of the 27 identified, 17 showed binding to a broad subset of RAB proteins with OCRL (oculocerebrorenal syndrome of Lowe) for example binding 16 different RAB isoforms (Fukuda et al., 2008). It is possible however that a single effector could bind multiple RAB proteins *in vitro* but only one under physiological conditions.

The pathogenesis of Warburg Micro syndrome has been linked to dysregulation of the RAB3 cycle through RAB3GAP1 and RAB3GAP2 which are implicated in RAB3 cycle regulation. RAB3A serves as an example of a RAB protein with several identified effectors, including RIM and RABPHILIN. RIM (RAB3-interacting molecule) is an evolutionary conserved 1,553 aa protein that specifically binds to GTP bound RAB3A (Wang et al., 1997). Subcellular fractionation experiments identified RIM to be enriched in the synaptic plasma membrane particularly at the presynaptic active zones but absent from synaptic vesicles, where RAB3A is reported to be localised (Wang et al., 1997). However, no reduction in the level of RIM was identified in RAB3A deficient mice (Wang *et al.,* 1997). RABPHILIN has been shown to colocalise with GTP bound RAB3A on synaptic vesicles and RAB3A deficient mice show a significant reduction (of approximately 70%) of the levels of RABPHILIN (Li et al., 1994). *Rabphilin* knock out mouse models have therefore also been generated to elucidate the role of RABPHILIN in RAB3 localisation and function. *Rabphilin* knockout mice are viable and fertile and show no gross phenotypic abnormalities or abnormalities in synaptic plasticity (Schluter et al.,

1999). Furthermore, no changes in RAB3 protein levels or localisation were observed, suggesting RABPHILIN functions as an effector of RAB3 but has no impact on regulation or targeting of RAB3 molecules in synaptic vesicle exocytosis (Schluter et al., 1999).

RAB proteins interact with effectors and are capable of mediating various stages of vesicular transport. As effector proteins for RAB18 are yet to be identified, examples of RAB proteins functioning at different stages will be discussed in more detail below.

Cargo selection and vesicle budding

The first step of membrane transport involves the selection of specific cargoes to be trafficked, the recruitment of coat proteins and vesicle budding (Stenmark, 2009). For example, studies have proposed a role for RAB9 in vesicle formation (Carroll et al., 2001). GTP bound RAB9 localises to endosomes, where it recruits the effector molecule TIP47. In turn RAB9 increases the affinity of TIP47 for its downstream cargo mannose-6-phosphate receptors thus mediating endosome to Golgi transport (Carroll et al., 2001).

Vesicle transport

Following cargo sorting and budding, vesicles are transported along microtubule and/or actin cytoskeletal tracks to sites of action, the donor membrane. Vesicular transport along actin filaments is driven by myosin motors and along cytoskeletal tracks by the molecular motors, kinesin (for anterograde transport) and dynein (for retrograde transport). RAB proteins can interact with molecular motors either directly or indirectly. For example GTP bound RAB6A directly interacts with RABKINESIN thereby regulating the transport of Golgi membranes and vesicles (Echard et al., 1998) whereas RAB3A interacts indirectly with KIF1Bβ/KIF1A via DENN/MADD (Niwa et al., 2008).

Tethering and membrane fusion

Once vesicles have trafficked along cytoskeletal tracks to their target (the donor membrane), the next step of the trafficking process involves bringing the vesicle into

contact with the target membrane and ‘tethering’ the two together. Tethering has been reported to involve either coiled-coil proteins functioning as a bridge to physically connect the vesicle and target membrane, or multisubunit protein complexes (Grosshans et al., 2006). An example of a RAB effector that acts as a tether is EEA1, GTP bound active RAB5 recruits EEA1 to endosomes where it functions to mediate the docking and localisation of transport vesicles to early endosomes (Christoforidis et al., 1999).

Once transport vesicles are docked to the target membranes, their lipid bilayers are then fused. Vesicular fusion involves the SNARE (*N*-ethylmaleimide-sensitive factor attachment protein receptors) family of proteins, whereby vesicle associated (v-SNAREs) and target membrane associated (t-SNAREs) form complexes at the target membrane, opening a fusion pore and fusing the two membranes together (Grosshans *et al.*, 2006).

1.6 RAB GAPs

Following effector interactions and function GTP bound RAB proteins interact with another set of RAB protein regulators the RAB GAPs (GTPase activating proteins) to curb RAB GTPase activity and cease interactions with effector molecules (Barr and Lambright, 2010). RAB proteins do naturally possess internal GTPase activity, however this occurs at a very slow rate of hydrolysis and as a result RAB proteins interact with RAB GAPs to increase the rate of GTP hydrolysis and thus rapidly inactivate RAB proteins. To date most of the reported RAB GAP proteins possess a TBC (Tre2/Bub2/Cdc16) domain and have aided the identification of novel RAB GAPs through sequence homology (Frasa et al., 2012). However, of the 44 identified TBC domain containing proteins, approximately only half have been assigned RABs (Frasa et al., 2012). Furthermore, a single TBC domain containing RAB GAP may inactivate multiple RABs or a single RAB can be modulated by more than one RAB GAP (Frasa et al., 2012).

The GAP for RAB18 is not known. However, the other identified Warburg Micro syndrome disease genes comprise two GAPs; TBC1D20 and the RABGAP complex

(RAB3GAP1/RAB3GAP2). It has not yet been definitively determined if RAB18 is a substrate for either of these GAPs.

1.6.1 TBC1D20

TBC1D20 functions as a GAP specifically towards the RAB1 and RAB2 family of proteins, however minimal GAP activity has also been reported towards RAB18 (Haas et al., 2007). TBC1D20 contains the characteristic TBC domain (Tre2/Bub2/Cdc16) of RAB GAPs. Haas *et al.,* identified TBC1D20 as one of two RAB GAPS (the other being RN-tre) that results in loss of normal Golgi morphology upon overexpression and redistribution of Golgi components to the cytosol (Haas et al., 2007). Like RAB18, TBC1D20 has also been shown to localise to lipid droplets (Nevo-Yassaf et al., 2012). However, in the case of TBC1D20, its recruitment to lipid droplets is induced by a viral protein non-structural protein 5A (NS5A), where it serves to impact lipid droplet metabolism and endorse hepatitis C viral life cycle (Nevo-Yassaf et al., 2012). Recently, RAB18 has also been reported to colocalise to NS5A around lipid droplets, preferentially in its GTP bound active form (Salloum et al., 2013). In addition, silencing of RAB18 or expression of a dominant negative (GDP locked) (S22N) mutant reduced the association of NS5A to lipid droplets, suggesting that RAB18 recruits NS5A to lipid droplets, and this recruitment is critical for hepatitis C virus genome replication (Salloum et al., 2013). This suggests a link between RAB18 and TBC1D20 in that RAB18 recruits NS5A to lipid droplets which in turn recruit TBC1D20. A further link has also been observed between TBC1D20 and RAB18 in our lab. Investigation of the localisation of EGFP-RAB18 in human fibroblasts reported an association of RAB18 around lipid droplets, to the endoplasmic reticulum (ER) and staining of the perinuclear region consistent with the *cis*-Golgi. However, examination of EGFP-RAB18 in *TBC1D20* (p.Gln98*) patient fibroblasts identified enhancement of ER staining to the expense of Golgi staining. Furthermore FRAP experiments identified that the EGFP-RAB18 ER interaction is more stable in *TBC1D20* cell lines suggesting that RAB18 may be a substrate for TBC1D20 (Mark Handley, personal communication).

1.6.2 RAB3GAP

RAB3GAP (RAB3GAP1/RAB3GAP2 complex) is a novel RAB GAP that to date is the only reported RAB GAP to lack the TBC domain. RAB3GAP1/2 has not been linked to RAB18 but to the RAB3 family. The RAB3 family are one of the major constituents of synaptic vesicles where they cycle on and off vesicles in coordination with exocytosis of hormones and neurotransmitters. Four members of the RAB3 family exist; RAB3A, RAB3B, RAB3C and RAB3D expressed at varying intensities in brain and endocrine tissues (Schluter et al., 2002). Of these RAB3A is the most abundant, accounting for over 25% of RAB protein binding in synaptosome fractions of the brain (Geppert et al., 1994). RAB3A, RAB3B and RAB3C localise to synaptic vesicles (Fischer von Mollard et al., 1990, Fischer von Mollard et al., 1994, Schluter et al., 2002). RAB3D meanwhile localises primarily to the endocrine pituitary and at lower levels in both exocrine cells and adipose tissue (Schluter et al., 2002). All four proteins have reported roles in cycling on and off synaptic vesicles in coordination with calcium mediated exocytosis of hormones and neurotransmitters (Fischer von Mollard et al., 1991, Geppert et al., 1994, Schluter et al., 2002, Sudhof, 2004) (Figure 1.2).

RAB3 preferentially binds with its effector molecules when in a GTP bound state, and these include the presynaptic proteins RIM, rabphilin and MUNC-13 (Sudhof, 2004). Upon vesicle fusion and exocytosis, GTP bound RAB3 is hydrolysed to GDP. It is this step in the RAB3 cycle that is regulated by the action of a heterodimeric enzyme complex composed of the catalytic subunit RAB3GAP1 and its non-catalytic counterpart RAB3GAP2. Initially Warburg Micro syndrome disease pathogenesis was therefore attributed to dysregulation of the RAB3 cycle, with defects in neurotransmission seemingly consistent with the observed disease phenotype.

RAB3GAP1 is a 981 aa protein of 130 kDa and has two protein-coding transcripts; a major transcript of 24 exons and a minor transcript lacking the first 50 aa encoding exons 1-3 but containing an additional N-terminal 3 aa exon. RAB3GAP1 was originally isolated as a 130 kDa protein from rat brain containing a C-terminal catalytic domain and is ubiquitously expressed in human and zebrafish tissues (Fukui

et al., 1997, Aligianis et al., 2005). RAB3GAP1 acts specifically on members of the RAB3 subfamily (RAB3A, B, C and D) regulating calcium mediated exocytosis of hormones and neurotransmitters (Fukui et al., 1997). RAB3GAP1 has also been identified in a novel proteomic screen for interacting partners of ERGIC-53 (Haines et al., 2012). Mutations in p97 proteins are observed in neurodegenerative disorders including Inclusion Body Myopathy Paget's disease of the bone and/or frontotemporal dementia (IBMPFD) and Amyotrophic Lateral Sclerosis (ALS) and are defective at binding UBXD1. UBXD1 interacts with ERGIC-53 and the RAB3GAP1/2 complex, however, further analysis of the exact protein constituents of this complex remains to be fully elucidated but could point towards the involvement of RAB3GAP1/2, UBXD1 and ERGIC-53 complexes in familial neurodegenerative diseases (Haines et al., 2012). Recently, a role for RAB3GAP1 has also been proposed in acquisition of the epidermal barrier during murine development (Youssef et al., 2013). Upon knock down of *Rab3gap1* by siRNA, abnormalities in Claudin-1 (critical component of tight junctions) expression and defects in barrier formation were observed. Their results suggest that RAB3GAP1 controls exocytosis of Claudin-1 to the cell surface and formation of the epidermal barrier during gestation (Youssef et al., 2013).

RAB3GAP2 is a 1,393 aa protein of 150 kDa encoded by 28 exons. RAB3GAP2 was originally identified as a 150 kDa protein copurifying with RAB3GAP1 upon column chromatography of the synaptic soluble fraction from rat brain (Fukui et al., 1997). *Rab3gap2* was then subsequently cloned in 1998 (Nagano et al., 1998). Like *RAB3GAP1, RAB3GAP2* is ubiquitously expressed in human tissues and similar to RAB3 enriched in the synaptic soluble fraction of rat brain (Nagano et al., 1998). Analysis of *rab3gap2* expression during zebrafish development by *in situ* hybridisation revealed restricted expression in the CNS (Aligianis et al., 2006).

RAB3GAP1 and RAB3GAP2 co-immunoprecipitated as a heterodimeric complex from the synaptic soluble fraction from rat brain (Nagano et al., 1998). However, RAB3GAP2 showed no GAP activity towards RAB3A, nor did it affect the GAP activity or localisation of RAB3GAP1 (Nagano et al., 1998). This suggested that RAB3GAP2 may therefore function as a mediator or regulator to maintain

RAB3GAP1 stability. However, since this study, research has suggested that RAB3GAP1 and RAB3GAP2 may not consistently serve as a complex, with RAB3GAP2 serving distinct functions from those reported for RAB3GAP1. For example, the RAB3 effector RABCONNECTIN-3 coimmunoprecipitates with RAB3 GEF and the noncatalytic subunit RAB3GAP2 but not RAB3GAP1 (Nagano et al., 2002). Further studies identified two subunits of RABCONNECTIN3, alpha and beta and showed an interaction of both subunits with RAB3GAP2 but not RAB3GAP1; but this interaction was not direct (Kawabe et al., 2003). Additionally, many plant species have homologues of RAB3GAP but lack RAB3 isoforms; this suggests that the RAB3GAP1/2 complex may serve functions distinct from that of GTPase activity (Barr and Lambright, 2010). As mentioned above studies are now underway to determine if RAB3GAP2 functions as a GEF for RAB18.

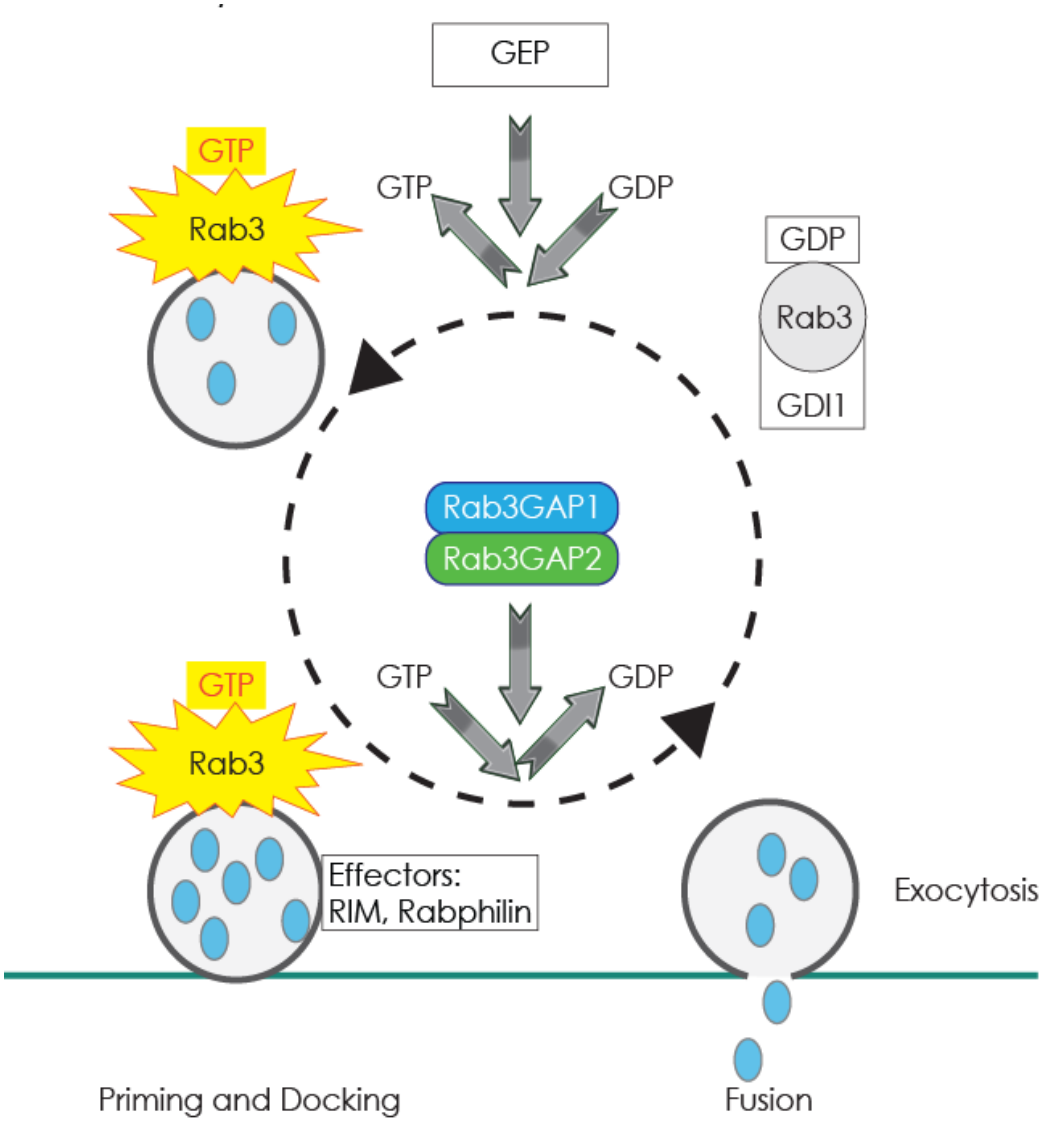

Figure 1.2 The RAB3 cycle

GTP bound 'activated' RAB3 (A, B, C and D isoforms) are geranylgeranylated at 2 C-terminal cysteine residues and inserted into the synaptic vesicle membrane. Following attachment to the target membrane, RAB3GAP1 and RAB3GAP2 form a heterodimeric enzyme complex that specifically stimulates the intrinsic GTP hydrolysis activity and converts GTP bound RAB3 to GDP bound, in coordination with the exocytosis of neurotransmitters and hormones. GDP bound RAB3 is then extracted from the membrane and sequestered in the cytosol by GDI1, where it can be reactivated by GEFs.

1.7 RAB GTPases and disease

RAB proteins function in multiple diverse steps of membrane trafficking and this is reflected in the diverse array of human diseases caused by mutations not only in RAB proteins but also their regulators and many effector proteins. In particular, mutations in RAB proteins give rise to infectious, neurological and endocrinological diseases and RAB dysfunction in many types of cancer is also now coming to light (Stenmark, 2009). In this section I will focus on the role of RAB proteins in pathogenesis of inherited disorders. Loss of function mutations in *RAB27A* have been reported in cases of Griscelli syndrome, type 2 characterised by albinism and immunodeficiency with neurological impairment occasionally observed (Menasche et al., 2000). Due to the well characterised role of RAB proteins in trafficking of synaptic vesicles and neurotransmitters, unsurprisingly mutations in RAB proteins have also been implicated in many disorders of neurological impairment. Mutations in *RAB23* have been associated with autosomal recessive Carpenter syndrome type I (Jenkins et al., 2007), characterised by acrocephaly, skeletal abnormalities, heart defects, growth retardation, developmental delay and microgenitalia (MIM 201000). Loss of function mutations in *RAB39B* cause mental retardation, X-linked 72 (Giannandrea et al., 2010) associated with microcephaly, seizures and in some cases epilepsy (MIM 300271). Mutations in *RAB7* are associated with Charcot-Marie-Tooth type 2B (Verhoeven et al., 2003) characterised by peripheral sensory neuropathy (MIM 600882). Additionally, as described above, loss of function mutations in *RAB3GAP1, RAB3GAP2, RAB18* and *TBC1D20* have been associated with Warburg Micro syndrome. Furthermore, mutations have also been identified in RAB regulatory proteins and effector proteins. For example, mutations in *GDI-alpha* are associated with mental retardation, X-linked 41 (D'Adamo et al., 1998) characterised by moderate to severe mental retardation and dysmorphic facial features occasionally noted (MIM 300849).

In addition to providing insight into genetic disease, as was the aim of this study, mouse models of RAB proteins have also proven invaluable to gain insight into protein function. For example, mutations in *Rab27A* (ashen mice), one of its regulators, RGGTaseα (gunmetal), a RAB27A effector melanophilin (Leaden) or a

motor protein (dilute) all show a similar phenotype of lightened coat colour and defects in pigment granule transport (Wilson et al., 2000, Detter et al., 2000, Mercer et al., 1991, Matesic et al., 2001), showing that a RAB, an effector, a motor protein and a regulator all functioning in the same cellular pathway can and do cause an identical phenotype. This also provides further evidence for all four Warburg Micro syndrome genes functioning in the same pathway, to cause an identical phenotype. Additionally, mutations in *Rab38* have been identified in the 'chocolate' mouse model with partial albinism, a lightened coat colour on C57BL/6J background (Loftus et al., 2002). Analysis of melanosome transport identified that trafficking of TYRP1 from the *trans*-Golgi network to melanosomes was impaired in $Rab38^{cht}$ mice and thus through characterisation of mouse models they have been able to propose *Rab38* as a potential target gene for the genetically heterogeneous disorder OCA (Oculocutaneous albinism) (Loftus et al., 2002). These studies have brought to light two important points; primarily the diseases associated with RAB protein dysfunction can be very different, supporting the idea that RAB proteins serve distinct functions. Secondly, mouse models can be a very powerful tool in dissecting the function of specific RAB proteins.

1.8 Warburg Micro syndrome disease pathogenesis

No histopathological data is available for Warburg Micro syndrome as patient families have declined post mortem. Prior to generation of the $Rab18^{-/-}$ mouse as presented in this study, previous studies focused on the RAB3 family of proteins in disease pathogenesis. RAB3GAP1 and RAB3GAP2 form a heterodimeric complex specifically targeting the RAB3 family of proteins in calcium mediated exocytosis of hormones and neurotransmitters, therefore loss-of-function mutations in either isoform could result in dysregulation of the RAB3 subfamily. Furthermore, mutations in effectors and regulators of the RAB3 subfamily including RAB GDI and RIM1 are implicated in neurological impairment and dysfunction of RAB3 could therefore potentially explain the cognitive features observed. For example, mutations in RAB GDIα cause X-linked mental retardation, type 41 (MIM 300849) and

mutations in the RAB3 effector RIM1 have been reported in cases of cone rod dystrophy additionally exhibiting enhanced cognition (Miki et al., 2007). Additionally, Warburg Micro syndrome patients exhibit microgenitalia, that is reported to be hypothalamic in origin. The RAB3B isoform has been reported to function in gonadotrophin release *in vitro* (Tasaka et al., 1998) and could therefore potentially explain the microgenitalia defect observed. Warburg Micro syndrome patients also present with progressive paralysis and structural brain defects. Furthermore, a reduction in RAB3A levels was noted in post-mortem brains of both Schizophrenia and Alzheimer disease patients (Blennow et al., 1996a, Blennow et al., 1996b), pointing towards an involvement of the synaptic protein in many neurodegenerative conditions.

The majority of studies examining RAB18 function both *in vitro* and *in vivo* have focused on the localisation of RAB18 to lipid droplets and a role in both lipolysis and lipogenesis has been reported (Ozeki et al., 2005, Martin et al., 2005). Recent studies have also reported enlarged lipid droplets in *RAB18, RAB3GAP1* and *TBC1D20* patient cell lines, suggesting that lipid droplet dysfunction may serve as a link between the identified proteins (Leigel *et al.,* 2013, in press). Lipid droplets are the primary storage site for neutral lipids, primarily composed of cholesteryl esters (Martin and Parton, 2006). Cholesterol metabolism disorders including Smith-Lemli-Opitz syndrome (MIM 270400) additionally show similar ocular, genital and neurological abnormalities to those observed in Warburg Micro syndrome including microcephaly, mental retardation, microgenitalia, hypotonia, cataracts, dysmorphic facial features and joint and limb abnormalities are occasionally observed. This suggests that cholesterol dysfunction may also be implicated in disease pathogenesis and should be the basis of future work.

1.9 Use of mouse models to aid understanding of disease

Animal models have proven invaluable in assigning function to previously uncharacterised genes and also dissecting the pathology underlying a vast array of human diseases. Experiments are routinely performed using yeast, worm and fly

models to study many aspects of biology. However, these invertebrate models are highly diverse from humans, lacking many organ systems and showing great variation in genome size. Recent studies have focused on fish models including the zebrafish (*Danio rerio*) due to the transparency of embryos allowing easy visualisation of development, short developmental timescale and amenability to treatment by pharmacological drugs. However, many genes have been duplicated since the divergence of mammalian and aquatic organisms, hindering human genetic studies, and fish physiology is very different from that of mammals. The large degree of conserved synteny between the human and mouse genomes and their similar size has made mouse models an ideal target for the study of human genes and disease. Unlike many other mammals, mouse models have an advantage in that they are reasonably cheap to maintain, have short gestation times and are amenable to colonial life in captivity. Furthermore, congenic lines can be generated by 10 generations backcross matings which eliminates any background variations that may impact on phenotype.

Studies have focused on mouse mutants generated through ENU (*N*-ethyl-*N*-nitrosourea) irradiation of males, many of which recapitulated human disease phenotypes (Rosenthal and Brown, 2007). However this forward genetics approach then required time consuming in-depth follow up studies to identify genes of interest through positional cloning and candidate gene approaches. As a result the underlying genetic mutations for many mutgenised mouse models are still to be identified. Following the completion of the mouse genome project there has been a coordinated effort to introduce specific mutations into endogenous genes that are transmitted through the germline, by homologous recombination in ES cells to knock out genes of interest that are then injected into blastocysts. However, this has the disadvantage of losing gene function from conception often resulting in embryonic lethality thus preventing the examination of late-onset phenotypes. As a result, the Cre/loxP system is becoming increasingly popular to generate temporal or tissue specific knockouts and thus enable examination upon loss of protein function in particular tissues and/or stages of development or adulthood. Additionally, it is now possible to knock in patient mutations or overexpress human genes within the mouse. This is particularly important for genes whose function is critical for embryonic

development and survival and has made it possible to examine phenotypes of a large number of human diseases arising from specific mutations altering gene function without losing expression in its entirety (Rosenthal and Brown, 2007). Mouse models for a variety of human genes are now available and in many cases have provided the first insight not only into protein function but also disease pathogenesis (see tables 6.1 and 6.2).

However, prior to this study characterisation of available animal models for Warburg Micro syndrome have not provided the detailed understanding of disease pathogenesis required. For example the *Rab3gap1* knockout mouse did not recapitulate the characteristic ocular or neurological features of the human disease, suggesting potential species specific or functional redundancy of *Rab3* isoforms (Sakane et al., 2006). Examination of RAB3A levels in the brain identified no significant differences in overall levels but accumulations of GTP bound RAB3A. Normal synaptic architecture was present in the brains of *Rab3gap1* deficient mice, and no abnormalities in synaptic vesicle protein levels including syntaxin, SNAP-23, synaptotgamin-1 and Munc-18 was reported. However, closer examination of synaptic transmission and plasticity by electrophysiology identified inhibition of calcium mediated glutamate release in synaptosomes. Altered short term synaptic plasticity was noted in the hippocampal CA1 with increased facilitation upon repetitive stimulation at a moderate frequency and little to no depression of excitatory postsynaptic current (EPSC) and increased paired-pulse facilitation (PPF) (Sakane et al., 2006).

Additionally, flies lacking *rab3gap1* were reported in a screen for genes involved in homeostatic signalling (Muller et al., 2011). *Rab3gap1* fly models showed abnormalities in synaptic homeostasis. Synaptic homeostasis refers to the upregulation of presynaptic activity when postsynaptic sensitivity is decreased. Muller *et al.*, identified abnormalities both in the upregulation of presynaptic activity in *rab3gap1* knockout flies when treated with PhTX (glutamate receptor antagonist philanthrotoxin-433) to block postsynaptic receptors or when crossed to *GluRIIA* mutant flies with persistent expression of synaptic homeostasis. However, synaptic efficiency during induction and homeostasis was normal in *rab3* mutant flies, and in

double *rab3gap1/rab3* knockout flies. This suggests that loss of *rab3gap1* causes its phenotypic effects via RAB3 gain-of-function effect rather than loss-of-function (Muller et al., 2011).

To elucidate the function of RAB3 proteins in development and synaptic plasticity, *Rab3* knockout mice have been generated (Schluter et al., 2002, Geppert et al., 1994). *Rab3a* knockout mice showed normal synaptic transmission and plasticity in hippocampal CA1 regions (including paired-pulse facilitation and long term potentiation). However, upon repetitive stimulation the depression of excitatory postsynaptic currents increased (Geppert et al., 1994). Following this, to examine the role of RAB3 proteins and remove the possibility of any potential functional redundancy, single, double, triple and quadruple *Rab3* knockout mice have been generated (Schluter et al., 2004). Upon loss of one or two *Rab3* isoforms no impact on viability or fertility was observed. However, triple (when *Rab3a* was knocked out) and quadruple *Rab3* knockout mice died shortly after birth due to respiratory failure. As a result, to examine for any synaptic plasticity abnormalities upon loss of all *Rab3* isoforms, hippocampal neurons were cultured from quadruple *Rab3* knockout mice. A decrease of approximately 30% in evoked responses was noted indicative of a decline in the probability of both synapse and vesicle release and suggestive of a critical function of RAB3 in calcium mediated exocytosis as previously reported, but not gross exocytosis (Schluter et al., 2006).

Tbc1d20 bs mice display ocular and genital abnormalities reminiscent of Warburg Micro syndrome but neurological impairment has not yet been reported. The *bs* mouse phenotype is characterised by bilateral cataracts, micropthalmia, male sterility and glossy coat condition in mice (Varnum, 1983). Further characterisation of the male sterility identified normal copulatory behaviour but germ cell depletion with little or no sperm observed and a failure of acrosome assembly in the immobile sperm that did survive (Sotomayor and Handel, 1986) (Leigel *et al.,* 2013, in press). Leigel *et al.,* 2013 identified onset of cataract development from P16 with bilateral vacuolar cataracts observed by P28. Microphthalmia was additionally observed, with the majority of the ocular phenotype restricted to the lens and lens fibre degeneration observed with large vacuoles and rupture of the lens (Leigel *et al.,* 2013, in press).

Mouse models deficient for *Rab3gap2* have not previously been reported. However, given its restricted sites of expression in the developing zebrafish relevant to the CNS, it would be of interest to generate *Rab3gap2* deficient mice and examine for any morphological/degenerative characteristics. However, mice deficient for *Rab3gap1* also exhibit severe reduction in levels of RAB3GAP2 (Sakane et al., 2006).

From the above literature it is evident that generation and characterisation of a mammalian model recapitulating the ocular and neurological phenotypes observed in Warburg Micro syndrome is critical to understand the pathogenesis of this devastating disease. Characterisation of morpholino knockdown of *rab18* in zebrafish recapitulating ocular and neurological phenotypes including micropthalmia, microcephaly and a reduction in overall body size, pointed towards an all-important role for RAB18 in disease pathogenesis (Bem et al., 2011). Furthermore, analysis of *RAB18* in *TBC1D20* cell lines and the suggestive link between RAB18 and RAB3GAP2 points towards the phenotype of Warburg Micro syndrome surrounding that of RAB18 dysfunction. The principle aim of this thesis was therefore to undertake detailed ocular and neurological characterisation of a novel *Rab18*$^{-/-}$ mouse model created as part of the EUMODIC screen.

1.10 Aims and objectives

Aim 1: Characterise the gross phenotype of *Rab18*$^{-/-}$ mice taking into consideration of the Warburg Micro syndrome patient phenotype

Aim 2: Examine the localisation of GFP-RAB18 in different cell types to determine whether RAB18 localisation may be relevant to a cellular phenotype that is common to all cells and results in pathology or serves a cell-specific/specialised localisation that is relevant to disease in affected cell types.

Aim 3: Undertake detailed characterisation of the ocular phenotypes observed in *Rab18*$^{-/-}$ mice through embryogenesis and adulthood

Aim 4: Undertake detailed neuropathological characterisation of hind limb weakness observed in *Rab18*$^{-/-}$ mice.

a) Examination of synaptic vesicle recycling in *Rab18*$^{-/-}$ mice

b) Investigate neuromuscular pathology and nerve-muscle connectivity in flexor digitorum brevis and lumbrical muscles from the hind paw and the transverse abdominal muscle from the abdominal wall.

c) Analyse axon morphology in the peripheral and central nervous systems through electron microscopy

d) Undertake a detailed proteomics screen to identify alterations in core molecular pathways in *Rab18*$^{-/-}$ mice compared to heterozygote littermates that could potentially explain the observed pathology

Chapter 2 Materials and Methods

2.1 Mouse generation and maintenance

2.1.1 Generation of the *Rab18*$^{-/-}$ mouse

The *Rab18* mouse (EUCOMM Project; strain C57BL/6 x 129P2/Ola (*Rab18*$^{Gt(EUCE0233a03)Hmgu}$) was generated as part of the EUMODIC programme by MRC Harwell. *Rab18* genetrap mice were created using the FlipRosaβGeo cassette inserted into intron 2 of *Rab18*. The genetrap was inserted into 129P2/OlaHsd (E14TG2a) embryonic stem (ES) cells, positive ES cell clones were injected into blastocysts and transferred to pseudopregnant foster mothers to generate chimeras. Mice were bred to 129P2/Ola to retain the ES cell background. Further details of genetrap and targeting can be found at http://www.informatics.jax.org/javawi2/servlet/WIFetch?page=alleleDetail&key=574626

2.1.2 Breeding and maintenance

Rab18+/- heterozygote mice on a 129P2/Ola background were obtained from MRC Harwell as part of the EUMODIC programme. Most analyses in this thesis were performed on *Rab18*$^{-/-}$ mice and littermate controls from C57BL/6J and 129P2/Ola first generation backcrosses. However, mice on pure 129P2/Ola and crossed for 9 generations to C57BL/6J showed the same overt phenotype. *Rab18* mice were maintained as heterozygote breeding pairs in the animal care facilities at the University of Edinburgh under standard conditions. All animal procedures were performed in accordance with Home Office regulations under the personal licence 60/13012.

2.1.3 Isolation of DNA from earclips and tailclips

DNA was isolated from tailclips (embryos and neonates) and earclips (weaned mice) using DirectPCR Lysis Reagent tail and ear respectively (Viagen Biotech Inc). Ear or tailclips were digested in 100µl DirectPCR lysis reagent and 4µl 100µg/mL

proteinase K. Samples were incubated overnight at 55ºC and proteinase K inactivated the next morning at 85ºC for 45 minutes. Samples were vortexed and 100µl H_2O added to dilute the reaction mix. 1µl was used in genotyping PCR as performed in 2.1.4.

2.1.4 Genotyping polymerase chain reaction

The majority of genotyping was performed using the Bio-X-Act long DNA polymerase (Bioline). However, towards the end of my PhD Bioline stopped producing Bio-X-Act and their alternative polymerase MyFII was used instead. For Bio-X-Act a 20µl reaction was set up containing 15.35µl H_2O, 2µl 10x Opti buffer, 0.6µl $MgCl_2$, 0.2µl each 10µM primer, 0.25µl Bio-X-Act, 0.4µl dNTPs and 1µl DNA. For MyFII a 25µl reaction was set up containing 16.5µl H_2O, 5µl MyFII buffer, 1µl each 10µM primer, 0.5µl MyFII polymerase and 1µl DNA. The following PCR programmes were used.

Bio-X-Act programme			MyFII programme		
1) Denaturation	94ºC	3 minutes	1) Denaturation	95ºC	1 minute
2) Denaturation	94ºC	30 seconds	2) Denaturation	95ºC	15 seconds
3) Annealing	58ºC	45 seconds	3) Annealing	58ºC	45 seconds
4) Extension	68ºC	1 minute	4) Extension	68ºC	1 minute
5) Cycle to step 2 for 34 more times			5) Cycle to step 2 for 34 more times		
6) Extension	68ºC	2 minutes	6) Extension	68ºC	2 minutes
7) Hold	15ºC	forever	7) Hold	15ºC	forever

PCR products were analysed by agarose gel electrophoresis as described in 2.2.1.

Table 2.1 Primers used in this thesis

Primer	Application	Sequence
Rab18 Intron2 Fwd	Genotyping PCR	TGCGTTCATGGTTGAGTTTG
Rab18 Intron2 Rev	Genotyping PCR	GGCTGTTTTCAAGGACTCCA
LoxP Rev	Genotyping PCR	CGATGGTGAAGCTTGGATAAC
Rab18 Ex1 Fwd	RT-PCR	AGAGTGGGGTGGGCAAGT
Rab18 Ex5 Rev	RT-PCR	CAAAGGTGTCTCTTCTTGTGACAT
Rab18 Ex3 Fwd	RT-PCR	AAAACGATTTCAGTGGATGGA
Rab18 Ex7 Rev	RT-PCR	GGTTCTCACTTTCCCACAGG
Rab18 Fwd	qPCR	GCTGGTCAAGAGAGGTTCAGA
Rab18 Rev	qPCR	GGTGTCTCTCTTGTGACATCATAG
GalT Fwd	Cloning	GAATTCGAATTCGCCATGAGGCTTCGGGAGCCGCT

GalT Rev	Cloning	GGATCCGGATCCCGGGGCACTGGGACCGAGGTCAA
Rab18 Fwd	Sequencing	GCTATTATAGAGGTGCACAGGG
Rab18 Rev	Sequencing	TTCGTGCAAATTTCAGGCCT

2.1.5 Agarose gel electrophoresis

DNA samples were separated by agarose gel electrophoresis and visualised using a UV transilluminator (BioDoc-It System, UVP). 5x loading dye (50% sucrose in H_2O containing phenol red) was added to each PCR sample, to produce a final 1x solution and 6µl of each reaction run on an agarose gel. Agarose gels were produced by dissolving agarose (Hi-Pure Low EEO agarose, Biogene) in 1x TBE buffer (89mM Tris base, 89mM boric acid and 20mM EDTA) in a microwave at full power producing final concentrations of 1%, 1.5% and 2% agarose/1xTBE (w/v). Once cooled 0.5µg/mL ethidium bromide was added to all gels. A DNA ladder of known sizes (Bioline HyperLadder II) was loaded in lane one of each gel for reference purposes. All gels were run at 80-150V for 20-45 minutes.

2.2 RNA protocols

2.2.1 RNA extraction from tissues

Intact E11.5 embryos (except for tailclips used in genotyping) were dissected and stored in RNAlater, RNA stabilization solution (Qiagen) at 4ºC for short term storage. Embryos were homogenised with a Pellet Pestle Cordless Motor (Kontes) and individual sterile pestle attachments and homogenate passed through a QIAshredder spin column (Qiagen). RNA was then extracted using the QIAamp RNA blood kit (Qiagen) according to manufacturer's instructions. RNA was eluted in 50µl RNase-free water following centrifugation at 10,000rpm for 1 minute. RNA concentration was quantified (see 2.3.2) and samples were stored at -80ºC to preserve RNA quality.

2.2.2 RNA extraction from cells

RNA was isolated from $5x10^5$ MEFs plated to 6 well plates and grown to confluency. Cells were lysed using buffer RLT (Qiagen) and the lysate added onto QIAshredder spin columns (Qiagen). RNA was then extracted using the QIAamp RNA blood kit

(Qiagen, following the purification of total RNA from animal cells using spin technology protocol) according to manufacturer's instructions. On column DNAse digestion with RNase free DNase (Qiagen) was also carried out. RNA was eluted in 30µl RNase-free water following centrifugation at 10,000rpm for 1 minute. RNA concentration was quantified (see 2.3.2) and samples were stored at -80ºC to preserve RNA quality.

2.2.3 RNA/DNA quantification

RNA and DNA concentrations were analysed using Nanodrop 1000 UV-Vis Spectrophotometer (Thermo Scientific) according to manufacturer's instructions.

2.2.4 cDNA synthesis

cDNA was synthesised from RNA using First Strand cDNA Synthesis Kit for RT-PCR (AMV) (Roche). 1µg template RNA was used in each reaction. 20µl reaction mixes were prepared containing 1x reaction buffer, 50 units RNase inhibitor, 5mM $MgCl_2$, 1mM deoxynucleotide mix, 1.6µg Oligo-$p(dT)_{15}$ primer mix and 20 units AMV reverse transcriptase. Samples were incubated in a PCR machine at 25ºC for 10 minutes, 42ºC for 1 hour, 99ºC for 5 minutes, held at 4ºC and samples stored at -80ºC. A negative control minus AMV reverse transcriptase (-RT) was performed alongside each reaction to examine for any contaminating DNA.

2.3.5 RT-PCR

For RT-PCR experiments, RNA isolated from tissues was carried out as in 2.3.1 and cDNA synthesised as in 2.3.3. Intron spanning primers (see table 2.1) were designed using Primer 3 software (http://bioinfo.ut.ee/primer3/). 2µl isolated cDNA was used in PCR with 6µl Reddymix (Thermo scientific), 0.4µM each forward and reverse primer and 3µL H_2O and the following PCR programme.

1) Denaturation 96ºC 5 minutes
2) Denaturation 96ºC 45 seconds
3) Annealing 57ºC 45 seconds
4) Extension 72ºC 45 seconds
5) Cycle to step 2 for 34 more times
6) Extension 72ºC 10 minutes
7) Hold 4ºC forever

Minus RT samples were also run as a negative control. 6µl of each reaction was run on an agarose gel see 2.2.1.

2.2.6 Quantitative RT-PCR

Quantitative RT-PCR was performed using the Roche LightCycler-480 and the Roche Universal Probe Library. Probe-primer combinations were designed using (http://www.roche-applied-science.com/webapp/wcs/stores/servlet/CategoryDisplay?catalogId=10001&tab=Assay+Design+Center&identifier=Universal+Probe+Library&langId=-1).

cDNA isolated from heterozygote and *Rab18*$^{-/-}$ MEFs (Mouse Embryonic Fibroblasts) was diluted 1 in 5 and 2.5µl used in each 10µl reaction containing 0.2µM each primer, 0.1µM probe #33, 1x Probemaster mix LC-480 (Roche) and 2µl H_2O. 1 in 2 diluted wild type cDNA was used to create a standard curve by further dilutions 1 in 10, 5 times. TBP plasmid (0.1ng/µl) was used as a control gene. The following programme was used for qRT-PCR:

1) Denaturation 95ºC 10 minutes
2) Denaturation 95ºC 10 seconds
3) Annealing/Extension 60ºC 30 seconds
4) Cycle to step 2 for 44 more times
5) Extension 40ºC 30 seconds

2.3 Protein protocols

2.3.1 Protein extraction from tissues

Sciatic nerves and lenses were dissected from *Rab18*$^{-/-}$ mice and littermate controls. Nerves and lenses were homogenised in 1x RIPA buffer (Thermo scientific) containing 1x protease inhibitor cocktail (Roche), using a Kontes handheld Pellet Pestle Cordless Motor. Samples were sonicated for 3 x 30 second pulses (Bioruptor, Diagenode) and centrifuged at 15,000 RPM, 4ºC for 15 minutes. The supernatant was then collected and stored at -20 or -80ºC.

2.3.2 Preparation of crude synaptosomes

Brains from wildtype, heterozygote and *Rab18*$^{-/-}$ mice were rapidly dissected and homogenised in isotonic sucrose solution on ice (5mM Tris-HCl, 1mM EDTA, 320mM sucrose, pH 7.4). Homogenates were centrifuged at 900g for 10 minutes and the supernatant collected. Resultant pellets were resuspended in isotonic sucrose solution and centrifuged at 900g for 10 minutes and the supernatant collected. The resultant supernatants were centrifuged at 20,000g for 15 minutes and the pellets combined in buffer A (20mM Tris-HCl, 1M KCl, 250mM sucrose, 2mM $MgCl_2$, 1mM DTT, pH 8.0), further centrifuged at 14,000 RPM for 1 hour and supernatants collected- cytosolic fraction. The resultant pellets were resuspended in detergent containing buffer B (10mM HEPES, 100mM KCl, 2mM $MgCl_2$, 1mM DTT, 5% CHAPS, pH 7.8), rotated for 45 minutes, centrifuged at 14,000 RPM for one hour and supernatants collected- membrane fraction. Cytosolic and membrane fractions were combined, and clarified by dialysis overnight in 25mM Tris-HCl, 50mM KCl, 1mM DTT, 0.1% CHAPS, pH 7.8.

2.3.3 Calculating protein concentration

Protein concentration was calculated using the bicinchoninic acid Protein Assay kit (Pierce). 10µl of each sample was mixed with 180µl reagent (50 parts reagent A to 1 part reagent B) and incubated for 30minutes at 37ºC. Samples were then cooled to room temperature and absorbance read at 562nm using the Thermo Multiskan Spectrum platereader. Bovine Serum Albumin (provided in BCA kit) was used to create a standard curve to calculate protein concentration.

Table 2.2: Antibodies used in this thesis

Antibody	Company (catalogue number)	Species	Dilution	Application
NEFM	DSHB (2h3)	Mouse	1 in 200	IF
β3 tubulin	Abcam (ab18207)	Rabbit	1 in 2000	IF
GM130	BD biosciences (558712)	Mouse	1 in 200	IF
hypophosphorylated NEFH	Abcam (ab82259)	Mouse	1 in 200	IF
NEFL	Chemicon internation (AB9568)	Rabbit	1 in 1000	IF
NEFH	Abcam (ab8135)	Rabbit	1 in 1000	IF
Periaxin	Sigma (HPA001868)	Rabbit	1 in 150	IF
sv2	DSHB (sv2)	Mouse	1 in 100	IF
ApoD	Sigma (SAB2700764)	Rabbit	1 in 1000	WB
APP	abcam (ab2072)	Rabbit	1 in 5000	WB
β3 tubulin	Sigma (T8578)	Mouse	1 in 5000	WB
KIF5A	abcam (ab5628)	Rabbit	1 in 200	WB
Rab3a	cell signalling (3930)	Rabbit	1 in 1000	WB
Rab3gap1	Bethyl laboratories (A310-750A)	Rabbit	1 in 250	WB
Rab3gap2	Abgent (AP9635b)	Rabbit	1 in 250	WB
Rab18	Eurogentec custom made , peptide CESENQNKGVKLSHRE	Rabbit	1 in 200	WB
PMP2	Proteintech (12717-1-AP)	Rabbit	1 in 1000	WB

2.3.4 SDS-PAGE

25µg crude synaptosomes, 3µg or 10µg sciatic nerve or 10µg lens samples were prepared in 1x sample loading buffer (Invitrogen) and 1x reducing agent (Invitrogen) and heated at 70ºC for 10 minutes. Samples were then loaded on a Novex 4-12% Bis-Tris pre-cast gels (Life Technologies) using the XCell surelock mini system with a ladder of known protein sizes in lane one (Novex Sharp protein ladder). Proteins were separated by running the gel at 200V for 55minutes in 1x MOPS running buffer (Invitrogen) plus 1x antioxidant (Invitrogen).

2.3.5 Western blotting

Following SDS-PAGE, the gel was removed from the cassette and proteins were electrophoretically transferred to Hybond nitrocellulose membranes (Hybond ECL, Amersham Biosciences) again using the Invitrogen XCell surelock Mini system. In brief the transfer system was prepared by pre-soaking Whatman filter paper and 5 sponges in transfer buffer (1x transfer buffer (Invitrogen), 10% methanol and 1% antioxidant in H_2O). The system was then prepared in the following order; 2x sponges, Whatmann paper, gel, membrane, Whatman paper, 3x sponges in transfer buffer and transfer carried out at 30V for 60 minutes. Membranes were blocked in 4% Marvel milk (w/v) (Premier foods) in 1xTBST (TBS containing 0.2% tween-20) for one hour at room temperature or overnight at 4ºC. Membranes were then incubated in primary antibody solutions (see Table 2.2 for concentrations) rolling overnight at 4ºC. For loading control experiments, where βIII tubulin was used, membranes were incubated in primary antibody rolling for 1 hour at room temperature. Membranes were then washed for 5 x 5 minutes in 1x TBST and incubated with relevant HRP conjugated secondary antibodies; donkey anti-rabbit and donkey anti-mouse HRP (Amersham ECL western blotting reagent pack) 1:10,000 for 1 hour rolling at room temperature. Membranes were then washed again in 1x TBST for 5 x 5 minutes and proteins detected with Amersham ECL plus western blotting detection system (GE Healthcare). Solutions A and B were mixed at a 40:1 ratio respectively and added to the membrane for 5 minutes at room temperature. Membranes were then passed through water and blotted to remove any

excess solution and exposed to photographic film (GE Healthcare, Amersham Hyperfilm ECL) which was developed using Konika SRX-101A developing system.

2.3.6 Coomassie staining

Alternatively, after SDS-PAGE, the gel was removed from the cassette and incubated in Coomassie (Expedeon, Instant Blue) for one hour rocking at room temperature. The gel was then rinsed in dH_2O and washed overnight in dH_2O at 4ºC. The gel was then imaged using ImageQuant LAS4000.

2.3.7 Densitometry

After Western blotting, membranes to be quantified via densitometry were exposed using the ImageQuant LAS4000 software rather than photographic film. Blot images were imported into ImageQuant TL software (GE Healthcare Life Sciences) and densitometry performed for 1-D gel analysis. Briefly, lanes were manually outlined and the background subtracted. Bands were then detected (with nonspecific bands removed from further analysis) and band intensities calculated. In some experiments band intensities were normalisied to that of βIII tubulin (where stated).

2.3.8 iTRAQ proteomics

The sciatic nerve from three 6week old heterozygote and *Rab18*$^{-/-}$ littermate controls was dissected in PBS and snap frozen in liquid nitrogen. Nerves from each genotype were pooled and homogenized using Kontes pellet pestle cordless motor in 1:40 weight/volume ratio of 0.5M triethylammonium bicarbonate pH8.5, 1% SDS and 1mM PMSF, sonicated for 3 x 30 second pulses and centrifuged at 14,400 RPM, 4ºC for 10 minutes and supernatant collected for iTRAQ undertaken by Dundee Cell Products. The following iTRAQ protocol was provided by Dundee Cell Products.

Protein digestion FASP

FASP Procedure - adapted from (Wisniewski *et al.,* 2009). In total, 50µg of each sample was used for this analysis. Based on the capacity of the filters, 7.5mg of protein lysate were diluted 5 times in 3mL FASP 1 (8M urea, 20mM DDT in 100mM Tris/HCL pH 8.5) and the equivalent of 2.5mg of protein lysate transferred to three Vivacon 500, 30k MWCO HY filters (Sartorius Stedim Biotech, VN01H22). The

sample was buffer exchanged using FASP1 several times by spinning the tube at 7000g to remove detergents. The protein lysate was concentrated by centrifugation and diluted in FASP 2 (100mM Tris/HCl pH 8.5) ready for trypsin digestion. The sample was reduced using 50mM fresh iodoacetamide (IAA) in FASP 2 in the dark for 30 minutes. Lysates were spun down to remove excess IAA and buffer exchanged into FASP 3 (100mM TEAB (triethyl ammonium bicarbonate). Trypsin (Roche) was dissolved in FASP 3 to give a 1:200 enzyme to protein ratio and added in a volume of at least 100µL for 4-6 hrs. This was repeated with fresh trypsin for a further overnight incubation. Lysates were spun down and washed with 0.5M NaCl and 150µL 10% trifluoroacetic acid (TFA) added to reduce the pH. Samples were desalted and then dried as described in (Thingholm et al., 2006).

iTRAQ procedure

1. iTRAQ labelling

iTRAQ labeling was performed using the iTRAQ Reagents Multiplex kit - 4 plex (AB Sciex, UK Ltd). 70µL ethanol was added to each vial of labelling reagent, i.e. labels 114, 115, 116 and 117, vortexed and centrifuged. A two way comparison was undertaken with samples run in duplicate; Rab18 114 and 116, het 115 and 117. Dried samples were re-suspended in 50 µl Dissolution buffer supplied by the kit manufacturer. 25µl of the contents of one vial of label was added to an equivalent volume of sample, vortexed then centrifuged. Samples were incubated with shaking at room temperature for one hour. After incubation, 100µl of water was added to each vial to quench the experiment and left for a further hour on the shaker. The four vials of labels with samples were pooled into one vial then speed vacuumed to dryness. Samples were desalted using as recommended by the iTRAQ kit manufacturer.

2) Offline strong cation exchange (SCX) fractionation

Samples were re-suspended in 100µL of 5mM KH_2PO_4 in 25% ACN (Buffer A), vortexed well and centrifuged for 10 minutes. The system set-up was as follows: Buffer A as above, Buffer B- 500mM KCl in 25% ACN. Gradient: 0-50 % B in 31 minutes, 50% B-100% B in 7mins, flow rate: 200µl/min. Column size was 2 x 200mm, 5µm (Poly LC). 90 µL of sample was injected into the fractionator and samples were collected in separate vials, every 3 minutes for the first two fractions,

then every minute for the remainder of the fractions. All fractions were dried down in a speedvac. Samples were then re-suspended in 1% fluoroacetic acid (FA).

Mass spectrometry analysis

Trypsin-digested peptides were separated using an Ultimate 3000 RSLC (Thermo Scientific) nanoflow LC system. 15µl of sample was loaded with a constant flow of 5µl/min onto an Acclaim PepMap100 nanoViper C18 trap column (100 µm inner-diameter, 2cm; Themro Scientific). After trap enrichment, peptides were eluted onto an Easy-Spray PepMap RSLC C18 column (75 µM x 50cm) (Thermo Scientific) with a linear gradient of 2–45% buffer B (80% acetonitrile with 0.08% formic acid) over 85 minutes with a constant flow of 300nl/min. The HPLC system was coupled to a linear ion trap Orbitrap hybrid mass spectrometer (LTQ-Orbitrap Velos Pro, Thermo Scientific) via a nanoelectrospray ion source (Thermo Scientific). The spray voltage was set to 1.9 kV, and the temperature of the heated capillary was set to 50°C. Full-scan MS survey spectra (*m*/*z* 335–1800) in profile mode was acquired in the Orbitrap with a resolution of 60,000 after accumulation of 1,000,000 ions. The ten most intense peptide ions from the preview scan in the Orbitrap were fragmented by *higher*-energy *collisional dissociation (HCD)* (two-step (6%) collision energy, 40%; activation Q, 0.250; and activation time, 0.1ms) in the LTQ after the accumulation of 10,000 ions. Maximal filling times were 1,000 ms for the full scans and 200ms for the MS/MS scans. Precursor ion charge state screening was enabled, and all unassigned charge states as well as singly charged species were rejected. The lock mass option was enabled for survey scans to improve mass accuracy (Olsen *et al.*, 2004). Data were acquired using the Xcalibur software.

Quantification and bioinformatics analysis

The raw mass spectrometric data files obtained for each experiment were collated into a single quantitated data set using Proteome Discoverer (Thermo Scientific) and the Mascot search engine. Enzyme specificity was set to that of trypsin, allowing for cleavage N-terminal to proline residues and between aspartic acid and proline residues. Other parameters used were: (i) variable modifications, methionine oxidation, protein N-acetylation, gln → pyro-glu; (ii) fixed modifications, cysteine carbamidomethylation; (iii) database: IPImouse_20130120; (iv) iTRAQ labels: standard iTRAQ 4-plex quant method with labels 114-117; (v) MS/MS tolerance:

FTMS- 10ppm, ITMS- 0.6Da; (vi) maximum peptide length, 6; (vii) maximum missed cleavages, 2; (viii) false discovery rate, 1%. Peptide ratios were calculated using the averaged ratios of 114 and 116 and 115 and 117 for samples Het/Rab18 and Rab18/Het. Protein ratios for all labelled peptides sequenced for each protein were normalized on the protein median ratio.

In Silico Protein Network Analysis:

To obtain further insight into potential cellular pathways that may be modified as a result of protein changes identified by our iTRAQ proteomic screen, the Ingenuity Pathways Analysis (IPA) application (Ingenuity Systems) was used. IPA dynamically generates networks of gene, protein, small molecule, drug, and disease associations on the basis of hand-curated data held in a proprietary database as previously described (Wishart et al., 2007) Filtered iTRAQ data was input into IPA. Networks generated by IPA were limited to a maximum of 35 members and experimentally observed relationships. Networks were ranked according to a score calculated via a right tailed Fisher¹s exact test. This test outputs a value that takes into account the original input proteins of interest and the size of the network generated. Further information on the computational methods implemented in IPA can be obtained from Ingenuity Systems (Wishart et al., 2010, Wishart et al., 2007, Wishart et al., 2012).

2.4 Bacterial cloning and DNA methods utilised during cloning

2.4.1 Plasmids used in this thesis

Plasmid	*Source*
GFP-RAB18	Gift from Prof. Francis Barr, Oxford and sequence verified
mCherry-RAB18	Subcloned from GFP-RAB18, Mark Handley
GFP-TBC1D20-RA	Gift from Prof. Francis Barr, Oxford
CFP-GalT	Cloned as a joint effort by Sarah Carpanini and Mark Handley

2.4.2 PCR for cloning

High-fidelity PCR for cloning reactions was carried out using KOD polymerase (Novagen). A 50µl reaction was set up containing 0.5µl human brain cDNA, 5µl 10x KOD buffer, 2µl $MgSO_4$, 5µl dNTP, 10µl 5M betaine, 1.5µl of each forward and reverse primers, 0.5µl KOD polymerase and 24µl H_2O. The following PCR conditions were used;

1) Denaturation 98ºC 30 seconds
2) Denaturation 98ºC 10 seconds
3) Annealing 55ºC 45 seconds
4) Extension 72ºC 90 seconds
5) Cycle to step 2 for 19 more times
6) Extension 72ºC 10 minutes
7) Hold 4ºC forever

2.4.3 Gel extraction

PCR reactions for cloning were run on 1% agarose gels as in 2.1.5 and DNA fragments of interest excised from the gel under UV light. DNA was then extracted using NBS biological DNA spin column gel extraction kit according to manufacturer's instructions.

2.4.4 Transformation of chemically competent cells

For high-fidelity GalT-CFP cloning Top10 cells (Life Technologies) were used for transformations. In brief, 2µl of PCR product was added to 0.5µl salt solution and 0.5µl D-Topo vector and incubated for 10 minutes at room temperature. The reaction mix was then transferred to 14ml round bottom falcon tubes and 25µl Top10 cells added and incubated on ice for 30 minutes. Cells were then heat shocked at 42ºC for 30 seconds and allowed to briefly recover on ice. 125µl of room temperature SOC media was then added and cells were shaken at 225rpm, 37ºC for 1 hour before spreading on antibiotic specific agar plates. Plates were incubated overnight at 37ºC.

2.4.5 Purification of DNA from bacterial cells by miniprep and maxiprep

For miniprep purification of DNA, a single bacterial colony was picked and added to 4ml L-broth containing the appropriate antibiotic and incubated overnight shaking at 225rpm and 37ºC. NBS biologicals spin column plasmid DNA miniprep kit was then carried out according to manufacturer's instructions.

For maxiprep purification of DNA, two colonies were picked from a transformed agar plate and used to inoculate 200mL L-Broth containing the appropriate antibiotic. Cultures were incubated overnight shaking at 225rpm and 37ºC. Qiagen hispeed maxiprep kit was then carried out according to manufacturer's instructions.

2.4.6 Restriction enzyme digestion

To confirm correct insertions, and cut eCFP-N1 destination vectors restriction enzyme digestions were performed. Restriction endonucleases (in this case BamHI and EcoRI, New England Biolabs) were incubated with their corresponding reaction buffers at 37ºC for 4 hours. The reaction mix contained 1µl miniprep, 0.25µl each restriction enzyme, 7.5µl H_2O and 0.1µl BSA where appropriate. Following incubation reactions were run on a 1% agarose gel.

2.4.7 Cloning of GalT-CFP

GalT was directionally cloned from wild type human fibroblast cDNA (first strand AMV kit, Roche). Primers were designed to include EcoRI and BamHI restriction sites for subsequent in frame insertion into ECFP-N1 vectors (see table 2.1). Inserts were initially cloned into pENTR/D-TOPO and used to transform Top-10 cells Invitrogen). The insert was then cloned into EcoRI and BamHI sites of CFP-N1vectors and used to transform XL-1 blue cells (Stratagene) according to manufacturer's instructions and plated on Kanamycin plates.

2.4.8 GFP-RAB18

GFP-RAB18 was a kind gift from Professor Francis Barr, University of Oxford. GFP-RAB18 was used to transform subcloning efficiency DH5α cells (Invitrogen).

1µl of GFP-RAB18 was added to 50µl DH5α cells and incubated on ice for 30 minutes. Cells were then heat shocked at 42ºC for 20 seconds and allowed to briefly recover on ice. 450µl of room temperature SOC media was then added and cells were shaken at 225rpm, 37ºC for 1 hour before spreading on agar plates containing kanamycin. Plates were incubated overnight at 37ºC. Constructs were then used to transform L-broth containing kanamycin and DNA purified by maxiprep. GFP-RAB18 was then sequence verified at the MRC Human Genetics Unit.

2.5 Cell culture

2.5.1 Preparation and maintenance of mouse embryonic fibroblasts (MEFs)

MEFs were isolated from E12.5 embryos from a HET x HET cross. Embryos were dissected in prewarmed MEF media (DMEM (Gibco, Invitrogen) containing 10% fetal calf serum (FCS), 1% penicillin/streptomycin (P/S) and 3.5µl β-mercaptoethanol (Sigma-Aldrich). Tails were removed for genotyping and head and abdominal organs removed and disposed of. Under sterile tissue culture conditions embryos were minced with a sterile scalpel and transferred to 25cm^3 flasks and cultured at 37ºC, 5% CO_2 and 3% O_2. After 3 days clumps of tissue were removed and MEFs were transferred to 75cm^3 flasks, where they were passaged every 2-3 days until passage 8 or earlier if differentiation occurred. Cells were plated at a density of 5x10^5 in 6 well plates for RNA extraction and at a density of 1x10^5 on acid treated coverslips (heated at 50-60ºC for 4-16 hours in 1M HCL, cooled to room temperature, rinsed in dH2O and washed in 50-70-100% ethanol, for a minimum of 10 minutes per wash) or glass bottom 24 well plates for transfection and immunofluorescence.

2.5.2 DNA transfection of MEFs with lipofectamine

For transfection experiments, MEFs were plated at a density of 1x10^5 in 24 well glass bottom plates and transfected using lipofectamine 2000 (Invitrogen). Briefly, 16-24 hours post plating 3µl of lipofetamine per well was added to 50µl of Opti-MEM (Invitrogen) and incubated for 5 minutes at room temperature. Meanwhile,

0.5µg of the desired DNA construct was added dropwise to 50µl of Opti-MEM per well and incubated for 20-30 minutes at room temperature. Media was removed from all wells and replaced with 400µl of Opti-MEM and 100µl of desired DNA construct/Opti-MEM/lipofectamine mix and incubated for 4-6 hours at standard tissue culture conditions. Following incubation, the transfection mixture was removed and replaced with complete media. Cells were returned to standard culture conditions for 16-24 hours prior to microscopic imaging.

2.5.3 Lipid loading of MEFs with oleic acid

For lipid loading experiments, MEFs were plated at a density of $1x10^5$ in 24 well glass bottom plates. 48 hours post plating; MEFs were loaded with 400µM oleic acid for 24 hours. Cells were then fixed in 4% PFA/PBS for 30 minutes and labelled with BODIPY (Life Technologies) in 150mM NaCl in H_2O for 20 minutes at room temperature. Cells were then washed 3 x in PBS and mounted in mowiol containing DAPI.

For live cell imaging of lipids, MEFs were plated at a density of $1x10^5$ in 24 well glass bottom plates. 24 hours post plating, MEFs were loaded with 400µM and 6µM $BODIPY_{558/564}$ C12 (Life Technologies) in complete media. 24 hours later the media was removed and replaced with complete media prior to microscopy on Nikon A1R.

2.5.4 Mouse hippocampal neuron culture conditions

Primary hippocampal neuron cultures were prepared from E17.5 wild type embryos. Brains from E17.5 embryos were dissected in ice cold dissection buffer (HBSS (Gibco) containing 0.7% HEPES (Invitrogen) and 1% Glutamax (Invitrogen). Hippocampai were then dissected from each brain into DMEM (Gibco) containing 10% FBS (Invitrogen) and 1% P/S (Invitrogen). Hippocampai were then pooled and dissociated in 0.1% TrypLE (Invitrogen, diluted 2:3 in dissection buffer) for 45 minutes at 37ºC. TrypLE solution was then aspirated and cells resuspended in 5ml complete DMEM before passing through a 40µm cell strainer. Cells were then spun for 5 minutes at 1500RPM and pellets resuspended in Neurobasal media (Gibco) containing 2% B27 (Invitrogen) and 1% glutamax (Invitrogen). $2.5x10^5$ or $5x10^5$ cells were plated on poly D-lysine (Sigma Aldrich) coated glass bottom 24 well

plates and cells maintained under standard conditions (37ºC, 5% CO_2), with half media changed every 3-4 days.

2.5.5 DNA transfection with Lonza Amaxa AD1 system

After 12-14 days *in vitro* (DIV) differentiated hippocampal neurons were transfected with GFP tagged RAB18 using the Lonza Amaxa AD1 system. Briefly, 17.5µg GFP-RAB18 was added to AD1 solution, producing a final volume of 350µl. The media was removed from all wells and kept and replaced with 350µl AD1/GFP-RAB18 construct mix. Cells were then transfected using the Amaxa AD1 system (Lonza) for 24 well plates and the IF-100 programme, chosen during optimisation for optimal transfection of GFP-RAB18 and neuron viability. Following transfection, the transfection mixture was removed and replaced with 700µl conditioned media. Cells were returned to the incubator and imaged 24 hours later.

2.5.6 Immunocytochemistry

Wild type, heterozygote and *Rab18*$^{-/-}$ MEFs were plated on acid coated coverslips in 24well plates at a density of $1x10^5$ cells per well. After 24 hours, cells were rinsed in PBS and fixed in 4% PFA/PBS for 10 minutes at room temperature. Cells were then permeabilised in 1x TBST (containing 0.1 Triton-X) for 10 minutes at room temperature before blocking in 10% donkey serum in 1x TBST for 1 hour at room temperature. Cells were then incubated in primary antibodies (see table 2.2) in blocking solution overnight at 4ºC. The next morning, cells were washed 3 x 5 minutes in 1x TBST and incubated in AlexaFluor conjugated secondary antibodies (Invitrogen) at a concentration of 1:500 in blocking solution for 1 hour at room temperature. Cells were then washed for 3 x 5 minutes in 1x TBST and mounted with mowiol containing DAPI.

Wild type primary neuron cultures after 12-14 DIV were rinsed in PBS and fixed in 4% PFA/PBS for 10 minutes at room temperature. Cells were then permeabilised in 1x TBST (containing 0.1 Triton-X) for 10 minutes at room temperature before blocking in 10% donkey serum in 1x TBST for 1 hour at room temperature. Cells were then incubated in primary antibodies (see table 2.2) in blocking solution overnight at 4ºC. The next morning, cells were washed 3 x 5 minutes in PBS and

incubated in AlexaFluor conjugated secondary antibodies (Invitrogen) at a concentration of 1:400 in blocking solution for 1 hour at room temperature. Cells were then washed for 3 x 5 minutes in PBS and mounted with mowiol.

2.6 Muscle dissections and immunohistochemistry

2.6.1 Muscle preparation

Lumbrical and flexor digitorum brevis (FDB) muscles from the hind paw and the transverse abdominus (TVA) from the anterior abdominal wall were dissected in PBS. All muscles were fixed rocking in 4% PFA/PBS at room temperature for 15 minutes (mid/late symptomatic mice) or 10 minutes (early symptomatic mice). Muscles were then rinsed several times in PBS and carefully subdissected to remove individual muscles from tendons and the TVA from the abdominal wall. All muscles were then processed for immunohistochemistry.

2.6.2 Immunohistochemistry

All muscles were permeabilised in 4% Triton-X in 1 x PBS for 1.5 hours (mid/late symptomatic) or 0.5 hours (early) and blocked in 4% bovine serum albumin and 2% Triton-X in PBS for 0.5 hours. Muscles were then incubated with primary antibodies in blocking solution (see table 2.2) for either two nights (mid/late) or one night (early symptomatic) rocking at 4ºC. After 4 x 30 minutes washing in PBS, muscles were incubated for 10 minutes in α-bungarotoxin solution conjugated to either TRITC or Alexa647 (5mg/ml, Biotium Inc.). Muscles were then exposed to secondary antibodies for 2.5 hours (swine anti-mouse 488, swine anti-rabbit 488 or swine anti-rabbit 594, all 1:50 Dako). Muscles were then mounted in Mowiol (Calbiochem) on glass slides and coverslips.

2.6.3 Quantification and statistics

Where possible at least 90 endplates from each muscle preparation, chosen at random, were assessed. For occupancy counts individual motor neuron endplates were classified as being fully occupied (neurofilament stain entirely covers the

endplate), partially occupied (neurofilament partially occupies the endplate) or vacant (no neurofilament present in the endplate). To calculate motor endplate area, images of motor endplates were imported into ImageJ and manually outlined. To calculate muscle fibre diameter, three diameter measurements from isolated muscle fibres were measured using ImageJ and the average taken. For G-ratio calculations TEM images were imported into ImageJ and the area of every intact axon and axon plus myelin calculated. From this the diameters were measured and g-ratio calculated (diameter axon/diameter axon plus myelin).

2.7 Histology

2.7.1 Eye histology

Eyes were dissected from neonates and E17.5 embryos and fixed in Davidson's solution (3ml 95% ethanol, 2ml 10% neutral buffered formalin (500µl formalin and 4.5ml phosphate buffer), 1ml glacial acetic acid and 3ml dH_2O)) rolling overnight at 4ºC. Whole embryos (E12.5) or embryo heads (E15.5) were fixed in 4% PFA in PBS overnight rolling at 4ºC. All samples were dehydrated through an ascending ethanol series of 30-50-70% ethanol and stored in 70% ethanol at 4ºC.

2.7.2 Wax embedding

Tissue samples in 70% ethanol were wax embedded using the VIP Tissue Processor. E12.5 embryos, E15.5 heads and P1.5 eyes were subjected to 30 minute cycles, E17.5 eyes to 15 minute cycles and adult eyes to 45 minute cycles. In brief, processing involved 85% ethanol, 95% ethanol, 2 cycles at 100% ethanol, 2 cycles in xylene and 4 cycles in molten paraffin wax at 58ºC. Samples were then embedded in paraffin in plastic cassettes and allowed to set. Samples were cut using a microtome to 7µm sections and mounted on Superfrost glass slides. Slides were then dried at 60ºC overnight prior to staining.

2.7.3 Haematoxylin and eosin staining of paraffin sections

Slides were dewaxed through 3 x 5 minute changes in xylene and 2 x 5 minute changes in 100% ethanol, followed by 2minutes in each of 90%, 70%, 50% and 30% ethanol and rinsed in H_2O. Slides were then stained in Harris' haematoxylin for 5

minutes, differentiated in acid/alcohol (1M HCl in 70% ethanol) for 5 seconds and washed in saturated lithium carbonate solution for 15 seconds. Slides were then counterstained in eosin for 3-5 minutes, quickly rinsed and then washed in 100% ethanol. Slides were then incubated for 3 x 5 minutes in 100% ethanol followed by 3 x 5 minutes in xylene and mounted with DPX (Sigma).

2.7.4 Immunohistochemistry on paraffin sections

Slides were dewaxed through 3 x 5 minute changes in xylene and 2 x 5 minute changes in 100% ethanol, followed by 2 minutes in each of 90%, 70%, 50% and 30% ethanol and rinsed in H_2O. Meanwhile, sodium citrate buffer for antigen retrieval was prepared containing 10mM sodium citrate, pH 6.4 and heated for 10 minutes in a microwave oven. Slides were then added to the sodium citrate buffer and heated for a further 2 x 10 minutes and allowed to cool to room temperature. Slides were blocked in 10% donkey serum (Sigma) in 1x TBST (TBS containing 0.1% triton-X) for 1 hour at room temperature. Slides were then incubated in primary antibodies diluted in blocking buffer (see table 2.2 for antibody concentrations) overnight at 4ºC. Slides were then washed for 3 x 5 minutes in 1x TBST in a coplin jar, rocking at room temperature. Alexafluor conjugated secondary antibodies (Invitrogen) were added at a concentration of 1:500 in 1x TBST, for 1 hour at room temperature in the dark. Slides were washed 3 x 5 minutes in 1x TBST and mounted in Vectashield plus DAPI (Vector labs).

2.7.5 LacZ staining using X-gal

E11.5 embryos were dissected in PBS and fixed in 4% PFA/PBS at 4ºC for 30 minutes. Samples were then washed in PBS followed by 3 x 20 minute washes in detergent wash solution (0.1M phosphate buffer pH 7.3, 2mM $MgCl_2$, 0.1% sodium deoxycholate and 0.02% NP40). Samples were then stained with X-Gal staining solutions (detergent wash containing 0.085% NaCl, 5mM K_4Fe, 5mM K_3Fe and 50mg/mL X-Gal) overnight at 37ºC wrapped in foil. The next morning the staining solution was removed and samples were washed 3 x 20 minutes in detergent wash solution and post-fixed in 4% PFA/PBS overnight at 4º. Stained embryos were then imaged with a macroscope see 2.8.3.

2.7.6 Optical projection tomography

Optical projection tomography (OPT) was performed by Harris Morrison. OPT was carried out on PFA fixed, albino, adult eyes which were mounted in 1% LMP agarose, dehydrated in methanol and then cleared overnight in BABB (1 part benzyl alcohol: 2 parts benzyl benzoate) as per (Sharpe et al., 2002). The eye was then imaged using a Bioptonics OPT Scanner 3001 (Bioptonics, Edinburgh, UK) using tissue autofluorescence (excitation 480 nm/emission 510nm). The scans were reconstructed using Bioptonicsproprietary software and then rendered using Drishti software (Ajay Lamaye, ANU, Canberra, Australia). Movies and stills were created using the same software.

2.8 Synaptic vesicle recycling assays

2.8.1 FM1-43fx staining of synaptic vesicle recycling

For synaptic vesicle recycling assays lumbrical muscles were dissected in oxygenated mammalian Ringer solution (120mM NaCl, 5mM KCl, 2mM $CaCl_2$, 1mM $MgCl_2$, 0.4mM NaH_2PO_4, 23.8mM $NaHCO_3$ and 5.6mM D-glucose bubbled with 95% O_2/5% CO_2). Post-synaptic acetylcholine receptors were stained with TRITC conjugated α-bungarotoxin (5mg/ml, Biotium, Inc.) for 5 minutes and muscles further washed in oxygenated Ringer solution for 5minutes. Synaptic vesicle recycling was then stimulated using a high potassium Ringer solution (75mM NaCl, 50mM KCl, 2mM $CaCl_2$, 1mM $MgCl_2$, 0.4mM NaH_2PO_4, 23.8mM $NaHCO_3$ and 5.6mM D-glucose bubbled with 95% O2/5% CO2) and vesicles labelled with the fluorescent styryl dye FM1-43fx (Molecular probes, 2.5μg/ml in high potassium Ringer) for 15 minutes. Following labelling of synaptic vesicles, mucles were washed for a further 15 minutes in oxygenated Ringer solution and fixed in 4% PFA/PBS for 5 minutes. Muscles were then further washed in PBS for 10 minutes to remove fixative and mounted in mowiol (Calbiochem).

2.8.2 Mouse cortical neuron culture and fluorescent imaging with pHluorin reporter (protocol provided by Dr Sarah Gordon)

Primary dissociated cortical neuronal cultures were prepared from E17.5 *Rab18*$^{-/-}$ (KO) and wild-type (WT) embryos and plated at a density of 1.0 x10^7 cells/coverslip on poly-D-lysine and laminin-coated coverslips. Cells were maintained in Neurobasal media containing B27, 0.5mM L-glutamine and 1% v/v penicillin/streptomycin. After 72 hours cells were supplemented with 1µM cytosine β-d-arabinofuranoside to inhibit glial proliferation.

Fluorescent imaging with sypHy was undertaken as reported previously (Gordon et al., 2011). Cortical neurons were transfected after 7 DIV with 1µg synaptophysin-pHluorin (sypHy, gift from L. Lagnado, LMB Cambridge) using lipofectamine 2000 and imaged after 14-16 DIV. SypHy-transfected cortical cultures were mounted in a Warner imaging chamber with embedded parallel platinum wires (RC-21BRFS) and visualised at 480 nm (>525 nm emission) using a x40 oil immersion objective on a Zeiss Axio Observer D1 epifluorescence microscope. Cultures were subjected to continuous perfusion with imaging buffer (in mM: 136 NaCl, 2.5 KCl, 2 $CaCl_2$, 1.3 $MgCl_2$, 10 glucose, 10 HEPES, pH 7.4) and were stimulated with a train of 300 action potentials delivered at 10 Hz (100 mA, 1 ms pulse width). Cultures were then subjected to alkaline imaging buffer (50 mM NH_4Cl substituted for 50 mM NaCl) to reveal total sypHy fluorescence (total vesicle pool). Fluorescent images were captured at 4 second intervals using a Hamamatsu Orca-ER digital camera (Hamamatsu City, Japan) and processed offline using ImageJ 1.43 software (NIH, USA). Regions of interest of identical size were placed over nerve terminals and the total fluorescence intensity was monitored over time. All statistical analyses were performed using Microsoft Excel and GraphPad Prism (La Jolla, CA) software. The pHluorin fluorescence change was calculated as FΔ/F0, normalised to either the peak stimulus-evoked fluorescence (to calculate endocytic time constant - τ) or to total sypHy fluorescence revealed with alkali buffer (to calculate peak evoked sypHy response). n refers to the number of independent experiments performed.

2.9 Sciatic nerve ligation surgery

Sugery was performed by Derek Thomson. Mice were anesthetised by inhalation with a mixed cocktail of dormitor and vetlar. Once anesthetised a small incision was made on the right leg just below the sciatic notch and the sciatic nerve exposed. The nerve was then tied off with a single tight surgical suture and the incision closed with a surgical suture. Mice were recovered from anesthesia with antisedan and observed for full recovery before returning to standard cages and conditions.

2.10 Microscopy

2.10.1 Fluorescence microscopy

Fluoresence microscopy was performed using a Zeiss Axioplan 2 fluorescence microscope with Plan-neofluar objectives (Carl Zeiss), with filter sets for DAPI, FITC and Texas Red. Images were captured with a Coolsnap HQ CCD camera (Photometrics Ltd.) using scripts written for IPLab/iVision scanalytics software.

2.10.2 Brightfield microscopy

Brightfield microscopy was performed using a Zeiss Axioplan II fluorescence microscope with Plan-neofluar objectives (Carl Zeiss). Images were captured with a QImaging camera (IndigoScientific) using scripts written for IPLab/iVision scanalytics software.

2.10.3 Macroscopic imaging

Macroscopic imaging was performed using a Nikon AZ100 macroscope. Images were captured with a Qimaging Micropublished 5 cooled camera using scripts written for IPLab/iVision scanalytics software.

2.10.4 Confocal microscopy on fixed samples

Confocal microscopy was performed using a Nikon A1R confocal set up, composed of a Nikon Eclipse TiE microscope with resonant scanner and spectral detector. The Nikon A1R setup utilises four lasers (two diode, multiline Argon and DPSS solid

state laser) for excitation at 405, 457, 488, 514, 561 and 638nm and images were captured using NIS elements software (Nikon).

2.10.5 Confocal microscopy-live cell imaging

Confocal microscopy on live cells was perfomed as above using the perfect focus system. Cell viability was maintained using a large incubation chamber regulating temperature at 37°C and 5% CO_2.

2.10.6 Transmission electron microscopy

Sciatic nerves were dissected from mid/late symptomatic *Rab18*$^{-/-}$ mice and littermate controls in PBS. Nerves were then pinned on dental wax and immersion fixed in 4% PFA/2.5% glutaraldehyde in PBS for two nights at 4°C. Following fixation, nerves were washed in PBS and immersed in 1% osmium tetroxide (sigma) overnight. Nerves were then dehydrated through 50%-70%-90%-100% ethanol and propylene oxide and embedded in Durcupan resin overnight. Ultrathin sections (approximately 60nm) were cut and collected on formvar-coated grids (Agar Scientific, UK). Grids were then stained with uranyl acetate and lead citrate and microscopy performed with a Philips CM12 transmission electron microscope equipped with Gatan camera.

2.11 Statistical analysis

All data was collected and analysed using ImageJ and GraphPad Prism 5 software where mean ± SEM, N= number of mice and n= number of muscles quantified. Statistics were calculated using the Mann-Whitney or unpaired student t-tests where appropriate.

Chapter 3 Generation and phenotypic characterisation of a novel *Rab18*$^{-/-}$ mouse

3.1 Introduction

Causative loss-of-function mutations for Warburg Micro syndrome have previously been identified in *RAB3GAP1* (Aligianis et al., 2005), *RAB3GAP2* (Borck et al., 2010), *RAB18* (Bem et al., 2011) and *TBC1D20* (Liegel *et al.*, 2013, paper in press). However mice lacking *Rab3gap1* do not recapitulate the disease phenotype (Sakane et al., 2006) and studies characterising the *blind sterile* mouse despite reporting ocular and endocrine abnormalities have not described any neurological deterioration (Liegel *et al.*, 2013, paper in press). A mammalian model recapitulating both the ocular and neurological aspects of Warburg Micro syndrome was therefore critical to provide insights into disease pathogenesis. Previous studies using morpholino knockdown of *rab18a* and *rab18b* in zebrafish suggested a role for RAB18 in normal eye and brain development (Bem et al., 2011). To investigate the role of RAB18 in disease, *Rab18* genetrap mice were generated by MRC Harwell as part of the EUMODIC (The European Mouse Disease Clinic) screen; a large consortium of 18 research clinics undertaking primary mouse phenotyping assessment (www.eumodic.org). *Rab18* genetrap mice were created using the FlipRosaβGeo cassette inserted into 129P2/OlaHsd (E14TG2a) embryonic stem (ES) cells (Figure 3.1). Details of the genetrap and targeting can be found at http://www.informatics.jax.org/javawi2/servlet/WIFetch?page=alleleDetail&key=574626. Positive ES cell clones were injected into blastocysts and transferred to pseudopregnant foster mothers to generate chimeras. Mice were bred to 129P2/Ola to retain the ES cell background, in keeping with the EUMODIC programme for phenotypic assessment.

The FlipRosaβGeo cassette is composed of a splice acceptor site (SA), a promoterless reporter gene and a premature polyadenylation and termination sequence (pA). The gene trap is inserted into an intron of a protein coding gene. The transcript is expressed from the endogenous promoter in frame to the β-geo reporter

gene and prematurely terminated at the polyadenylation sequence, resulting in a truncated version of the protein which is likely to be non-functional. The cassette is flanked by frt and F3 sites, targets for FLPe recombinase and loxP and lox5171 sites, targets for Cre recombinase, enabling directional recombination under the action of FLPe and Cre to generate a site-specific or temporal specific conditional allele (Schnutgen et al., 2005).

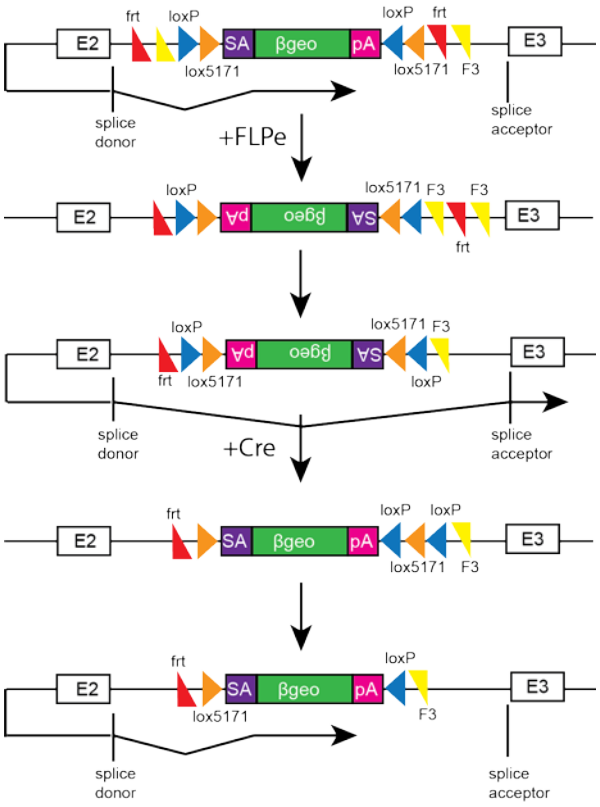

Figure 3.1- The FlipRosaβGeo cassette

Schematic of the FlipRosaβGeo cassette adapted from Schnutgen 2005. Transcripts are transcribed from the endogenous promoter to the splice acceptor site in the genetrap cassette and terminated prematurely at the polyadenylation sequence. When crossed with FLPe the cassette is inverted onto the antisense, non-coding strand at either FRT or F3 sites and excises paired heterotypic repeats, locking the cassette in its inverse orientation. When crossed with Cre the cassette is reinverted onto the sense, coding strand at either loxP or lox5171 sites, repairing splicing and reintroducing the mutation. LTR, long terminal repeat; frt and F3 target for FLPe recombinase, loxP and lox511 targets for Cre recombinase; SA, splice acceptor; βgeo, β-galactosidase/neomycin phosphotransferase fusion gene; pA, polyadenylation sequence.

The *Rab18* genetrap mouse was created using the *Rab18*$^{Gt(EUCE0233a03)Hmgu}$ allele (hereafter referred to as *Rab18*$^{-}$), inserting the genetrap cassette into intron 2 of *Rab18*. This allele was chosen as the homozygous L24Q (c.71T>A, p.Leu24Gln) *RAB18* patient mutation in exon 2 has previously been shown to be pathogenic resulting in a functionally null protein that is incapable of binding guanine (Bem et al., 2011). Additionally, RAB protein structure is highly conserved. All RAB proteins have a C-terminal hypervariable domain with one or two cysteine residues that are prenylated by RAB GGTase (Rab geranylgeranyltransferase) (Pereira-Leal et al., 2001). This prenylation is essential for membrane localisation (Kinsella and Maltese, 1992) and as a result a small unprenylated polypeptide without this geranygeranylation target site is unlikely to be functional.

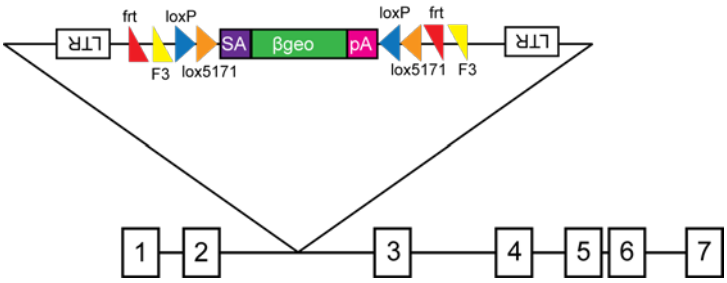

Figure 3.2- Generation of *Rab18*$^{-/-}$ mice
Rab18$^{-/-}$ mice, allele *Rab18*$^{Gt(EUCE0233a03)Hmgu}$ were generated from ES cells with insertion of the FlipRosaβGeo cassette into intron 2 of *Rab18*. Black boxes represent *Rab18* exons.

In this chapter I describe the genotyping and phenotypic characterisation of a novel *Rab18*$^{-/-}$ mouse model that recapitulates many of the characteristic features of Warburg Micro syndrome including congenital cataracts, atonic pupils and progressive hind limb weakness.

3.2 Results:

129P2/OlaHsd *Rab18*$^{+/-}$ heterozygotes were obtained from MRC Harwell and intercrossed with littermates to generate a pure 129P2/OlaHsd strain. However, as 129P2/Ola females are poor breeders with small litter sizes, 129P2/OlaHsd heterozygotes were also backcrossed onto C57BL/6J. No phenotypic differences were observed between the two strains. The majority of experiments described in this thesis were undertaken on *Rab18*$^{-/-}$ mice backcrossed to C57BL/6J for one or two generations however, gross phenotypic analysis of *Rab18*$^{-/-}$ backcrossed for nine generations revealed no overt differences.

3.2.1 Genotyping of *Rab18*$^{-/-}$ mice

PCR primers were designed to distinguish between wild type, heterozygote and *Rab18*$^{-/-}$ mice (Figure 3.3). Primers F1 and R1 were designed in intron 2 upstream and downstream of the cassette insertion site respectively. Primer R2 was designed within the loxP site of the genetrap cassette. DNA was extracted from tail clip (embryos) or ear clip (weaned pups) from each mouse and amplified by PCR. Multiplex PCR often gave variable results with the wild type allele dominating over the mutant allele, and heterozygote mice often mistyped as wild type. As a result two PCRs were routinely set up for each mouse. Primer F1 and primer R1 (Figure 3.3A) produced a band of 467 bp for the wild type allele and primer F1 and primer R2 (Figure 3.3C) produced a band of 825 bp for the mutant allele. Upon insertion of the genetrap cassette the region between primers F1 and R1 was too large to amplify by the PCR protocol used and no band appeared in the wild type reaction. Heterozygote *Rab18*$^{+/-}$ mice showed bands in both PCR reactions. All genotyping results were confirmed by phenotyping blind to genotyping (see below). Figure 3.3D shows an example of genotyping PCR and gel electrophoresis.

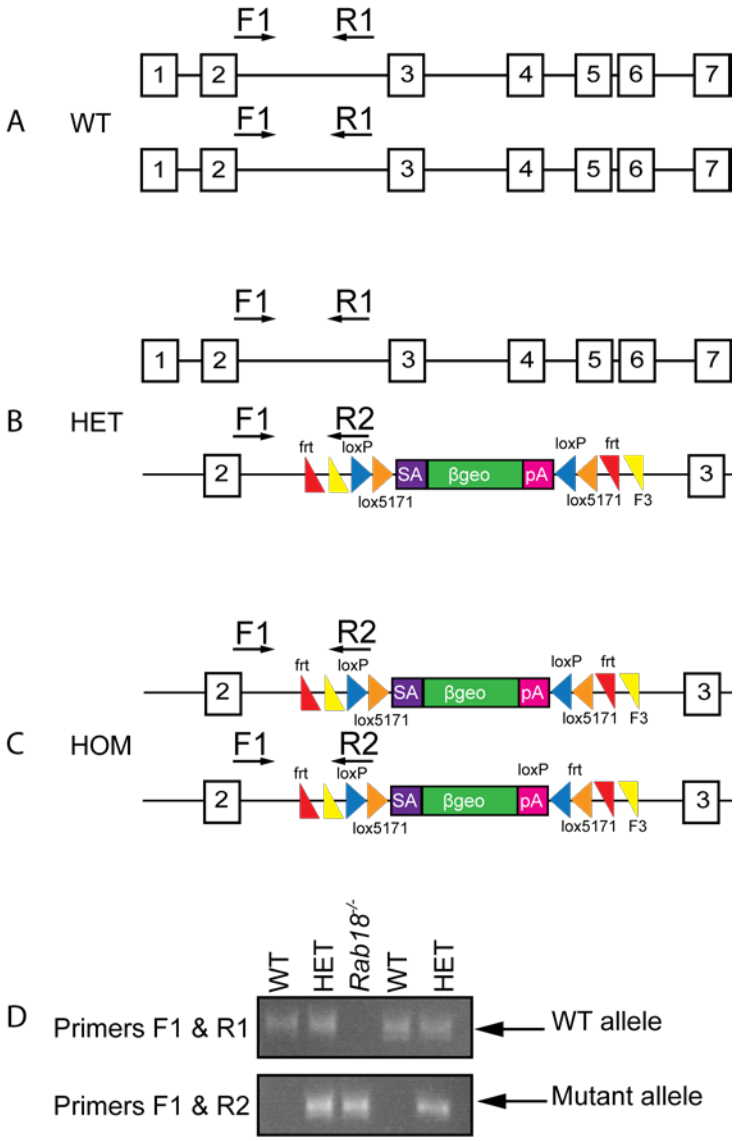

Figure 3.3 PCR genotyping of *Rab18*$^{-/-}$ mice

Rab18$^{-/-}$ mice are genotyped by PCR and gel electrophoresis for presence or absence of the genetrap cassette. (A-C) Schematic of the wild type (WT), heterozygote (HET) and *Rab18*$^{-/-}$ alleles, arrows F1, R1 and R2 represent primer locations used for genotyping. (D) PCR genotyping of WT, HET and *Rab18*$^{-/-}$ mice. Primers F1 upstream and primer R1 downstream of the cassette shows a band of 467 bp for the WT allele. Primer F1 and Primer R2 in the loxP site of the cassette shows a band of 825 bp for the mutant allele. Heterozygote mice show both bands.

3.2.2 Preliminary data suggests *Rab18* is ubiquitously expressed at E11.5

The FlipRosaβGeo genetrap cassette contains a βGeo reporter gene. As the cassette is transcribed from the endogenous *Rab18* promoter this can be used to provide a

visual readout of *Rab18* gene expression. Analysis of β-galactosidase expression by X-gal staining in embryonic day 11.5 (E11.5) embryos showed *Rab18* to be ubiquitously expressed in developing embryos (Figure 3.4).

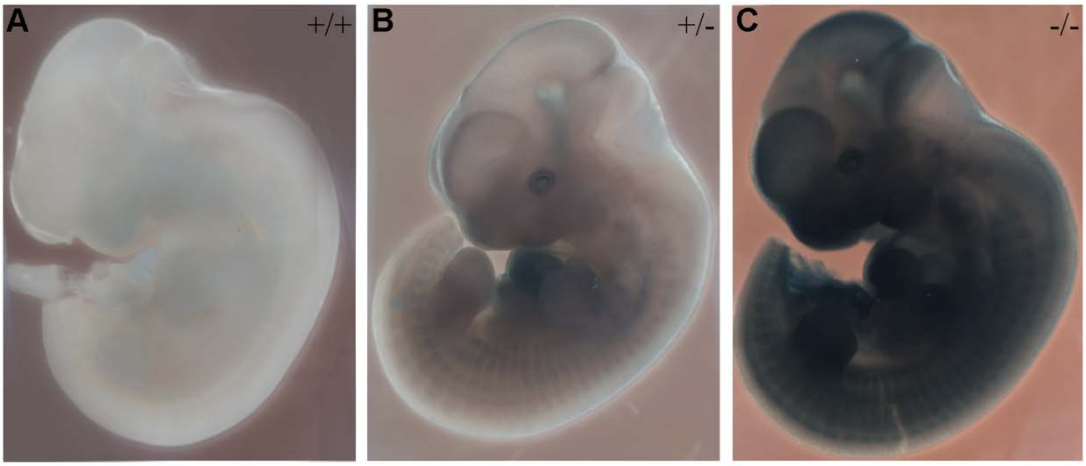

Figure 3.4 *Rab18* appears ubiquitously expressed in E11.5 embryos

The FlipRosaβGeo cassette inserts a βGeo reporter gene under the control of the endogenous *Rab18* promoter, marking *Rab18* gene expression. In E11.5 embryos *Rab18* is ubiquitously expressed in heterozygote (B, HET) and $Rab18^{-/-}$ (C) embryos compared to wild type (A, WT).

3.2.3 $Rab18^{Gt(EUCE0233a03)Hmgu}$ allele represents the null phenotype of RAB18

The genetrap cassette is designed to initiate transcription from the endogenous promoter and terminate it prematurely at the polyadenylation sequence resulting in a severely truncated protein which should be non-functional. To examine the consequence of the genetrap insertion on *Rab18* expression, RNA was isolated from E11.5 embryos and from which cDNA was synthesised for RT-PCR and qRT-PCR analysis. Reverse transcriptase PCR (RT-PCR) using primers flanking the genetrap insertion site (exons 1-5, red arrows in Figure 3.5A) showed very weak *Rab18* expression in $Rab18^{-/-}$ embryos (Figure 3.5B upper panel). Reduced expression levels were also apparent in the heterozygote compared to wild type control, however only

one sample was examined in the analysis. Analysis using primers 3' to the cassette insertion site (exons 3-7, blue arrows in Figure 3.5A) detected *Rab18* expression in all genotypes examined, albeit at a slightly lower intensity in *Rab18*$^{-/-}$ mice. This suggested the possibility of an alternative transcription start site, however, quantitative RT-PCR (qRT-PCR) using primers amplifying exons 4-5 showed no residual *Rab18* mRNA expression compared to the control gene TBP (TATA binding protein) in *Rab18*$^{-/-}$ mouse embryonic fibroblasts. Additionally, Western blot analysis on wild type, heterozygote and *Rab18*$^{-/-}$ sciatic nerve using an antibody raised against the C-terminal of RAB18 showed a doublet band of the correct size (23 kDa) in control samples which was absent in *Rab18*$^{-/-}$littermates. I can therefore conclude that the *Rab18*$^{-/-}$mice represent the null phenotype of *Rab18.*

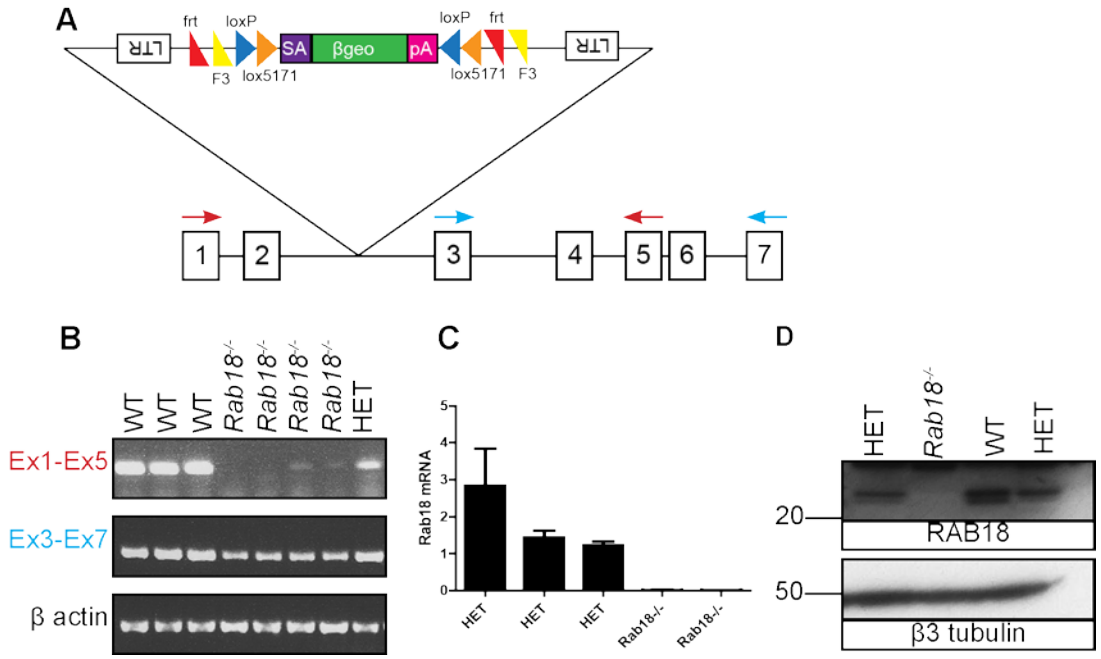

Figure 3.5 *Rab18*$^{-/-}$ mice represent the null phenotype of RAB18
Rab18$^{-/-}$ mice were generated by insertion of the FlipRosaβGeo genetrap cassette into intron 2 of *Rab18.* (A) Red and blue arrows represent primers used in RT-PCR. (B) RT-PCR analysis for *Rab18* mRNA expression in E11.5 wild type (WT), heterozygote (HET) and *Rab18*$^{-/-}$ embryos. Primers flanking the genetrap cassette (exons 1-5, red arrows in A) showing residual mRNA expression in *Rab18*$^{-/-}$ embryos. Primers C-terminal to the cassette insertion site (exons 3-7, blue arrows in A) show bands in all genotypes examined albeit at a slightly lower intensity in *Rab18*$^{-/-}$ suggesting an alternative transcription start site, β-actin was used as a loading control. (C) quantitative RT-PCR analysis (graph shows mean and standard deviation for 3 technical replicates) shows no residual transcript in *Rab18*$^{-/-}$ mouse embryonic fibroblasts normalised to control gene TBP. (D) Western blot analysis in

Rab18$^{-/-}$ sciatic nerves with an antibody targeting the C-terminal hypervariable domain of RAB18, shows no RAB18 protein expression, β3 tubulin was used as a loading control. Numbers to the left of the blots represent molecular weight in kDa.

3.2.4 Lack of gross organ pathology in *Rab18*$^{-/-}$ mice

To determine the consequence of loss of *Rab18*$^{-/-}$ on gross organ development and viability a comprehensive necropsy analysis was undertaken by pathologist Dr David Brownstein on two 15 week old mid/late symptomatic *Rab18*$^{-/-}$ mice and heterozygote and wild type littermate controls. Mice were examined for histopathology including but not limited to the following (Appendix 2); internal organs (for example heart, liver and lungs), head, long bones, thigh muscle and spinal cord. No significant differences were found between any of the three genotypes examined (Figure 3.9, representative pictures). This suggests that loss of *Rab18*, despite being ubiquitously expressed, does not affect gross organ development but rather, that the pathology maybe restricted to the cellular level.

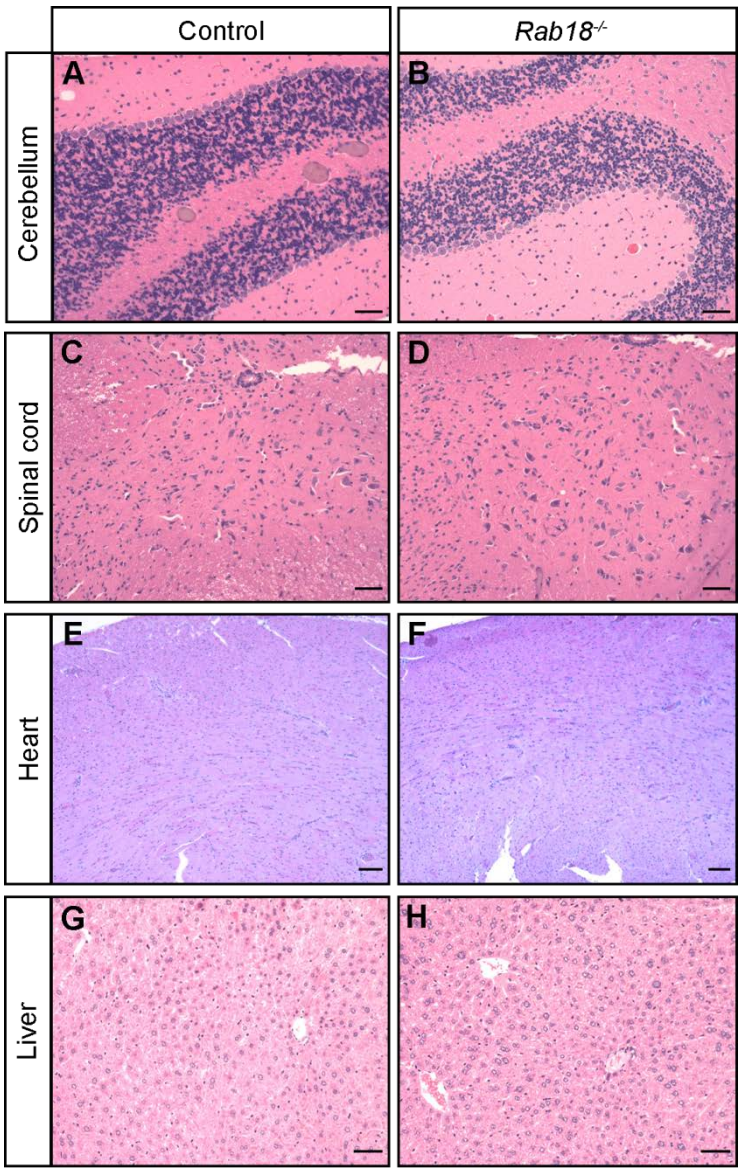

Figure 3.6 Loss of *Rab18* does not affect gross organ histology

15 week old mid/late symptomatic *Rab18*$^{-/-}$ mice and littermate controls (N=2) underwent detailed necropsy analysis performed by David Brownstein. (A-H) Representative micrographs of cerebellum (A-B), spinal cord (C-D), heart (E-F) and liver (G-H) from control and *Rab18*$^{-/-}$ littermates stained with H&E showing no gross organ pathology. Panels A-D and G-H scale bar represents 50µm, E-F scale bar represents 100µm.

3.2.5 General phenotyping of *Rab18*$^{-/-}$ mice

Warburg Micro syndrome patients present with abnormalities affecting the ocular, neurological and endocrine systems (Aligianis et al., 2005, Borck et al., 2010, Bem et al., 2011, Warburg et al., 1993, Handley et al., 2013). I therefore performed gross phenotypic analysis of *Rab18*$^{-/-}$ mice taking into consideration the Warburg Micro syndrome patient phenotype. *Rab18*$^{-/-}$ mice were viable and fertile. At eye opening (approximately postnatal day 12, P12) *Rab18*$^{-/-}$ mice presented with dense nuclear congenital cataracts (Figure 3.6A). Examination of the pupillary response with the mydriatic agent tropicamide was undertaken by Lisa McKie and identified permanently constricted pupils that do not respond to dark or mydriatic agents (data not shown). *Rab18*$^{-/-}$ mice therefore recapitulated characteristic Warburg Micro syndrome ocular phenotypes with complete penetrance. This allowed me to distinguish *Rab18*$^{-/-}$ mice from wild type and heterozygote littermates blind to genotyping.

From three weeks of age, when elevated by the tail, *Rab18*$^{-/-}$ mice displayed abnormal hind limb clasping compared to littermate controls (Figure 3.6B, left wild type, right *Rab18*$^{-/-}$). This abnormal clasping reflex is observed in many mouse models for neurodegenerative disease and is seen as an indicator of neuronal dysfunction (Lalonde and Strazielle, 2011). As the mice age, the phenotype progressively deteriorated with variation in age of onset; the hind limb clasping became more prominent, the gait splayed and a noticeable decline in movement was observed. Due to home office regulations all mice were culled at this stage (Figure. 3.6C) and are referred to as mid/late symptomatic throughout the remainder of this thesis. Taken together, *Rab18*$^{-/-}$ mice recapitulated many of the characteristic ocular and neurological features of Warburg Micro syndrome. Heterozygote mice were indistinguishable from wild type littermates and unless distinguished were used interchangeably in all subsequent experiments.

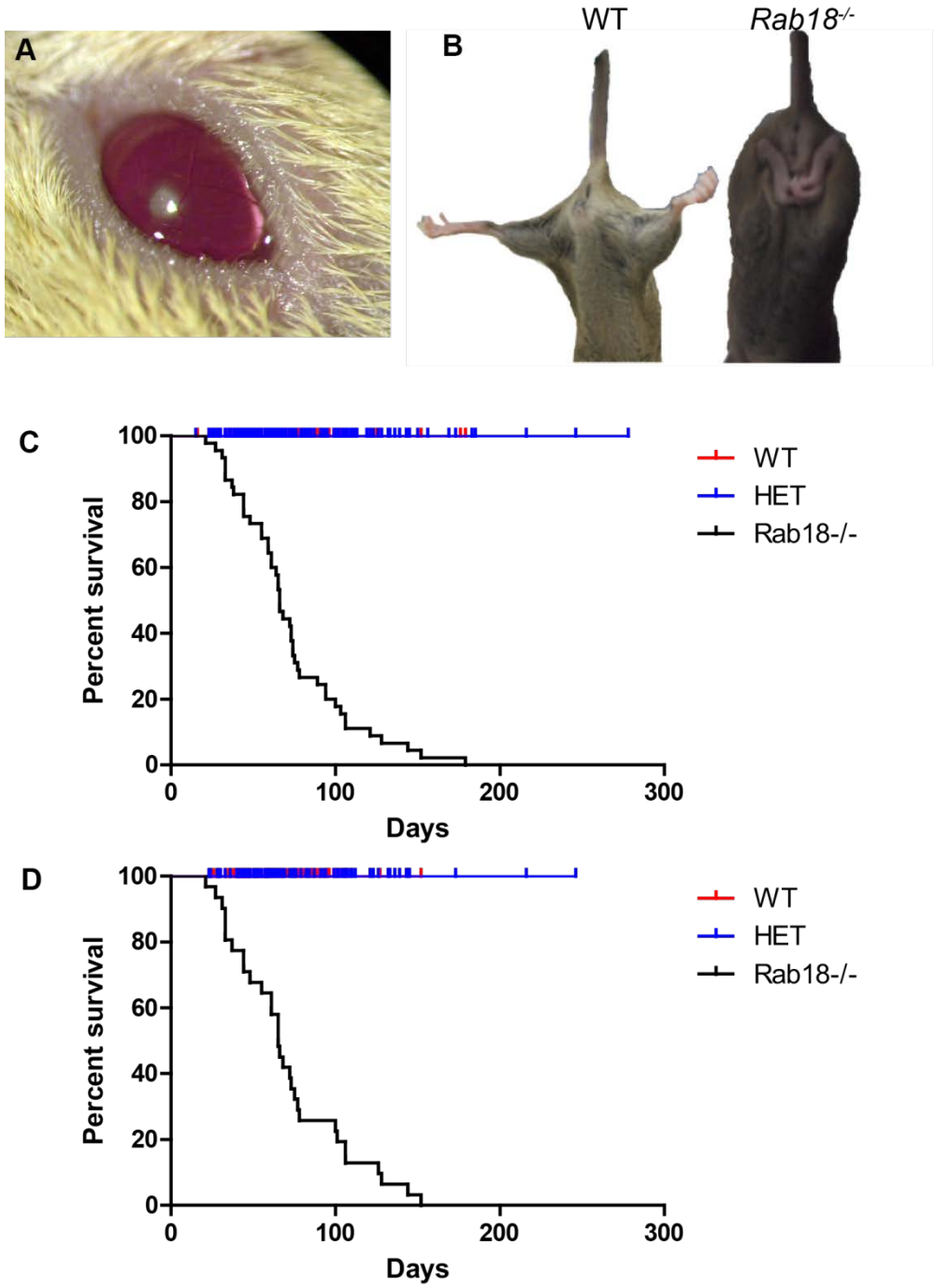

Figure 3.7 *Rab18*$^{-/-}$ mice show congenital nuclear cataracts, progressive hindlimb spasticity and reduced survival, recapitulating the Warburg Micro syndrome disease phenotype

Gross phenotypic analysis of *Rab18*$^{-/-}$ mice. At eye opening (approximately P12) *Rab18*$^{-/-}$ mice are identifiable from littermates by the presence of congenital nuclear cataracts. (A) Slit lamp picture of cataracts in *Rab18*$^{-/-}$ adult lens. From three weeks of age *Rab18*$^{-/-}$ mice show abnormal hind limb clasping when elevated by the tail (B,

Rab18$^{-/-}$) compared to littermate controls (B, WT) who spread their hind limbs. The hind limb phenotype progresses to splayed/weak limbs and the mice are culled at mid/late symptomatic time points. (C) Kaplan-Meirer Survival curve of all mice irrespective of background, log-rank (Mantel-Cox) test, Chi-squared 412.2, 2df, $p<0.0001$. (D) Kaplan-Meier Survival curve of all mice first generation backcross to C57BL/6J, log-rank (Mantel-Cox) test, Chi-squared 254.5, 2df, $p<0.0001$.

Rab18$^{-/-}$ mice were viable and fertile, however both heterozygote and *Rab18*$^{-/-}$ mice were found at non-Mendelian ratios at weaning (Table 3.1, Chi-squared $p<0.0001$). *Rab18*$^{-/-}$ mice have been backcrossed to C57BL/6J for nine generations to generate a more congenic line, and studies are currently underway to determine whether this reduction in numbers is still observed. While carrying out the backcross, I also analysed the numbers of wild type and heterozygote mice born from a male heterozygote x female C57BL/6J cross and identified a reduction in the number of heterozygotes born (Table 3.1, Chi-squared $p<0.0001$). However, no significant differences were observed when male C57BL/6J mice were crossed to female heterozygotes. It must be noted that the number of litters examined when a female heterozygote was used in the cross was far fewer than male (11 litters compared to 44). This reduction in heterozygotes could potentially be attributed to a sperm abnormality, with wild type sperm dominating over mutant and hence more wild type mice born. However, it must be noted that loss of a functional allele does not necessarily mean that the protein would be absent from the sperm, indeed HET *bs* mice can still pass on the null *Tbc1d20* allele while the homozygotes are sterile (Leigel *et al.*, 2013, paper in press). I therefore performed histological analysis of wax-embedded testis from control and *Rab18*$^{-/-}$adult littermates and identified normal testis morphology with sperm heads and tails clearly visible (Figure 3.7). To further examine the fertility of *Rab18*$^{-/-}$ mice, crosses were set up between female *Rab18*$^{-/-}$ mice and heterozygote males and male *Rab18*$^{-/-}$ with heterozygote females. Only one attempt was taken to breed with a female *Rab18*$^{-/-}$ as she died very shortly after giving birth. Attempts at breeding female heterozygotes to *Rab18*$^{-/-}$ males proved successful. Together our results suggest that *Rab18*$^{-/-}$ mice are fertile.

Despite the reduction in number of *Rab18*$^{-/-}$ and heterozygote mice observed at weaning, analysis of different embryonic stages (E11.5-E17.5, Table 3.1) showed no significant difference in numbers. This suggested that heterozygote and *Rab18*$^{-/-}$

mice may die at or immediately following birth. However, no noticeable reduction in litter size was observed at weaning (average of 7.7 pups for HET x HET crosses compared to an average of 6.6 for male HET x female C57BL/6J and 7.125 for male C57BL6/J and female HET). It must also be noted that the number of embryonic litters examined was far smaller than those weaned.

Table 3.1 *Rab18*$^{-/-}$ mice are found at non-Mendelian ratios at weaning

Genotype	WT	HET	*Rab18*$^{-/-}$	No. litters	Chi-squared
All HET x HET litters weaned	336	388	164	118	p<0.0001
Female HET x male C57BL/6J	188	104		44	p<0.0001
Male HET x female C57BL/6J	38	34		11	Ns
E11.5 HET x HET	6	16	11	4	Ns
E12.5 HET x HET	12	20	10	5	Ns
E13.5 HET x HET	6	13	9	3	Ns
E15.5 HET x HET	18	38	13	9	Ns
E16.5 HET x HET	1	7	3	1	Ns
E17.5 HET x HET	26	46	23	13	Ns

Ns-not significant

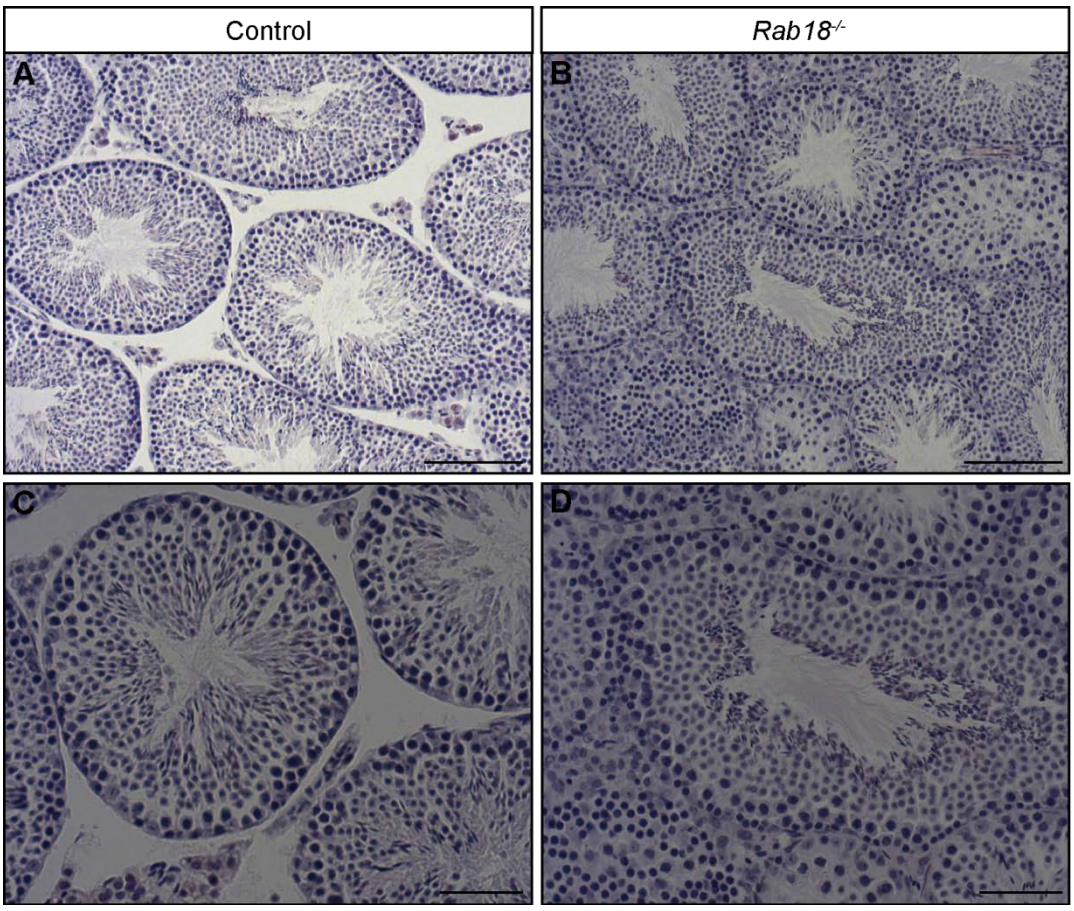

Figure 3.8 Loss of *Rab18* does not result in gross testis histopathology
Haematoxylin and eosin histological analysis of wax embedded testes from 17 week old control (A and C) and *Rab18*$^{-/-}$ (B and D) littermates showing no gross testes pathology with sperm heads and tails clearly visible. N=1, A-B scale bar represents 100µm, C-D scale bar represents 50µm.

Initial analysis of *Rab18*$^{-/-}$ mice crossed for one generation to C57BL/6J showed no obvious noticeable differences in size or weight. However, after backcrossing for 9 generations, preliminary weight measurements on a defined background have shown a reduction in weight of *Rab18*$^{-/-}$ mice at weaning (Table 3.2 and Figure 3.8, N=2). However, one mutant went on to gain weight comparable to littermate controls at 6 weeks of age whereas the other remained runted. Further studies are underway to examine additional mice.

Table 3.2 9th generation to C57BL/6J *Rab18*$^{-/-}$ mice weigh less than littermate controls at weaning

	3wk	4wk	5wk	6wk
WT	6.9g	10.9g	16g	19.0g
WT	6.1g	10.6g	14.8g	17.0g
HET	7.2g	10.8g	13.3g	15.0g
Rab18$^{-/-}$	5.1g	4.5g	5.6g	7.0g
Rab18$^{-/-}$	4.9g	6.4g	10.0g	14.0g

Rab18$^{-/-}$ mice crossed for nine generations to C57BL/6J were weighed every week from weaning (3 weeks of age). Preliminary data shows *Rab18*$^{-/-}$ mice (N=2) to be reduced in weight at weaning.

3.3 Discussion

In this chapter I describe the genotyping and phenotypic characterisation of a novel *Rab18*$^{-/-}$ mouse model. I have shown that *Rab18* is ubiquitously expressed in the developing embryo. To examine the role of RAB18 in disease pathogenesis, *Rab18*$^{-/-}$ genetrap mice were generated using the FlipRosaβGeo cassette and are null for *Rab18*. *Rab18*$^{-/-}$ mice were viable and fertile. I have shown that loss of *Rab18* does not cause gross developmental defects but specific abnormalities in the lens and hind limbs, recapitulating many of the characteristic ocular and neurological features of Warburg Micro syndrome.

3.3.1 RAB18 appears ubiquitously expressed in the developing embryo and *Rab18*$^{-/-}$ mice represent the null phenotype of *Rab18*

Rab18$^{-/-}$ mice were created using the FlipRosaβGeo cassette inserted into intron 2 of *Rab18.* Analysis of β-galactosidase expression by X-gal staining showed that *Rab18* is ubiquitously expressed in E11.5 developing embryos (Figure 3.4). However, this is preliminary analysis; in detailed expression analysis would require immunohistochemistry and RNA *in situ* hybridisation experiments to be performed at various ages of embryogenesis and in different organ types of the adult. RAB18 ubiquitous expression has previously been demonstrated in adult rat and mouse tissues and 24hpf zebrafish morphants (Lutcke et al., 1994, Yu et al., 1993, Bem et al., 2011). However, all three studies reported various levels of enrichment, with the greatest expression found in the brain. It would therefore be of interest to examine *Rab18* expression in more detail in neuronal and non-neuronal tissues by *in situ* hybridisation to determine whether expression is enriched in organs showing pathological phenotypes. Additionally, how loss of a ubiquitous protein results in abnormalities in a specific subset of organs/tissues remains to be determined. However, this is a common attribute of many additional neurodegenerative diseases including spinal muscular atrophy (mutations in *SMN*) specifically causing neuronal phenotypes despite ubiquitous expression (Monani, 2005). The neuronal and ocular

phenotype observed in our *Rab18*$^{-/-}$ model could be attributed to loss of RAB18 having a greater functional consequence in neuronal and ocular systems than other tissues.

The genetrap cassette was predicted to terminate expression of *Rab18* in intron 2 and result in a truncated and non-functional version of the protein. I have demonstrated that *Rab18*$^{-/-}$ mice represent the null phenotype of *Rab18.* RT-PCR analysis using primers 3' of the gene trap cassette insertion site (Figure 3.5A) did suggest the possibility of a potential alternative transcription start site. However, through qRT-PCR and Western blot analysis targeting C-terminal to the cassette, I have shown that the genetrap results in no residual *Rab18* expression. The *Rab18*$^{-/-}$ genetrap mouse presented in this study shows phenotypes that occur upon the earliest possible loss of *Rab18.* The FlipRosaβGeo cassette provides the added benefit of being an inducible system and enabling the generation of a site- or temporal-specific conditional allele (Schnutgen et al., 2005). Experiments are currently ongoing where *Rab18*$^{-/-}$ mice have initially been crossed to FLPe to repair the mutation and then to tamoxifen inducible Cre-ER to generate temporal specific knockouts and examine *Rab18* loss at different ages and/or stages of development and delineate the role of *Rab18* in degeneration compared to development. This will be of particular interest in the lens to question whether loss of *Rab18* in adulthood causes age-related cataracts or whether the underlying abnormality is in fact developmental in origin.

3.3.2 *Rab18*$^{-/-}$ mice recapitulate characteristic ocular and neurological phenotypes of Warburg Micro syndrome

Rab18$^{-/-}$ mice were viable and fertile. At eye opening *Rab18*$^{-/-}$ mice presented with dense nuclear congenital cataracts and atonic pupils. From three weeks of age they showed abnormal hind limb clasping upon tail suspension which progressed to a splayed gait and a noticeable decline in movement. *Rab18*$^{-/-}$ mice therefore recapitulated characteristic ocular and neurological phenotypes of Warburg Micro syndrome with complete penetrance. However, more detailed analyses in the future may show additional features as either recapitulated or absent, for example,

micropthalmia and microcornea are characteristic presenting features of Warburg Micro syndrome but as of yet have not been observed in our mouse model. Further analyses and eye measurements would need to be undertaken to examine this in greater detail. Warburg Micro syndrome patients additionally show many neurological abnormalities including progressive spastic paraplegia and polymicrogyria. Although no gross brain pathology was observed in the necropsy analysis presented here, it remains possible that neuronal migration abnormalities may still be apparent. However, as mice have very few gyri or sulci, polymicrogyria is much more difficult to identify than in humans and studies looking for subtle abnormalities in neuronal migration would have to be undertaken.

Warburg Micro syndrome patients additionally show postnatal growth retardation. The preliminary observation that after backcrossing for 9 generations to C57BL/6J *Rab18*$^{-/-}$ mice were smaller than littermate controls at weaning suggested that this feature of the disease may also be recapitulated. However, further analyses will need to be undertaken to confirm this. Additionally, it would be of interest to examine the weight of *Rab18*$^{-/-}$ embryos and neonates to determine whether this observed reduction is post-natal or pre-natal in origin.

As *Rab18*$^{-/-}$ mice were generated by MRC Harwell, primary phenotypic assessment is currently being undertaken as part of the EUMODIC programme, examining dysmorphology, weight, clinical chemistry and behaviour. When available, data will be published at www.europhenome.org.

3.3.3 Other mammalian models for Warburg Micro syndrome

Despite the fact that loss-of-function mutations in any of the four causative genes causes a clinically indistinguishable patient phenotype (Aligianis et al., 2005, Bem et al., 2011, Borck et al., 2010)(Leigel *et al.,* 2013, in press), other mammalian models for Warburg Micro syndrome have failed to report any neurological phenotypes (Sakane et al., 2006)(Leigel *et al.,* 2013, in press). *RAB3GAP1* is encoded by a major transcript of 24 exons and a minor transcript that lacks the first 50 aa (exons 1-3) and has a small additional exon of 3 aa. The only reported causative mutation in exon 1 of *RAB3GAP1* to date is a C.9delC, p.Asp4Thrffs*51 frameshift mutation in one

Martsolf family. RT-PCR analysis performed by Handley *et al.* (Handley et al., 2013) reported a reduction in expression of the full-length transcript and an upregulation of the shorter transcript in patient cDNA. This suggested that the alternative transcript may partially fulfil the function of full length RAB3GAP1 and ameliorate the more severe Warburg Micro syndrome phenotype observed when the full length transcript is lost. *Rab3gap1* deficient mice targeting exons 1 and 2 and flies targeting exon 1 have been generated (Sakane et al., 2006, Muller et al., 2011). Both models displayed subtle alterations in synaptic plasticity but failed to recapitulate any of the characteristic ocular or neurological phenotypes of the human disease. To date only one protein-coding transcript has been identified in the mouse (Ensembl GRCm38), however, a previous fly assembly (Ensembl BDGP5.4) has reported an alternative shorter transcript (rab3-GAP-RB). Additionally, a recent paper analysing RAB3GAP1 levels in rat epidermal keratinocytes identified a short 80kDa isoform and an alternative transcription start site at the start of exon 3 (Youssef et al., 2013). These models may therefore represent incomplete disruption of the gene.

Causative mutations for Warburg Micro syndrome have recently been identified in *TBC1D20* and the *blind sterile* (*bs*) mouse model (Leigel *et al.*, 2013, in press). *bs* mice presented with lenticular cataracts and male sterility with abnormalities in the sperm head (Sotomayor and Handel, 1986, Varnum, 1983) however, gross phenotypic analysis did not identify any hind limb clasping and future work would need to be undertaken to examine whether any neurological phenotypes are recapitulated. Additionally, the *Tbc1d20* mutation in *bs* mice is an in-frame p.Arg232_Val235del deletion that results in a dramatic reduction in GAP activity but not complete loss. Furthermore, protein stability in the mouse mutant was not assessed.

As *Rab18*$^{-/-}$ recapitulate many of the characteristic ocular and neurological phenotypes of Warburg Micro syndrome, we believe the phenotype to be centralised around loss of *Rab18*. Studies are currently being undertaken in the laboratory to examine a link between the RAB3GAP complex, TBC1D20 and RAB18.

3.3.4 Summary

In summary, I have described a novel *Rab18*$^{-/-}$ mouse model that presents with congenital cataracts, atonic pupils and progressive hind limb weakness. Chapters 5 and 6 will further examine the observed ocular and neurological phenotypes.

Chapter 4 RAB18 localisation

4.1 Introduction

RAB18's role in trafficking is still emerging and its cellular effectors are yet to be identified. RAB18 is ubiquitously expressed but found at varying intensities in different cell types and tissues (Figure 3.4 and (Lutcke et al., 1994)). Over the past 20 years several conflicting publications examining RAB18's cellular localisation and function in different cell types have been reported. Initial studies localised RAB18 to mouse kidney tubule and intestinal epithelial cells and proposed a role in endocytosis (Lutcke et al., 1994). Additional studies have localised RAB18 to lipid droplets in adipocytes, fibroblasts and epithelial cells (Vero, 3T3-L1 fibroblasts and differentiated adipocytes and HepG2 cells) and reported a role in both lipolysis and lipogenesis (Martin et al., 2005, Ozeki et al., 2005, Pulido et al., 2011). In vero cells, RAB18 has also been shown to localise to the endoplasmic reticulum and in variable degrees to the Golgi apparatus (Martin et al., 2005, Dejgaard et al., 2008). RAB18 has also been reported to have a role in Golgi to ER trafficking through the COPI-independent pathway (Dejgaard et al., 2008), however systematic screens of multiple RAB proteins have failed to identify RAB18 in this pathway (Fuchs et al., 2007, Haas et al., 2007). Studies in neuroendocrine cells and pituitary melanotropes have also identified an interaction of RAB18 with secretory granules where it seemingly functions to inhibit their exocytosis (Vazquez-Martinez et al., 2007).

As part of my detailed characterisation of the *Rab18*$^{-/-}$ genetrap mouse I examined the localisation of RAB18 in mouse embryonic fibroblasts (MEFs) and primary hippocampal neurons. I set out to determine whether RAB18 localisation may be relevant to a cellular phenotype that is common to all cells and results in pathology. Or alternatively, does RAB18 serve to distinguish a cell-specific/specialised localisation that is relevant to disease in affected cell types.

4.2 Results:

Many commercially available and custom-made RAB18 antibodies have been generated targeting the C-terminus. Despite the high structural conservation amongst the RAB protein family, the C-terminus is hyper-variable and as such an ideal target for the design of antibodies that should in theory not cross react with other RABs. Immunofluorescence experiments testing RAB18 antibody specificity have previously been undertaken in our laboratory (including many of the antibodies used in published studies) on wild type and *Rab18*$^{-/-}$ MEFs. However, in our hands no differences in staining intensity or pattern were observed between the two genotypes (Mark Handley, personal communication). Consequently, I have examined the localisation of overexpressed RAB18 using GFP or mCherry tagged constructs. GFP tagged proteins are routinely used in the study of RAB protein localisation (Dejgaard et al., 2008, Handley et al., 2007) and have previously been reported to show comparable localisation of exogenous GFP tagged and endogenous proteins as demonstrated directly in the case for RAB18 by Ozeki *et al.,* (Ozeki et al., 2005). RAB proteins are always tagged with fluorescent proteins at the N-terminus. N-terminal modification should not disrupt RAB protein function (Tolmachova et al., 2004), whereas the C-terminal hypervariable domain contains the target site for geranylgeranylation and hence is essential for membrane insertion and localisation (Pereira-Leal and Seabra, 2001, Kinsella and Maltese, 1992).

4.2.1 GFP-RAB18 localisation and dynamics in control and *Rab18*$^{-/-}$ mouse embryonic fibroblasts

To study the cellular phenotypes of control and *Rab18*$^{-/-}$ mice, MEFs were isolated from E11.5 embryos and transfected with GFP or mCherry tagged RAB18 constructs. GFP and mCherry tagged RAB18 constructs showed the same staining pattern and as a result were used interchangeably. All transfected MEFs for co-localisation experiments were imaged live 24 hours post-transfection in order to exclude the potential for artefacts following PFA fixation and cell permeabilisation.

Wild type MEFs transfected with mCherry-RAB18 showed a reticular pattern of labelling, reminiscent of the ER (Figure 4.1A). This is consistent with previous

reports in Vero, COS7 and NRK cells (Martin et al., 2005, Dejgaard et al., 2008). Co-transfection experiments were therefore undertaken with mCherry-RAB18 and GFP-TBC1D20-RA to confirm this localisation. TBC1D20 is a reported RAB1 and RAB2 GAP that has a well characterised localisation to the ER (Haas et al., 2007). The RA (p.R150A) mutation is catalytically inactive, thus overexpression should have limited consequences for localisation but can be used as a cellular marker for the ER. Immunofluorescence experiments on live cells identified co-localisation of RAB18 with TBC1D20, suggesting RAB18 localises to the ER in MEFs (Figure 4.1A-C). To examine for any abnormalities in ER morphology upon loss of RAB18, MEFs derived from control and *Rab18*$^{-/-}$ littermates were transfected with GFP-TBC1D20-RA and again imaged live. No obvious discernible differences were noted between the two genotypes suggesting RAB18 localised to the ER, but upon loss of RAB18 no gross abnormalities in ER morphology were observed (Figure 4.1D-E).

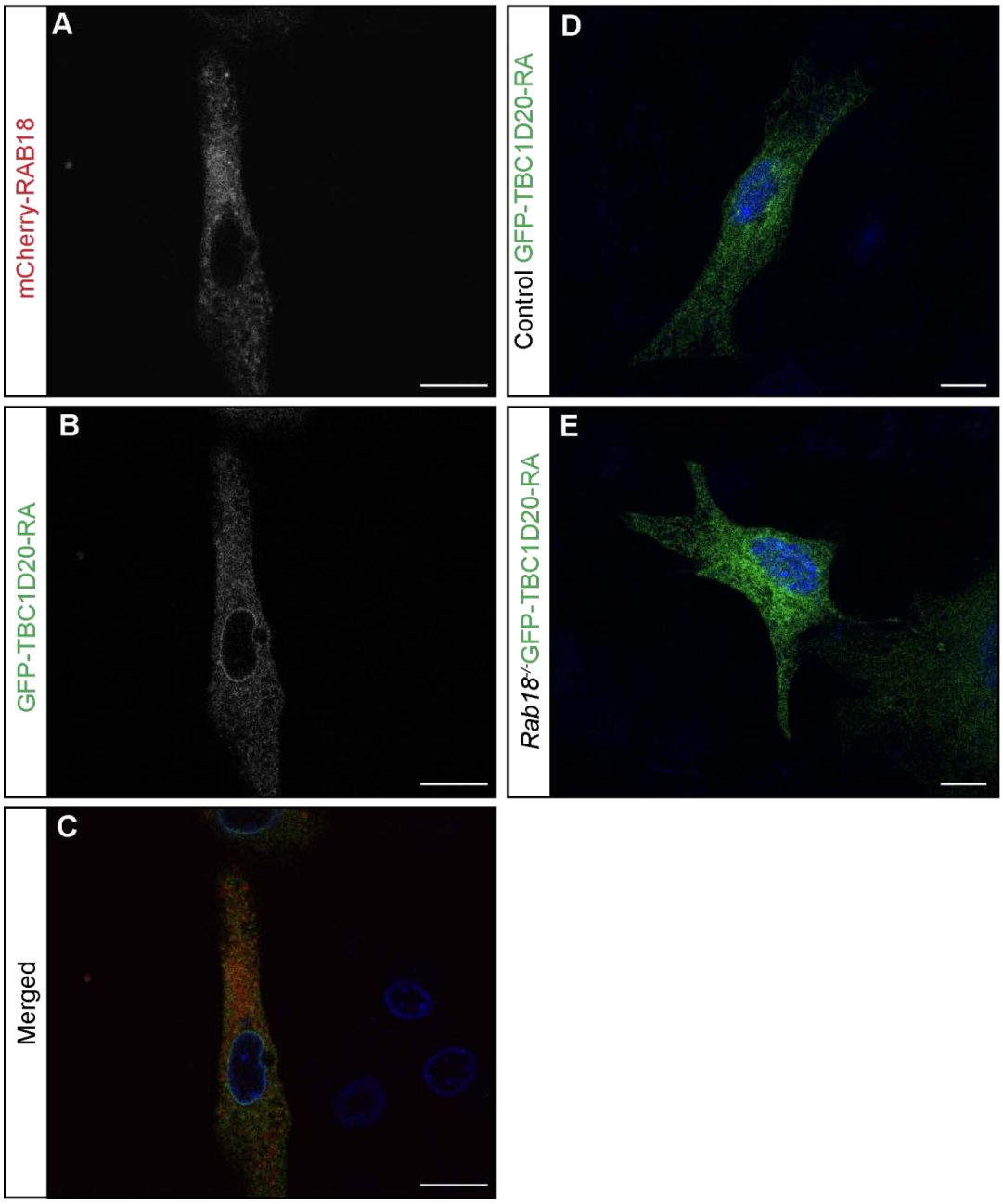

Figure 4.1 mCherry-RAB18 localises to the ER protein in mouse embryonic fibroblasts

(A-C) Wild type mouse embryonic fibroblasts co-transfected with mCherry-RAB18 (red) and the catalytically inactive ER protein, GFP-TBC1D20-RA (green) showing localisation of RAB18 to the endoplasmic reticulum. Merged image (C) is a composite of mCherry-RAB18 (A) and GFP-TBC1D20-RA (B). (D-E) Control (D) and *Rab18*$^{-/-}$ (E) mouse embryonic fibroblasts transfected with the ER protein GFP-TBC1D20-RA (green) and the nuclear stain Hoescht (blue) showing no gross differences in ER morphology upon loss of RAB18. Scale bar represents 10µm.

When wild type MEFs were transfected with mCherry-RAB18 to examine ER morphology, an enrichment of RAB18 in the perinuclear region was also observed (Figure 4.1A). This is consistent with localisation to the Golgi apparatus. RAB18 localisation primarily to the *cis*-Golgi has previously been described in COS7, Vero and NRK cell lines (Dejgaard et al., 2008). Multiple attempts to clone *cis*-Golgi markers GRASP65 or GM130 into GFP or mCherry tagged vectors were unsuccessful, so the *trans*-Golgi was targeted for localisation experiments. To confirm the co-localisation of RAB18 to the Golgi, MEFs from wild type embryos were co-transfected with GFP-RAB18 and CFP-GalT (Figure 4.2A-C). GalT (*trans*/TGN enzyme β1,4-galactosyltransferase) is mainly located in the *trans*-cisternae and TGN (trans Golgi network) and was used as a marker for the *trans*-Golgi (Storrie et al., 1998). MEFs co-transfected with GFP-RAB18 and CFP-GalT confirmed localisation of RAB18 to the Golgi apparatus (Figure 4.2C). The Dejgaard study additionally noted that upon overexpression of GFP-RAB18 the Golgi apparatus fragmented and appeared dispersed in different cell lines (Dejgaard et al., 2008). I did not observe any obvious fragmentation of the Golgi upon overexpression of GFP-RAB18 in MEF lines. To examine for any abnormalities in Golgi morphology upon loss of RAB18, PFA fixed wild type (Figure 4.2D) and *Rab18*$^{-/-}$ (Figure 4.2E) MEFs were stained with the *cis*-Golgi antibody GM130 (green) and the nuclear counterstain DAPI (blue) and imaged by confocal microscopy. Five randomly selected images from each sample (N=3 wild type and N=3 *Rab18*$^{-/-}$) were imported into Volocity 3D image analysis software and mean Golgi area per cell (μm^2) calculated. No differences were observed in mean Golgi area between wild type or *Rab18*$^{-/-}$ MEFs, suggesting that loss of RAB18 had no effect on Golgi size (Figure 4.2F).

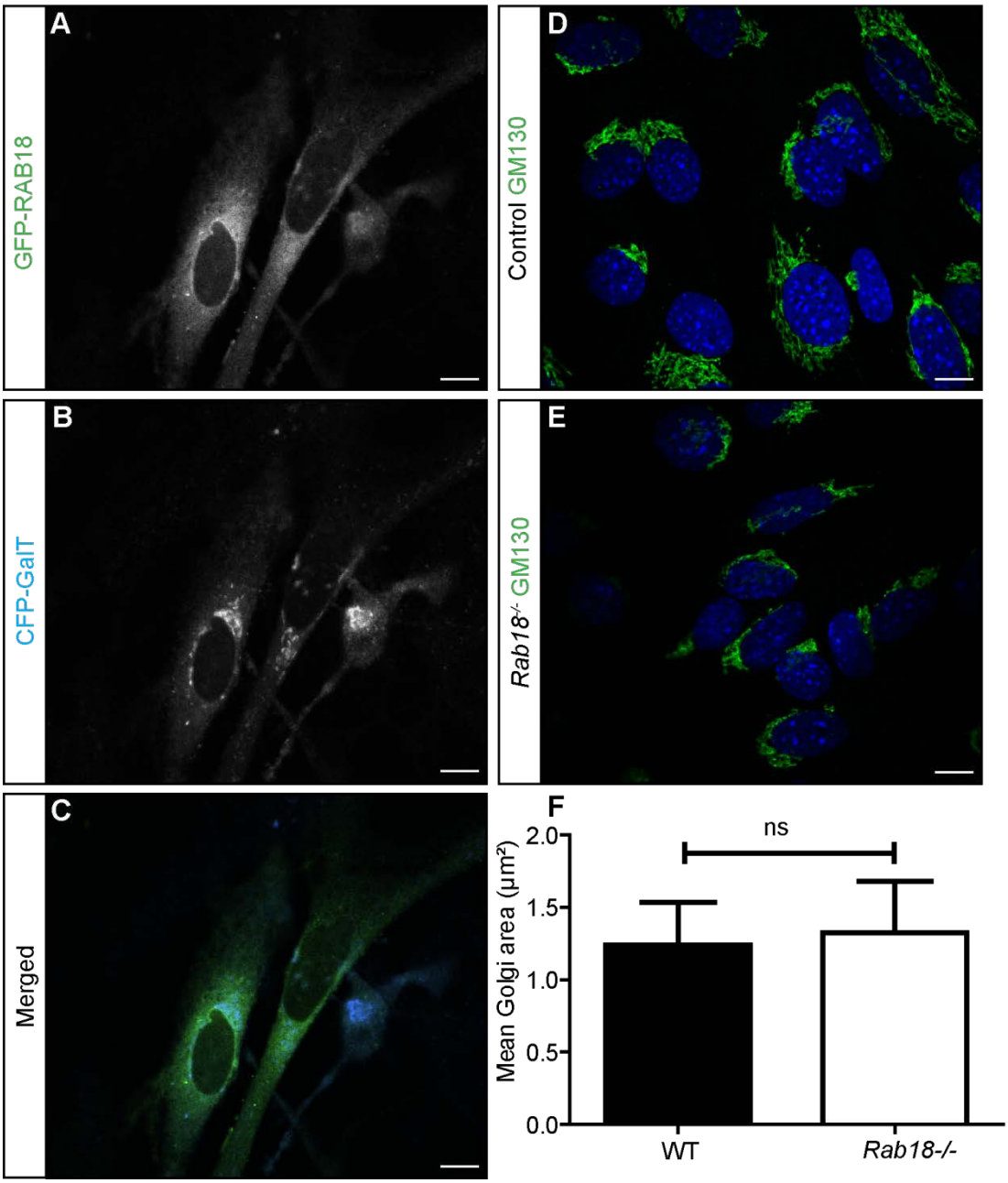

Figure 4.2 GFP-RAB18 colocalises with the Golgi marker GalT in mouse embryonic fibroblasts but has no effect on Golgi area upon loss of RAB18

(A-C) Mouse embryonic fibroblasts co-transfected with GFP-RAB18 (green) and the *trans*-Golgi marker CFP-GalT (blue) showing enrichment of GFP-RAB18 at the Golgi apparatus. Merged image (C) is a composite of GFP-RAB18 (A) and CFP-GalT (B). (D-F) Fixed control (D) and *Rab18*$^{-/-}$ (E) mouse embryonic fibroblasts co-stained with the *cis*-Golgi marker GM130 (green) and the nuclear stain DAPI (blue). (F) Quantification of Golgi area using Volocity software shows that loss of RAB18

has no major effect on Golgi size. N=3, mean ± SEM, ns= unpaired t-test not significant. Scale bar represents 10μm.

RAB18 has been identified as a major component of lipid droplets in an in-depth proteomics screen (Ozeki et al., 2005) and subsequent studies have confirmed its localisation to lipid droplets in adipocytes, fibroblasts and epithelial cell lines (Ozeki et al., 2005, Martin et al., 2005, Pulido et al., 2011). To examine the localisation of RAB18 to lipid droplets in MEFs, wild type cells were transfected with GFP-RAB18 and incubated overnight in parallel with oleic acid conjugated to bovine serum albumin (BSA) to induce lipid droplet formation, and the neutral lipid stain BODIPY 558/568 C_{12} to label these lipid droplets. GFP-RAB18 staining was again observed in the ER but appeared enriched in rings immediately surrounding lipid droplets (Figure 4.3 A-C). This is in agreement with previous reports (Pulido et al., 2011, Martin et al., 2005, Ozeki et al., 2005). To quantify for any abnormalities in lipid droplet morphology upon loss of *Rab18,* control and *Rab18*$^{-/-}$ MEFs were treated with oleic acid for 24 hours, fixed in PFA and labelled with the neutral lipid stain BODIPY 493/503 (green) and DAPI (blue) (Figure 4.3 D-E). Five images from each cell line (N=3 wild type, N=3 *Rab18*$^{-/-}$) were imported into ImageJ and the size of each lipid droplet measured (particle size plugin). The mean lipid droplet size (in pixels) for each sample was quantified rather than fluorescence intensity as variations in staining intensity were frequently observed between wells. Our analysis identified an enlargement of lipid droplets in *Rab18*$^{-/-}$ MEFs compared to controls (mean lipid droplet size, 8.89 ± 0.24 pixels in control and 12.82 ± 1.23pixels in *Rab18*$^{-/-}$).

Taken together our data suggests that loss of RAB18 in MEFs does not result in gross abnormal morphology of the ER or Golgi. However, enlarged lipid droplets in *Rab18*$^{-/-}$ cells compared to wild type was observed upon loading with exogenous lipids.

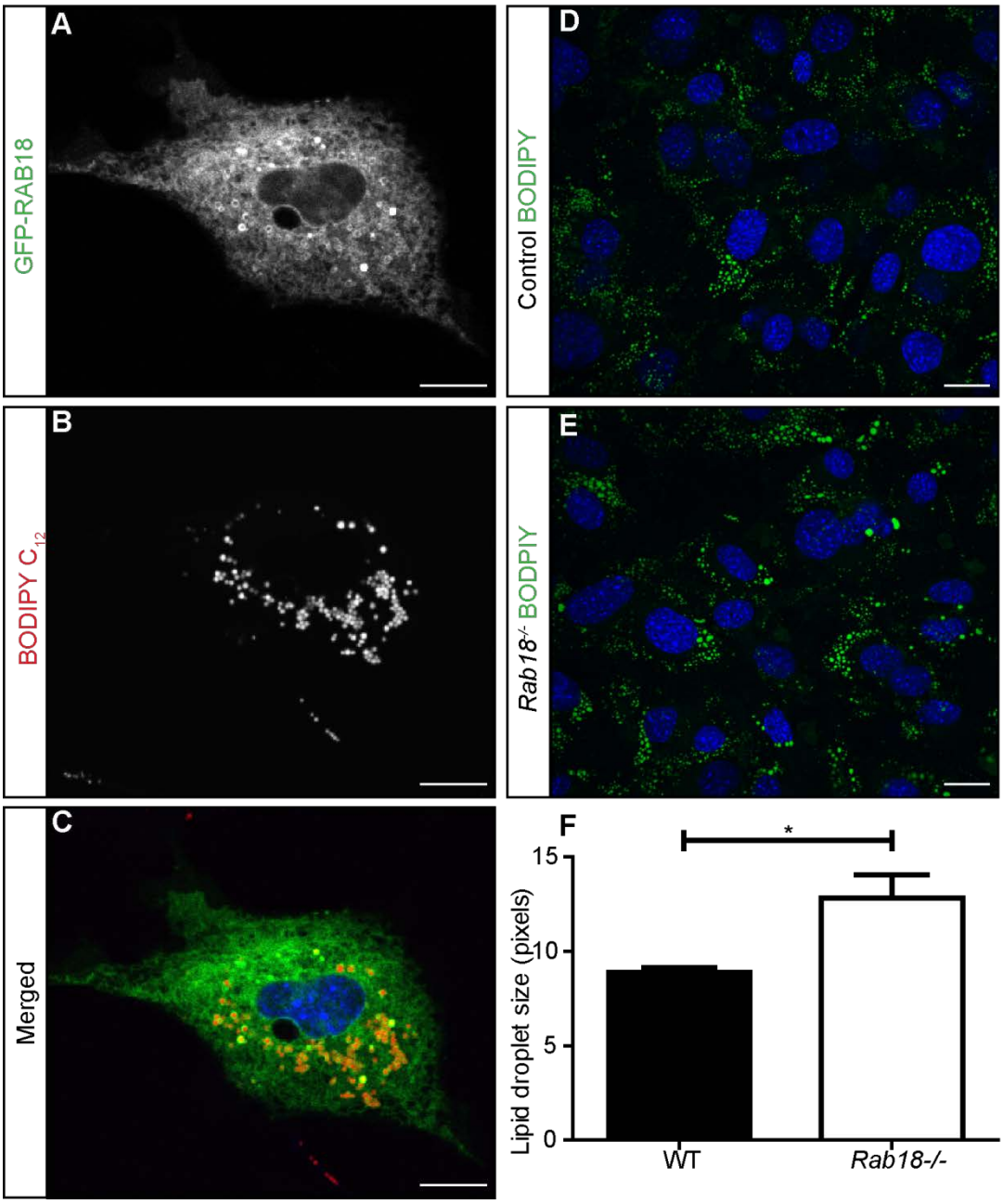

Figure 4.3 Localisation of GFP-RAB18 to lipid droplets in mouse embryonic fibroblasts

(A-C) Mouse embryonic fibroblasts transfected with GFP-RAB18 (green) and loaded with oleic acid and the neutral lipid stain BODIPY 558/568 C_{12} (red) and the nuclei stain Hoescht (blue) showing localisation of RAB18 in rings surrounding lipid droplets. Merged image (C) is a composite of GFP-RAB18 (A) and Bodipy C_{12} (B) and. (D-F) Control (D) and *Rab18*$^{-/-}$ (E) mouse embryonic fibroblasts treated with oleic acid for 24 hours then fixed and stained with the neutral lipid stain BODIPY 493/503 (green) and DAPI (blue). (F) Quantification of lipid droplet size showing enlarged lipid droplets in *Rab18*$^{-/-}$MEFs. N=3, mean ± SEM, (mean lipid droplet size,

8.9 pixels in control and 12.8 pixels in *Rab18*$^{-/-}$), *p<0.05 unpaired t-test. Scale bar represents 10μm.

4.2.2 GFP-RAB18 localisation and dynamics in primary hippocampal neurons

Abnormalities affecting the peripheral and central nervous systems are hallmark features of Warburg Micro syndrome; patients exhibit severe developmental delay and polymicrogyria, indicative of possible neuronal migration abnormalities and axonal peripheral neuropathy. To examine if the reported localisations of RAB18 were also present in a specific cell type that may be relevant to disease, localisation experiments were performed in primary hippocampal neurons. Hippocampal neurons were isolated from E17.5 wild type embryos and cultured for 12-14 days *in vitro* (DIV) to reach developmental maturity. Attempts to co-transfect neurons with GFP-RAB18 and the *trans*-Golgi marker GalT proved unsuccessful, so to confirm the localisation of RAB18 to the Golgi, GFP-RAB18 transfected primary hippocampal neurons were PFA fixed and immunofluorescence performed with the *cis*-Golgi antibody GM130 (Figure 4.4). We observed that, as in MEFs, GFP-RAB18 co-localised with the Golgi apparatus in the soma of primary hippocampal neurons.

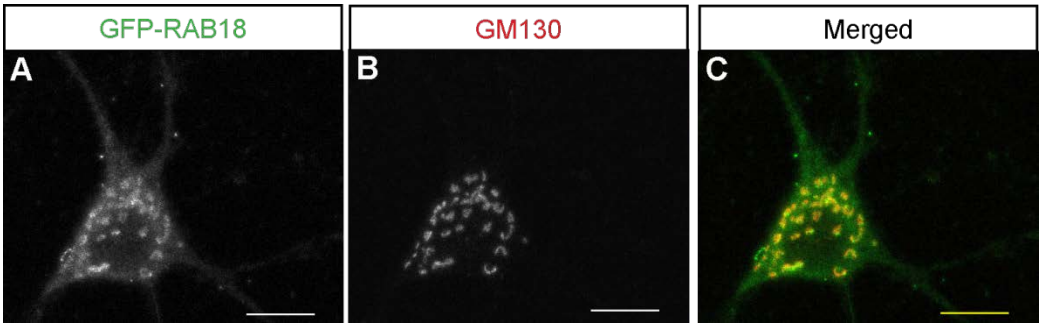

Figure 4.4 GFP-RAB18 colocalises with the *cis*-Golgi marker GM130 in primary hippocampal neurons

(A-C) Primary hippocampal neurons transfected with GFP-RAB18 (green) and immunostained with the *cis*-Golgi marker GM130 (red) showing co-localisation of RAB18 and the *cis*-Golgi in hippocampal neuron soma. Merged image (C) is a composite of GFP-RAB18 (A) and GM130 (B). Scale bar represents 10µm.

To further examine the localisation of GFP-RAB18 and to counteract any effects of fixation, wild type primary hippocampal neurons were transfected with GFP-RAB18 and imaged live by confocal microscopy. When microscope intensity levels were increased (until staining in the soma became saturated), GFP-RAB18 staining was observed throughout the neuronal processes (Figure 4.5A). However, frequently, we observed variable accumulations of signal along processes. Time lapse recording over multiple hours (2 minute intervals for 16 hours) revealed that GFP-RAB18 occassionally slowly accumulated in puncta within neurite processes that were then retrogradely transported back up the neuronal process towards the cell soma. This novel observation of the localisation and behaviour of RAB18 in hippocampal neurons suggests that RAB18 may play distinct roles in neuronal processes from that in the cell body and potentially point towards a role for RAB18 in axonal transport.

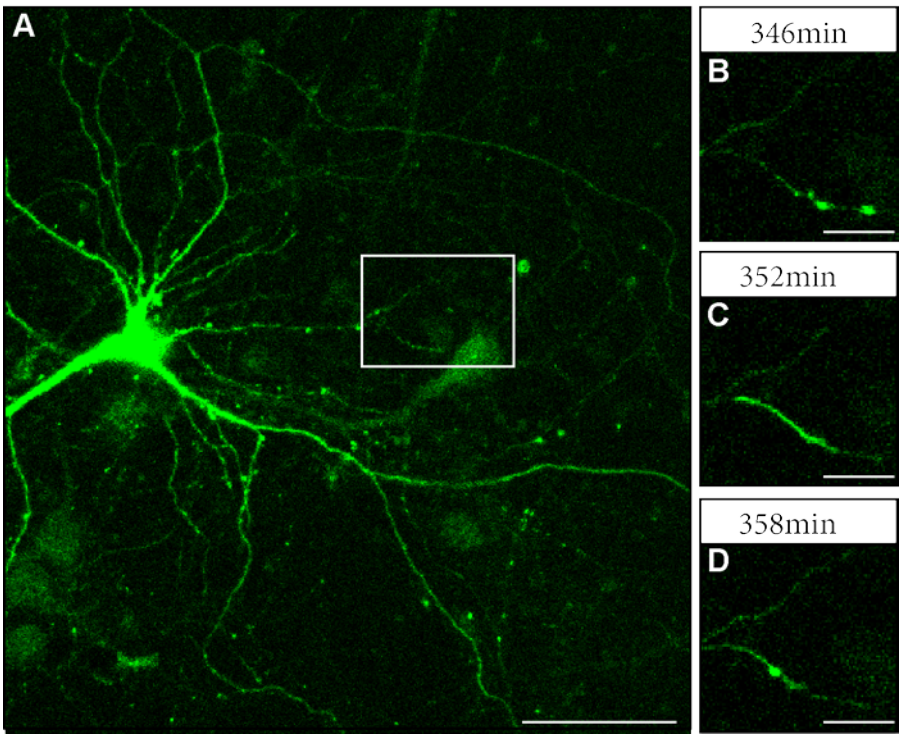

Figure 4.5 GFP-RAB18 localises to neuronal processes in primary hippocampal neurons and is mobile

(A) Primary hippocampal neurons transfected with GFP-RAB18 (green) and live imaged with a confocal microscope. GFP-RAB18 localises throughout neurons including in dense puncta in neuronal processes. GFP-RAB18 transfected neurons were imaged in real time and panels B-D show boxed region in A at 346 (B), 352 (C) and 358 minutes (D) indicating that RAB18 positive puncta are dynamically trafficked along processes in a retrograde manner. Scale bar represents 10μm.

4.3 Discussion

In this chapter I report the localisation of RAB18 to the ER and Golgi, a broad consensus localisation previously reported in multiple different cell types (Dejgaard et al., 2008, Martin et al., 2005). Although this is not the first study examining RAB18 localisation in fibroblasts, I report for the first time the localisation of RAB18 and the cellular consequences of its loss in MEFs. My studies have shown that loss of *Rab18* does not result in gross morphological abnormalities in the ER or Golgi, but an enlargement of lipid droplets. Although I have been unable to rule out the hypothesis that Warburg Micro syndrome pathology originates from some ubiquitous cellular function, I have provided evidence for GFP-RAB18 localising throughout the neuron and in accumulations along neurite processes which are mobile. This may underlie a cell-type specific function of RAB18 and future work has been directed towards investigation of pathological events in the nervous system of *Rab18*$^{-/-}$ mice (chapter 6).

4.3.1 Confirmation of previously reported localisations of GFP-RAB18

The majority of the work described in this chapter was carried out on live cells transfected with GFP or mCherry tagged proteins to examine the localisation of RAB18. Overexpression of a fluorescently tagged protein can disrupt normal endogenous function and localisation (Spector and Goldman, 2010). It is therefore of great importance to determine whether the localisations reported here are in agreement with normal RAB18 function prior to further analysis. The easiest way to determine if a fusion protein is correctly localised is to perform immunocytochemistry with a specific antibody. There are multiple cases in the literature whereby the localisation of RAB18 has been examined by immunofluorescence and showed consistent results with GFP transfection. However, during the course of this project the specificity of many commercially available and custom-made RAB18 antibodies was examined and could not distinguish differences between control and *Rab18*$^{-/-}$ MEFs (undertaken by Dr Mark Handley). This could be attributed to differences in antibody specificity in human and mouse cells or

potentially differences in fixation and permeabilisation protocols. As a result, care must be taken when drawing conclusions from the novel protein localisation I have identified. However, several of the results presented here suggest that GFP-RAB18 recapitulates normal endogenous RAB18 localisation. Primarily, I along with others (Martin et al., 2005, Ozeki et al., 2005, Pulido et al., 2011) have identified GFP-RAB18 to localise to the surface of lipid droplets. RAB18 was also independently identified in an in-depth proteomics screen for molecules involved in lipid droplet function (Ozeki et al., 2005). Additionally, I and others have also reported the localisation of RAB18 to the ER and Golgi complex, using independently generated GFP and mCherry-tagged RAB18 constructs and the localisation of RAB18 to the ER has also been confirmed by electron microscopy (Martin et al., 2005).

Experiments to confirm the localisation of RAB18 to polarised epithelial cells, as shown in Lutcke *et al.*, 1994 were not performed as other studies have failed to recapitulate the co-localisation of RAB18 with endosomal markers (Ozeki et al., 2005).

4.3.2 RAB18 and lipid droplets

Lipid droplets are dynamic organelles composed of a phospholipid monolayer surrounding a dense core of neutral lipids (Martin and Parton, 2006). In this study I have reported the localisation of RAB18 to the surface of lipid droplets in agreement with previous studies (Martin et al., 2005, Ozeki et al., 2005, Pulido et al., 2011) and an enlargement of lipid droplet area in *Rab18*$^{-/-}$ MEFs.

Recent proteomic analysis has identified many additional RAB proteins on lipid droplets including RAB1, 2, 5, 6, 7, 8, 10, 14, 18 and 32 (Ozeki *et al.,* 2005) suggesting a link between lipid droplets and membrane trafficking. Furthermore, many of these identified RAB proteins link lipid droplets to specific membranes, providing further evidence for their dynamic nature. For example, RAB5 is found on the surface of lipid droplets where specifically in its GTP bound state it recruits early endosome markers, including EEA1 (Liu et al., 2007). Additionally, overexpression of RAB18 resulted in translocation of lipid droplets within close contact to and occasional encroachment by the rough ER membrane (Ozeki et al., 2005).

RAB18 has been reported to function in both triacylglycerol accumulation and hydrolysis with RAB18 labelling at the surface of lipid droplets enhanced upon induction of lipolysis with isoproterenol or forskolin (Martin et al., 2005) and also upon lipogenesis induction with insulin treatment (Pulido et al., 2011). It is interesting how RAB18 may be implicated in two isolated processes. One possibility is that RAB18 may be involved in lipid droplet trafficking and thus mediating the exchange of materials between the lipid droplet and ER membranes. Furthermore, Martin *et al.,* 2005 have shown that RAB18 labelled lipid droplets are highly mobile and undergo rapid oscillatory movements to the cell periphery and also reported movement of GFP-RAB18 positive ER structures to the periphery and lipid droplet surface (Martin et al., 2005). As I and others have localised RAB18 to the ER (Dejgaard et al., 2008) it is therefore tempting to speculate that RAB18 may be specifically involved in the lipid droplet to ER point of contact, however, it cannot be ruled out that RAB18 may potentially have a more generalised role in linking the ER to other organelles. Detailed analysis of RAB function on early endosomes identified that RAB5 and RAB11 undergo cyclical activity on and off lipid droplet membranes in a GTP dependent manner. However, the same analyses showed that RAB GDI did not extract RAB18 from lipid droplets (Liu et al., 2007). This may potentially point to RAB18 having a more stable association with lipid droplets as compared to the transient association observed with other RABs. This could suggest that RAB18 may directly regulate lipid droplets, consistent with our findings. Enlarged lipid droplets have also been observed in *RAB3GAP1, RAB3GAP2* and *TBC1D20* patient cell lines and *bs* MEFS (Liegel *et al.,* 2013, in press), suggesting that the lipid droplet phenotype may be related to Warburg Micro syndrome pathogenesis. It would be of interest to determine whether enlarged lipid droplets are recapitulated in cells relevant to the Warburg Micro syndrome phenotype.

4.3.3 Insights into RAB18 function in primary hippocampal neurons

Many of the patient phenotypes associated with Warburg Micro syndrome are neuronal in origin and hence point towards a role for the causative genes in neuronal homeostasis. As a result, the localisation of GFP-RAB18 was examined in a more

relevant cell type for pathogenesis, primary hippocampal neurons. Wild type primary hippocampal neurons transfected with GFP-RAB18 co-localised with the *cis*-Golgi marker GM130 in the cell soma. Additionally, when laser intensity was increased GFP-RAB18 localisation was observed throughout the neuron with puncta accumulations observed along some neuronal processes. Time lapse imaging revealed that frequently these accumulations were mobile and trafficked along the axon in what appears to be a retrograde manner. This novel localisation and behaviour of RAB18 suggests it may fulfil distinct functions in neuronal processes and points towards a potential role in axonal transport. Neurological phenotypes associated with Warburg Micro syndrome may therefore result from perturbations of specialised, RAB18-dependent pathways in neurons. Experiments were also performed transfecting neurons with GFP only constructs and this puncta localisation and mobility was not observed (data not shown).

RAB protein localisation and expression has previously been examined in *Drosophila* brains and identified 10 neuronal specific RABs (RABX1, RAB3, RABX4, RAB9, RAB19, RAB21, RAB23, RAB26, RAB27 and RAB32) with enriched or exclusive localisation to neuronal synapses (Chan et al., 2011). RAB18 however, was found to be ubiquitously expressed, but analysis of the posterior portion of the ventral ganglion showed preferential localisation to the cell body. We also observed GFP-RAB18 to preferentially localise to the cell body in neurons but additionally localise along neuronal processes. Additionally, in the fly model, overexpressed RAB18 co-localised with the early endosomal marker RAB5 and altered RAB5 localisation. As both RAB18 and RAB5 localise to the surface of lipid droplets (Liu et al., 2007, Ozeki et al., 2005) it would be of interest to examine whether the punctae observed in our GFP-RAB18 transfected neurons overlap with the endosomal compartment. Furthermore, the majority of the neuronal specific RABs were also found to co-localise with synaptic vesicle markers (Chan et al., 2011). Given the well established roles of the RAB3 family of proteins in synaptic vesicle exocytosis (Schluter et al., 2002) and the identification of RAB18 being implicated in the negative regulation of exocytosis (Vazquez-Martinez et al., 2007) it is of great importance to determine whether the puncta localisation of GFP-RAB18 in hippocampal neurons coincides with that of synaptic vesicles.

4.3.4 Summary

In this chapter I have examined the localisation of RAB18 in MEFs and compared wild type and *Rab18*$^{-/-}$cellular phenotypes. I have shown that GFP-RAB18 localised to the ER, Golgi apparatus and lipid droplets in agreement with previous reports and that loss of *Rab18* resulted in enlarged lipid droplets. I also examined the localisation of RAB18 in hippocampal neurons, and identified that its co-localisation with the *cis*-Golgi was mostly consistent with what was seen in MEFs, but an additional, possibly cell-type specific function in neuronal processes was observed. From this data, we have shown that the disease relevant function of RAB18 may be ubiquitous or potentially cell type specific. To further our analysis of neuronal specific phenotypes associated with Warburg Micro syndrome, I have undertaken detailed pathological analysis of neuronal phenotypes in *Rab18*$^{-/-}$ mice and this data will be presented in chapter 6.

Chapter 5 Characterisation of the *Rab18*$^{-/-}$ ocular phenotype

5.1 Introduction

In this chapter I will focus on characterisation of the ocular phenotypes observed in Warburg Micro syndrome patients and *Rab18*$^{-/-}$ mice.

5.1.1 Anatomy of the eye

The eye is surrounded by a thick outer protective sclera and thin inner pigmented choroid. At the anterior of the eye, the sclera develops into the thin, transparent cornea, and the choroid forms the iris which gives the eye its coloured appearance and regulates the amount of light that enters the eye through the pupil, a hole in the iris. The cornea together with the lens functions to refract incoming light rays and focus the observed object on the retina. The ciliary body, a complex set of smooth muscles, functions to hold the lens in place and alter its biconvex shape to focus on objects near and far. The lens and ciliary body divide the eye into two chambers, the foremost filled with aqueous humour secreted by the ciliary epithelium and posterior with vitreous humour, which accounts for 80% of the volume of the eye. The retina is located interior to the choroid and is where the light sensitive photoreceptors (rods and cones) can be found.

5.1.2 Warburg Micro syndrome ocular abnormalities

Warburg Micro syndrome patients present with eye abnormalities including congenital bilateral cataracts, microphthalmia, microcornea (<10mm diameter) and small atonic pupils (Warburg et al., 1993). During general phenotyping of our *Rab18*$^{-/-}$ mouse model we observed no obvious abnormalities in eye size (although studies are currently underway to quantify this) but atonic pupils and congenital cataracts with complete penetrance. The majority of our analyses have focused on identifying the histological abnormalities underlying ocular development and congenital cataracts in *Rab18*$^{-/-}$ mice.

5.1.3 Mouse lens development

Several reviews which have described the development and morphology of the murine lens in detail are summarised below (Graw, 2009, Graw, 2004, Graw, 1999, Graw, 2003, Francis et al., 1999, Cvekl and Piatigorsky, 1996, Michael and Bron, 2011, Fitzpatrick and van Heyningen, 2005).

Figure 5.1 shows the major morphological events in mammalian lens development. At approximately late gastrulation, the eye field, a population of cells in the anterior neural plate of the primitive ectoderm, laterally splits into two optic vesicles that extend towards the surface ectoderm. As the optic vesicle comes into close proximity with the surface ectoderm the ectoderm thickens to form the lens placode, and the optic vesicle invaginates to form the early optic cup (Figure 5.1A). At approximately E10.5, the lens placode invaginates into the optic cup forming the lens pit (Figure 5.1B). At E11.5 the two edges of the lens pit approach and fuse to form the lens vesicle (Figure 5.1C). The lens vesicle then detaches from the surface ectoderm which recovers and goes on to differentiate into the prospective cornea. Epithelial cells lining the posterior of the lens vesicle then differentiate and elongate upwards to form the primary lens nucleus that fills the internal cavity and this process is complete by E13.5. A subpopulation of epithelial cells at the anterior pole of the lens retain their epithelial characteristics and form a monolayer of ‘stem-like’ cells (Figure 5.1D). These epithelial cells travel to the dorsal and ventral equators where they elongate and differentiate into secondary lens fibre cells throughout life forming concentric rings surrounding the lens nucleus (Figure 5.2A).

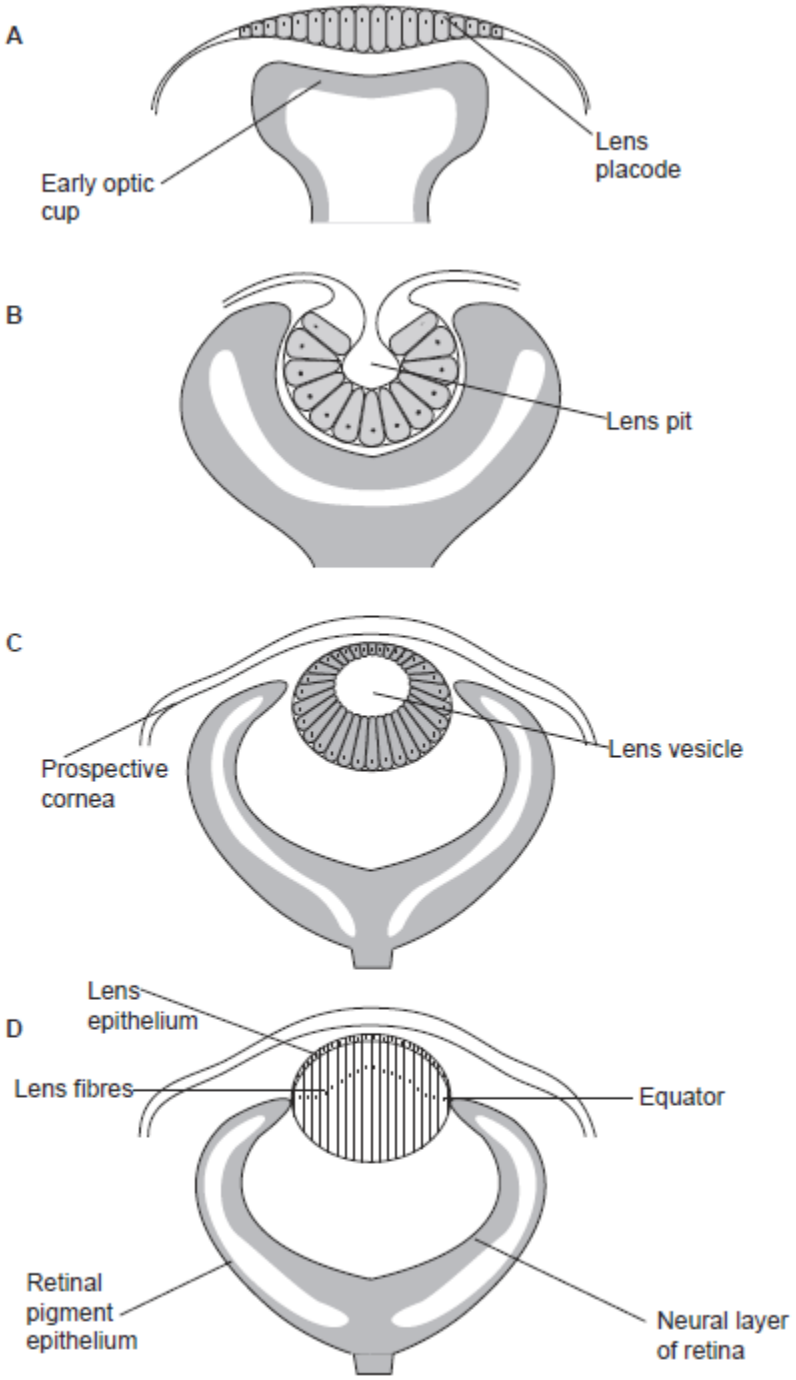

Figure 5.1: Mouse lens development

Lens development commences at approximately E9.5-E10 with thickening of the surface ectoderm to form the lens placode (the future lens) (A). (B) At E10.5, the lens placode invaginates into the optic cup forming the lens pit. (C) By E11.5, the two edges of the lens pit come together to form the lens vesicle and detach from the surface ectoderm. (D) By E13.5, epithelial cells lining the posterior of the vesicle have elongated and differentiated into primary fibre cells, closing the lens vesicle. A monolayer of epithelial cells surrounds the anterior of the lens. (Adpated from Cveki & Piatigorsky 1996).

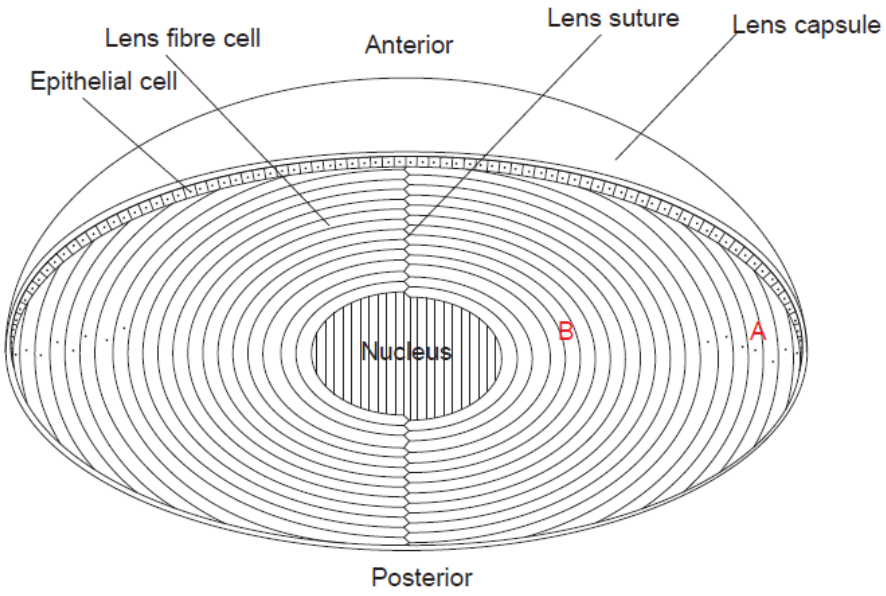

Figure 5.2: Adult lens morphology and organisation

The lens is surrounded by a thick protective lens capsule. At the anterior of the lens is a mono layer of epithelial cells. As the lens forms from the lens vesicle the primary fibre cells differentiate from the posterior epithelial cells and elongate to the anterior forming the lens nucleus. A second wave of fibre formation then commences with the differentiation of epithelial cells at the dorsal and ventral equators meeting at the lens suture (A). As fibre cells differentiate they lose their nuclei and organelles to prevent light scattering (B) (Adapted from Song *et al.* 2009).

As lens fibre cells differentiate they lose their organelles, nuclei and mitochondria and accumulate large quantities of crystallin proteins (Figure 5.2B). For primary fibre cells this process takes place approximately E17/E18 in the mouse, whereas secondary fibre cells which grow throughout life lose their organelles as they migrate from the periphery to the cortex. The centre of the mature lens is thus composed of a highly ordered network of metabolically inactive hexagonal lens fibre cells with minimal intracellular spaces. Fibre cells are therefore avasculature and are dependent upon ion pumps between cells to enable cell-cell communication and maintain homeostasis. Greater than 90% of soluble protein in the mature lens is made up of the crystallin family (α, β and γ subfamilies). Crystallin proteins are present in very large quantities in the lens and all three families are essential to preserve normal lens transparency by increasing the refractive index of the lens. α-crystallin however, has an additional role functioning as a chaperone to aid the retention of proteins in their normal natured state (Horwitz, 1992). Other proteins in the lens include cytoskeletal proteins such as vimentin, CP49 (phakinin) and CP115/CP95 (filensin) who function to maintain the strict arrangement of hexagonal lens fibre cells. Abnormalities in denucleation, retention of organelles or mutations in crystallin, cytoskeletal or connexin proteins result in loss of normal lens transparency and cataract development.

5.1.4 Congenital cataracts

Unlike age related cataracts, congenital cataracts are in fact rare, with an incidence of 30 in every 100,000 births in the developed world (Graw et al., 2004). The majority of our understanding into isolated nonsyndromic cases of congenital cataracts has arisen from the use of mouse models with many spontaneously arisen and induced mutations after ENU, X-ray or γ-ray irradiation characterised to identify the morphological abnormalities underlying cataract development. For example, mutations in the β and γ-crystallin gene family (*Cryg*) result in a spectrum of opacities in both heterozygote and homozygote mice (Graw et al., 2004). *Crygd*^{enu910} and *Cryge*^{enu449}mutations result in a mild phenotype with a subtle mass in the centre of the lens and abnormal nuclei degradation suggestive of a defect in lens fibre differentiation. *Crygc*^{enu369} and *Crygd*^{k10} mutations cause a more severe phenotype

with a shift of the lens nucleus to the anterior and many large vacuoles (Graw et al., 2004). Additionally, the *Crygb*^{Nop} mouse shows swollen anterior and posterior lens fibres, abnormalities in organisation of the nuclear bow and polar cataracts (Graw et al., 1990). However, most incidences of congenital cataract are syndromic and associated with other abnormalities, for example cataracts are observed in Smith-Lemli-Opitz syndrome (Cotlier and Rice, 1971) and 1.4% of Down's syndrome cases in a Danish cohort (Haargaard and Fledelius, 2006).

As stated above normal lens development is dependent upon processes involving cell migration and cellular differentiation, with abnormalities in either process resulting in loss of normal lens transparency and cataract development. In this chapter I therefore describe histological examination for migration and cellular differentiation abnormalities in *Rab18*$^{-/-}$mice. To examine the role of RAB18 in cell migration I analysed lenses at different stages of embryogenesis to examine for any abnormalities in lens formation and closure. Additionally, to investigate the process of fibre cell differentiation I examined the denucleation process and lens fibre organisation in *Rab18*$^{-/-}$ neonates.

5.2 Results:

5.2.1 Defective lens development in *Rab18*$^{-/-}$ mice

Initial characterisation of the *Rab18*$^{-/-}$phenotype (described in chapter 4) identified congenital nuclear cataracts and atonic pupils with complete penetrance. To further characterise the lens defects and examine for any underlying morphological abnormalities, eyes from control and *Rab18*$^{-/-}$ mice were histologically assessed at various stages of embryogenesis. Intact embryos (E12.5), heads (E15.5) or dissected eyes (E17.5 and P1.5) were wax-embedded and eye morphology investigated through haematoxylin and eosin staining. Analysis at E12.5 identified no abnormalities in the developing retina, the optic stalk or the vitreous body in control or *Rab18*$^{-/-}$ mice suggesting that eye development initiates normally in *Rab18*$^{-/-}$ mutants (Figure 5.3 A-B). However, by this stage of development in control lenses the epithelial cells lining the posterior of the lens vesicle had differentiated and elongated to the anterior, filling the lens vesicle with primary fibre cells and forming the lens nucleus (Figure 5.3A). In *Rab18*$^{-/-}$ littermates at the same stage the primary fibre cells were yet to elongate to the tip of the lens vesicle, suggestive of a delay in lens development (Figure 5.3B). To further analyse lens morphology subsequent histological analyses were undertaken at E15.5, E17.5 and P1.5. By E15.5 the lens vesicle in *Rab18*$^{-/-}$ mice had now filled but small vacuoles were apparent at the anterior of the lens (Figure 5.3D). Higher magnification images at E17.5 showed these vacuoles had become enlarged and the characteristic monolayer of epithelial cells surrounding the anterior of the lens is multicellular (Figure 5.3F). As fibre cells differentiate they lose their organelles and nuclei within the centre of the lens, resulting in an organelle free zone (OFZ) to prevent light scattering, as observed in the control lens at P1.5 (Figure 5.3G). However, analysis of *Rab18*$^{-/-}$lenses at P1.5 identified large nuclear aggregates and pyknotic nuclei within the centre of the lens (Figure 5.3H). Control lenses showed normal morphology at all stages examined (Figure 5.3A, C, E and G). Taken together this data suggests that loss of *Rab18* results in a delay in closure of the lens vesicle, vacuoles within the lens and abnormalities in fibre cell denucleation.


Control
Rab18-/-
A
B
C
D
E
F
G
H
E12.5
E15.5
E17.5
P1.5

Figure 5.3: *Rab18*$^{-/-}$ mice show defective lens development as early as E12.5

Haematoxylin and eosin staining on control and *Rab18*$^{-/-}$eyes at E12.5 (A-B), E15.5 (C-D), E17.5 (E-F) and P1.5 (G-H). (A-B) Analysis at E12.5 showing a delay in closure of the lens vesicle in *Rab18*$^{-/-}$ lenses (B) compared to control (A). (C-D) Analysis at E15.5 showing the lens vesicle in *Rab18*$^{-/-}$ eyes has now closed but vacuoles have developed at the anterior of the lens (D). (E-F) Analysis at E17.5 showing enlargement of the vacuoles in *Rab18*$^{-/-}$ mice and the epithelium surrounding the lens has become multilayered (F) as opposed to the monolayer of epithelial cells observed in control eyes (E). (G-H) Analysis at P1.5 showing the fibre cells in the centre of the control eye have lost their nuclei and organelles to prevent light scattering (G); however, pyknotic nuclei and large vacuoles are evidentt in the centre of the *Rab18*$^{-/-}$ lens (H). Panels A-D and G-H scale bar represents 200µm, panels E-F scale bar represents 50µm.

5.2.2 *Rab18*$^{-/-}$ eye abnormalities are restricted to the lens in adult mice

To examine the consequences of loss of *Rab18* on ocular structures in the mature adult eye, further histological (haematoxylin and eosin) staining was performed on eyes from 7 week old control and *Rab18*$^{-/-}$ littermates. No obvious pathological changes were identified in the retinal layers (Figure 5.4 A-B) in wild type or *Rab18*$^{-/-}$ eyes, suggesting the observed phenotype in *Rab18*$^{-/-}$ mice may be restricted to the lens. Note, that the *Rab18*$^{-/-}$ eye examined in figure 5.4B was unpigmented so no RPE (retinal pigment epithelium) is observed. As adult lenses are difficult to section with cracking and shattering regularly observed, in detailed histological analysis to examine cataract and eye morphology in adult mice was undertaken using optical projection tomography (OPT performed by Harris Morrison). OPT enables examination of biological tissues in 3D space. As with the histological analysis OPT identified large nuclear cataracts in the centre of the lens but no gross abnormalities in other ocular tissues.

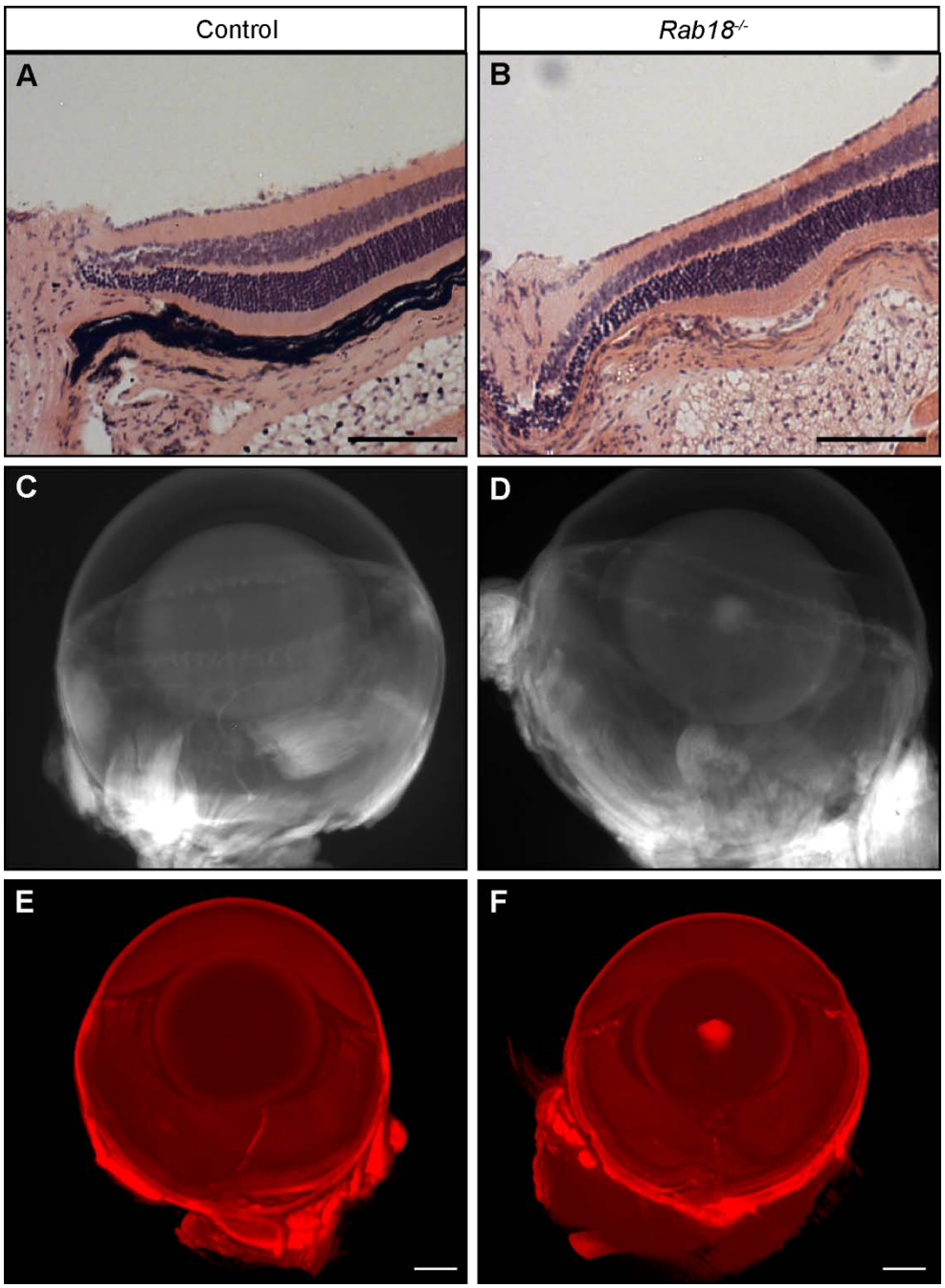

Figure 5.4: Ocular defects in *Rab18*$^{-/-}$ mice are restricted to the lens
Rab18$^{-/-}$ mice present at eye opening with dense nuclear congenital cataracts. (A-B) Histological analysis with haematoxylin and eosin on 7 week old wax-embedded eyes showing normal retinal morphology in control (A) and *Rab18*$^{-/-}$ (B) mice. Note that the eye in B is unpigmented and no retinal pigment epithelium is observed. (C-F) Optical projection tomography performed on 6 week old albino control (C and E) and *Rab18*$^{-/-}$ (D and F) eyes. Panels A-B scale bar represents 100µm, panels E-F scale bar represents 400µm.

5.2.3 Abnormalities in organisation and denucleation of lens fibre cells

Normal lens transparency is dependent upon the tight organisation of lens fibre cells, narrow intercellular spaces and loss of nuclei and organelles. Abnormalities in any of these processes results in loss of lens transparency and cataract development. I therefore set out to examine for any abnormalities in the organisation or denucleation of the lens in *Rab18*$^{-/-}$mice.

During my initial histological analysis of embryonic cataract development in the *Rab18*$^{-/-}$ lens centralised pyknotic nuclei were evident in the lens from E17.5 (Figure 5.3). To further examine nuclei distribution in the lens, eyes from P1.5 control and *Rab18*$^{-/-}$ littermates were stained with DAPI (Figure 5.5). At P1.5 fibre cells in the centre of the control lens have undergone denucleation resulting in an organelle free zone whereas newly differentiated fibres at the equatorial zone retain their nuclei (Figure 5.5A). In *Rab18*$^{-/-}$lenses nuclei are present in the equatorial zone but also clearly retained in the centre of the lens suggestive of abnormalities in lens fibre denucleation (Figure 5.5B).

Additionally, DAPI staining revealed that the epithelial cells in *Rab18*$^{-/-}$ mice were not a strict monolayer but multi-layering of cells was observed immediately anterior to the lens fibres (Figure 5.5).

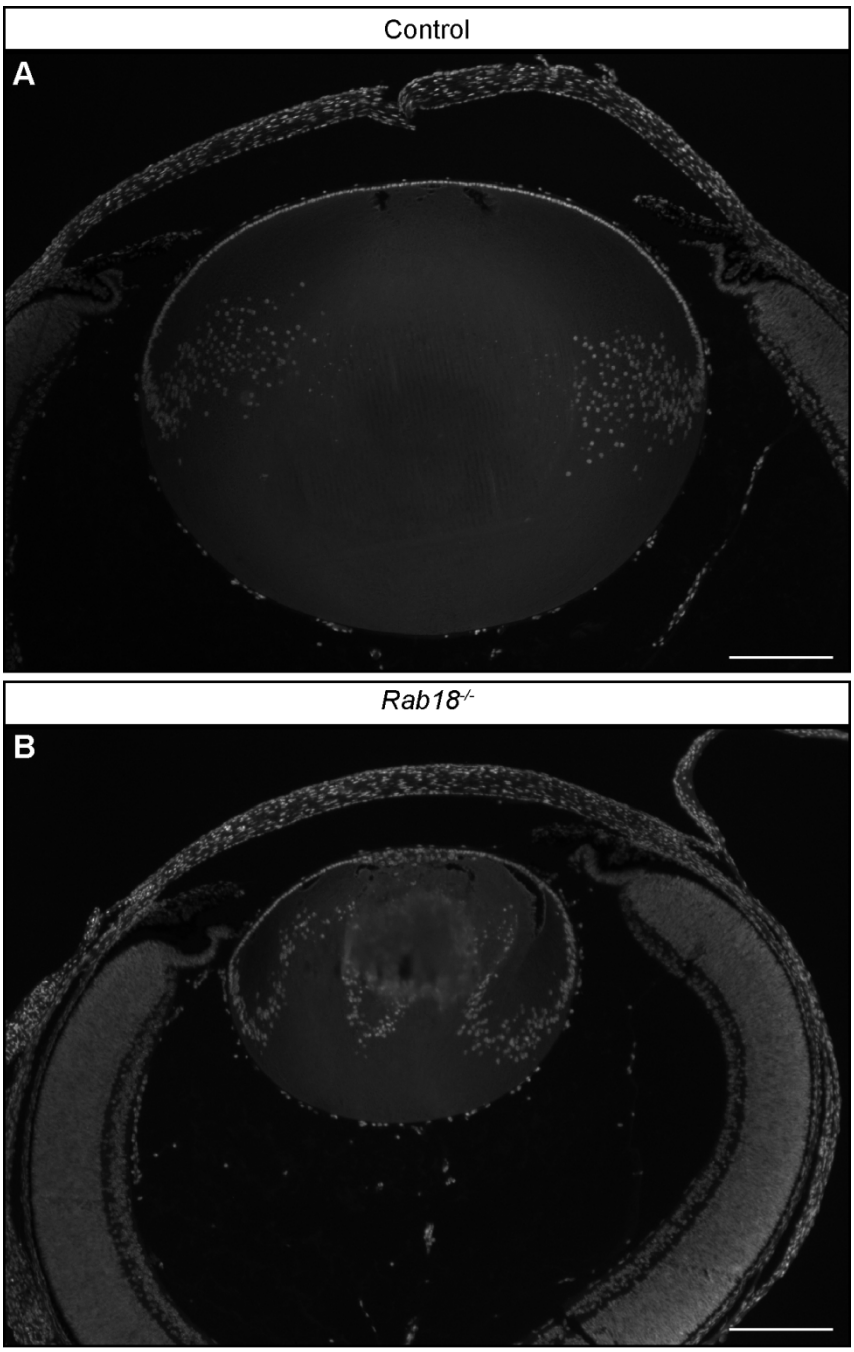

Figure 5.5: Abnormalities in fibre cell denucleation in *Rab18*$^{-/-}$ lenses
As fibre cells differentiate those in the centre of the lens lose nuclei and organelles to maintain transparency. (A) Eyes from P1.5 control mice stained with DAPI to examine nuclei distribution shows nuclei to be restricted to the younger lens fibre cells added at the equatorial zone (Figure 5.2). (B) Eyes from *Rab18*$^{-/-}$ littermates show cell nuclei to be distributed throughout the lens, suggesting abnormalities in fibre cell denucleation. Panels A-B scale bar represents 200µm.

In order to examine the organisation of lens fibre cells in more detail preliminary studies were undertaken to label P1.5 control and *Rab18*$^{-/-}$ sagittally sectioned eyes with periaxin (Figure 5.6). Periaxin has previously been shown to localise to the lens fibre cell plasma membrane (Maddala et al., 2011). Analysis of lens fibre cells at the equatorial zone, where the newest fibres are laid down showed normal organisation in control and *Rab18*$^{-/-}$lenses (Figure 5.6 D-E). However, staining of fibre cells at the tip of the anterior pole showed gross discrepancies between control and *Rab18*$^{-/-}$ samples. In the control eye the lens fibre cells were highly organised whereas in the *Rab18*$^{-/-}$lens swellings in the fibres were often seen (Figure 5.6 F-G). However, to examine the organisation of fibre cells in more detail periaxin staining would need to be repeated on control and *Rab18*$^{-/-}$ eyes sectioned through the equatorial plane to show the characteristic honeycomb architecture of lens fibre cells.

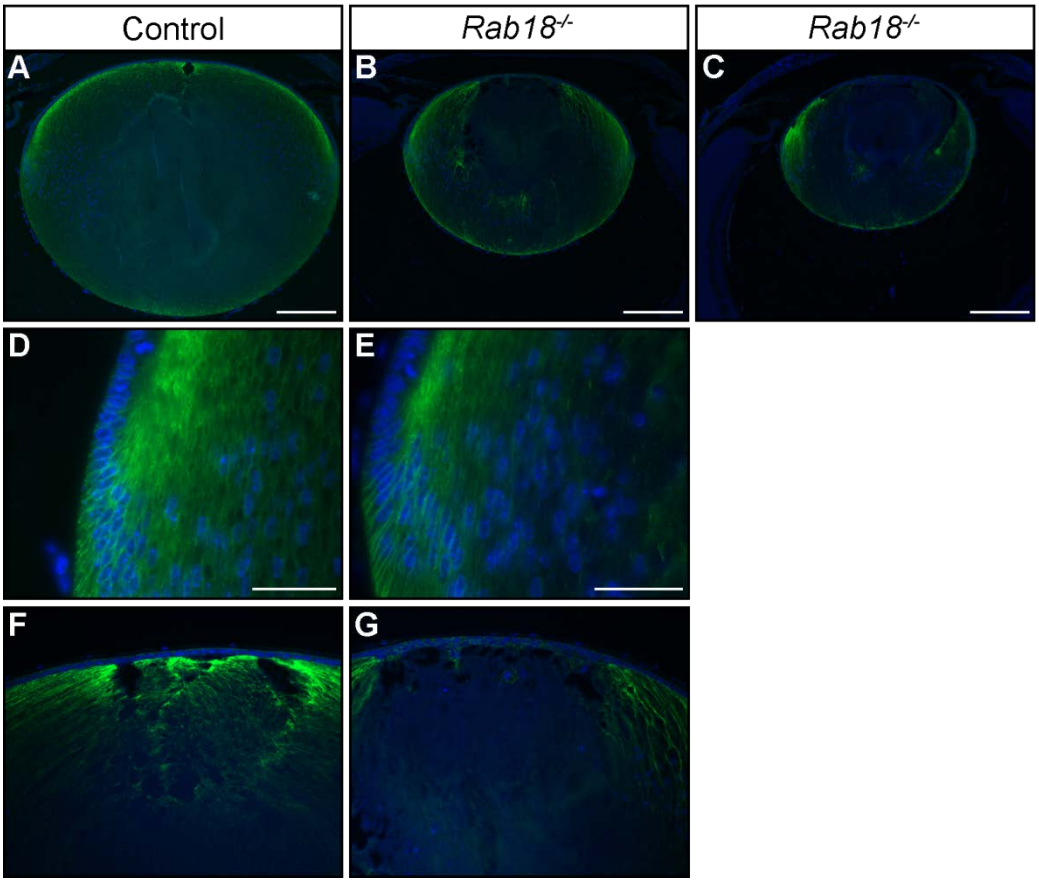

Figure 5.6: Abnormalities in fibre cell organisation in *Rab18*$^{-/-}$ lenses
(A-C) Analysis of lens fibre organisation in P1.5 eyes stained with periaxin (green). Cell nuclei were labelled with DAPI (blue) in control (A) and *Rab18*$^{-/-}$ eyes (B-C). (D-E) Periaxin staining at the equator where epithelial cells differentiate into primary fibre cells shows normal organisation in control (D) and *Rab18*$^{-/-}$ lenses. (F-G) Periaxin staining at the top of the lens, just below the lens epithelium shows swelling of fibre cells in *Rab18*$^{-/-}$ lenses (G) compared to control (F). Panels A-C scale bar represents 200µm, panels D-G scale bar represents 50µm.

5.2.4 RAB18 is not expressed in the bulk of adult lens

As loss of *Rab18* results in lens abnormalities including congenital nuclear cataracts I set out to determine whether RAB18 is expressed in the adult lens. Lenses from control and *Rab18*$^{-/-}$mice were dissected and immediately homogenised in RIPA buffer, separated by electrophoresis on an SDS-PAGE gel and immunoblotted for RAB18 (Figure 5.7). As the RAB18 antibody shows many bands on western blotting heterozygote sciatic nerve was also loaded as a positive control. The heterozygote

sciatic nerve sample showed two bands at approximately 23 kDa that I have previously shown to be missing in the *Rab18*$^{-/-}$ sciatic nerves (Figure 3.5D). Lens protein extracts from heterozygote and *Rab18*$^{-/-}$ mice showed one band run at slightly lower molecular weight, which failed to disappear in the *Rab18*$^{-/-}$ sample, indicating that RAB18 is not expressed in the bulk of the adult lens. The same membrane was also stained with ponceau S to determine protein expression in the lens and no differences observed (Figure 5.7B). As ponceau S is less sensitive than coomassie blue staining, supernatants from different lens extracts were run on an SDS-PAGE gel and stained with Coomassie blue to determine any differences in total protein content between control and *Rab18*$^{-/-}$ samples. No obvious differential bands were identified between genotypes (Figure 5.8). Furthermore, as cataractous lenses often show nuclear aggregates within the lens the resultant pellets following protein extraction were boiled in SDS-PAGE buffer and run on a coomassie gel to determine whether any aggregates may have been retained in the pellet that could be attributed to the lenticular cataract. Again, no differences between control and *Rab18*$^{-/-}$samples were observed (Figure 5.8). However, despite the fact that we failed to observe RAB18 expression in the adult lens; this does not necessarily mean it is absent from the entire lens. The bulk of the lens is composed of fibre cells which are metabolically inactive, however, a small niche of ‘stem-like’ epithelial cells exist anterior to the lens, but in such small numbers that epithelial specific proteins would probably be undetectable. Our data therefore suggests that RAB18 does not appear to be a major constituent of mature fibre cells, which make up the bulk of the lens.

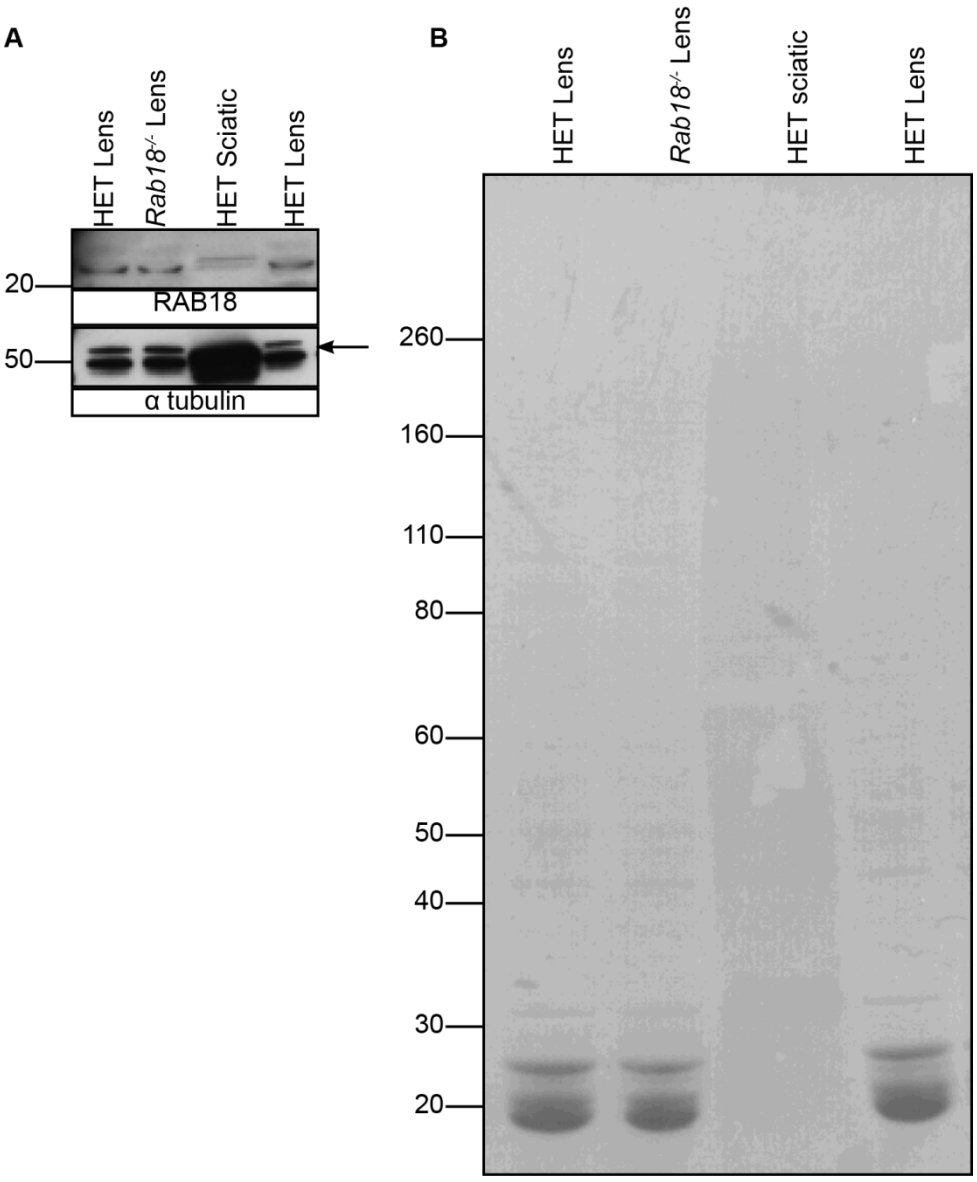

Figure 5.7: RAB18 is not expressed in the bulk of the adult lens

Analysis of RAB18 expression in the adult mouse lens. (A) Western blot analysis of lens and sciatic nerve extracts from heterozygote (HET) and *Rab18*$^{-/-}$ adult mice. RAB18 is expressed as a doublet in sciatic nerves samples, however, lens extracts show a band of lower molecular weight which does not disappear in the *Rab18*$^{-/-}$ sample and is not believed to be RAB18; α-tubulin was used as a loading control, N=3. (B) Ponceau staining of membrane used in (A) showing protein expression in the lens.

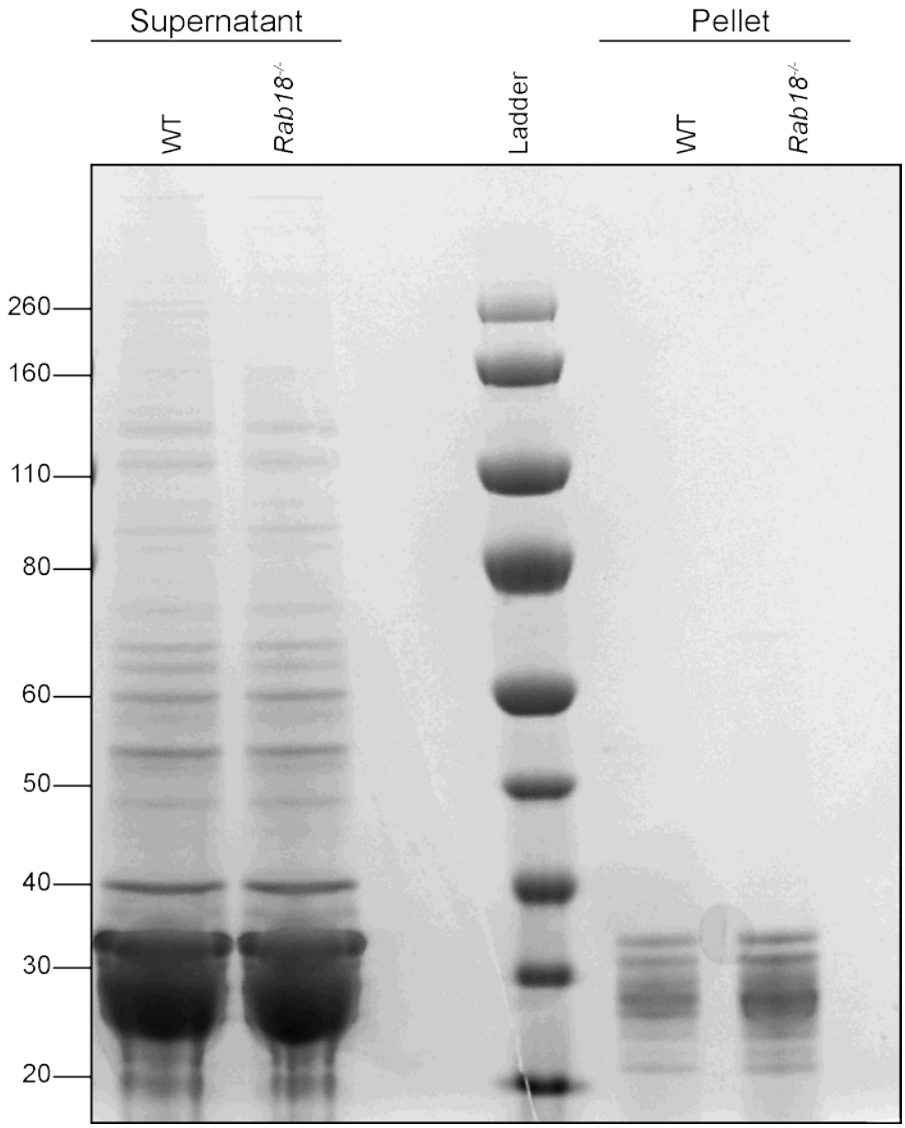

Figure 5.8: No obvious protein differences in supernatant or pellet lens extracts in control and *Rab18*$^{-/-}$ mice

Coomassie stained SDS-PAGE analysis of control and *Rab18*$^{-/-}$ lens extracts showing no obvious differences in protein expression in either supernatant or pelleted samples from control or *Rab18*$^{-/-}$ lenses.

5.3 Discussion

In this chapter I describe detailed characterisation of the congenital cataracts identified in *Rab18*$^{-/-}$ mice. Through histological examination I have identified a delay in closure of the lens vesicle at E12.5. Examination of adult eyes by histology and OPT identified no other ocular abnormalities suggesting the phenotype is restricted to the lens. Additionally, preliminary studies identified abnormalities in denucleation and organisation of lens fibre cells in *Rab18*$^{-/-}$ neonates suggestive of a defect in lens fibre differentiation.

5.3.1 Warburg Micro syndrome ocular phenotypes

During initial phenotypic characterisation of *Rab18*$^{-/-}$ mice, I identified congenital cataracts and atonic pupils recapitulating ocular phenotypes associated with Warburg Micro syndrome. However, Warburg Micro syndrome patients also characteristically present with other ocular abnormalities including micropthalmia, microcornea, cortical blindness and optic atrophy. Our analyses to date have focused on the congenital cataracts but further investigation into the other ocular features would be essential to definitively confirm or deny their presence.

5.3.2 Ocular defects in *Rab18*$^{-/-}$ mice include delayed lens closure and cataract development

Histological analysis at E12.5 in *Rab18*$^{-/-}$ mice identified a delay in closure of the lens vesicle suggestive of a timed delay in ocular development. This retardment could potentially be attributed to retarded growth of the eye and it would therefore be of interest to examine eye sizes compared to body weight at all stages examined. This would also aid clarification of whether *Rab18*$^{-/-}$ mice recapitulate the micropthalmia observed in Warburg Micro syndrome patients. Furthermore, it must be noted that in our analyses small lenses were observed in some *Rab18*$^{-/-}$ neonates but not all. Further characterisation of eye and lens size should now be undertaken. By E15.5 the lens vesicle in *Rab18*$^{-/-}$ mice appeared to have closed but vacuoles were apparent at the anterior below the lens epithelium. Intermediate embryonic stages would need to be examined to determine whether the vesicle closes in its entirety

prior to vacuole formation or are the vacuoles a result of specific areas of the lens vesicle that do not close. By E17.5 the vacuoles had become enlarged and the metabolically active epithelial cells that should be in a monolayer on the anterior of the lens were now multi-layered in *Rab18*$^{-/-}$ mice. As lens fibre cells differentiate they lose organelles and nuclei, become metabolically inactive and are dependent upon the metabolic activity of the epithelial cells and superficial fibre cells to pass small ions and nutrients through gap junctions to the centre of the lens. It would be of interest to determine whether this increase in epithelial cell number could be linked to an increased need of epithelial precursors for lens fibre differentation. At P1.5 control mice show a mature lens with differentiated fibre cells lacking organelles and nuclei resulting in an OFZ in the centre of the lens. However, *Rab18*$^{-/-}$ mice at the same stage show large nuclear aggregates and evidence of centralised pyknotic nuclei suggestive of abnormalities in lens fibre differentiation.

5.3.3 *Rab18*$^{-/-}$ mice show abnormalities in lens fibre cell differentiation and organisation

Lens transparency is retained via denucleation and loss of organelles in the centre of the lens and the tightly ordered packaging of lens fibre cells. To further examine for defects in lens fibre differentiation P1.5 control and *Rab18*$^{-/-}$ eyes were stained with DAPI to label the cell nuclei. Our analyses showed that P1.5 control eyes have an OFZ in the centre of the lens whereas *Rab18*$^{-/-}$lenses retain nuclei in the centralised fibre cells, suggestive of abnormalities in fibre cell denucleation. It would be of interest to also stain the lens with apoptosis markers such as TUNEL to determine whether the nuclei are slowly degenerating and undergoing apoptosis but in a delayed manner or whether the process in its entirety is blocked. Lenses from control and *Rab18*$^{-/-}$mice should also be labelled with differentiation makers such as the α, β and γ-crystallins, whose expression increases dramatically upon fibre cell differentiation to further confirm for any gross defects in differentiation.

Analysis of lenticular organisation was undertaken in P1.5 *Rab18*$^{-/-}$lenses labelled with periaxin (PRX), a lens fibre membrane marker (Maddala et al., 2011). Preliminary analysis of sagittal lens sections hinted at a disorganisation of lens fibre

cells, however, to further characterise their morphology sectioning at the equatorial plane of the eye would need to be undertaken to examine the characteristic honeycomb architecture and quantifications of fibre cell length to width ratio calculated, as shown to be altered upon loss of ephrin-A5 (Cooper et al., 2008). The morphology and microarchitecture of individual fibre cells could also be analysed by scanning electron microscopy.

5.3.4 Suggested abnormalities in lens epithelial cells

In addition to abnormalities in denucleation of lens fibre cells, histological analysis of the epithelial cell monolayer in P1.5 *Rab18*$^{-/-}$ eyes stained with DAPI identified overgrowth of the monolayer and potential infringement of epithelial cells into the lens fibre cells. This is also observed in a TGFβ-induced mouse model. However, these mice displayed anterior subcapsular cataracts suggesting that the infringement of epithelial cells into the lens fibres disrupts the organisation and causes cataracts (Lovicu et al., 2004). In our *Rab18*$^{-/-}$ mouse model this was not observed. I have identified nuclear congenital cataracts, suggesting that the epithelial cell phenotype maybe a secondary or unrelated consequence and not a primary phenotype, however further studies would need to be undertaken to examine this further.

5.3.5 RAB18 is not expressed in the bulk of the adult lens

Interestingly, I have shown that RAB18 was not present in the bulk of the adult lens. The developmental expression of RAB18 has not been evaluated as yet but studies such as Western blot anlaysis on embryonic or neonatal lenses or sectioning of LacZ stained embryonic or neonatal eyes could examine the location and timecourse of RAB18 expression in the developing lens. The early lens phenotype observed upon loss of *Rab18* points towards a role for RAB18 in early eye development. However, loss of very early expressed genes for example *Pax6* and *Sox2* by contrast result in much more severe phenotypes such as anophthalmia (Graw, 2004), suggesting that RAB18's expression could in fact be slightly later in eye development and would need to be characterised further.

5.3.6 The role of RAB proteins in lens and cataract development

Studies performed by Rao *et al.,* have identified several small GTPases in the monkey and human lens (Rao et al., 1997b) that redistributed from the membrane to the cytosol and induced cataract formation upon lovastatin treatment (Rao et al., 1997a). Lovastatin and other HMG-COA reductase inhibitors block the first step of the cholesterol biosynthesis pathway and as a result inhibit isoprenoid production. RAB proteins like other small GTPases are dependent upon isoprenylation for attachment into membranes and hence normal function (Rao et al., 1997a, Kinsella and Maltese, 1992). This supports my results of the involvement of small GTPases in cataract development. However, to my knowledge further characterisation of the role of RAB GTPases in the lens has yet to be undertaken.

Previous studies have reported RAB18 to localise to lipid droplets and play a role in lipolysis and lipogenesis (Martin et al., 2005, Ozeki et al., 2005, Pulido et al., 2011), and *Rab18*$^{-/-}$ MEFS show enlarged lipid droplets (Figure 4.3). Lipid droplets are the storage sites of neutral lipids the major lipid being cholesterol. Cholesterol is an essential component of lens fibre cell membranes and as a result the lens contains the highest levels of cholesterol observed in the human body where it is observed in patches in the lipid bilayer (Borchman and Yappert, 2010). It is interesting that many of the features of Warburg Micro syndrome including cataracts are recapitulated in another genetic disorder with mutations in cholesterol metabolism, such as Smith-Lemli-Opitz syndrome (Cotlier and Rice, 1971). This suggests a link between RAB18, lipids and cataract development, and hopefully analyses of lipid and cholesterol levels in the *Rab18*$^{-/-}$ lens may provide the basis of future studies.

5.3.7 Summary

In summary, I have described here detailed histological characterisation of the congenital cataracts observed during initial phenotyping of *Rab18*$^{-/-}$ mice. I have identified a delay in closure of the lens vesicle at E12.5 and abnormalities in lens fibre organisation and differentiation in neonates. Histological and OPT analysis of adult eyes restricted the phenotypic abnormalities to the lens.

The *Rab18*$^{-/-}$ mouse has made it possible to examine the aetiology of the Warburg Micro syndrome ocular phenotypes in a manner that is not possible in human patients. The data reported here has also enabled us to draw conclusions about the human disease, for example we have examined not only the role of RAB18 in disease but also in eye development and have identified a deficit in fibre cell differentiation which may be specific to these cells or relate to a more general role. As such fibre cell differentiation could potentially provide a model system in which to study the molecular functions of RAB18 and/or RAB18 dysfunction which may or may not have a similar effect in lens fibre cells and neurons (Frederikse et al., 2012).

Chapter 6 Characterisation of neurological pathology in *Rab18*$^{-/-}$ mice

6.1 Introduction

Children with Warburg Micro syndrome are severely handicapped and characteristically show truncal hypotonia. From approximately 8-12 months, they develop progressive lower limb spasticity, eventually leading to spastic quadriplegia by the teenage years. Progressive axonal neuropathy has also been noted (Bem et al., 2011, Handley et al., 2013, Abdel-Salam et al., 2007, Derbent et al., 2004). In chapter 3 of this thesis I reported neurological deterioration of the hind limbs in *Rab18*$^{-/-}$ mice progressing from abnormal hind limb clasping, to splayed limbs, extended gait and a noticeable decline in movement. Additionally, we have observed the novel localisation of GFP-RAB18 to distinct mobile puncta along neuronal processes, pointing towards a previously unreported role for RAB18 within neurons.

Given that notable advances in our understanding of pathological mechanisms underlying human neurological conditions have come from the characterisation of mouse models lacking or overexpressing a particular gene of interest, we set out to further characterise the hind limb weakness observed in *Rab18*$^{-/-}$ mice with the aim of providing insights into neuropathological changes underlying the Warburg Micro syndrome phenotype.

Given the progressive lower limb spasticity in Warburg Micro syndrome patients and observed hind limb weakness in *Rab18*$^{-/-}$ mice we focused the majority of our analyses on the morphology and function of lower motor neurons. Motor neurons can be divided into two main sub-types. Upper motor neurons project into the spinal cord from higher centres in the brain and brainstem, where they synapse (either directly or indirectly) with lower motor neurons. Lower motor neuron cell bodies are located in cranial nerve nuclei or the ventral grey horn of the spinal cord, with their axons projecting into peripheral nerves and their synaptic terminals synapsing with skeletal muscle fibres at the neuromuscular junction (NMJ). Thus, motor neurons are the

longest cells in the human body, with some cells (for example those innervating the extremities of the lower limb) over 1 meter in length. As a result, they are highly sensitive to perturbations in protein transport or cytoskeletal organisation and are the site of pathological deterioration in many neurodegenerative diseases, including spinal muscular atrophy, hereditary spastic paraplegia and amyotrophic lateral sclerosis (Kasher et al., 2009, El-Kadi et al., 2007, Ikenaka et al., 2012, Dale et al., 2011).

6.1.1 The neuronal cytoskeleton

Motor neurons, like many other cell types, contain a highly organised cytoskeleton; providing structure, support and the tracks on which axonal transport takes place. The neuronal cytoskeleton is comprised of three classes of proteins; actin microfilaments, microtubules and intermediate filaments. For in detailed reviews please see (El-Kadi et al., 2007, Perrot and Eyer, 2009, Ikenaka et al., 2012, Yuan et al., 2012).

Both microtubules and microfilaments play critical roles in axonal transport, forming the tracks on which proteins are transported (El-Kadi et al., 2007). Microtubule filaments are formed from 13 tracks of alternating α and β tubulin heterodimers, producing a final filament of 24 nm. Microtubules thus form long but discontinuous tracks throughout the axon. They are highly polarised structures with slow growing (minus) ends pointing towards the cell body and fast growing (plus) ends growing towards the axon termini. Microtubule filaments form the tracks for long range transport, and their organisation is critical for efficient transport and hence neuronal survival (Conde and Caceres, 2009). Actin microfilaments are shorter (6-8nm) microfilaments formed from two twisted strands of β and γ actin monomers. Like microtubules, actin filaments are also polarised with plus and minus ends and are thought to provide the tracks for short range axonal transport.

Six classes of intermediate filaments exist; neurofilament triplet proteins, α-internexin, peripherin, vimentin, nestin and synemin, varying in temporal and spatial expression patterns (Perrot and Eyer, 2009). Neurofilament proteins comprise the largest cytoskeletal component of myelinated axons, where they function to establish

and maintain axonal calibre (Yuan et al., 2012, Perrot and Eyer, 2009). Three different classes of neurofilament exist; 68kDa NEFL (neurofilament light chain), 165kDa NEFM (neurofilament medium chain) and 200kDa NEFH (neurofilament heavy chain). The three neurofilament isoforms share a common tripartite structure composed of; an approximately 310 amino acid highly conserved α-helical coiled coil rod domain, an N-terminal head domain and a C-terminal tail domain that varies in length between isoforms (Geisler et al., 1983). Two α-helical coiled coil domains (one from NEFL and the other from NEFM or NEFH) come together to form a parallel dimer (Szaro and Strong, 2009). Two of these resultant dimers join in an antiparallel fashion to form tetramers. Unlike microtubules and microfilaments, neurofilaments thus lack polarity. Eight tetramers can then form an approximately 60nm length filament that join end to end producing the final intermediate filament. The tail domains of NEFM and NEFH radiate externally from the filament where they interact with organelles and other neurofilaments and thus primarily function as 'spacers' defining the axonal calibre and hence axonal conduction velocity (Szaro and Strong, 2009).

Neurofilament function and expression is regulated through vast post-translational modifications. For example neurofilament proteins are phosphorylated at head and tail domains and this is thought to play a key role in the regulation of neurofilament assembly (Hisanaga et al., 1990). Neurofilament proteins are synthesised in the cell body and transported bidirectionally along microtubules via kinesin and dynein/dynactin motor proteins (Wagner et al., 2004, Brown et al., 2005, Yabe et al., 1999). Additionally, phosphorylation at KSP (KSXXP) motifs within NEFM and NEFH tail domains has previously been shown to regulate neurofilament transport (Ackerley et al., 2003).

Accumulations of neurofilament proteins and aberrant phosphorylation of different neurofilament isoforms are hallmark features observed in many human disorders characterised by both central nervous system and motor neuron dysfunction. Genetic mapping and the generation and characterisation of mouse models have helped delineate the functional role of neurofilament proteins and their involvement in neurodegeneration (Table 6.1). These studies have identified that neurofilament

accumulations can result from mutations in neurofilament proteins themselves, for example, mutations in NEFL cause Charcot-Marie-Tooth type II with characteristic peripheral neuropathy and reduced nerve conduction velocities (Jordanova et al., 2003), and transfection of CMT mutant neurofilaments into SW13 cells and neurons disrupts both the assembly and transport of neurofilaments (Brownlees et al., 2002). Additionally, accumulations may result from mutations in the molecular machinery responsible for their transport. For example, postnatal deletion of KIF5A in neurons with a Cre- recombinase transgene resulted in accumulations of all three neurofilament isoforms in neuronal cell bodies (Xia et al., 2003). Furthermore, correct stochiometry of different neurofilament isoforms is required for their function as generation of transgenic mice overexpressing human NEFH (a model for ALS) displayed perikaryal neurofilament accumulations and abnormalities in neurofilament transport (Julien et al., 1995).

Table 6.1: Mouse models of neurodegenerative disease with accumulations of neurofilament

NMJ-Neuromuscular junction, SMA- Spinal Muscular atrophy, HSP-Hereditary Spastic Paraplegia, NF- neurofilament. Please note that this is not an exhaustive list due to the large number of mouse models now generated but shows evidence of neurofilament accumulation in many distinct neurodegenerative diseases.

Mouse model	Human disease	Phenotype	Reference
$Smn^{F7}/Smn^{\Delta 7}$, NSE-Cre^{+}	SMA	Accumulations of NEFM and phosphorylated NEFH at the NMJ, but no change in total levels.	(Cifuentes-Diaz et al., 2002)
$Smn^{-/-}$;SMN2	SMA	Accumulation of neurofilaments, deneverated endplates and muscular atrophy	(Murray et al., 2008)
$Smn^{-/-}$;SMN2;Δ7	SMA	Accumulation of neurofilaments, deneverated endplates and muscular atrophy	(Murray et al., 2008)
$Spg7^{-/-}$ (paraplegin knockout)	HSP	Accumulation of NF and organelles in the spinal cord and peripheral axons accompanied by axonal swellings and morphologically abnormal mitochondria	(Ferreirinha et al., 2004)
Wobbler mouse	Motor neuron disease	Accumulation of NF and motor neuron degeneration in the ventral horn of the cervical spinal cord	(Pernas-Alonso et al., 2001)
$KIF5A^{null}/KIF5A^{flox}$; $Cre^{synapsin}$	HSP (SPG10)	Accumulations of NEFL, NEFM and NEFH within cell bodies of peripheral sensory neurons, also loss of large calibre axons was observed	(Xia et al., 2003)
G1H (human SOD1 G93A overexpression)	ALS	Spheroids rich in neuronal isoforms including NF and phosphorylated NF isoforms in spinal cord and prominent astrocytosis	(Tu et al., 1996)

6.1.2 Axonal transport

The majority of axonal proteins are synthesised in the neuronal cell body and transported to their sites of function via axonal transport. Efficient protein transport is therefore critical for the development and survival of axons and the correct function of nerve terminals. For detailed reviews please see (De Vos et al., 2008, Millecamps and Julien, 2013, El-Kadi et al., 2007).

The majority of axonal transport occurs on microtubule tracks driven by two distinct classes of molecular motors driving transport with structural polarity. Kinesin motor proteins drive anterograde transport from the cell body to the synaptic termini. Dyenin motor proteins together with its adaptor protein dynactin drive retrograde transport from the termini back towards the soma. A third class of motor proteins, the myosin motors also exist and are responsible for short distance axonal trafficking in a bidirectional manner along actin microfilaments.

Proteins or protein subunits (that are then assembled at the synapse) can be trafficked along microtubules by either fast or slow axonal transport. Fast axonal transport moves organelles such as lysosomes, endosomes and mitochondria, at a rate of 1µm per second. Slow axonal transport transports cytoskeletal and cytosolic proteins at a rate of 1mm per day (De Vos et al., 2008). Recent studies have identified that the transport velocity of axonal components is not dependent upon the rate of transport but rather the amount of time spent in a paused state. For example previous studies have identified that neurofilaments are trafficked along microtubules in a bidirectional manner, alternating between rapid movements and prolonged pauses (Brown et al., 2005).

Accumulations of proteins such as neurofilament at either the axon termini and/or the cell body are hallmark features of many neurodegenerative diseases. This suggests that disruption to axonal transport and hence abnormalities in axonal homeostasis may underlie or be a consequence of many neurodegenerative diseases (Table 6.2). It is therefore of interest to definitively determine whether protein accumulations themselves are pathogenic or present an epiphenomenom resulting from an underlying defect in transport or trafficking.

Table 6.2: Mouse models of neurodegenerative disease with axonal transport defects

NMJ-Neuromuscular junction, SMA- Spinal Muscular atrophy, HSP-Hereditary Spastic Paraplegia, NF- neurofilament. Again please note that this is not an exhaustive list but represents the growing body of evidence identifying axonal transport defects implicated in the underlying pathology of many neurodegenerative diseases.

Mouse model	Human disease	Phenotype	Reference
Transgenic mice overexpressing human NF-H	ALS	Reduction in transport of NF, tubulin and actin. Degenerating axons lacking neurofilaments, mitochondria and small ER.	(Collard et al., 1995)
Transgenic mice overexpressing human SOD1 (G93A)	ALS	Abnormal retrograde transport of adenovirus containing *E.coli* lacZ injected into gastrocnemius muscles	(Murakami et al., 2001)
SMA$^{\Delta 7}$	SMA	Normal global distribution of NF. Reduction in fast anterograde transport of SV-2 and synaptotagmin. Reduction in dynein levels in agreement with NF accumulations at NMJ.	(Dale et al., 2011)
Spg7$^{-/-}$ (paraplegin knockout)	HSP	Disorganisation of cytoskeleton in spinal cord and sciatic nerve and retardation in retrograde transport.	(Ferreirinha et al., 2004)
KIF5A$^{-/-}$	HSP	Primary motor neuron cultures from KIF5A$^{-/-}$ mice reduction in anterograde and retrograde transport of mitochondria.	(Karle et al., 2012)
EMRC/36.5c (c.1092+2T>G in Spastin exon 7)	HSP	Primary cortical neurons→ axonal swellings of tubulin and mitochondria, tau , NF and APP, anterograde transport defects of APP and mitochondria.	(Kasher et al., 2009)
Gjb1$^{-/-}$ null	CMT1X	Impairment of anterograde and retrograde axonal transport of synaptic vesicle proteins and abnormal accumulation of kinesin and dynein following sciatic nerve ligation	(Vavlitou et al., 2010)

6.1.3 The neuromuscular junction

Many studies examining nerve-muscle connectivity and hence synaptic pathology have focused upon examination of the neuromuscular junction (NMJ) (Ribchester, 2009, Cifuentes-Diaz et al., 2002, Ribchester et al., 2004). Importantly, NMJ disruption is also a common early event in lower motor neuron pathology, so assessments of NMJ integrity are often used as a sensitive assay for motor neuron viability (Fischer et al., 2004, Cifuentes-Diaz et al., 2002); as a result NMJ morphology was examined in this study.

As the axon of a lower motor neuron nears its target of skeletal muscle fibres it loses its myelin sheath and splits into multiple branches, with each branch forming a synapse with an individual muscle fibre: the neuromuscular junction (NMJ). The NMJ functions to transmit chemical signals from nerve to muscle, principally via release of acetylcholine (ACh) (Sanes and Lichtman, 1999, Hughes et al., 2006).

The NMJ is comprised of four distinct cell types; the presynaptic motor nerve terminal, the post synaptic endplate of the muscle fibre, terminal Schwann cells and the recently identified Kranocyte (Sanes and Lichtman, 1999, Court et al., 2008). As branches of the motor neuron meet skeletal muscle fibres they lose their myelin sheath and form the presynaptic motor nerve terminal. The motor nerve terminal is highly polarised with mitochondria directed away from the terminal and large amounts of synaptic vesicles clustered at active zones, sites of release of the neurotransmitter acetylcholine (ACh). As an action potential reaches the presynaptic nerve terminal, calcium channels open resulting in a large calcium influx. Increases in internal calcium concentration depolarise the nerve terminal and drive synaptic vesicles to fuse with the plasma membrane and release their contents of ACh into the synaptic cleft. The synaptic cleft is approximately 50nm thick and largely composed of basal lamina as a support matrix and the enzyme acetylcholinesterase (AChE), which rapidly hydrolyses ACh and prevents prolonged activation. The postsynaptic membrane is designed for rapid response to ACh release. Its membrane invaginates to form multiple secondary synaptic folds placed immediately opposite active zones; the tips of such folds hold the acetylcholine receptor (AChR). AChR receive the released ACh and produce a post synaptic potential, the EPP (endplate potential),

which propagates through the muscle fibre leading to muscle contraction (Sanes and Lichtman, 1999, Hughes et al., 2006).

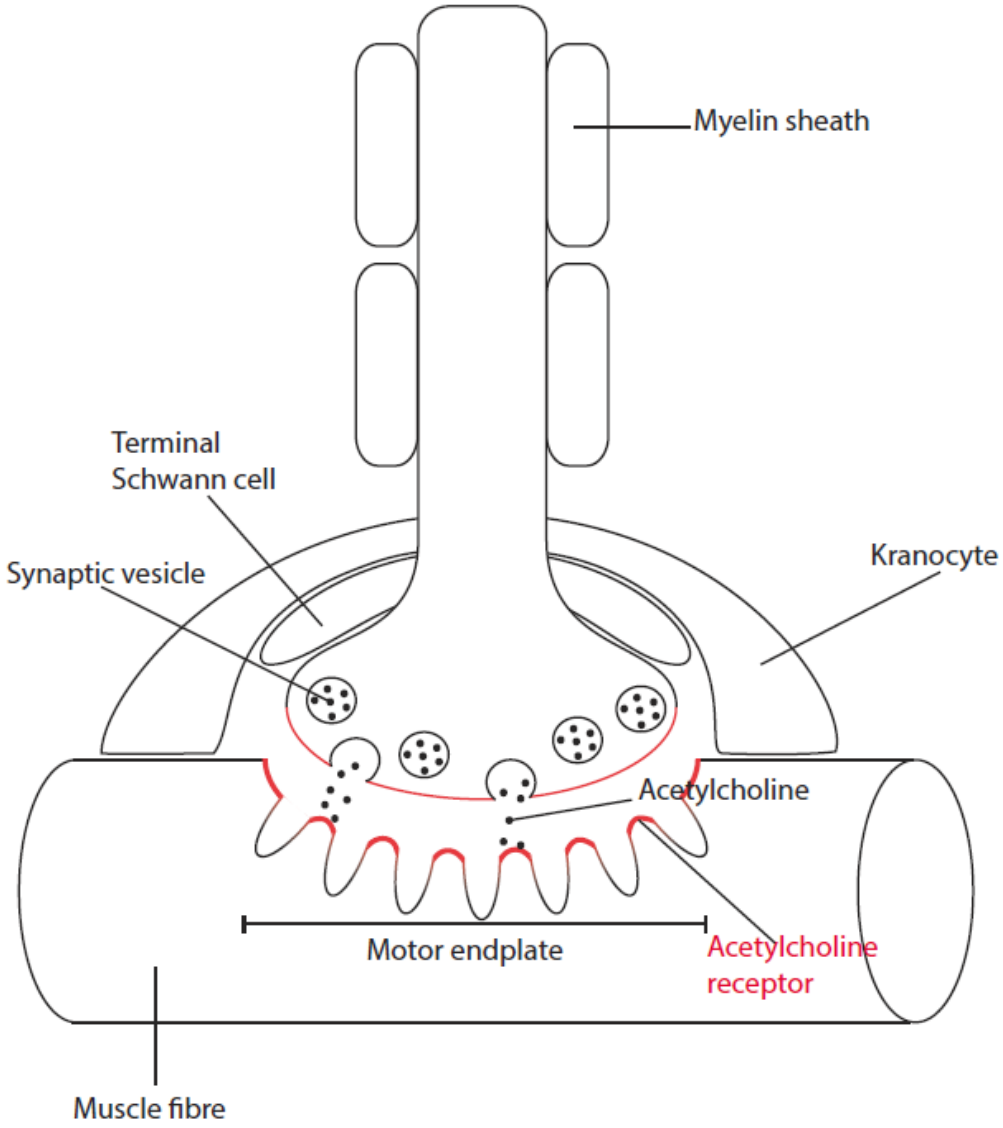

Figure 6.1: The neuromuscular junction
As motor axons meet muscle fibres, they lose their myelin sheath and split into multiple branches that each innervate an individual muscle fibre at the neuromuscular junction. The motor nerve terminal forms a presynaptic bouton filled with acetylcholine filled synaptic vesicles. Upon induction of an action potential, vesicles release acetylcholine into the synaptic cleft where they are taken up by the acetylcholine receptors on the post-synaptic muscle fibre. Additionally, the motor nerve terminal is encapsulated with a terminal Schwann cell and kranocyte to 'insulate' the NMJ.

In this chapter I have directed my focus towards characterisation of neuropathology underlying the progressive hind limb weakness observed in the *Rab18*$^{-/-}$ mouse model.

6.2 Results:

Warburg Micro syndrome patients develop lower limb spasticity from 8-12 months of age that is progressive, leading to spastic quadriplegia and axonal peripheral neuropathy later in life. Interestingly, the *Rab18*$^{-/-}$ mouse also presents with progressive hind limb weakness from weaning (3 weeks of age). No histopathological data is available from patients as most families decline post-mortem examination, so I set out to use the *Rab18*$^{-/-}$ mouse model to investigate the underlying causes of neuromuscular defects in *Rab18*$^{-/-}$ mice that could hopefully be extrapolated to Warburg Micro syndrome patients.

6.2.1 Normal synaptic vesicle recycling in *Rab18*$^{-/-}$ mice

At the start of this study loss-of-function mutations in *RAB3GAP1*, *RAB3GAP2* or *RAB18* only were reported to result in clinically indistinguishable Warburg Micro syndrome phenotypes (Aligianis et al., 2005, Borck et al., 2010, Bem et al., 2011). I therefore initially set out to examine the expression levels of RAB3GAP1, RAB3GAP2 and RAB3A, a specific target of RAB3GAP1 and RAB3GAP2, to determine whether loss of *Rab18*$^{-/-}$ results in their aberrant expression. The RAB3 family of proteins are specifically localised to synaptic vesicles and function in synaptic neurotransmitter release (Fischer von Mollard et al., 1990, Fischer von Mollard et al., 1991, Schluter et al., 2002). To analyse the levels of RAB3GAP1, RAB3GAP2 and RAB3A at the synapse of *Rab18*$^{-/-}$ mice, synapse enriched fractions (crude synaptosomal protein extracts) were isolated from 4 wild type (WT), 6 heterozygote (HET) and 5 *Rab18*$^{-/-}$ brains in ice cold isotonic sucrose solution and analysed by Western blotting (Figure 6.2). As the RAB3GAP1 and RAB3GAP2 antibodies used in this study resulted in many additional non specific bands upon Western blotting, myc tagged RAB3GAP1 and RAB3GAP2 transfected HEK293 cell extracts (generated by Dr Mark Handley) were also run as positive controls to definitively confirm the correct band. The addition of a molecular tag should have no major impact on protein function but run at a slightly higher molecular weight. Western blot analysis identified no differences in expression levels of RAB3GAP1, RAB3GAP2 and RAB3A in crude synaptosomes isolated from wild type, heterozygote and *Rab18*$^{-/-}$ mice. Thus, loss of *Rab18* had no gross impact on protein

levels of RAB3GAP1 and RAB3GAP2, suggesting that the neurological deterioration observed is not due to downstream consequences of altered RAB3GAP1 and/or RAB3GAP2 expression.

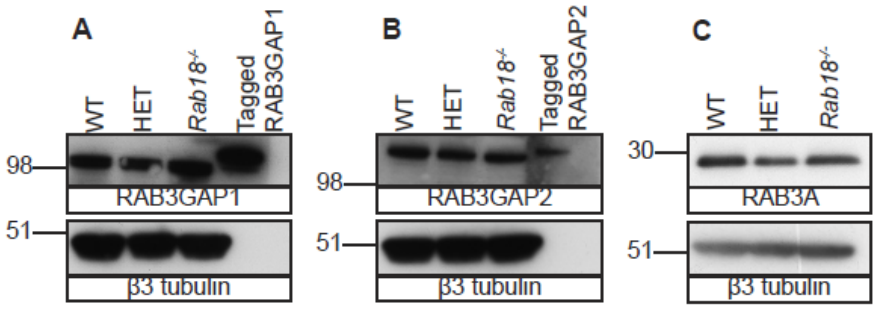

Figure 6.2 Loss of RAB18 has no effect levels of RAB3GAP1, RAB3GAP2 and RAB3A in synaptosomes

Western blot analysis of crude synaptosomes isolated from wild type, heterozygote and *Rab18*$^{-/-}$ mouse brains were blotted for RAB3GAP1 (A), RAB3GAP2 (B) and RAB3A (C) and showed no differences in overall protein levels. In (A) and (B) MYC tagged RAB3GAP1 and RAB3GAP2 were used as a positive control. β3 tubulin was used as a loading control for all westerns, note that the β3 tubulin antibody used specifically targets the neuronal specific isoform and as a result no loading band is shown in the HEK293 transfected cell extracts. Marker sizes are shown in kDa to the left of each blot.

RAB3GAP1 and RAB3GAP2 have well established roles in regulation of the RAB3 family in synaptic vesicle recycling (Nagano et al., 1998, Fukui et al., 1997, Fischer von Mollard et al., 1991, Schluter et al., 2002). I therefore set out to determine whether the neurological deterioration observed in *Rab18*$^{-/-}$ mice could be attributed to gross abnormalities in synaptic vesicle recycling at peripheral nervous system (PNS) or central nervous system (CNS) synapses.

To evaluate synaptic vesicle recycling in the PNS, synaptic vesicles at neuromuscular synapses were labelled with the styryl dye FM1-43fx. Styryl dyes are composed of a positively charged head attached to a lipophilic tail by a double or multiple double-bond bridge and routinely used in *in vitro* studies of the synaptic vesicle cycle (Cochilla et al., 1999). In brief, the styryl dye is added to the external media and binds to the outer leaflet of the plasma membrane. Upon stimulation of exocytosis, synaptic vesicles fuse with the plasma membrane, undergo exocytosis

and reciprocal endocytosis taking up the styryl dye (Cochilla et al., 1999). Any non-internalised dye was removed by multiple washes in oxygenated Ringer solution, so only that endocytosed by synaptic vesicles was examined in our analyses. To analyse synaptic vesicle recycling in the PNS I examined recycling synaptic vesicles at active neuromuscular junctions (NMJs) in lumbrical muscles (hind paw) of control and mid/late symptomatic *Rab18*$^{-/-}$ mice. Post synaptic acetylcholine receptors of the motor endplate were labelled with TRITC-α-BTX (red) and recycling synaptic vesicles with FM1-43fx (green). I utilised a fixable analogue of FM1-43 (FM1-43fx), this enabled retention of the fluorescent signal whilst I dissected individual muscles from their attached tendons prior to microscopy analysis. Upon stimulation of synaptic vesicle recycling with a high potassium solution, both control and *Rab18*$^{-/-}$ synapses efficiently endocytosed the FM dye (Figure 6.3 A-F). To quantify for any abnormalities in the number of active NMJs with recycling synaptic vesicles, the percentage of endplates (stained with TRITC-α-BTX, red) positive for FM1-43 staining (green) was calculated. No significant differences were observed between genotypes (Figure 6.3 G). Additionally, the fluorescence intensity of the FM dye normalised to TRITC-α-BTX staining was calculated to quantify for any abnormalities in the number of synaptic vesicles or the rate of recycling, and again no significant differences were observed (Figure 6.3 H). Taken together, this suggests that loss of *Rab18* has no major effect on gross parameters of synaptic vesicle recycling in the PNS.

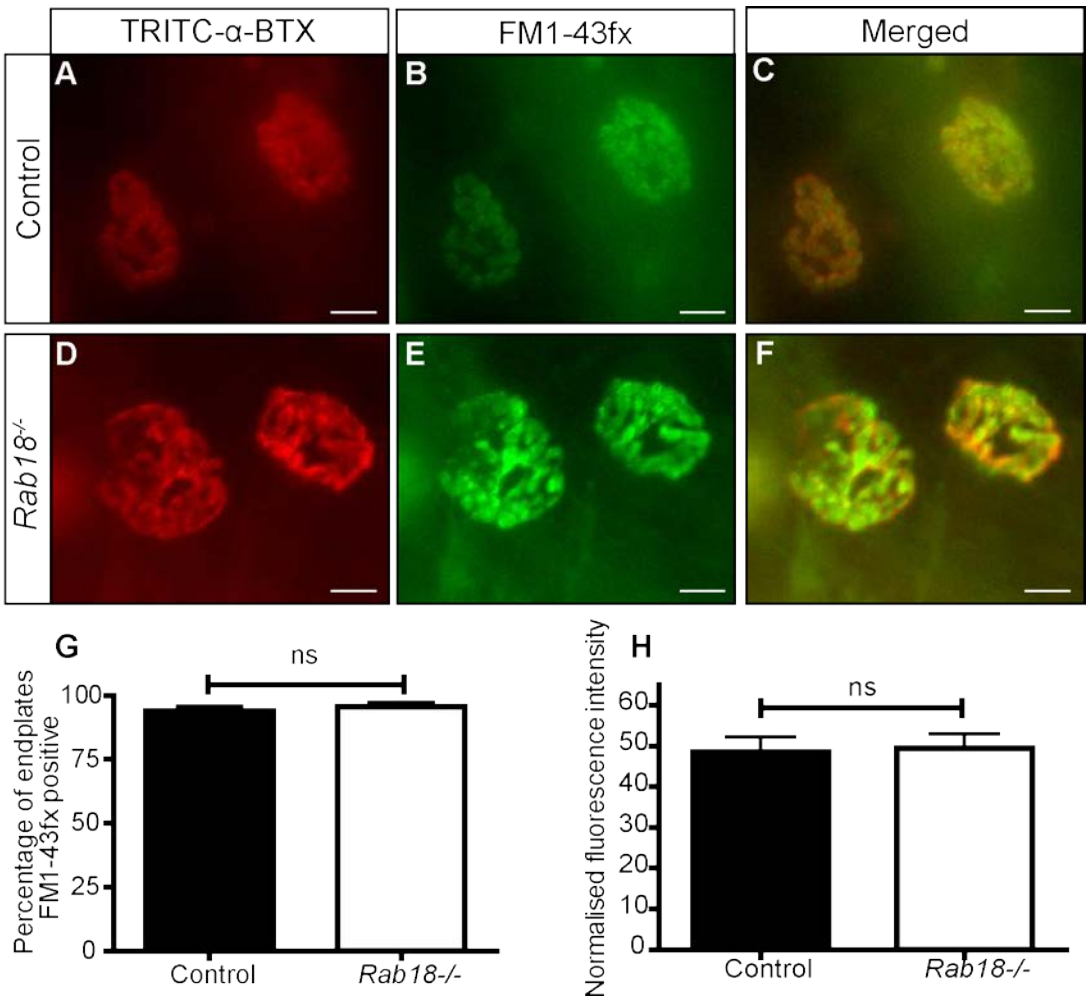

Figure 6.3 Loss of *Rab18* has no major effect on synaptic vesicle recycling in the PNS

(A-F) Fluorescence micrographs of synaptic vesicle recycling at the neuromuscular junctions of control (A-C) and mid/late symptomatic *Rab18*$^{-/-}$ (D-F) mice. Post-synaptic acetylcholine receptors of the motor endplate were labelled with TRITC-conjugated α-bungarotoxin (A and D, red) and recycling synaptic vesicles labelled with FM1-43fx following a high potassium solution to induce synaptic vesicle recycling (B and E, green). Merged images (C and F) are composites of TRITC-conjugated α-bungarotoxin (A and D) and FM1-43fx (B and E). (G) Bar chart (mean ± SEM) showing the majority of endplates examined effectively took up the FM1-43fx styryl dye irrespective of genotype (*Mann-Whitney test, two tailed, p value=0.3786, n=12 muscles*). (H) Bar chart (mean ± SEM) showing no difference in FM1-43fx fluorescence intensity normalised to TRITC-conjugated α-bungarotoxin in control and *Rab18*$^{-/-}$ littermates *(unpaired two tailed t-test, p value=0.8624, n=10 muscles control and 11 muscles Rab18*$^{-/-}$*). ns= not significant*, scale bar represents 5µm.

To examine synaptic vesicle recycling specifically at CNS synapses, isolated primary cortical neurons from wild type and *Rab18*$^{-/-}$ embryos were transfected with the genetic reporter synaptophysin-pHluorin (sypHy) (Granseth et al., 2006) in collaboration with Dr Sarah Gordon (Centre for Integrative Physiology). pHluorins are pH sensitive variations on GFP, and are routinely used in the study of neurotransmitter release as molecular markers of the pH of their surrounding environment. The pHluorin fluorescence is quenched in acidic environments, and increases at neutral pH (Fig 6.4 A). In the case of sypHy, the pHluorin is fused to the second intralumenal domain of synaptophysin, such that its fluorescence is quenched by the acidic pH inside synaptic vesicles (approximately pH 5.5). Upon exocytosis, sypHy is exposed to the neutral pH of extracellular medium (approximately pH 7.4) resulting in an increase in fluorescence. The pHluorin is then endocytosed, and following vesicle reacidification its fluorescence is again quenched. Vesicle reacidification is very fast, so the decrease in fluorescence acts as a reporter of the rate of endocytosis (Atluri and Ryan, 2006). To examine the consequences of loss of *Rab18* on the synaptic vesicle cycle, sypHy transfected cortical neurons from wild type (WT) and *Rab18*$^{-/-}$ (KO) embryos were stimulated at 10 Hz with a train of 300 action potentials to induce synaptic vesicle recycling and examine the kinetics of endocytosis. Cells were then additionally pulsed with ammonia buffer (NH_4Cl) to deacidify the synaptic vesicles and report the total pHluorin fluorescence (Figure 6.4 B). pHluorin traces were normalised to NH_4Cl to reveal the total amount of synaptic vesicles exocytosed upon electrical stimulus and revealed no significant differences in the amount of vesicles released by the evoked stimulus (Figure 6.4 C). Normalisation of the sypHy trace to the peak of the evoked stimulus is used to report differences in the kinetics of endocytosis (Fig 6.4 D). One-phase exponential decay curves were fit to the endocytosis component of the sypHy traces (from 50-200s) and the endocytic time constant (tau,τ) was calculated. There was no difference in τ between WT and *Rab18*$^{-/-}$ neurons. Thus, loss of *Rab18* has no major impact on gross synaptic vesicle recycling at PNS or CNS synapses.

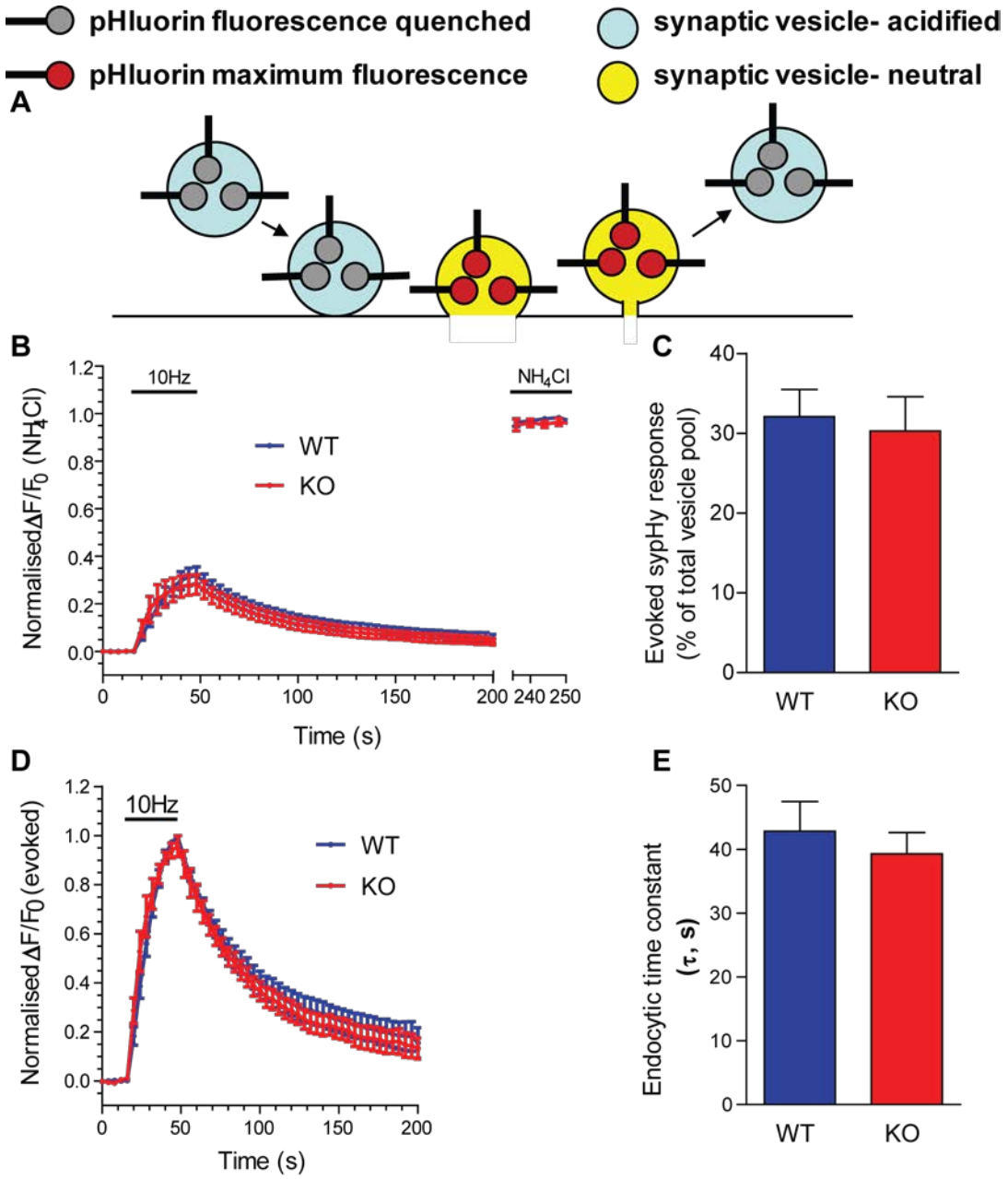

Figure 6.4 Loss of *Rab18* has no major effect on synaptic vesicle recycling in the CNS

Experiments performed in collaboration with Dr Sarah Gordon. (A) pHluorin mechanism of action. (B-E) Analysis of synaptic vesicle recycling in cortical neurons isolated from wild type (WT) and *Rab18*$^{-/-}$ (KO) E17.5 embryos. (B and D) Cortical neurons transfected with sypHy were stimulated with a train of 300 action potentials (10 Hz) and subsequently perfused with NH_4Cl to induce synaptic vesicle deacidification and reveal total pHluorin fluorescence. Traces illustrate the average fluorescence response over time (wild-type (WT, blue circles, n = 9) and *Rab18*$^{-/-}$ (KO, red circles, n = 7) ± SEM). (B) Traces were normalised to NH_4Cl to reveal the total vesicle pool and identified (C) the lack of effect of RAB18 deletion on size of total vesicle pool *(t-test p=0.74)*. (D) Traces were normalised to the stimulation peak

(10Hz) and (E) identified no differences in the average speed of endocytosis, endocytic time contast τ *(t-test p=0.55).*

6.2.2 Anatomical characteristics of FDB, lumbrical and TVA muscles used for investigation of PNS pathology

Rab18$^{-/-}$ mice present at weaning with abnormal hind limb clasping, deteriorating to progressive, hind limb weakness, abnormal gait and decline in movement. In order to determine whether motor neuron pathology was contributing to this phenotype, neuromuscular junctions were initially examined across a range of different muscle groups from control and *Rab18*$^{-/-}$ mice at both early symptomatic (3 weeks of age, onset of abnormal grasping phenotype) and mid/late symptomatic (splayed hind limbs, often dragged behind the body) time points. The following muscles were used for analyses; the transverse abdominus (TVA) a slow-twitch, postural muscle from the abdominal wall, the lumbrical muscles, a group of four fast-twitch muscles from the hind paw innervated by the medial and plantar branches of the tibial nerve and the flexor digitorum brevis (FDB), a fast-twitch muscle from the hind paw innervated by the medial plantar nerve.

6.2.3 Hind limb weakness in *Rab18*$^{-/-}$ mice is not due to gross abnormalities in skeletal muscles

To determine whether the observed hind limb weakness in *Rab18*$^{-/-}$ mice could be partly attributed to atrophy of skeletal muscle fibres as has been noted in other mouse models of neurodegenerative disease (Murray et al., 2008) I quantified for any abnormalities in skeletal muscle fibre morphology. During lumbrical muscle dissections skeletal muscle fibres were teased apart to visualise individual fibres and brightfield pictures taken. Images were imported into ImageJ and three measurements of muscle fibre diameter were taken along the length of each fibre (as shown in Figure 6.5A) and the average calculated. No significant difference in muscle fibre diameter was noted in lumbrical muscle preparations from *Rab18*$^{-/-}$ mice and littermate controls (Figure 6.5B).

Additionally, to quantify for atrophy of motor endplates at the NMJ, post synaptic acetylcholine receptors from control, early and mid/late symptomatic *Rab18*$^{-/-}$ FDB,

lumbrical and TVA muscle preparations were labelled with TRITC-conjugated-α-BTX (TRITC-α-BTX). Fluorescence micrographs encompassing a minimum of 30 endplates from each individual muscle were imaged. Images were imported into ImageJ and endplate area manually outlined as in Figure 6.5C. Quantification revealed no significant differences in endplate area in any muscle types examined in either early or mid/late symptomatic *Rab18*$^{-/-}$ mice (Figure 6.5 D-F). Taken together the data shows that the hind limb weakness observed in *Rab18*$^{-/-}$ mice cannot be attributed to gross perturbations in muscle fibre size or endplate area suggesting that the primary pathological target in *Rab18*$^{-/-}$ mice is not muscular in origin.

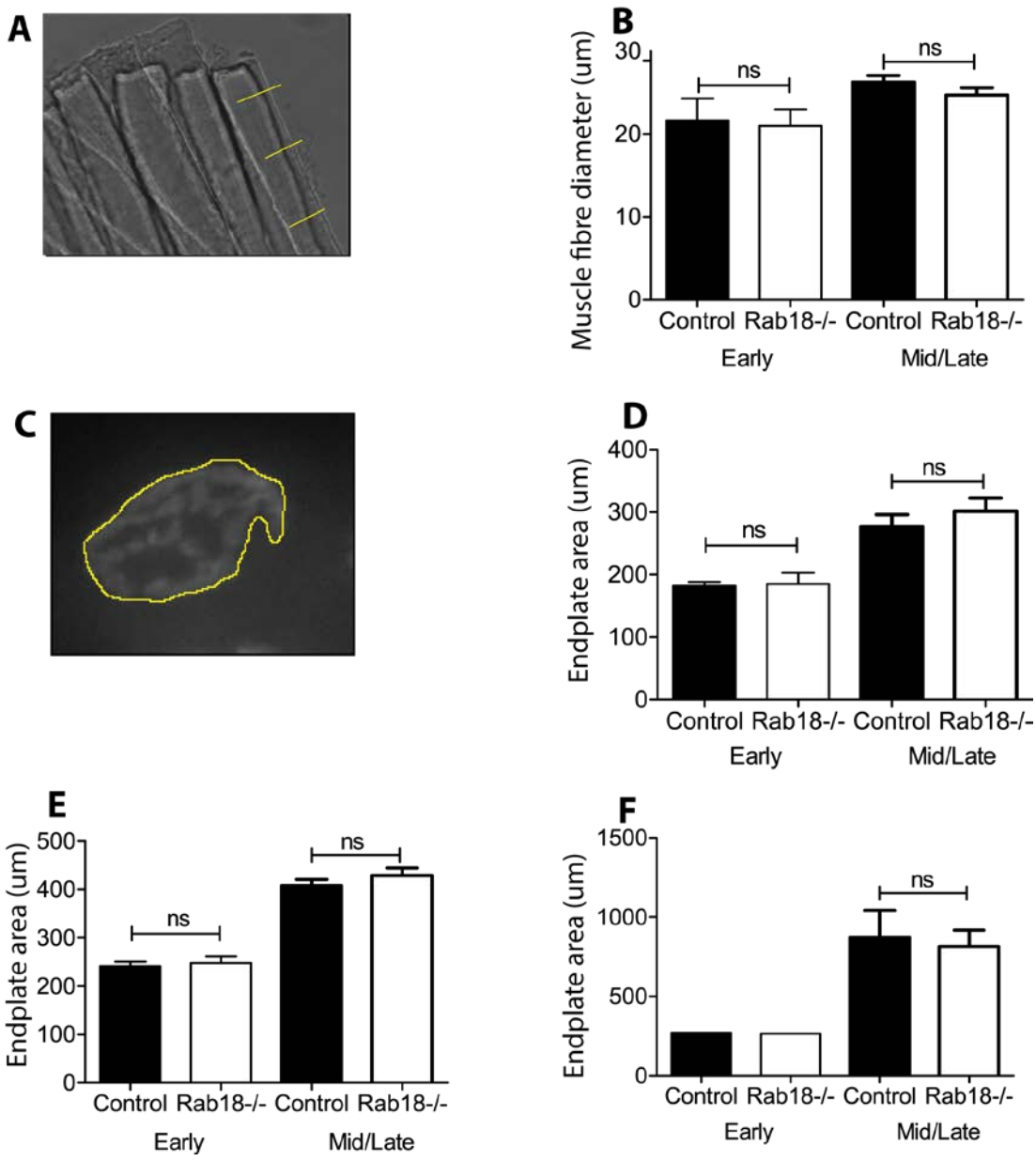

Figure 6.5 No differences in muscle fibre diameter or endplate area in control and *Rab18*$^{-/-}$ mice

(A-B) Muscle fibre diameter. Three diameter measurements along each muscle fibre were taken as in (A) and the average calculated. (B) Bar chart of muscle fibre diameter measurements showing no significant differences between control and *Rab18*$^{-/-}$ mice *(unpaired two tailed t-test, early symptomatic p value=0.8484, n=10 muscles, mid/late symptomatic p value=0.2091, n=10 muscles).* (C-F) Endplate area. Motor endplates were manually outlined as shown in (C). (D-F) Bar charts showing no differences in endplate area measurements from FDB (D), lumbrical (E) and TVA (F) muscle preparations from control, early (3 week old) and mid/late symptomatic *Rab18*$^{-/-}$ mice. *Unpaired two-tailed t-test. Early symptomatic: FDB p value=0.8661, n=7 muscles, lumbrical p value= 0.6966, n=10 muscles, TVA n=1 muscle. Mid/late symptomatic: FDB p value=0.4038, n=9 muscles control and n=8 muscles Rab18*$^{-/-}$*,*

lumbrical p value p value=0.2887, n=10 muscles, TVA p value=0.7290, n=3 muscles. ns= not significant.

6.2.4 Normal NMJ innervations but pathological accumulations in motor nerve terminals of *Rab18*$^{-/-}$ mice

As I had determined that loss of *Rab18* does not result in gross perturbation of synaptic vesicle recycling or atrophy of skeletal muscle fibres I next set out to look for any pathological abnormalities in nerve-muscle connectivity at the NMJ, as a readout for the health-status of the lower motor neuron. NMJs from whole-mount FDB, lumbrical and TVA muscle preparations were examined in *Rab18*$^{-/-}$ mice and littermate controls at both early symptomatic and mid/late symptomatic timepoints. Post synaptic acetylcholine receptors of the motor endplate were labelled with TRITC-α-BTX (Figure 6.6, red), innervating axons with antibodies against 165kDa neurofilament protein (NEFM) (Figure 6.6, green) and presynaptic synaptic terminals with antibodies against the synaptic vesicle protein, SV2 (Figure 6.6, green).

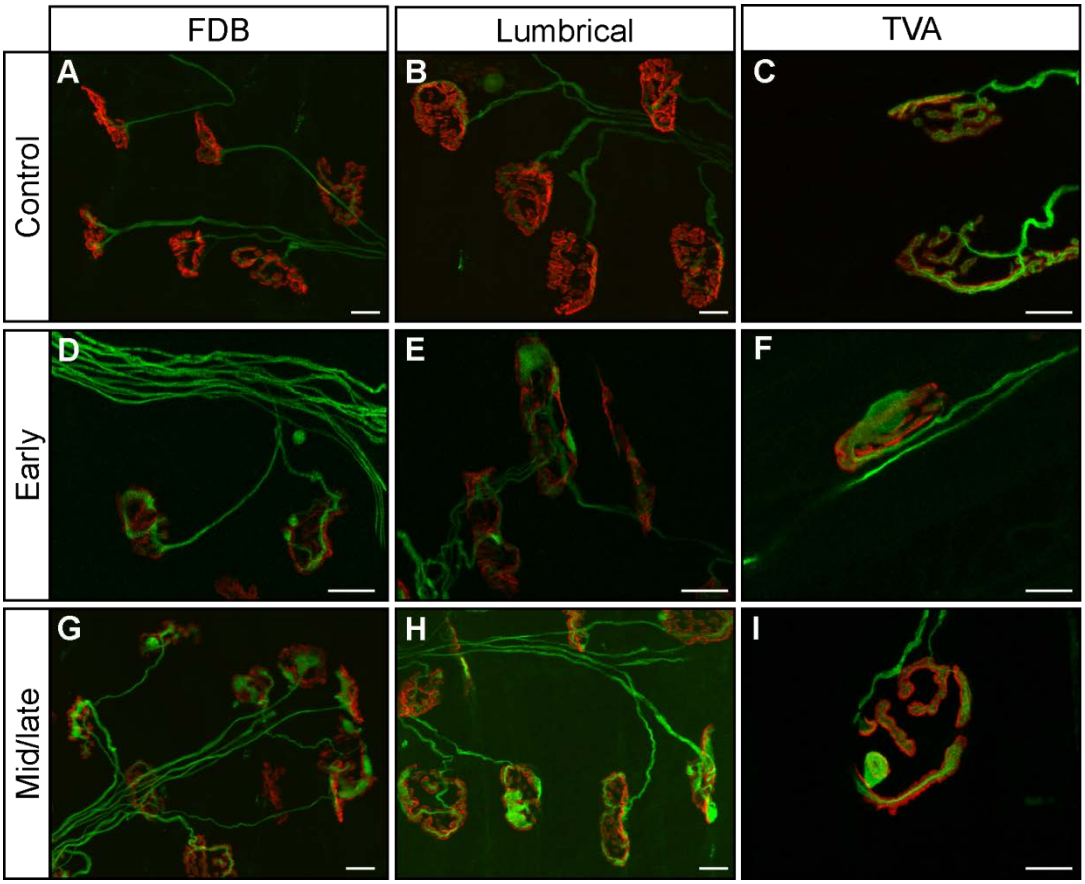

Figure 6.6 Immunohistochemistry of the neuromuscular junction in control and *Rab18*$^{-/-}$ mice

Representative confocal micrographs of neuromuscular junctions in FDB (A, D and G), lumbrical (B, E and H) and TVA (C, F and I) muscle preparations from control (A-C), early (D-F) and mid/late symptomatic *Rab18*$^{-/-}$ mice. Post synaptic acetylcholine receptors of motor endplates were immunohistochemically labelled with TRITC-conjugated α-bungarotoxin (red), neurofilaments with 165kDa NEFM (green) and synaptic vesicles with SV2 (green). Scale bar represents 10μm.

During early postnatal development of the NMJ, the majority of skeletal muscle fibres are initially innervated by multiple motor axons. Over a period of several days following birth motor endplates undergo a highly competitive process of synapse elimination, losing many of their innervated branches, leaving only one input per endplate (Sanes and Lichtman, 1999). To quantify for any perturbations in the formation of appropriate neuromuscular connectivity, or any abnormalities in development, NMJs from control and mid/late symptomatic *Rab18*$^{-/-}$ mice were quantified for the number of synaptic inputs. All NMJs analysed had established innervations from a lower motor neuron. Additionally, at mid/late symptomatic timepoints no differences in the number of innverating axons per NMJ were identified in FDB and TVA muscles, however, a small increased in lumbrical muscles was observed (Figure 6.7). Furthermore, many mouse models of neurodegenerative disease show abnormalities in synaptic innervations with vacant endplates observed during late stages of disease (Cifuentes-Diaz et al., 2002, Achilli et al., 2009). To determine whether nerve muscle connectivity at the NMJ was maintained in the presence of the observed hind limb phenotype, NMJs from control, early and mid/late symptomatic *Rab18*$^{-/-}$ mice were quantified as being fully occupied (post synaptic SV2 staining completely overlies the endplate), partially occupied (less than 70% of the endplate is overlaid by SV2 staining) or vacant (no SV2 staining). The majority of motor endplates examined in *Rab18*$^{-/-}$ mice were fully occupied at both early and mid/late symptomatic time points (Figure 6.8). Taken together this suggests that *Rab18*$^{-/-}$ NMJs retain normal synaptic innervation despite progression of the hind limb phenotype.

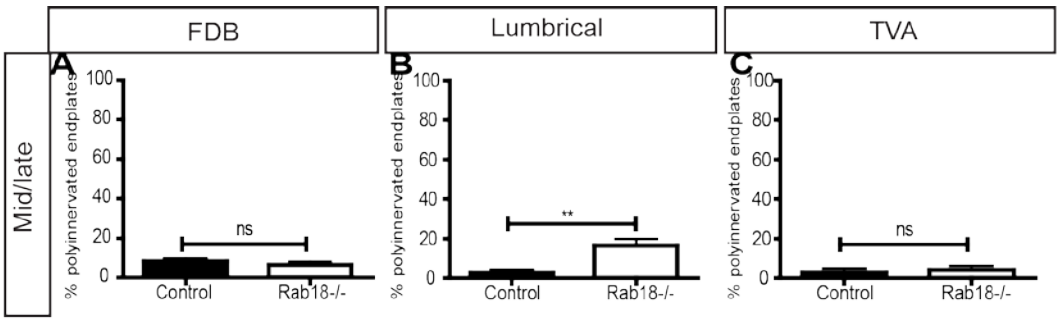

Figure 6.7 Number of synaptic inputs at the NMJ of *Rab18-/-* mice
Quantification of number of synaptic inputs in FDB (A), lumbrical (B) and TVA (C) muscle preparations from control and mid/late symptomatic *Rab18-/-* mice identified no significant difference in FDB and lumbrical muscles but an increase in polyinnervated endplates in mid/late symptomatic *Rab18-/-* lumbrical muscles. *Mann Whitney test. FDB p value=0.3947, n=6 muscles control and n=5 muscles Rab18-/-, lumbrical p value= 0.0033, n=7 muscles, TVA p value=1.0, n=3 muscles.*

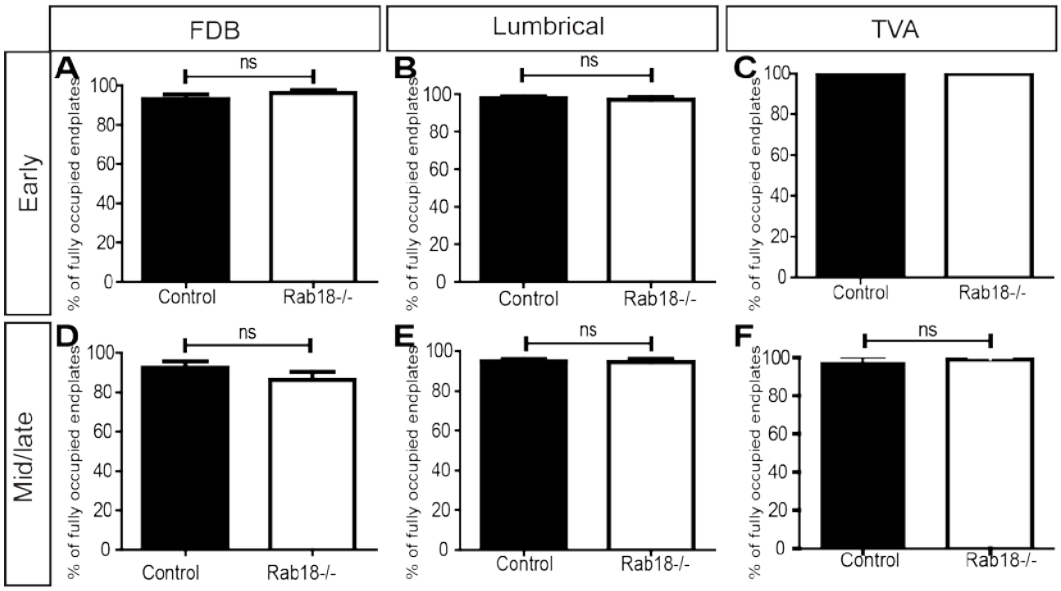

Figure 6.8 No evidence for NMJ loss in *Rab18-/-* mice
Quantification of endplate occupancy in FDB (A and D), lumbrical (B and E) and TVA (C and F) muscle preparations from control, early (A-C, 3 week old) and mid/late symptomatic *Rab18-/-* (D-F) mice. Endplates were counted as fully occupied when SV2 staining entirely overlaid the TRITC-conjugated α-BTX staining. *Mann Whitney test. Early symptomatic: FDB p value=0.5553, n=8 muscles control and n=7 muscles Rab18-/-, lumbrical p value= 0.8120, n=10 muscles control and n=8 muscles Rab18-/-, TVA n=1 muscle. Mid/late symptomatic: FDB p value=0.3523, n=9 muscles control and n=8 muscles Rab18-/-, lumbrical p value=1.0, n=10 muscles, TVA p value=1.0, n=3 muscles. Ns= not significant.*

6.2.5 Abnormal accumulation of neurofilament proteins at the NMJ in *Rab18*$^{-/-}$ mice

Whilst conducting endplate occupancy and innervation counts we routinely observed large accumulations in the presynaptic motor nerve terminal at NMJs from *Rab18*$^{-/-}$ mice at both early and mid/late symptomatic time points (Figure 6.6). During our initial experiments innervating axons were stained with antibodies against 165kDa NEFM and presynaptic terminals with the synaptic vesicle protein SV2, both visualised with the same secondary antibodies. To determine the nature of the accumulations separate immunohistochemical experiments were undertaken labelling the NMJ of whole-mount lumbrical muscles from mid/late symptomatic *Rab18*$^{-/-}$ mice with TRITC-α-BTX and one of either NEFM (Figure 6.9 A-C) or SV2 (Figure 6.9 D-F). Separate immunostaining showed the accumulations were composed of neurofilament proteins, and normal levels of synaptic vesicles were observed (Figure 6.9).

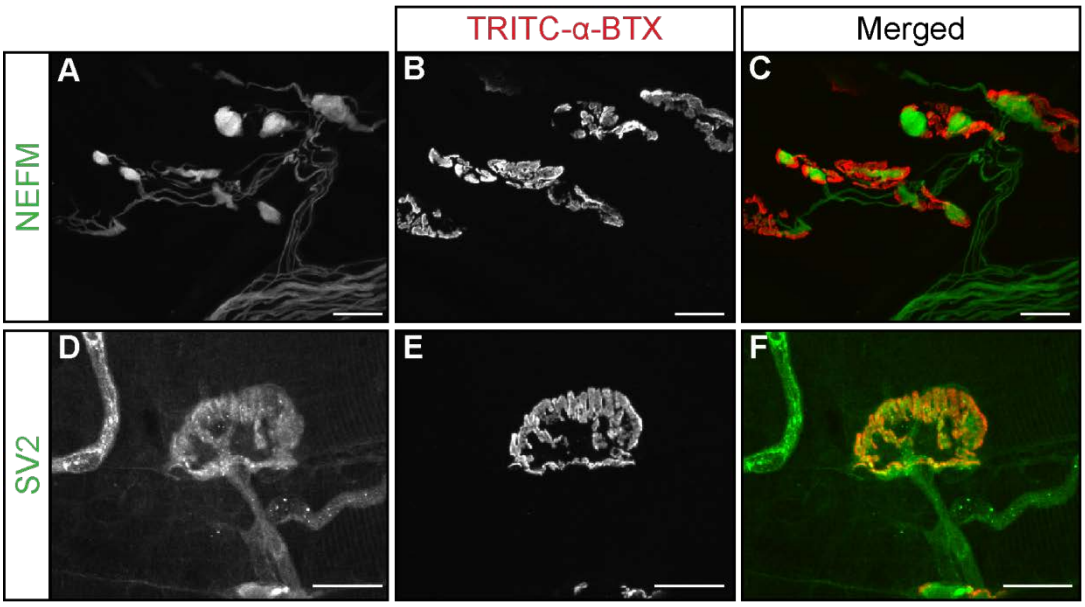

Figure 6.9 Neurofilament accumulations but normal synaptic vesicle levels at the NMJ of *Rab18*$^{-/-}$ mice

(A-F) Confocal micrographs of neuromuscular junctions in lumbrical muscle preparations from mid/late symptomatic *Rab18*$^{-/-}$ mice. Post synaptic acetylcholine receptors of motor endplates were immunohistochemically labelled with TRITC-conjugated α-bungarotoxin (red), and co-stained with either 165kDa NEFM (green, A) and synaptic vesicles with SV2 (green, D). (C and F) are merged composites of (A and B) and (D and E) respectively. Note the accumulations of NEFM at the NMJ

of *Rab18*$^{-/-}$ mice (C) but normal levels of synaptic vesicle proteins (F). Scale bar represents 10µm.

To determine whether the neurofilament accumulations increased with disease progression the number of endplates positive for accumulations of neurofilament in FDB, lumbrical and TVA muscle preparations from control, early and mid/late symptomatic *Rab18*$^{-/-}$ mice were quantified. NMJs were identified as containing neurofilament accumulations if they contained 1 or more large aggregates of staining at the motor nerve terminal not matching the underlying motor endplate labelling with TRITC-α-BTX. 20% of endplates in FDB and lumbrical muscles from early symptomatic *Rab18*$^{-/-}$ mice had accumulations of neurofilament increasing to approximately 60% by mid/late symptomatic time points (Figure 6.10 A-B and D-E). The postural transverse abdominus muscle also contained accumulations of neurofilament in approximately 20% of NMJs at early symptomatic time points but this stayed at a steady state level despite disease progression (Figure 6.10 C and F). Taken together this suggests that loss of *Rab18* results in neurofilament accumulations at the NMJ, which increased with disease progression in hind limb muscles where I had previously observed an overt neurological phenotype.

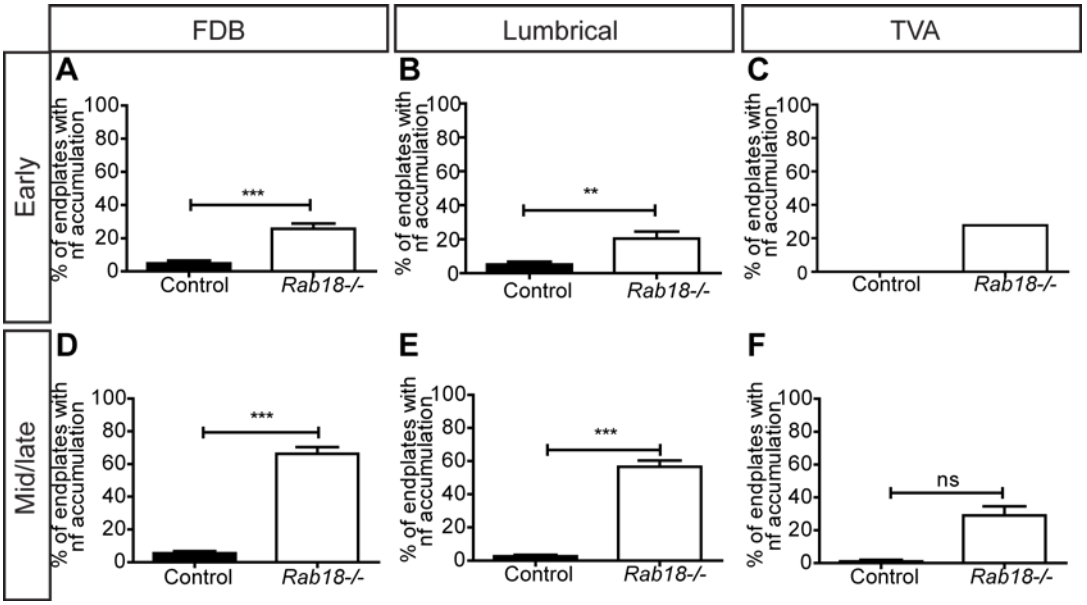

Figure 6.10 Neurofilament accumulations at the neuromuscular junction in *Rab18*$^{-/-}$ mice

Quantification of percentage of motor endplates with neurofilament (nf) accumulations in FDB (A and D), lumbrical (B and E) and TVA (C and F) muscle preparations from control, early (A-C, 3 week old) and mid/late symptomatic *Rab18*$^{-}$

$^{-/-}$ (D-F) mice. *Mann Whitney test. Early symptomatic: FDB p value=0.0026, n=8 muscles control and n=7 muscles Rab18$^{-/-}$, lumbrical p value= 0.0096, n=10 muscles control and n=8 muscles Rab18$^{-/-}$, TVA n=1 muscle. Mid/late symptomatic: FDB p value=0.0005, n=9 muscles control and n=8 muscles Rab18$^{-/-}$, lumbrical p value=0.0002, n=10 muscles, TVA p value=0.0765, n=3 muscles. Ns= not significant, ** p<0.005, ***p<0.001.*

As we observed large accumulations of neurofilament medium protein (NEFM) at the neuromuscular junctions; I therefore set out to determine whether these accumulations contained other isoforms of neurofilament or differentially phosphorylated neurofilaments as observed in many other neurodegenerative diseases (Table 6.1). NMJs from whole-mount lumbrical muscle preparations were stained with Alexa647-α-BTX labelling the post synaptic acetylcholine receptors of the motor endplate (Figure 6.11 A and B, magenta), and innervating axons with a combination of 165kDa neurofilament (NEFM) (Figure 6.11, green) and 200kDa neurofilament (NEFH) (Figure 6.11, green) or hypophosphorylated NEFH (Figure 6.13, red) and 68kDa neurofilament (NEFL) (Figure 6.12, green). Confocal micrographs imaged at the same intensity levels identified that accumulations at the neuromuscular junction of *Rab18*$^{-/-}$ mice are composed of all three isoforms of neurofilament; NEFL, NEFM and NEFH. Taken together this suggests that loss of *Rab18* results in a gross disorganisation of neurofilaments rather than targeting one specific isoform. We additionally observed accumulations of hypophosphorylated NEFH at the NMJ (Figure 6.12, red). Hypophosphorylation of neurofilament isoforms has been reported to increase neurofilament transport (Jung et al., 2000, Ackerley et al., 2003) and could potentially serve as a possible explanation for the observed neurofilament accumulations at the NMJ of *Rab18*$^{-/-}$ mice.

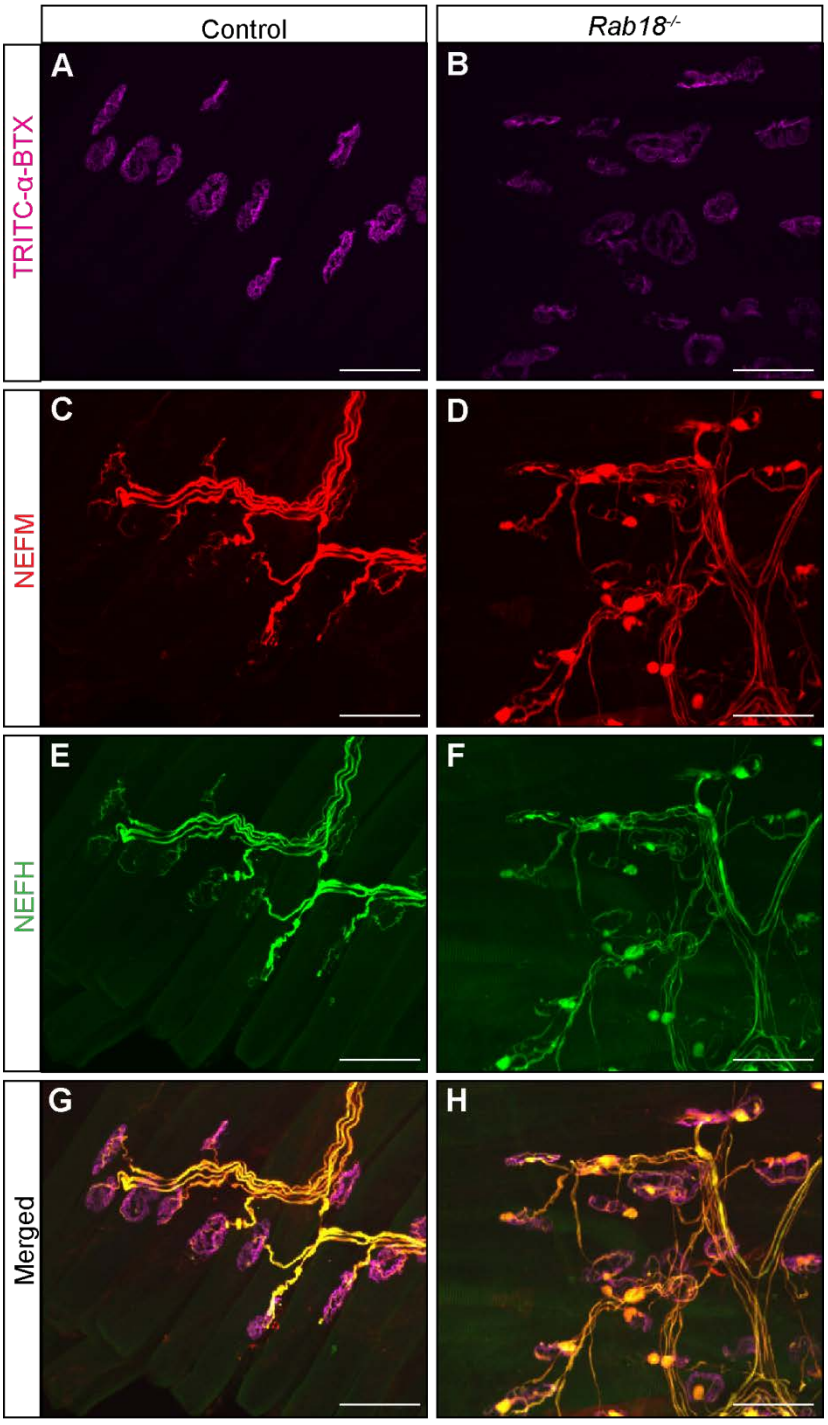

Figure 6.11 Accumulation of NEFM and NEFH at the neuromuscular junction in *Rab18*$^{-/-}$ mice

Confocal micrographs of neuromuscular junctions in lumbrical muscle preparations from control (A, C, E and G) and mid/late symptomatic *Rab18*$^{-/-}$ (B, D, F and H) mice. Post synaptic acetylcholine receptors of motor endplates were immunohistochemically labelled with Alexa647-conjugated α-bungarotoxin (magenta), 165kDa NEFM (red) and 200kDa NEFH (green). Note the accumulations of NEFM and NEFH in *Rab18*$^{-/-}$ mice. Scale bar represents 50µm.

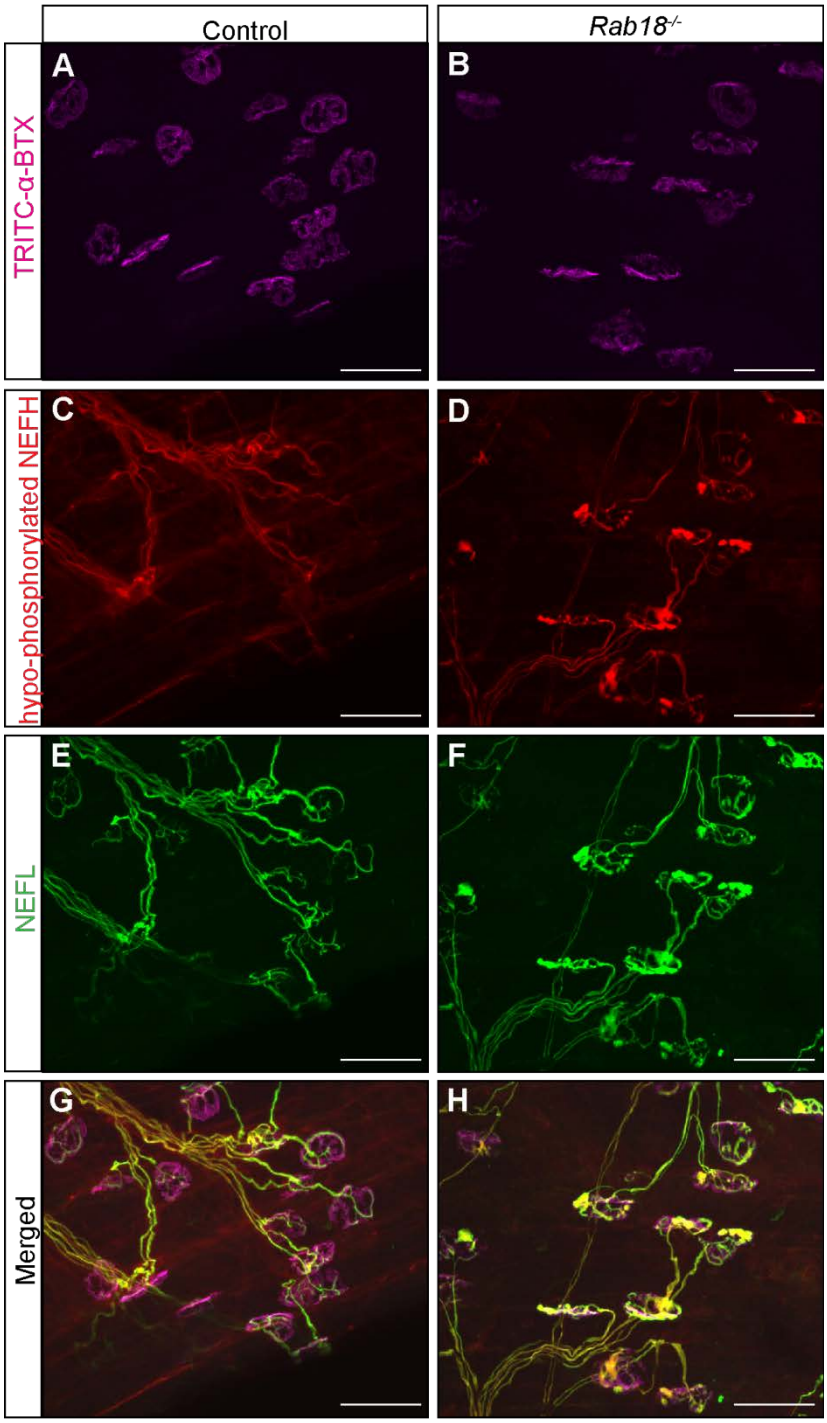

Figure 6.12 Accumulation of hypophosphorylated NEFH and NEFL at the neuromuscular junction in *Rab18*$^{-/-}$ mice

Confocal micrographs of neuromuscular junctions in lumbrical muscle preparations from control (A, C, E and G) and mid/late symptomatic *Rab18*$^{-/-}$ (B, D, F and H) mice. Post synaptic acetylcholine receptors of motor endplates were immunohistochemically labelled with Alexa647-conjugated α-bungarotoxin (magenta), hypophosphorylated 200kDa NEFH (red) and 68kDa NEFL (green). Note the accumulations of hypophosphorylated NEFH and NEFL in *Rab18*$^{-/-}$ mice. Scale bar represents 50µm.

6.2.6 Widespread neuronal cytoskeletal disorganisation in *Rab18*$^{-/-}$ mice

To determine whether the observed neurofilament accumulations could be attributed to abnormalities in organisation of the cytoskeleton in general and/or disruption to axonal transport processes as observed in other mouse models of neurodegenerative disease (Table 6.2), I next focused my attention on examination of axonal structure in the sciatic nerve of *Rab18*$^{-/-}$ mice. To identify any abnormalities in the structure of axons from *Rab18*$^{-/-}$ mice I examined the ultrastructure of the sciatic nerve from control (Figure 6.13 A) and mid/late symptomatic *Rab18*$^{-/-}$ mice (Figure 6.13B) by transmission electron microscopy. In all cases the nerve was dissected from the sciatic notch and along the tibial branch to the knee joint. Initial ultrastructural analyses identified that both genotypes failed to show any characteristic markers of degeneration (such as myelin thinning/unwrapping and breakdown), in agreement with our observations at the NMJ. Similarly, the gross morphology of axonal mitochondria was unchanged in *Rab18*$^{-/-}$ mice.

At higher magnification, normal organisation of the cytoskeleton (incorporating both neurofilament and microtubule networks) was seen in sciatic nerves from control mice, with vertically orientated filaments observed (Figure 6.13 C). In contrast, gross disorganisation of the axonal cytoskeleton was observed in *Rab18*$^{-/-}$ mice (Figure 6.13 D) with randomly orientated filaments, suggestive of gross abnormalities in cytoskeletal organisation. To confirm the observation of normal myelination in *Rab18*$^{-/-}$ mice G-ratio calculations were undertaken (G-ratio=diameter of axon/diameter of axon plus myelin), and identified no gross differences in G-ratio (Figure 6.13 E) or relationship of axon diameter to G-ratio (Figure 6.13 F and G). Thus, loss of *Rab18* resulted in disorganisation of the axonal cytoskeleton in peripheral nerve occurring in the absence of any overt neurodegeneration or de/dys-myelination phenotypes.

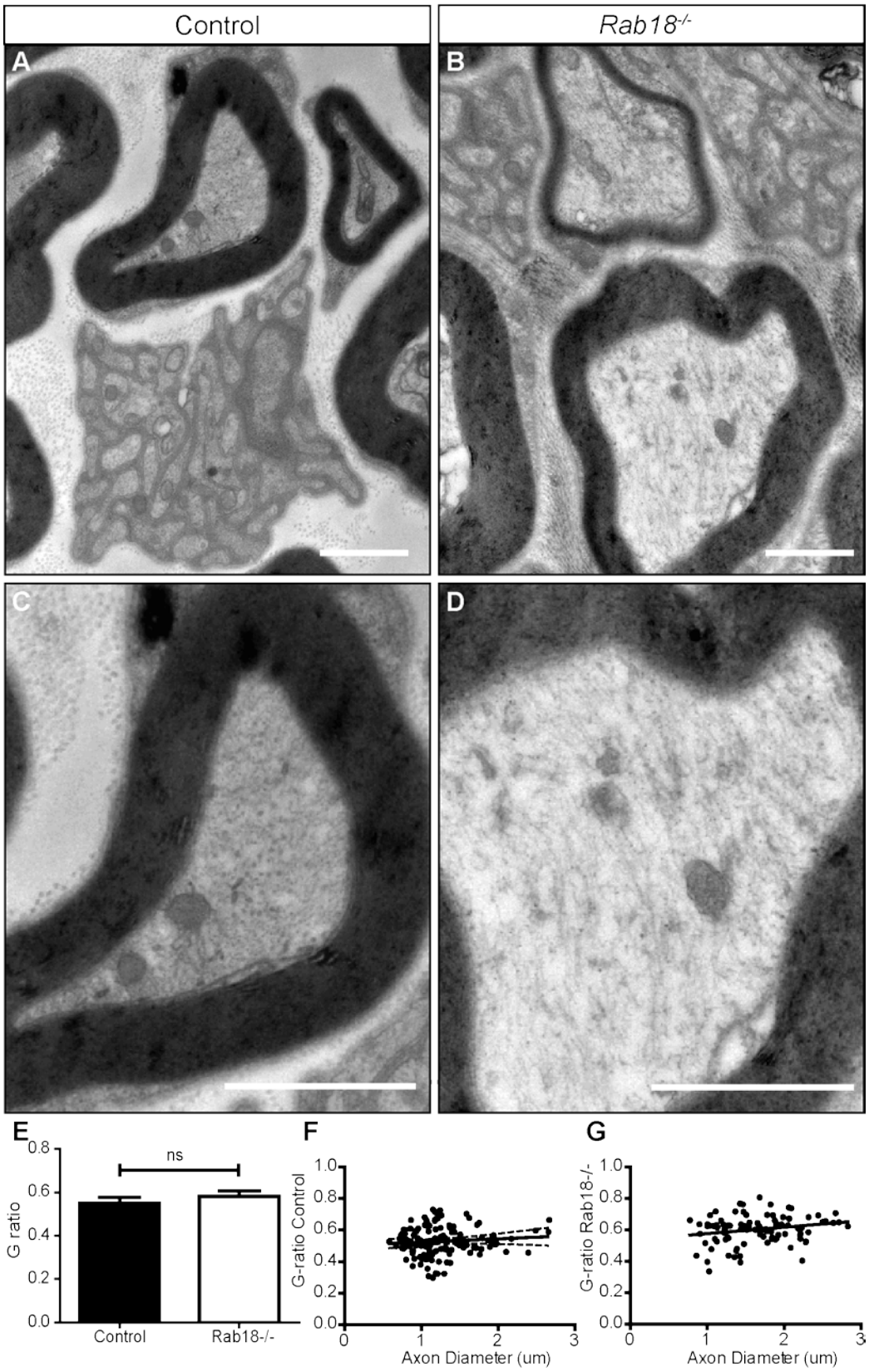
Control
Rab18-/-
A
B
C
D
E
F
G
ns
G ratio
0.0
0.2
0.4
0.6
0.8
Control
Rab18-/-
G-ratio Control
G-ratio Rab18-/-
1.0
0
1
2
3
Axon Diameter (um)

Figure 6.13 Cytoskeletal disorganisation of the sciatic nerve in *Rab18*$^{-/-}$ mice

(A-B) Ultrastructural analysis of the sciatic nerve in control (A) and *Rab18*$^{-/-}$ (B) mice by transmission electron microscopy. No evidence of myelin sheath breakdown or axonal degeneration observed was observed in either genotype. (C-D) Higher magnification images of the axonal cytoskeleton from a single axon in A and B respectively. (C) In control mice both microtubule and neurofilaments are orientated vertically and shown as dense puncta. (D) Gross disorganisation of the cytoskeleton (microtubules and neurofilaments) in *Rab18*$^{-/-}$ littermates, with random orientated filaments. (E-G) Quantification of myelination identified no abnormalities in G-ratio (G-ratio=diameter of axon/diameter of axon plus myelin) *Unpaired two-tailed t-test. G-ratio p value=0.7610, N=3 mice* (E) or spread of axon diameter compared to G-ratio in control (F) and *Rab18*$^{-/-}$ mice (G). Panels A-D scale bar represents 1µm.

The neurological symptoms of the Warburg Micro syndrome phenotype are not restricted to the PNS, with patients presenting with central nervous system and ocular abnormalities. Therefore, I examined whether the cytoskeletal disorganisation observed in the PNS also extended to axons in the CNS of *Rab18*$^{-/-}$ mice. Eyes were removed from culled mice and the intact optic nerve dissected from immediate connection to the eye, with care taken during dissection to avoid damage to the nerve. Transmission electron microscopy on sections of the optic nerve in control (Figure 6.14 A) and mid/late symptomatic *Rab18*$^{-/-}$ (Figure 6.14 B) mice again identified no markers of degeneration, with both myelination and axonal morphology appearing normal. However, upon closer examination of the axon, disorganisation of the cytoskeleton (microtubules and neurofilaments) was also observed in some axon profiles of the optic nerve of *Rab18*$^{-/-}$ mice (Figure 6.14C). Taken together these data suggest that loss of *Rab18* results in disorganisation of the cytoskeleton throughout the nervous system.

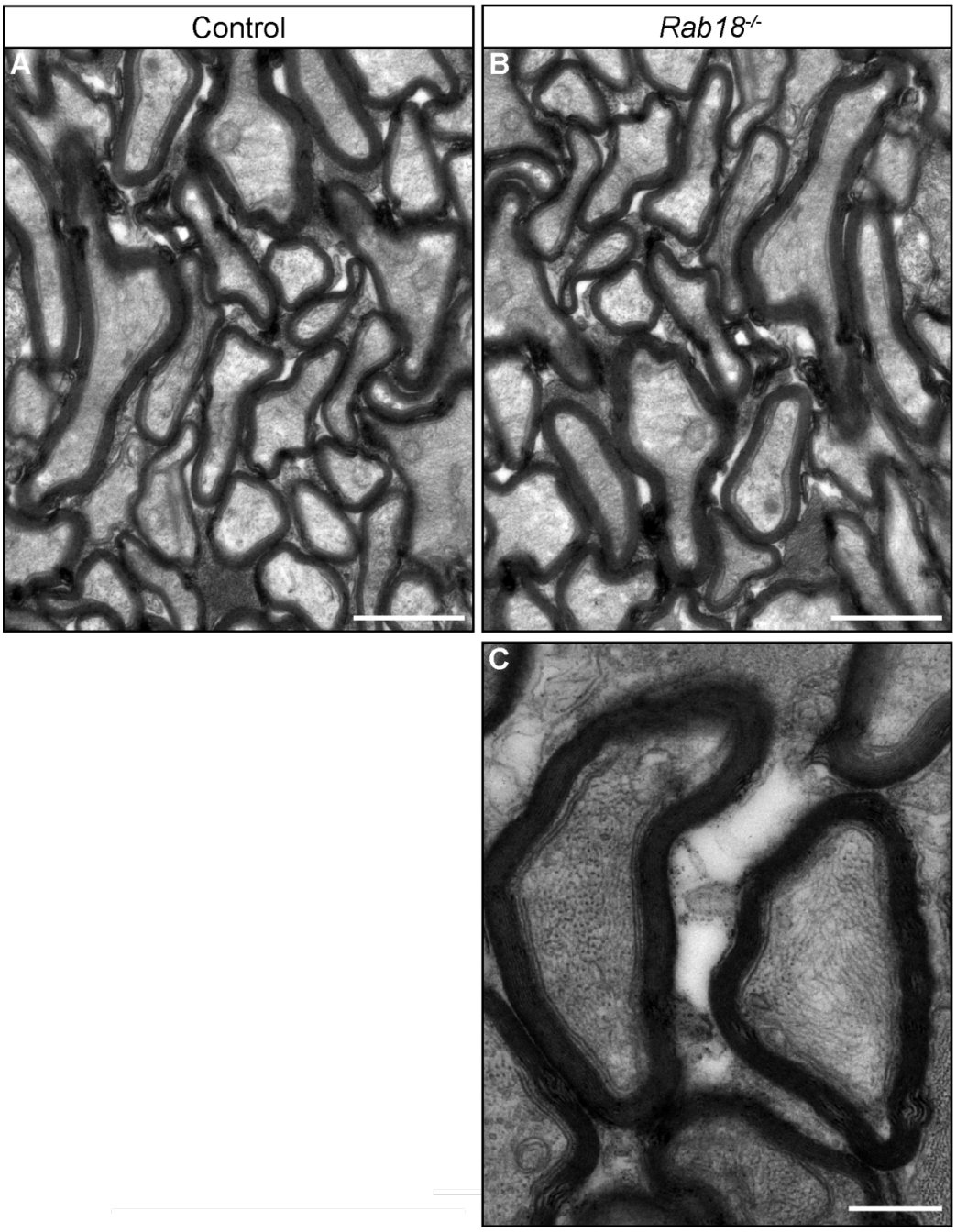

Figure 6.14 Ultrastructural examination of the optic nerve by electron microscopy showing gross cytoskeletal disorganisation in *Rab18*$^{-/-}$ mice

Transmission electron micrographs of the optic nerve from control (A) and mid/late symptomatic *Rab18*$^{-/-}$ mice (B and C). (A-B) Note the myelin sheaths remain intact. (C) High magnification images showing disorganisation of the cytoskeleton in some but not all axon profiles in *Rab18*$^{-/-}$optic nerves. N=1, panels A-B scale bar represents 1µm, panel C scale bar represents 5µm.

6.2.7 Accumulations of microtubules at the NMJ in *Rab18*$^{-/-}$ mice

My observations of neurofilament accumulations at the NMJ and disorganisation of the axonal cytoskeleton (incorporating both neurofilament and microtubule networks) pointed towards the possibility that other cytoskeletal proteins may additionally be accumulating in motor neurons. I therefore returned to the whole-mount muscle/NMJ preparations to establish whether *Rab18*$^{-/-}$ mice also exhibit accumulations of microtubules at the NMJ. NMJs in whole-mount FDB muscle preparations from control (Figure 6.15 A) and mid/late symptomatic *Rab18*$^{-/-}$ (Figure 6.15 B) mice were labelled with TRITC-α-BTX staining the post synaptic acetylcholine receptors and neuronal specific βIII tubulin, as a marker of microtubules. Again, as expected, normal innervation and endplate morphology were observed in both genotypes. However, gross accumulations of microtubule proteins were observed at the NMJ of *Rab18*$^{-/-}$ animals, phenocopying the morphologies observed in previous labelling with neurofilament antibodies.

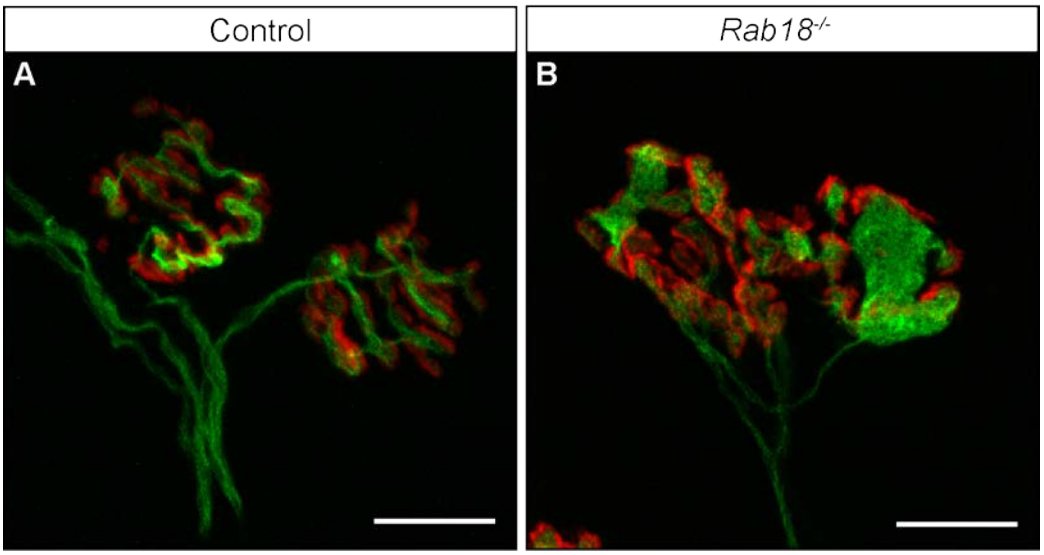

Figure 6.15 Microtubule accumulation at the neuromuscular junction in *Rab18*$^{-/-}$ mice

Confocal micrographs of neuromuscular junctions in FDB muscle preparations from control (A) and mid/late symptomatic *Rab18*$^{-/-}$ (B) mice. Post synaptic acetylcholine receptors of motor endplates were immunohistochemically labelled with TRITC-conjugated α-bungarotoxin (red) and neuronal specific βIII tubulin (green). Note the accumulations of microtubules in *Rab18*$^{-/-}$ mice. Scale bar represents 10μm.

6.2.8 Examination of axonal transport by sciatic nerve ligation experiments

My results so far have identified grossly abnormal accumulations of neurofilament and microtubule proteins at the NMJ alongisde cytoskeletal disorganisation of axons in the sciatic nerve. I therefore wanted to establish whether the observed accumulations could be attributed, at least in part, to perturbations in axonal transport.

The study of neurofilament transport is well-established and many studies have now identified that, under normal circumstances, neurofilaments are trafficked along microtubules in a bidirectional manner, by slow axonal transport alternating between short rapid movements and prolonged pauses (Brown et al., 2005). Furthermore, studies have identified that the molecular motor KIF5A is critical for efficient neurofilament transport (Xia et al., 2003, Wang and Brown, 2010). Mutations that are predicted to result in a dominant negative or loss-of-function of KIF5A kinesin activity cause a form of hereditary spastic paraplegia (SPG10) (Reid et al., 2002). Additionally, *KIF5A* null mouse models are embryonic lethal with accumulations of neurofilament protein observed in cell bodies, indicative of an abnormality in neurofilament axonal transport (Xia et al., 2003). I therefore analysed levels of KIF5A protein in the sciatic nerve of *Rab18*$^{-/-}$ mice.

Sciatic nerves were dissected from control and mid symptomatic *Rab18*$^{-/-}$ mice and cut into two segments proximal and distal to the tibial branchpoint. No significant differences were observed in the amount of total KIF5A in proximal and distal portions of control or mid symptomatic *Rab18*$^{-/-}$ nerves (Figure 6.16 A). We therefore utilised unilateral sciatic nerve ligation experiments with the aim of identifying any potential deficits in trafficking, such as you might hypothesise to occur when the organisation of the axonal cytoskeleton is disrupted. Tight ligature of the sciatic nerve prevents the transport of proteins between proximal and distal segments. As a result, any accumulations observed proximal to the ligature are indicative of anterograde transport abnormalities and any abnormalities distal representing retrograde transport abnormalities. Mid symptomatic *Rab18*$^{-/-}$ mice at 6

weeks of age were selected for sciatic nerve ligation experiments after the onset of abnormal hind limb grasping but before the mice became too sick to ensure a healthy recovery following surgery. The sciatic nerve from one leg was ligated with a surgical suture knot to tie off the nerve just below the sciatic notch. After 24 hours mice were sacrificed and segments proximal and distal to the ligature site taken. The unligated nerve from the other leg was taken as control. As kinesin proteins function as anterograde motors, sciatic ligation would be expected to cause an accumulation of KIF5a proximal to the ligature and a reduction distal to the ligature in a healthy nerve. In three independent experiments this expected pattern was observed in nerves from both control and *Rab18*$^{-/-}$ mice (Figure 6.16 B). However, upon closer comparison of KIF5A levels, a reduction of KIF5a was observed distal to the ligature in *Rab18*$^{-/-}$ nerve (Figure 6.16 C). Ratio comparisons of KIF5a levels in proximal compared to distal nerve stumps identified a significant increase in the proximal:distal ratio in *Rab18*$^{-/-}$ nerves as compared to wild-type nerves (Figure 6.16 D). Together this points towards an abnormality in the retrograde transport of KIF5A, the molecular motor responsible for neurofilament trafficking.

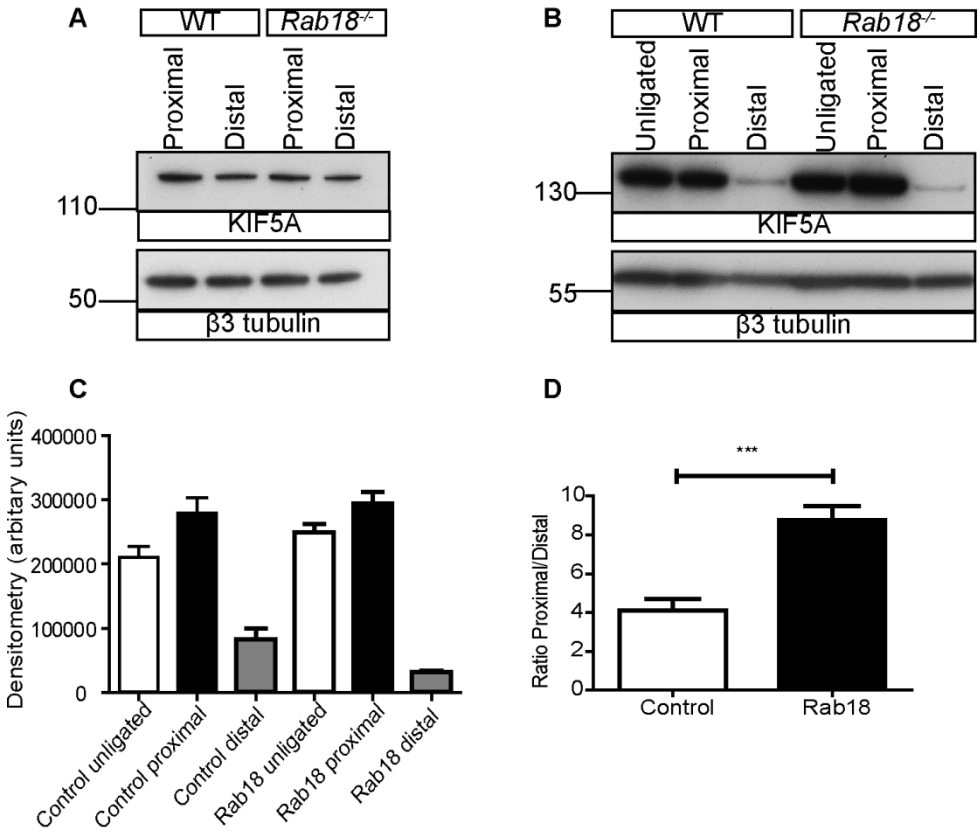

Figure 6.16 Abnormalities in axonal transport of KIF5A

Western blot analysis of levels of KIF5a in unligated wild-type and *Rab18*$^{-/-}$ sciatic nerves, showing no gross differences in KIF5A levels (A). β3 tubulin was used as a loading control. (B) Representative western blot of levels of KIF5a following sciatic nerve ligation in wild-type and *Rab18*$^{-/-}$ sciatic nerves, β3 tubulin was used as a loading control, representative blot was not used for densitometry. (C) Quantification of KIF5a levels in ligated sciatic nerves from control and *Rab18*$^{-/-}$ mice. (D) The ratio between proximal and distal samples calculated, showing an increased ratio of proximal:distal in *Rab18*$^{-/-}$ nerves. Values were normalised to tubulin loading in each lane. *N=3, ***=p>0.001, unpaired two-tailed t-test.*

To investigate whether this finding represented a global defect in axon trafficking, we examined trafficking of a known molecular cargo of fast axonal transport, amyloid precursor protein (APP), following sciatic nerve ligation (Figure 6.17A). These experiments identified a decrease of APP proximal to the ligature and an increase in the distal portion of the *Rab18*$^{-/-}$ nerve (Figure 6.17 B). Ratiometric analysis of proximal:distal in *Rab18*$^{-/-}$ mice did show a trend with a slight reduction in the distal *Rab18*$^{-/-}$ samples, however, variations between samples were observed and as a result did not reach significant levels (Figure 6.17 C). These results indicate

that KIF5a-dependent retrograde axonal transport may be specifically affected in *Rab18*$^{-/-}$ nerves and may potentially point towards the possibility that RAB18 influences trafficking of neurofilaments in neurons by regulating this specific aspect of axonal transport. APP pathways showed no significant changes, however, more studies would need to be performed to examine this further.

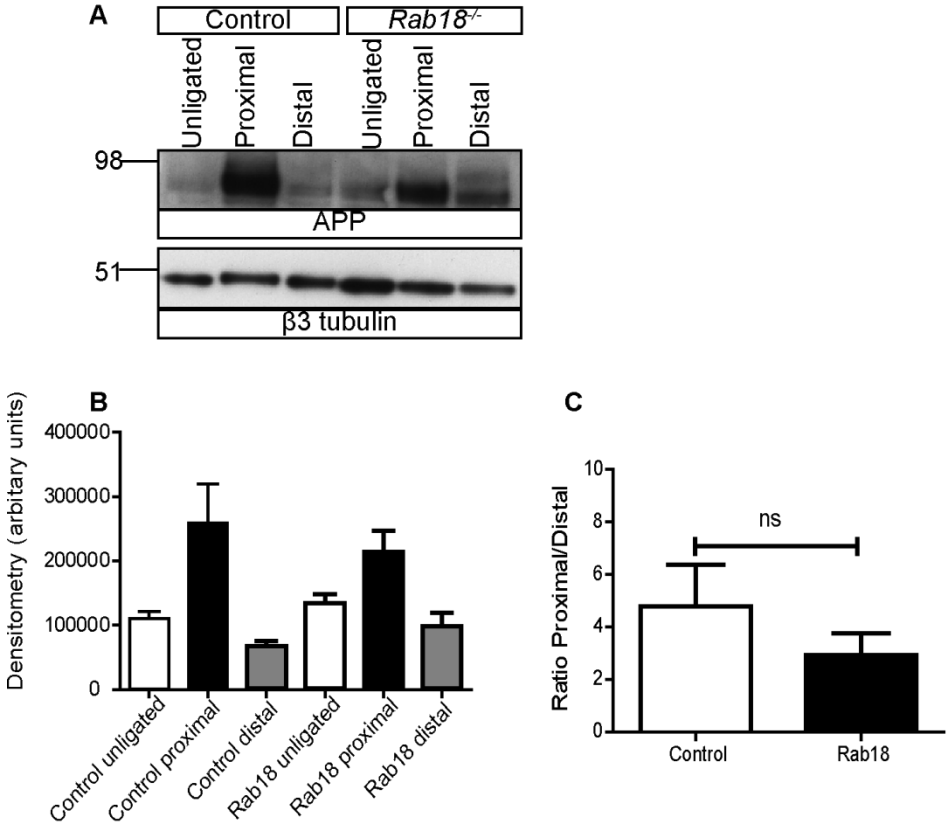

Figure 6.17 Normal trafficking of amyloid precursor protein (APP) in *Rab18*$^{-/-}$ mice following sciatic nerve ligation

(A)Representative western blot of levels of amyloid precursor protein (APP) following sciatic nerve ligation in wild-type and mid-symptomatic (6 week old) *Rab18*$^{-/-}$ mice, showing no significant differences in levels of APP. β3 tubulin was used as a loading control. (B) Quantification of APP levels in unligated and ligated sciatic nerves from control and *Rab18*$^{-/-}$ mice. (C) The ratio between proximal and distal samples calculated, showing no significant differences in APP levels between control and *Rab18*$^{-/-}$ nerves. Values were normalised to tubulin loading in each lane. *N=3, unpaired two-tailed t-test, ns=not significant.*

In our aforementioned sciatic nerve ligation experiments βIII tubulin was used as a control for loading. Due to their high abundance and usually constant levels, antibodies targeting various tubulin isoforms are routinely used as loading controls for Western blotting experiments. However, there are several potential problems with this approach. Principally, in my data reported here I have identified accumulations in filament proteins (neurofilament and microtubule) in studies of the NMJ. To confirm its validity as a loading control in our experiments, βIII tubulin levels in sciatic nerve extracts were compared to those of Myelin protein zero (MP0) and observed no significant differences (Figure 6.18). MP0 was selected as previous ultrastructural analysis of the sciatic nerve and G-ratio quantifications identified no abnormalities in myelination. Additionally, in the above sciatic nerve ligation experiments densitometry was performed with and without normalisation to tubulin and identified no significant alterations in expression pattern. Taken together, I believe this validates the use of βIII tubulin in the ligation experiments.

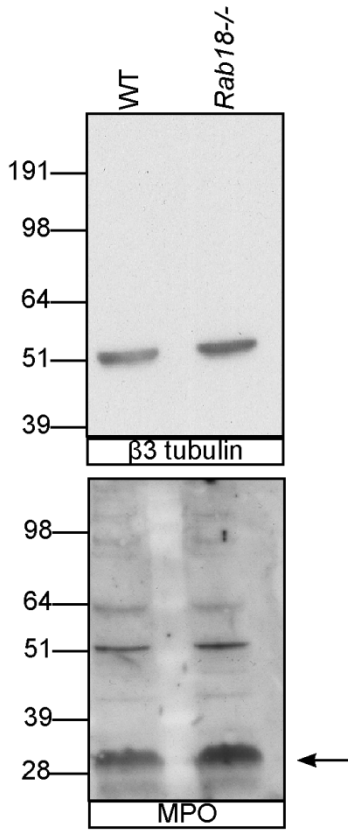

Figure 6.18 Rationale behind using β3 tubulin as a loading control for sciatic nerve ligation experiments
Western blot analysis of βIII tubulin levels in intact unligated sciatic nerves. In this case myelin protein zero (MP0) was used as a loading control and identified no significant differences between wild type (WT) and *Rab18*$^{-/-}$ nerves.

6.2.9 iTRAQ proteomics screening of the peripheral nerve proteome in *Rab18*$^{-/-}$ mice

In order to undertake a large-scale, unbiased analysis of the consequences of RAB18 depletion on the molecular composition of the PNS, iTRAQ proteomics analyses were performed on sciatic nerves isolated from 6 week old heterozygote control and *Rab18*$^{-/-}$ mice. All samples used in this analysis were taken from male mice from the same breeding pair, backcrossed for 9 generations to C57BL/6J, in order to eliminate any variation in background effects. Six nerves from each of three heterozygote and three homozygote mice were pooled and homogenised in 1/40 weight/volume 0.5M triethylammonium bicarbonate, 1% SDS and 1mM PMSF. To quantify protein levels

in these samples, 2µl of each was run on a SDS-PAGE gel alongside 5µg, 10µg and 14µg of wild type sciatic nerve and stained with Coomassie blue (Figure 6.19). The nerve sample used for comparison was previously homogenised in 1x RIPA buffer and so it was possible to determine protein concentration with a Pierce BCA protein assay kit.

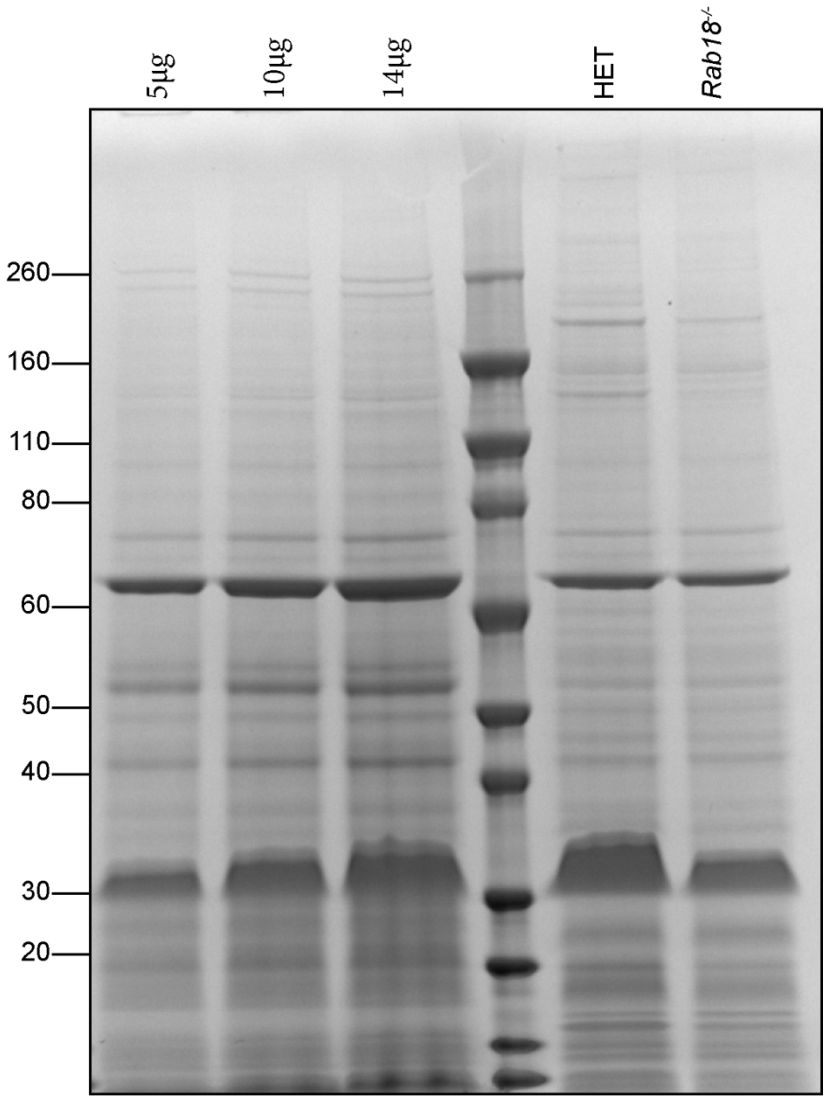

Figure 6.19 Coomassie stain of sciatic nerve samples sent for proteomic analysis

5µg, 10µg and 14µg of wild type sciatic nerve previously homogenised in 1x RIPA buffer and protein concentration calculated with Pierce BCA protein assay kit was run as a positive control alongside 2µl of the resultant homogenate for iTRAQ proteomics. The aforementioned samples were run on an SDS-PAGE gel and stained with Coomassie blue.

Samples were then sent to Dundee Cell products for isobaric tag for relative and absolute quantitation **(**iTRAQ**)** proteomic analysis and the resultant mass spectrometry data searched against the Mascot Search Engine using the following parameters; enzyme specificity trypsin, false discovery rate 1%, database IPImouse_20130120, max peptide length 6 and max missed cleavages 2. Their analysis identified 1337 proteins for which expression levels could be compared between the two genotypes. In order to identify proteins differentially expressed in *Rab18*$^{-/-}$ compared to heterozygote nerves, we set a stringent filtering criteria of 20% difference in levels and identified by two or more unique peptides. From this criteria, 202 proteins were significantly altered, 112 upregulated (Appendix 3) and 90 downregulated (Appendix 4) upon loss of *Rab18.* Interestingly, both neurofilament and tubulin isoforms were downregulated in *Rab18*$^{-/-}$ nerves (Appendix 4), further supporting our identification of cytoskeletal abnormalities in *Rab18*$^{-/-}$ nerves. It should also be noted that *Rab18* was the second highest protein downregulated in our study at a ratio of 0.315 compared to heterozygote controls but was only found by one unique peptide and so was removed from the filtered tables. This is in agreement with our Western blotting analysis showing no observable RAB18 in sciatic nerves of *Rab18*$^{-/-}$ mice compared to controls.

To examine whether the altered proteins are specific and the effects on protein levels are present in all mice without *Rab18,* I examined the levels of one upregulated protein Apolipoprotein D (ApoD) and one downregulated protein peripheral myelin protein 2 (PMP2) in isolated sciatic nerve samples from wild type (WT), heterozygote (HET) and *Rab18*$^{-/-}$ mid symptomatic mice. I carried out western blotting for levels of APOD in heterozygote and *Rab18*$^{-/-}$ sciatic nerves and showed APOD to be very dramatically upregulated in *Rab18*$^{-/-}$ nerves (Figure 6.20 A). It was surprising that PMP2 showed a decrease in proteomic analysis of *Rab18*$^{-/-}$ sciatic nerves given that we did not observe any myelination defects upon EM. I therefore carried out western blotting on levels of PMP2 in wild type, heterozygote and *Rab18*$^{-/-}$ sciatic nerves and did not confirm the proteomics finding, suggesting that some hits are artefacts (Figure 6.20 C). In both cases, a parallel blot of the same protein samples was run and stained with Coomassie blue for analysis of protein loading (Figure 6.20 B and D).

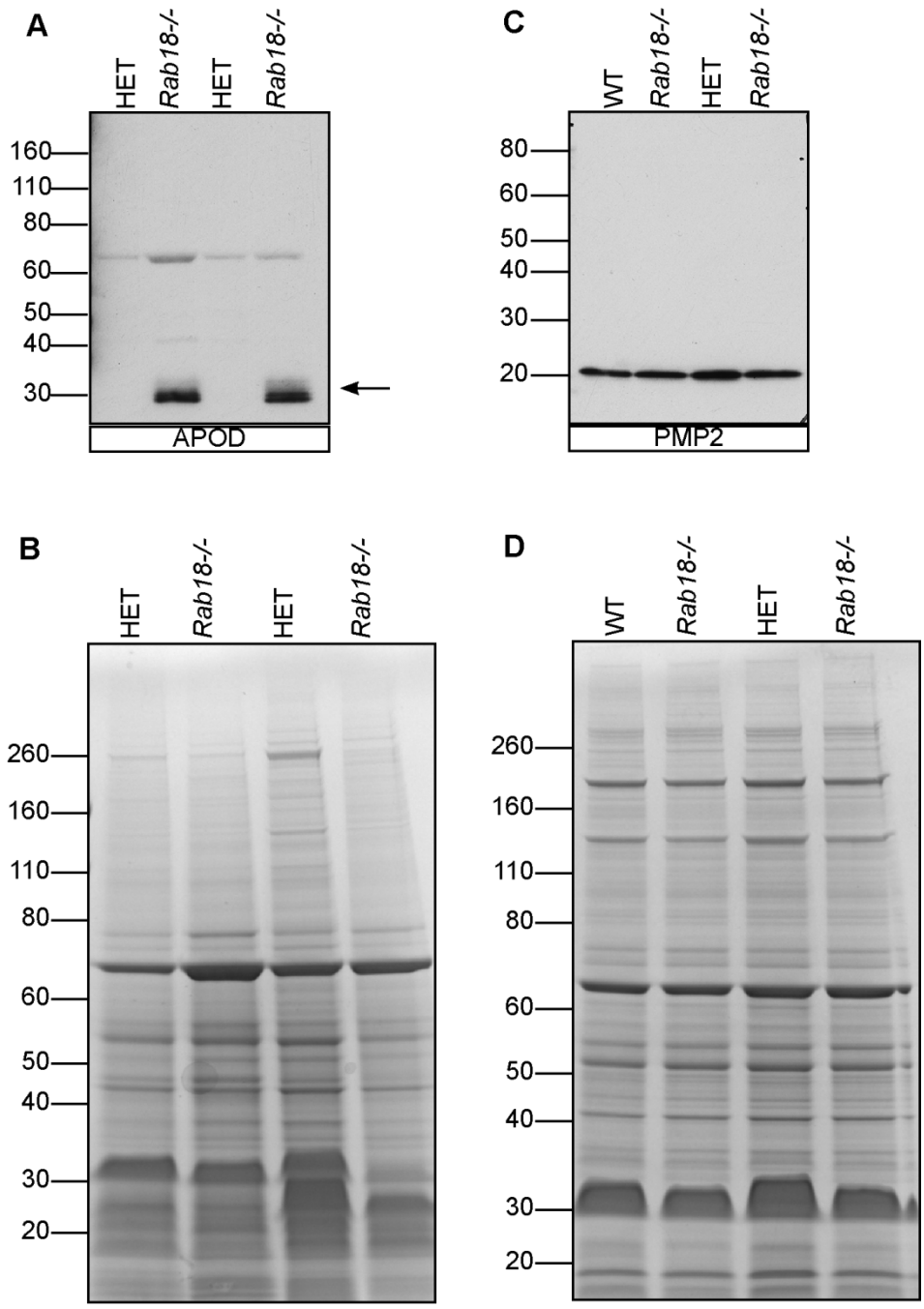

Figure 6.20 Proteomic validation

(A) Representative western blot analysis of heterozygote (HET) and *Rab18*$^{-/-}$ mice, not used for iTRAQ analysis showing increased levels of Apolipoprotein D (ApoD) in *Rab18*$^{-/-}$ mice compared to controls, thus validating the proteomics screen. (B) Coomassie stained gel of samples run in (A) showing no gross discrepancies in protein loading that could account for the observed effect. (C) Representative western blot analysis of wild type (WT), heterozygote (HET) and *Rab18*$^{-/-}$ mice, (samples were not used for iTRAQ analysis) showing equal levels of PMP2 in all lanes. (D) Coomassie stained gel of parallel samples to those run in (C) confirming equal protein loading in all lanes.

To identify functional molecular pathways altered upon loss of *Rab18* in the sciatic nerve, we performed Ingenuity Pathway Analysis (IPA) (in collaboration with Tom Wishart). IPA software utilises published information of direct and indirect protein interactions to identify clustering of proteins in particular core pathways or linked to biological function and/or disease. Ontology analysis identified 44 proteins clustered around movement disorders and 35 around neuromuscular disorders (Table 6.3). Of particular interest to us was clustering of proteins and pathways relating to cellular assembly and organisation; including 28 proteins with known roles and/or links to organisation of the cytoskeleton and 25 in microtubule dynamics (Table 6.4). This suggests that loss of *Rab18* results in many cellular downstream consequences in pathways regulating organisation of the cytoskeleton.

Table 6.3: Ingenuity pathway analysis highlights clustering of proteins associated with neurological diseases.

Category	Functions Annotation	Molecules	# Molecules	p-Value
Neurological Disease	Movement Disorders	ALDH2,ANXA2,APOA4,APOD,ASPA,ATP2B1,BCAS1, BGN,C3,CAPNS1,CAV1,CKB,CNTF,CTSD,DHCR7, DYNC1I1,FGG,HNRNPU,HSP90AA1,HSPA1A/HSPA1B, HSPA8,LDHB,LMNA,LUM,MDH1,NAPA,NDUFB6,NEFL, NME1,PGK1,PLP1,PRDX6,PRX,RPL13A,RPL15,RPS4X, RTN1,SERPINA1,THY1,TUBA1A,TUBA4A,TUBB3,VSNL1, YWHAZ	44	1.53E-11
	Neuromuscular Disease	ALDH2,ANXA2,APOA4,APOD,ATP2B1,BCAS1,C3, CAPNS1,CKB,CNTF,DHCR7,DYNC1I1,FGG,HNRNPU, HSP90AA1,HSPA1A/HSPA1B,HSPA8,LDHB,MDH1, NAPA,NDUFB6,NEFL,NME1,PGK1,PRDX6,RPL13A, RPL15,RPS4X,RTN1,SERPINA1,THY1,TNXB,TUBA1A, VSNL1,YWHAZ	35	6.84E-09

Table 6.4: Ingenuity pathway analysis of functional clustering highlights alterations in cellular assembly and organisation.

Category	Functional Annotation	Molecules	# Molecules	p-Value
Cellular Assembly and Organization	organization of cytoskeleton	ATP2B1,CAPNS1,CAV1,CNTF,CTNND1,DAG1, DDAH1,DYNC1LI1,DYNLL1,EPB41L2,FSCN1, HSP90AA1,JUP,MAPRE3,MARCKS,MYH4,NEFH, NEFL,NEFM,NME1,PICALM,PRKCA,RAP2A, RUFY3,THY1,TUBB,TUBB3,YWHAH	28	3.09E-03
	microtubule dynamics	ATP2B1,CAPNS1,CAV1,CNTF,CTNND1,DAG1, DDAH1,DYNLL1,FSCN1,HSP90AA1,MAPRE3, MARCKS,MYH4,NEFH,NEFL,NEFM,NME1, PICALM,PRKCA,RAP2A,RUFY3,THY1,TUBB, TUBB3,YWHAH	25	2.61E-03
	proliferation of connective tissue cells	BGN,CAPNS1,CAV1,COL1A1,CTSD,DCN,DDX5, HSPA1A/HSPA1B,Ighg2a,JUP,KRT10,KRT2, LGALS3,LUM,MIF,PGK1,POSTN,PRKCA,RPL29, TFG	20	5.67E-05
	morphology of nervous system	ASPA,ATP1A2,CAV1,CKB,Ckmt1,CNTF,COL1A1, CTSD,EPB41L2,FBXO2,GMFB,LAMB2,LMNA, MARCKS,NEFH,NEFL,NEFM,PLP1,PRX,SYNCRIP	20	5.88E-03
	Progressive Motor Neuropathy	ANXA2,APOD,BCAS1,CNTF,LDHB,MDH1,NEFH,NEF NEFM,PGK1,RPL13A,RPL15,RPS4X,RTN1,THY1, TNXB,TUBA1A	17	2.15E-05
	formation of filaments	ACTC1,CAV1,COL6A3,CTNND1,CYB5R3,DYNLL1, GNG12,KRT14,MIF,NEFH,NEFL,NEFM,POSTN, RAP1GDS1,THY1,TUBB	16	2.75E-05
	organization of organelle	ANXA2,BGN,CAV1,COL1A1,COL1A2,DCN,DRP2, JUP,LAMB2,LMNA,MYH4,NEFH,NEFL,NEFM, TNXB,TUBB	16	1.15E-04
	organization of filaments	ANXA2,BGN,COL1A1,COL1A2,DCN,JUP,MYH4, NEFH,NEFL,NEFM,TNXB,TUBB	12	1.66E-06
	transport of protein	CAV1,COL1A1,Ighg2a,JUP,NAPA,PICALM, SEC23A,SNX6,YWHAH	9	7.96E-03
	abnormal morphology of axons	CKB,Ckmt1,LMNA,NEFH,NEFL,NEFM,PLP1	7	3.83E-05
	formation of microtubules	CAV1,DYNLL1,NEFH,NEFL,NEFM,TUBB	6	9.76E-05

In summary, our data reported here supports a critical role for RAB18 in maintenance of cytoskeletal organisation and dynamics in neurons.

6.3 Discussion:

In this chapter I describe characterisation of the neuropathological hind limb phenotype observed in *Rab18*$^{-/-}$ mice, resulting in 6 major findings. First, I identified normal levels of RAB3GAP1, RAB3GAP2 and RAB3A in *Rab18*$^{-/-}$ mice, suggesting that the phenotype of Warburg Micro syndrome is not a result of gross dysregulation of the RAB3 cycle. Additionally, analysis of synaptic vesicle recycling at PNS and CNS synapses identified no gross discrepancies in synaptic vesicle exocytosis or endocytosis. Second, I showed that the hind limb weakness observed in *Rab18*$^{-/-}$ mice occurred in the absence of any characteristic hallmark features of degeneration at either PNS synapses or axon profiles of the sciatic nerve, with normal myelination, endplate occupancy and muscle fibre morphology all observed. Third, I identified gross accumulation of neurofilament and microtubule proteins at the NMJ, directly correlating with disease progression. Fourth, I identified gross disorganisation of axonal cytoskeletal architecture in *Rab18*$^{-/-}$ mice. Fifth, preliminary analysis of axonal transport identified potential selective abnormalities in KIF5A specific pathways, although studies of APP transport showed no significant alterations. Further studies are needed to examine this in more detail. Finally, I have demonstrated through in depth proteomic and ontology analysis that loss of *Rab18* results in perturbations in cellular pathways regulating cytoskeletal organisation and maintenance in sciatic nerves.

6.3.1 Neurofilament and microtubule accumulations at the NMJ and cytoskeletal disorganisation in peripheral nerves

One of the most striking observations in *Rab18*$^{-/-}$ mice was the abnormal accumulation of cytoskeletal proteins at the NMJ and gross disorganisation of the cytoskeleton without accompanying loss of innervation or skeletal muscle. However, studies examining motor neuron dysfunction are now bringing to light isolation of pre and post synaptic and axonal and synaptic pathology in a range of different muscle types. For example Shen *et al.*, reported muscular pathology in hNF-L^{E397K} mice modelling Charcot-Marie-Tooth type 2E without significant nerve and NMJ pathology (Shen et al., 2011). Additionally, Murray *et al.*, reported dissociation of

pre and post synaptic pathology in SMN mice, with some vacant endplates showing normal morphology (Murray et al., 2008). Furthermore, studies examining ALS mouse models have definitively isolated axonal transport deficits and neurodegeneration (Marinkovic et al., 2012). Our study could therefore possibly point towards a specific involvement of axonal transport deficits and cytoskeletal disruption distinct from neurodegeneration and muscular pathology. Furthermore, our observations of accumulations at the NMJ and cytoskeletal disorganisation of axons in the sciatic nerve implies that the accumulations may be associated with a deficit that affects nerve function without instigating cell death pathways. For example, it would be of interest to examine whether the progressive hind limb phenotype could potentially be due to deterioration of nerve conduction velocities as could be explored with specialist electrophysiological techniques.

Accumulations of cytoskeletal proteins and aberrant post-translational modifications are hallmark features of many neurodegenerative diseases (Table 6.1). Interestingly, we observed accumulations of all three isoforms of neurofilament protein (NEFL, NEFM and NEFH) at the NMJ. Quantification of the number of endplates positive for NEFM accumulations in early and mid/late symptomatic *Rab18*$^{-/-}$ mice revealed that these accumulations increased with disease severity. Furthermore, axons innervating the hind limb muscles, where we previously observed deterioration, contained more endplates with accumulations than in axons innervating truncal muscles. This suggests that neurofilament accumulations may be a correlate of disease progression in *Rab18*$^{-/-}$ mice and potentially Warburg Micro syndrome patients. However, it would be of interest to examine neurofilament levels in pre-symptomatic *Rab18*$^{-/-}$ mice to determine whether the observed neurofilament accumulations in approximately 20% of endplates in all early symptomatic muscles examined represents a baseline upon depletion of *Rab18* or a marker of onset of disease progression. Preliminary studies also identified large accumulations of hypo-phosphorylated NEFH. However, further experiments would need to be conducted comparing antibody levels specifically directed against hypo-, hyper- and normally phosphorylated NEFM and NEFH isoforms before we can definitively confirm or rule out the involvement of aberrant post-translational modifications of neurofilament in the phenotype of our *Rab18*$^{-/-}$ mouse model. At this stage it remains

unclear whether altered phosphorylation causes the observed neurofilament accumulations or is the result of them, our data reporting a defect in trafficking of KIF5A the molecular motor implicated in neurofilament transport appears to support the latter.

Axonal transport is a fundamental process for axonal viability as the vast majority of axonal proteins are synthesized in the cell body and transported through the axon along cytoskeletal tracks to specific compartments for example synaptic proteins targeted to the axon terminal (De Vos et al., 2008). Interestingly, however, it appears that the cytoskeletal disorganization observed in *Rab18*$^{-/-}$ mice does not represent global deficiencies in axonal transport. This was unsurprising as we did not observe deterioration of axons and NMJs, pointing towards the fact that at least some axonal transport must be occurring normally for cell viability to be ensured. Furthermore, no significant differences were observed in the trafficking of APP, although variation was seen between samples, at this stage I cannot say whether APP pathways may be definitely altered or not. We did observe a reduction in KIF5A distal to the ligature site in *Rab18*$^{-/-}$ nerves indicative of a reduction in retrograde transport. KIF5A is the molecular motor attributed to driving the anterograde (and a small proportion of retrograde) transport of neurofilaments (Xia et al., 2003, Wang and Brown, 2010) and mutations cause SPG10 (Reid et al., 2002). Neurofilament transport in axons occurs via slow axonal transport; with rapid bursts interchanged with prolonged pauses (Brown et al., 2005). However, studies examining conditional deletion of NEFL in mice and EGFP-NEFL dynamics in primary cortical neurons have identified only a minority of neurofilaments undergo slow axonal transport, with the majority maintained in a fixed stationary lattice (Millecamps et al., 2007, Yuan et al., 2009). Additionally, we also identified accumulations of the microtubule marker βIII tubulin at *Rab18*$^{-/-}$ nerve terminals. Microtubules form the cytoskeleton tracks on which axonal transport occurs. However, studies have brought to light that, like neurofilaments, the majority of microtubules are stationary forming discontinuous cytoskeletal tracks, but a subset of short microtubule polymers are transported rapidly along axons, with speeds similar to that of the molecular motors dynein and kinesin, interchanged with frequent prolonged pauses (Wang and Brown, 2002). Our analysis presented here has identified accumulations of microtubule and

neurofilament proteins at the NMJ. Furthermore, our proteomic and ontology analysis of proteins altered by greater than 20% in the sciatic nerves of *Rab18*$^{-/-}$ compared to heterozygote littermates identified alterations in core proteins implicated in cytoskeleton assembly and organisation, further supporting a role for RAB18 in cytoskeletal dynamics for example reductions in the levels of NEFL, NEFM and NEFH, and four tubulin isoforms (tubulin alpha-4a, tubulin alpha-1a, tubulin beta-5 chain, tubulin beta-3) were observed in *Rab18*$^{-/-}$ sciatic nerves. However, it remains unclear whether the observed reduction in levels of components of the cytoskeleton in axons (neurofilament and tubulin proteins) by iTRAQ and accumulations at the NMJ are the result of trafficking defects or the result of this disorganisation. Following this, it is also possible that the disorganisation could disrupt the microtubule tracks and result in trafficking abnormalities. It is therefore of particular interest that although the axonal cytoskeleton showed gross disorganisation, analysis of protein levels by iTRAQ and potentially trafficking of the anterograde cargo APP, identified that many abundant proteins are trafficked normally, it may be therefore that neurofilaments and microtubules are particularly sensitive to trafficking perturbations or loss of *Rab18* may target specific trafficking pathways, as suggested by the KIF5A data. Interestingly, we also identified alterations to many proteins previously shown to be implicated in neurodegenerative disease. It would be of interest to examine sciatic nerve architecture in early symptomatic *Rab18*$^{-/-}$ mice to aid the isolation of disorganisation or accumulations as the primary pathological hallmark of Warburg Micro syndrome pathology in peripheral nerves. Through this we could hopefully decipher whether cytoskeletal disorganisation increases in severity concomitantly with neurofilament accumulations or whether *Rab18*$^{-/-}$ mice exhibit abnormalities in organisation from early axon development, and it is solely the neurofilament and microtubule polymers that accumulate with disease.

Proteomic validation was undertaken examining the levels of apolipoprotein D (ApoD) in isolated *Rab18*$^{-/-}$ sciatic nerves, and confirmed significant enrichment upon loss of *Rab18*. Apolipoprotein D is a member of the apolipoprotein family functioning in lipid binding and transport and characterisation of the *ApoD* knockout mouse model has shown ApoD to be critical for maintenance of the myelin sheath

and its expression level elevated in response to injury (Ganfornina et al., 2010). As we observed normal myelination in *Rab18*$^{-/-}$ mice, as shown through EM and G-ratio calculations, it is therefore possible that the large increase observed in *Rab18*$^{-/-}$ sciatic nerves could point towards ApoD serving a neuroprotective role potentially against the cytoskeletal disorganisation. Therefore, this finding of a dramatic increase in the levels of ApoD upon loss of *Rab18* is akin to injury of the motor neurons rather than death. Further studies examining cellular stress markers such as IL6 and Vegfa and apoptotic markers such as TUNEL staining are warranted to determine the level of stress in *Rab18*$^{-/-}$ mice.

6.3.2 Normal synaptic vesicle endocytosis and exocytosis in *Rab18*$^{-/-}$ neurons

Abnormalities in cytoskeletal organisation and axonal trafficking could both potentially result in abnormalities in the number and rate of synaptic vesicle recycling at *Rab18*$^{-/-}$ synapses. To characterise for gross abnormalities in synaptic vesicle recycling, we utilised two well-established techniques (FM1-43 and sypHy) to demonstrate no gross abnormalities in presynaptic function at the PNS or size of the total vesicle pool or endocytosis at CNS *Rab18*$^{-/-}$ synapses. This suggests that, perhaps surprisingly, loss of *Rab18* has no major impact on synaptic vesicle recycling in PNS or CNS synapses, however, this is consistent with our observations of normal innervation at the NMJ.

Causative loss-of-function mutations have previously been identified in *RAB3GAP1*, *RAB3GAP2* or *RAB18* resulting in a clinically indistinguishable patient phenotype. RAB3GAP1 and RAB3GAP2 specifically function in regulating the RAB3 family in calcium mediated exocytosis of hormones and neurotransmitters (Sudhof, 2004, Aligianis et al., 2005). Prior to generation of the *Rab18*$^{-/-}$ mouse, analysis of pathological mechanisms underlying Warburg Micro syndrome were focused around the role of RAB3 and synaptic vesicle recycling. It must be noted however, that none of the mouse or fly models published for *Rab3* or *Rab3* regulatory proteins have any reported neurological deteriorations in the CNS or PNS. For example; mice and flies deficient for the catalytic subunit, *Rab3gap1* identified subtle alterations in synaptic

plasticity but failed to recapitulate any of the characteristic ocular or neurological phenotypes of the human disease (Sakane et al., 2006, Muller et al., 2011). Furthermore, examination of synaptic plasticity in *Rab3* quadruple knockout mice (*Rab3a, Rab3b, Rab3c* and *Rab3d)* showed normal docking of synaptic vesicles at active zones in hippocampal neurons, normal axonal conductivity and a discrete reduction in synaptic vesicle exocytosis (Schluter et al., 2004). *Rab3gep*$^{-/-}$ mice (GEP- GDP/GTP exchange protein) die shortly after birth with no evoked responses in the diaphragm or gastrocnemius muscles. However, they showed normal axonal conductivity in the spinal cord and phrenic nerve but neuromuscular transmission abnormalities with few to no synaptic vesicles at *Rab3gep*$^{-/-}$ axon terminals (Tanaka et al., 2001).

I propose that further studies should now be undertaken to examine for neurofilament and microtubule abnormalities and cytoskeletal disorganisation in animal models lacking *Rab3* and *Rab3* regulatory proteins. The *Rab3gap1*$^{-/-}$ mouse did not report any neurological deterioration but due to the identical phenotype observed upon *RAB3GAP1, RAB3GAP2* or *RAB18* loss it could potentially also exhibit slight increased levels of neurofilament. Additionally, if similar neuropathological abnormalities were observed in the *Rab3gap1* mice but not *Rab3* or *Rab3GEF* for example this may help to distinguish RAB3GAP function from that reported to regulate RAB3. Furthermore, quadruple *Rab3* knockouts die very soon after birth due to respiratory failure, this could be due to neuronal dysfunction or a general defect of exocytosis, further studies would now be warranted to examine this.

6.3.3 Summary

In summary, I have described here detailed neuropathological characterisation of the hind limb weakness observed during initial phenotyping of *Rab18*$^{-/-}$ mice. I have demonstrated that loss of *Rab18* does not result in gross abnormalities in synaptic vesicle recycling at PNS or CNS synapses but rather results in accumulations of microtubules and neurofilament proteins in motor neuron terminals. Furthermore, through electron microscopy of axons and proteomic analysis of *Rab18*$^{-/-}$ sciatic nerves I have identified RAB18-dependent disorganisation of microtubules and

neurofilaments and alterations in core molecular pathways implicated in assembly and confirmation of the cytoskeleton.

Chapter 7 Summary and general discussion

7.1 Summary of findings in this study

The principle aim of this study was to undertake a detailed characterisation of a novel *Rab18*$^{-/-}$ mouse model created by MRC Harwell as part of the EUMODIC screen.

Rab18 genetrap mice were generated using the FlipRosaβGeo cassette. Initially, I carried out analysis of the genetrap and identified no residual mRNA or protein expression upon RT-PCR, qRT-PCR or Western blotting for RAB18. I therefore consider *Rab18*$^{-/-}$ mice to represent the null phenotype of *Rab18.* In humans, homozygous loss-of-function mutations in *RAB18* cause Warburg Micro syndrome. I therefore utilised the *Rab18*$^{-/-}$ mouse model to examine for phenotypes relevant to Warburg Micro syndrome. Detailed phenotypic analysis identified specific abnormalities in the lens and the hind limbs, recapitulating many of the characteristic ocular and neurological features of Warburg Micro syndrome.

Secondly, I set out to determine the localisation of RAB18 in mouse embryonic fibroblasts to determine whether loss of RAB18 resulted in a ubiquitous cellular phenotype. I have shown that RAB18 localises to the ER, Golgi apparatus and lipid droplet surface, in agreement with previous reports (Martin et al., 2005, Ozeki et al., 2005, Pulido et al., 2011, Dejgaard et al., 2008). Interestingly, loss of RAB18 had no gross consequences on ER or Golgi apparatus morphology but resulted in enlarged lipid droplets. I was therefore unable to rule out the possibility that Warburg Micro syndrome pathology originates from a ubiquitous cellular function. However, my analyses of GFP-RAB18 localising to mobile accumulations along neurite processes of primary hippocampal neurons, potentially points towards a cell-type specific function for RAB18 in neurons.

My subsequent work aimed to provide a more detailed characterisation of the ocular and neurological features observed during general phenotyping of the *Rab18*$^{-/-}$ mouse model. *Rab18*$^{-/-}$ mice presented at eye opening with dense nuclear congenital

cataracts and atonic pupils and went on to develop progressive hind limb weakness. Histological examination of embryonic and neonatal lens identified a delay in closure of the lens vesicle from E12.5, with large vacuoles, pyknotic nuclei and nuclear aggregates evident in the lens by birth. Additionally, preliminary analysis identified potential abnormalities in denucleation and organisation of lens fibre cells in *Rab18*$^{-/-}$ neonates suggestive of a defect in lens fibre cell differentiation.

Detailed investigation of the neuronal pathology underlying the observed hind limb weakness suggested that, contrary to expectation, loss of RAB18 resulted in no major abnormalities in synaptic vesicle recycling at either PNS or CNS synapses. Additionally, normal levels of RAB3GAP1, RAB3GAP2 and RAB3A in crude synaptosomes isolated from *Rab18*$^{-/-}$ mice were observed. However, gross accumulations of microtubules and neurofilament proteins were observed at *Rab18*$^{-/-}$ NMJs and disorganisation of the axonal cytoskeletal architecture was seen in sciatic nerve profiles. Furthermore, in- depth proteomic and gene ontology analysis in sciatic nerves showed that loss of *Rab18* resulted in modifications to several canonical pathways regulating cytoskeletal organisation and maintenance. Preliminary analysis of axonal transport by sciatic nerve ligation experiments, also pointed towards a potential abnormality in KIF5A dependent transport pathways.

7.2 Link between the ocular and neurological phenotypes observed in Warburg Micro syndrome patients and *Rab18*$^{-/-}$ mice

Rab18$^{-/-}$ mice exhibit dense nuclear congenital cataracts and progressive hind limb weakness. It is of interest how loss of a ubiquitously expressed protein can result in such specific abnormalities affecting both ocular and neurological systems whilst other cells and tissues remain essentially unaffected. As discussed in chapter 3, the phenomenon of restricted neuronal vulnerability upon loss of a ubiquitously expressed protein is observed in many models of neurodegenerative disease (Monani, 2005). How loss of RAB18 specifically affects neurological and ocular systems must now be further examined. Many other disorders also exhibit neurodegeneration and

congenital cataracts including atypical familial lipodystrophy, hypomyelination and congenital cataract, and congenital cataract facial dysmorphism neuropathy syndrome (Berger et al., 2002, Biancheri et al., 2007, Shabo et al., 2005). Recent studies have therefore tried to establish a potential link between lens fibre cells and neurons and have identified a large degree of similarity; for example a number of gene products thought to be neuronal specific, have now also been shown to be expressed in the lens (Frederikse et al., 2012). Similarities in vesicular transport machinery have also been identified between neurons and lens fibre cells with RT-PCR of 6 week old lens identifying the presence of molecular motors (including KIF5A), RAB proteins (including RAB3A), synapsin and synaptic vesicle proteins (including synaptotagmin I and synaptophysin I) (Frederikse et al., 2004). Additionally, Lo *et al.,* 2003 have shown that lens fibre cells and neurons share a comparable morphology with an orientated microtubule system, with newly differentiated lens fibre cells containing polarised microtubules along their long axes and kinesin and dynein molecular motors. Furthermore, the Golgi apparatus and membranous vesicles reminiscent of vesicular transport mechanisms are evident in differentiating fibre cells of the outer cortex, but not found in either the inner cortex or the differentiated lens nucleus (Lo et al., 2003).

It is therefore important to try and identify a link between the neuronal pathologies including neurofilament and microtubule accumulations and cytoskeletal disorganisation with the lenticular anomalies observed in *Rab18*$^{-/-}$ mice. A previous study characterising mice overexpressing neurofilament light chain reported the development of cataracts consistent with the possibility that cataract development may be linked to neurofilament abnormalities (Monteiro et al., 1990). This may in turn suggest a link between the cellular pathology observed in the lens fibre cells in *Rab18*$^{-/-}$ mice and those seen in the peripheral nervous system. Preliminary experiments have pointed towards abnormalities in lens fibre organisation properties in *Rab18*$^{-/-}$ mice. Future work should therefore focus on examining the microtubule architecture in the developing lens by electron microscopy and identifying levels of intermediate filament proteins in *Rab18*$^{-/-}$ lenses either by western blotting or immunohistochemistry.

7.3 Role of a RAB protein in cytoskeletal disorganisation

RAB proteins primarily function in regulating vesicular trafficking so the identification of an unexpected role for RAB18 in cytoskeletal organisation is potentially interesting. One possible explanation for this finding has come from analysis of the smooth endoplasmic reticulum existing as a continuous network of tubules in axons. I, along with others, have shown RAB18 to be linked to the ER in multiple cell types (chapter 4) (Martin et al., 2005). It is now widely established that the smooth ER interacts with the neuronal cytoskeleton (Renvoise and Blackstone, 2010). For example, previous studies have identified a link between the smooth ER and neurofilaments in transected squid giant axons and frog olfactory axons (Burton and Laveri, 1985, Metuzals et al., 1995). It is therefore not unfathomable that a deficit in RAB18 at the smooth ER may result in disorganisation to the axonal cytoskeleton. Other proteins are known to mediate associations between the ER and the cytoskeleton such as spastin and the REEP1-4 family of proteins and mutations in these genes cause peripheral neurological abnormalities similar to those observed in Warburg Micro syndrome (Renvoise and Blackstone, 2010, Montenegro et al., 2012). Additionally, examination of the reticulon-like-1 fly orthologue of human reticulon 2 showed disorganisation of the smooth ER, microtubules and mitochondria in motor axons and at the NMJ (O'Sullivan et al., 2012). A role for atlastin (another hereditary spastic paraplegia gene) has also been reported in regulation of lipid droplet size, with knockdown causing a decreased diameter of lipid droplets (Klemm et al., 2013), and could potentially link the cytoskeleton disorganisation and lipid phenotype observed. Potentially, RAB18 may therefore function to maintain a link between the smooth ER and the cytoskeleton in peripheral nerves.

Interestingly, I have also identified GFP-RAB18 to localise to dense puncta along processes of primary mouse hippocampal neurons that are trafficked rapidly in a retrograde manner. It has also been brought to light that a small component of the ER functions in large vesicular structures in dendrites that are rapidly trafficked in a bidirectional manner (Bannai et al., 2004). This trafficking is dependent on

microtubule organisation and the molecular motor, kinesin (Bannai et al., 2004). Analysis of ER vesicular trafficking in axons identified movement in a bidirectional manner and insensitive to nocodazole treatment (Aihara et al., 2001). It would now be of interest to identify whether these accumulations co-localise with markers of the smooth endoplasmic reticulum to determine if the punctae observed in GFP-RAB18 transfected neurons represent the vesicular subcompartment of the ER showing rapid movement.

Interestingly, there is a precedent for RAB proteins mediating a link between membrane trafficking and the cytoskeleton. One way they do this is via molecular motors. For example, GTP bound RAB6A directly interacts with KIF20A (Echard et al., 1998) whereas RAB3A interacts indirectly with KIF1Bβ/KIF1A via DENN/MADD (Niwa et al., 2008). I have shown in chapter 4 that GFP-RAB18 positive puncta appear to be trafficked in a specifically retrograde manner. Future work should therefore determine whether RAB18 functions via a molecular motor. Preliminary studies in chapter 5 have suggested abnormalities in KIF5A dependent pathways; however, at this stage it is unclear whether this is the result of the cytoskeletal disorganisation or a cause of it.

7.4 Future work

In this thesis I have performed a detailed characterisation of pathological changes in *Rab18*$^{-/-}$ mice, a model for Warburg Micro syndrome. The majority of potential future work has been presented in the discussion section of each relevant chapter. Here, I will therefore focus on future work that could hopefully provide us with a link between not only the four causative genes but also pathological abnormalities observed in this study. Warburg Micro syndrome is a highly heterogeneous disorder, with mutations in one of *RAB3GAP1, RAB3GAP2, RAB18* or *TBC1D20* accounting for approximately 50% of cases. Further heterogeneity is therefore evident. Whole exome sequencing is currently being undertaken to identify other causative genes for Warburg Micro syndrome. It is hoped that the identification of further genes may aid the elucidation of the RAB protein network implicated in disease pathogenesis.

In this study I have primarily focused on the congenital cataracts and progressive hind limb weakness observed during general phenotyping of the *Rab18*$^{-/-}$ mouse model. Definitive analysis and characterisation of other phenotypes observed in Warburg Micro syndrome patients are now critical. For example, examination of any central nervous system or endocrine abnormalities should now be a focus of future work.

7.4.1 Link between phenotypes observed

A novel finding of this study was the identification of gross accumulations of neurofilament in motor neurons from *Rab18*$^{-/-}$ mice. Preliminary work also suggested that cytoskeletal disorganisation is a feature of the lens pathology. This raises the question of whether the pathology in the motor neurons and lenses result from deficiencies in the same, RAB18-regulated process. In order to further characterise the links between RAB18 and the cytoskeleton in each of these systems further studies should initially be focused on examination of levels of lens differentiation markers such as the α, β and γ-crystallins, in control and *Rab18*$^{-/-}$ mice. Also, sectioning of the equatorial plane of the lens and staining with PRX or scanning electron microscopy should be performed to definitively confirm or rule out abnormalities in the organisation of lens fibre cells in *Rab18*$^{-/-}$ mice. Additionally, the lens also expresses intermediate filament proteins, the principle of which being vimentin (FitzGerald, 2009), examination of intermediate filament levels in the lens by Western blotting should also be performed. Neurofilament accumulations are also observed in the CNS in many neurodegenerative diseases. For example, accumulations of neurofilament are observed in Lewy bodies in Parkinson disease brains (Goldman et al., 1983). Warburg Micro syndrome patients also display many central nervous system abnormalities including polymicrogyria and severe developmental delay; it would therefore be of interest to examine the levels of neurofilament proteins in the central nervous system of *Rab18*$^{-/-}$ mice.

As discussed in section 7.3, RAB18 and its role in cytoskeletal disorganisation and transport may involve interactions with the smooth ER. To enable further characterisation of a link between RAB18 and the smooth ER, future studies should examine the morphology of the smooth ER in peripheral nerves by EM and examine

the NMJ to determine whether the smooth ER also accumulates with neurofilament and microtubules.

I also observed accumulations of GFP-RAB18 along processes of primary mouse hippocampal neurons that are trafficked rapidly in a retrograde manner. Further characterisation of the nature of these accumulations to determine whether they represent synaptic vesicles (given the well-established roles of RAB3 proteins) or ER markers should now be undertaken. RAB18 is a member of the RAB family of small GTPases functioning as master regulators of vesicular trafficking. It would be of interest to examine the nucleotide binding properties of RAB18 in primary hippocampal neurons by transfection of GDP or GTP mutants and examine localisation. Co-transfection experiments with GFP-RAB18 and mCherry-RAB3GAP1, RAB3GAP2 or TBC1D20 would be useful in determining the respective localisation of the four proteins.

7.4.2 Link between Warburg Micro syndrome causative genes

At this stage of our analysis it is now important to determine a link between the four causative genes that would result in an identical phenotype. As previously stated experiments are now being undertaken to determine if RAB3GAP2 has GEF activity towards RAB18 and TBC1D20 functions as a GAP for RAB18. However, it would also be of interest to examine for protein levels of TBC1D20 in *Rab18*$^{-/-}$ mice and RAB18 levels in *Tbc1d20 bs* mice. Furthermore, as studies undertaken by Leigel *et al.,* have reported enlarged lipid droplets in *RAB3GAP1, RAB3GAP2* and *TBC1D20* patient fibroblasts. A biochemical screen of lipid and cholesterol levels in *Rab18*$^{-/-}$ mice would be important to characterise any abnormalities.

7.4.3 Generation of conditional knockouts

The *Rab18*$^{-/-}$ mouse presented in the study was created using the FlipRosaβGeo cassette. This genetrap cassette utilises pairs of heterotypic lox and frt sites to allow the generation of temporal and tissue specific knockouts. I have crossed *Rab18*$^{-/-}$ mice to FLPe to flip the cassette into the reverse orientation on the antisense strand and thus repair the mutation. Litters from this mating have now been born and are positive for insertion of the cassette by primer specific PCR and gel electrophoresis

but negative for congenital cataracts or hind limb weakness. Crosses are now underway to breed Flipped *Rab18*$^{-/-}$ mice to CreER a tamoxifen inducible Cre, to reinvert the cassette onto the sense strand and reinsert the mutation. When these mice reach 6 weeks of age they will be injected with tamoxifen to knock out *Rab18* and characterise any phenotypes in the adult nervous system, it is hoped that this will enable us to delineate the role of *Rab18* in degeneration compared to development.

7.5 Conclusion

In summary, this study reports the first characterisation of a mouse model for *Rab18*, recapitulating both ocular and neurological features of Warburg Micro syndrome. *Rab18*$^{-/-}$mice present with dense nuclear congenital cataracts, atonic pupils and progressive hind limb weakness, all phenotypes associated with Warburg Micro syndrome disease pathogenesis. I have shown that the abnormal ocular phenotypes in *Rab18*$^{-/-}$ mice begin from E12.5 with delay in closure of the lens vesicle. Analyses of the observed hind limb pathology have shown that loss of RAB18 does not result in abnormalities in synaptic vesicle recycling or RAB3 proteins, suggesting the pathology of Warburg Micro syndrome may not be centred on dysregulation of the RAB3 pathway as previously proposed. Furthermore, I have identified that loss of RAB18 results in accumulations of microtubule and neurofilament proteins at the NMJ and gross disorganisation of the neuronal cytoskeleton in sciatic nerve profiles. iTRAQ proteomic analysis of *Rab18*$^{-/-}$ peripheral nerve identified abnormalities in core molecular pathways implicated in organisation and maintenance of the axonal cytoskeleton. *Rab18*$^{-/-}$ mice model the major disease characteristics of Warburg Micro syndrome and I therefore propose a novel role for RAB18 in eye development and maintenance of cytoskeletal architecture in neurons, thus providing for the first time a platform for investigating ocular and neurological disease pathogenesis and therapeutic interventions.

Chapter 8: Bibliography

ABDEL-SALAM, G. M., HASSAN, N. A., KAYED, H. F. & ALIGIANIS, I. A. 2007. Phenotypic variability in Micro syndrome: report of new cases. *Genet Couns,* 18**,** 423-35.

ACHILLI, F., BROS-FACER, V., WILLIAMS, H. P., BANKS, G. T., ALQATARI, M., CHIA, R., TUCCI, V., GROVES, M., NICKOLS, C. D., SEBURN, K. L., KENDALL, R., CADER, M. Z., TALBOT, K., VAN MINNEN, J., BURGESS, R. W., BRANDNER, S., MARTIN, J. E., KOLTZENBURG, M., GREENSMITH, L., NOLAN, P. M. & FISHER, E. M. 2009. An ENU-induced mutation in mouse glycyl-tRNA synthetase (GARS) causes peripheral sensory and motor phenotypes creating a model of Charcot-Marie-Tooth type 2D peripheral neuropathy. *Dis Model Mech,* 2**,** 359-73.

ACKERLEY, S., THORNHILL, P., GRIERSON, A. J., BROWNLEES, J., ANDERTON, B. H., LEIGH, P. N., SHAW, C. E. & MILLER, C. C. 2003. Neurofilament heavy chain side arm phosphorylation regulates axonal transport of neurofilaments. *J Cell Biol,* 161**,** 489-95.

AIHARA, Y., INOUE, T., TASHIRO, T., OKAMOTO, K., KOMIYA, Y. & MIKOSHIBA, K. 2001. Movement of endoplasmic reticulum in the living axon is distinct from other membranous vesicles in its rate, form, and sensitivity to microtubule inhibitors. *J Neurosci Res,* 65**,** 236-46.

AINSWORTH, J. R., MORTON, J. E., GOOD, P., WOODS, C. G., GEORGE, N. D., SHIELD, J. P., BRADBURY, J., HENDERSON, M. J. & CHHINA, J. 2001. Micro syndrome in Muslim Pakistan children. *Ophthalmology,* 108**,** 491-7.

ALIGIANIS, I. A., JOHNSON, C. A., GISSEN, P., CHEN, D., HAMPSHIRE, D., HOFFMANN, K., MAINA, E. N., MORGAN, N. V., TEE, L., MORTON, J., AINSWORTH, J. R., HORN, D., ROSSER, E., COLE, T. R., STOLTE-DIJKSTRA, I., FIEGGEN, K., CLAYTON-SMITH, J., MEGARBANE, A., SHIELD, J. P., NEWBURY-ECOB, R., DOBYNS, W. B., GRAHAM, J. M., JR., KJAER, K. W., WARBURG, M., BOND, J., TREMBATH, R. C., HARRIS, L. W., TAKAI, Y., MUNDLOS, S., TANNAHILL, D., WOODS, C. G. & MAHER, E. R. 2005. Mutations of the catalytic subunit of RAB3GAP cause Warburg Micro syndrome. *Nat Genet,* 37**,** 221-3.

ALIGIANIS, I. A., MORGAN, N. V., MIONE, M., JOHNSON, C. A., ROSSER, E., HENNEKAM, R. C., ADAMS, G., TREMBATH, R. C., PILZ, D. T., STOODLEY, N., MOORE, A. T., WILSON, S. & MAHER, E. R. 2006. Mutation in Rab3 GTPase-activating protein (RAB3GAP) noncatalytic subunit in a kindred with Martsolf syndrome. *Am J Hum Genet,* 78**,** 702-7.

ALORY, C. & BALCH, W. E. 2001. Organization of the Rab-GDI/CHM superfamily: the functional basis for choroideremia disease. *Traffic,* 2**,** 532-43.

ATLURI, P. P. & RYAN, T. A. 2006. The kinetics of synaptic vesicle reacidification at hippocampal nerve terminals. *J Neurosci,* 26**,** 2313-20.

AYALEW, M., LE-NICULESCU, H., LEVEY, D. F., JAIN, N., CHANGALA, B., PATEL, S. D., WINIGER, E., BREIER, A., SHEKHAR, A., AMDUR, R., KOLLER, D., NURNBERGER, J. I., CORVIN, A., GEYER, M., TSUANG, M. T., SALOMON, D., SCHORK, N. J., FANOUS, A. H., O'DONOVAN, M. C. & NICULESCU, A. B. 2012. Convergent functional genomics of schizophrenia: from comprehensive understanding to genetic risk prediction. *Mol Psychiatry,* 17**,** 887-905.

BANNAI, H., INOUE, T., NAKAYAMA, T., HATTORI, M. & MIKOSHIBA, K. 2004. Kinesin dependent, rapid, bi-directional transport of ER sub-compartment in dendrites of hippocampal neurons. *J Cell Sci,* 117**,** 163-75.

BARR, F. & LAMBRIGHT, D. G. 2010. Rab GEFs and GAPs. *Curr Opin Cell Biol,* 22**,** 461-70.

BEM, D., YOSHIMURA, S., NUNES-BASTOS, R., BOND, F. F., KURIAN, M. A., RAHMAN, F., HANDLEY, M. T., HADZHIEV, Y., MASOOD, I., STRAATMAN-IWANOWSKA, A. A., CULLINANE, A. R., MCNEILL, A., PASHA, S. S., KIRBY, G. A., FOSTER, K., AHMED, Z., MORTON, J. E., WILLIAMS, D., GRAHAM, J. M., DOBYNS, W. B., BURGLEN, L., AINSWORTH, J. R., GISSEN, P., MULLER, F., MAHER, E. R., BARR, F. A. & ALIGIANIS, I. A. 2011. Loss-of-function mutations in RAB18 cause Warburg micro syndrome. *Am J Hum Genet,* 88**,** 499-507.

BERGER, J. R., ORAL, E. A. & TAYLOR, S. I. 2002. Familial lipodystrophy associated with neurodegeneration and congenital cataracts. *Neurology,* 58**,** 43-7.

BIANCHERI, R., ZARA, F., BRUNO, C., ROSSI, A., BORDO, L., GAZZERRO, E., SOTGIA, F., PEDEMONTE, M., SCAPOLAN, S., BADO, M., UZIEL, G., BUGIANI, M., LAMBA, L. D., COSTA, V., SCHENONE, A., ROZEMULLER, A. J., TORTORI-DONATI, P., LISANTI, M. P., VAN DER KNAAP, M. S. & MINETTI, C. 2007. Phenotypic characterization of hypomyelination and congenital cataract. *Ann Neurol,* 62**,** 121-7.

BLENNOW, K., BOGDANOVIC, N., ALAFUZOFF, I., EKMAN, R. & DAVIDSSON, P. 1996a. Synaptic pathology in Alzheimer's disease: relation to severity of dementia, but not to senile plaques, neurofibrillary tangles, or the ApoE4 allele. *J Neural Transm,* 103**,** 603-18.

BLENNOW, K., DAVIDSSON, P., GOTTFRIES, C. G., EKMAN, R. & HEILIG, M. 1996b. Synaptic degeneration in thalamus in schizophrenia. *Lancet,* 348**,** 692-3.

BLUMER, J., REY, J., DEHMELT, L., MAZEL, T., WU, Y. W., BASTIAENS, P., GOODY, R. S. & ITZEN, A. 2013. RabGEFs are a major determinant for specific Rab membrane targeting. *J Cell Biol,* 200**,** 287-300.

BORCHMAN, D. & YAPPERT, M. C. 2010. Lipids and the ocular lens. *J Lipid Res,* 51**,** 2473-88.

BORCK, G., WUNRAM, H., STEIERT, A., VOLK, A. E., KORBER, F., ROTERS, S., HERKENRATH, P., WOLLNIK, B., MORRIS-ROSENDAHL, D. J. & KUBISCH, C. 2010. A homozygous RAB3GAP2 mutation causes Warburg Micro syndrome. *Hum Genet,* 129**,** 45-50.

BRIGHOUSE, A., DACKS, J. B. & FIELD, M. C. 2010. Rab protein evolution and the history of the eukaryotic endomembrane system. *Cell Mol Life Sci,* 67**,** 3449-65.

BROWN, A., WANG, L. & JUNG, P. 2005. Stochastic simulation of neurofilament transport in axons: the "stop-and-go" hypothesis. *Mol Biol Cell,* 16**,** 4243-55.

BROWNLEES, J., ACKERLEY, S., GRIERSON, A. J., JACOBSEN, N. J., SHEA, K., ANDERTON, B. H., LEIGH, P. N., SHAW, C. E. & MILLER, C. C. 2002. Charcot-Marie-Tooth disease neurofilament mutations disrupt neurofilament assembly and axonal transport. *Hum Mol Genet,* 11**,** 2837-44.

BURTON, P. R. & LAVERI, L. A. 1985. The distribution, relationships to other organelles, and calcium-sequestering ability of smooth endoplasmic reticulum in frog olfactory axons. *J Neurosci,* 5**,** 3047-60.

CARROLL, K. S., HANNA, J., SIMON, I., KRISE, J., BARBERO, P. & PFEFFER, S. R. 2001. Role of Rab9 GTPase in facilitating receptor recruitment by TIP47. *Science,* 292**,** 1373-6.

CHAN, C. C., SCOGGIN, S., WANG, D., CHERRY, S., DEMBO, T., GREENBERG, B., JIN, E. J., KUEY, C., LOPEZ, A., MEHTA, S. Q., PERKINS, T. J., BRANKATSCHK, M., ROTHENFLUH, A., BUSZCZAK, M. & HIESINGER, P. R. 2011. Systematic discovery of Rab GTPases with synaptic functions in Drosophila. *Curr Biol,* 21**,** 1704-15.

CHAVRIER, P., GORVEL, J. P., STELZER, E., SIMONS, K., GRUENBERG, J. & ZERIAL, M. 1991. Hypervariable C-terminal domain of rab proteins acts as a targeting signal. *Nature,* 353**,** 769-72.

CHRISTOFORIDIS, S., MCBRIDE, H. M., BURGOYNE, R. D. & ZERIAL, M. 1999. The Rab5 effector EEA1 is a core component of endosome docking. *Nature,* 397**,** 621-5.

CIFUENTES-DIAZ, C., NICOLE, S., VELASCO, M. E., BORRA-CEBRIAN, C., PANOZZO, C., FRUGIER, T., MILLET, G., ROBLOT, N., JOSHI, V. & MELKI, J. 2002. Neurofilament accumulation at the motor endplate and lack of axonal sprouting in a spinal muscular atrophy mouse model. *Hum Mol Genet,* 11**,** 1439-47.

COCHILLA, A. J., ANGLESON, J. K. & BETZ, W. J. 1999. Monitoring secretory membrane with FM1-43 fluorescence. *Annu Rev Neurosci,* 22**,** 1-10.

COLLARD, J. F., COTE, F. & JULIEN, J. P. 1995. Defective axonal transport in a transgenic mouse model of amyotrophic lateral sclerosis. *Nature,* 375**,** 61-4.

CONDE, C. & CACERES, A. 2009. Microtubule assembly, organization and dynamics in axons and dendrites. *Nat Rev Neurosci,* 10**,** 319-32.

COOPER, M. A., SON, A. I., KOMLOS, D., SUN, Y., KLEIMAN, N. J. & ZHOU, R. 2008. Loss of ephrin-A5 function disrupts lens fiber cell packing and leads to cataract. *Proc Natl Acad Sci U S A,* 105**,** 16620-5.

CORBEEL, L. & FRESON, K. 2008. Rab proteins and Rab-associated proteins: major actors in the mechanism of protein-trafficking disorders. *Eur J Pediatr,* 167**,** 723-9.

COTLIER, E. & RICE, P. 1971. Cataracts in the Smith-Lemli-Opitz syndrome. *Am J Ophthalmol,* 72**,** 955-9.

COURT, F. A., GILLINGWATER, T. H., MELROSE, S., SHERMAN, D. L., GREENSHIELDS, K. N., MORTON, A. J., HARRIS, J. B., WILLISON, H. J. & RIBCHESTER, R. R. 2008. Identity, developmental restriction and reactivity of extralaminar cells capping mammalian neuromuscular junctions. *J Cell Sci,* 121**,** 3901-11.

CVEKL, A. & PIATIGORSKY, J. 1996. Lens development and crystallin gene expression: many roles for Pax-6. *Bioessays,* 18**,** 621-30.

D'ADAMO, P., MENEGON, A., LO NIGRO, C., GRASSO, M., GULISANO, M., TAMANINI, F., BIENVENU, T., GEDEON, A. K., OOSTRA, B., WU, S. K., TANDON, A., VALTORTA, F., BALCH, W. E., CHELLY, J. & TONIOLO, D. 1998. Mutations in GDI1 are responsible for X-linked non-specific mental retardation. *Nat Genet,* 19**,** 134-9.

DALE, J. M., SHEN, H., BARRY, D. M., GARCIA, V. B., ROSE, F. F., JR., LORSON, C. L. & GARCIA, M. L. 2011. The spinal muscular atrophy mouse model, SMADelta7, displays altered axonal transport without global neurofilament alterations. *Acta Neuropathol,* 122**,** 331-41.

DE VOS, K. J., GRIERSON, A. J., ACKERLEY, S. & MILLER, C. C. 2008. Role of axonal transport in neurodegenerative diseases. *Annu Rev Neurosci,* 31**,** 151-73.

DEJGAARD, S. Y., MURSHID, A., ERMAN, A., KIZILAY, O., VERBICH, D., LODGE, R., DEJGAARD, K., LY-HARTIG, T. B., PEPPERKOK, R., SIMPSON, J. C. & PRESLEY, J. F. 2008. Rab18 and Rab43 have key roles in ER-Golgi trafficking. *J Cell Sci,* 121**,** 2768-81.

DERBENT, M., AGRAS, P. I., GEDIK, S., OTO, S., ALEHAN, F. & SAATCI, U. 2004. Congenital cataract, microphthalmia, hypoplasia of corpus callosum and hypogenitalism: report and review of Micro syndrome. *Am J Med Genet A,* 128A**,** 232-4.

DETTER, J. C., ZHANG, Q., MULES, E. H., NOVAK, E. K., MISHRA, V. S., LI, W., MCMURTRIE, E. B., TCHERNEV, V. T., WALLACE, M. R., SEABRA, M. C., SWANK, R. T. & KINGSMORE, S. F. 2000. Rab geranylgeranyl transferase alpha mutation in the gunmetal mouse reduces Rab prenylation and platelet synthesis. *Proc Natl Acad Sci U S A,* 97**,** 4144-9.

DIRAC-SVEJSTRUP, A. B., SUMIZAWA, T. & PFEFFER, S. R. 1997. Identification of a GDI displacement factor that releases endosomal Rab GTPases from Rab-GDI. *EMBO J,* 16**,** 465-72.

DOU, T., JI, C., GU, S., CHEN, F., XU, J., YE, X., YING, K., XIE, Y. & MAO, Y. 2005. Cloning and characterization of a novel splice variant of human Rab18 gene (RAB18). *DNA Seq,* 16**,** 230-4.

DUMAS, J. J., ZHU, Z., CONNOLLY, J. L. & LAMBRIGHT, D. G. 1999. Structural basis of activation and GTP hydrolysis in Rab proteins. *Structure,* 7**,** 413-23.

DURSUN, F., GUVEN, A. & MORRIS-ROSENDAHL, D. 2012. Warburg Micro syndrome. *J Pediatr Endocrinol Metab,* 25**,** 379-82.

ECHARD, A., JOLLIVET, F., MARTINEZ, O., LACAPERE, J. J., ROUSSELET, A., JANOUEIX-LEROSEY, I. & GOUD, B. 1998. Interaction of a Golgi-associated kinesin-like protein with Rab6. *Science,* 279**,** 580-5.

EHARA, H., UTSUNOMIYA, Y., IESHIMA, A., MAEGAKI, Y., NISHIMURA, G., TAKESHITA, K. & OHNO, K. 2007. Martsolf syndrome in Japanese siblings. *Am J Med Genet A,* 143A**,** 973-8.

EL-KADI, A. M., SOURA, V. & HAFEZPARAST, M. 2007. Defective axonal transport in motor neuron disease. *J Neurosci Res,* 85**,** 2557-66.

FERREIRINHA, F., QUATTRINI, A., PIROZZI, M., VALSECCHI, V., DINA, G., BROCCOLI, V., AURICCHIO, A., PIEMONTE, F., TOZZI, G., GAETA, L., CASARI, G., BALLABIO, A. & RUGARLI, E. I. 2004. Axonal degeneration in paraplegin-deficient mice is associated with abnormal mitochondria and impairment of axonal transport. *J Clin Invest,* 113**,** 231-42.

FISCHER, L. R., CULVER, D. G., TENNANT, P., DAVIS, A. A., WANG, M., CASTELLANO-SANCHEZ, A., KHAN, J., POLAK, M. A. & GLASS, J. D. 2004. Amyotrophic lateral sclerosis is a distal axonopathy: evidence in mice and man. *Exp Neurol,* 185**,** 232-40.

FISCHER VON MOLLARD, G., MIGNERY, G. A., BAUMERT, M., PERIN, M. S., HANSON, T. J., BURGER, P. M., JAHN, R. & SUDHOF, T. C. 1990. rab3 is a small GTP-binding protein exclusively localized to synaptic vesicles. *Proc Natl Acad Sci U S A,* 87**,** 1988-92.

FISCHER VON MOLLARD, G., STAHL, B., KHOKHLATCHEV, A., SUDHOF, T. C. & JAHN, R. 1994. Rab3C is a synaptic vesicle protein that dissociates from synaptic vesicles after stimulation of exocytosis. *J Biol Chem,* 269**,** 10971-4.

FISCHER VON MOLLARD, G., SUDHOF, T. C. & JAHN, R. 1991. A small GTP-binding protein dissociates from synaptic vesicles during exocytosis. *Nature,* 349**,** 79-81.

FITZGERALD, P. G. 2009. Lens intermediate filaments. *Exp Eye Res,* 88**,** 165-72.

FITZPATRICK, D. R. & VAN HEYNINGEN, V. 2005. Developmental eye disorders. *Curr Opin Genet Dev,* 15**,** 348-53.

FRANCIS, P. J., BERRY, V., MOORE, A. T. & BHATTACHARYA, S. 1999. Lens biology: development and human cataractogenesis. *Trends Genet,* 15**,** 191-6.

FRASA, M. A., KOESSMEIER, K. T., AHMADIAN, M. R. & BRAGA, V. M. 2012. Illuminating the functional and structural repertoire of human TBC/RABGAPs. *Nat Rev Mol Cell Biol,* 13**,** 67-73.

FREDERIKSE, P. H., KASINATHAN, C. & KLEIMAN, N. J. 2012. Parallels between neuron and lens fiber cell structure and molecular regulatory networks. *Dev Biol,* 368**,** 255-60.

FREDERIKSE, P. H., YUN, E., KAO, H. T., ZIGLER, J. S., JR., SUN, Q. & QAZI, A. S. 2004. Synapsin and synaptic vesicle protein expression during embryonic and post-natal lens fiber cell differentiation. *Mol Vis,* 10**,** 794-804.

FUCHS, E., HAAS, A. K., SPOONER, R. A., YOSHIMURA, S., LORD, J. M. & BARR, F. A. 2007. Specific Rab GTPase-activating proteins define the Shiga toxin and epidermal growth factor uptake pathways. *J Cell Biol,* 177**,** 1133-43.

FUKUDA, M., KANNO, E., ISHIBASHI, K. & ITOH, T. 2008. Large scale screening for novel rab effectors reveals unexpected broad Rab binding specificity. *Mol Cell Proteomics,* 7**,** 1031-42.

FUKUI, K., SASAKI, T., IMAZUMI, K., MATSUURA, Y., NAKANISHI, H. & TAKAI, Y. 1997. Isolation and characterization of a GTPase activating protein specific for the Rab3 subfamily of small G proteins. *J Biol Chem,* 272**,** 4655-8.

GANFORNINA, M. D., DO CARMO, S., MARTINEZ, E., TOLIVIA, J., NAVARRO, A., RASSART, E. & SANCHEZ, D. 2010. ApoD, a glia-derived apolipoprotein, is required for peripheral nerve functional integrity and a timely response to injury. *Glia,* 58**,** 1320-34.

GEISLER, N., KAUFMANN, E., FISCHER, S., PLESSMANN, U. & WEBER, K. 1983. Neurofilament architecture combines structural principles of intermediate filaments with carboxy-terminal extensions increasing in size between triplet proteins. *EMBO J,* 2**,** 1295-302.

GEPPERT, M., BOLSHAKOV, V. Y., SIEGELBAUM, S. A., TAKEI, K., DE CAMILLI, P., HAMMER, R. E. & SUDHOF, T. C. 1994. The role of Rab3A in neurotransmitter release. *Nature,* 369**,** 493-7.

GIANNANDREA, M., BIANCHI, V., MIGNOGNA, M. L., SIRRI, A., CARRABINO, S., D'ELIA, E., VECELLIO, M., RUSSO, S., COGLIATI, F., LARIZZA, L., ROPERS, H. H., TZSCHACH, A., KALSCHEUER, V., OEHL-JASCHKOWITZ, B., SKINNER, C., SCHWARTZ, C. E., GECZ, J., VAN ESCH, H., RAYNAUD, M., CHELLY, J., DE BROUWER, A. P., TONIOLO, D. & D'ADAMO, P. 2010. Mutations in the small GTPase gene RAB39B are responsible for X-linked mental retardation associated with autism, epilepsy, and macrocephaly. *Am J Hum Genet,* 86**,** 185-95.

GOLDMAN, J. E., YEN, S. H., CHIU, F. C. & PERESS, N. S. 1983. Lewy bodies of Parkinson's disease contain neurofilament antigens. *Science,* 221**,** 1082-4.

GOODY, R. S., RAK, A. & ALEXANDROV, K. 2005. The structural and mechanistic basis for recycling of Rab proteins between membrane compartments. *Cell Mol Life Sci,* 62**,** 1657-70.

GORDON, S. L., LEUBE, R. E. & COUSIN, M. A. 2011. Synaptophysin is required for synaptobrevin retrieval during synaptic vesicle endocytosis. *J Neurosci,* 31**,** 14032-6.

GRAHAM, J. M., JR., HENNEKAM, R., DOBYNS, W. B., ROEDER, E. & BUSCH, D. 2004. MICRO syndrome: an entity distinct from COFS syndrome. *Am J Med Genet A,* 128A**,** 235-45.

GRANSETH, B., ODERMATT, B., ROYLE, S. J. & LAGNADO, L. 2006. Clathrin-mediated endocytosis is the dominant mechanism of vesicle retrieval at hippocampal synapses. *Neuron,* 51**,** 773-86.

GRAW, J. 1999. Cataract mutations and lens development. *Prog Retin Eye Res,* 18**,** 235-67.

GRAW, J. 2003. The genetic and molecular basis of congenital eye defects. *Nat Rev Genet,* 4**,** 876-88.

GRAW, J. 2004. Congenital hereditary cataracts. *Int J Dev Biol,* 48**,** 1031-44.

GRAW, J. 2009. Mouse models of cataract. *J Genet,* 88**,** 469-86.

GRAW, J., NEUHAUSER-KLAUS, A., KLOPP, N., SELBY, P. B., LOSTER, J. & FAVOR, J. 2004. Genetic and allelic heterogeneity of Cryg mutations in eight distinct forms of dominant cataract in the mouse. *Invest Ophthalmol Vis Sci,* 45**,** 1202-13.

GRAW, J., WERNER, T., MERKLE, S., REITMEIR, P., SCHAFFER, E. & WULFF, A. 1990. Histological and biochemical characterization of the murine cataract mutant Nop. *Exp Eye Res,* 50**,** 449-56.

GRONEMEYER, T., WIESE, S., GRINHAGENS, S., SCHOLLENBERGER, L., SATYAGRAHA, A., HUBER, L. A., MEYER, H. E., WARSCHEID, B. & JUST, W. W. 2013. Localization of Rab proteins to peroxisomes: a proteomics and immunofluorescence study. *FEBS Lett,* 587**,** 328-38.

GROSSHANS, B. L., ORTIZ, D. & NOVICK, P. 2006. Rabs and their effectors: achieving specificity in membrane traffic. *Proc Natl Acad Sci U S A,* 103**,** 11821-7.

HAARGAARD, B. & FLEDELIUS, H. C. 2006. Down's syndrome and early cataract. *Br J Ophthalmol,* 90**,** 1024-7.

HAAS, A. K., YOSHIMURA, S., STEPHENS, D. J., PREISINGER, C., FUCHS, E. & BARR, F. A. 2007. Analysis of GTPase-activating proteins: Rab1 and Rab43 are key Rabs required to maintain a functional Golgi complex in human cells. *J Cell Sci,* 120**,** 2997-3010.

HAINES, D. S., LEE, J. E., BEAUPARLANT, S. L., KYLE, D. B., DEN BESTEN, W., SWEREDOSKI, M. J., GRAHAM, R. L., HESS, S. & DESHAIES, R. J. 2012. Protein interaction profiling of the p97 adaptor UBXD1 points to a role for the complex in modulating ERGIC-53 trafficking. *Mol Cell Proteomics,* 11**,** M111 016444.

HANDLEY, M. T., HAYNES, L. P. & BURGOYNE, R. D. 2007. Differential dynamics of Rab3A and Rab27A on secretory granules. *J Cell Sci,* 120**,** 973-84.

HANDLEY, M. T., MORRIS-ROSENDAHL, D. J., BROWN, S., MACDONALD, F., HARDY, C., BEM, D., CARPANINI, S. M., BORCK, G., MARTORELL, L., IZZI, C., FARAVELLI, F., ACCORSI, P., PINELLI, L., BASEL-VANAGAITE, L., PERETZ, G., ABDEL-SALAM, G. M., ZAKI, M. S., JANSEN, A., MOWAT, D., GLASS, I., STEWART, H., MANCINI, G., LEDERER, D., ROSCIOLI, T., GIULIANO, F., PLOMP, A. S., ROLFS, A., GRAHAM, J. M., SEEMANOVA, E., JACKSON, I. J., MAHER, E. R. & ALIGIANIS, I. A. 2013. Mutation Spectrum in RAB3GAP1, RAB3GAP2 and RAB18 and Genotype-Phenotype Correlations in Warburg Micro syndrome and Martsolf Syndrome. *Hum Mutat,* 34**,** 686-96.

HASHIM, S., MUKHERJEE, K., RAJE, M., BASU, S. K. & MUKHOPADHYAY, A. 2000. Live Salmonella modulate expression of Rab proteins to persist in a specialized compartment and escape transport to lysosomes. *J Biol Chem,* 275**,** 16281-8.

HENNEKAM, R. C., VAN DE MEEBERG, A. G., VAN DOORNE, J. M., DIJKSTRA, P. F. & BIJLSMA, J. B. 1988. Martsolf syndrome in a brother and sister: clinical features and pattern of inheritance. *Eur J Pediatr,* 147**,** 539-43.

HISANAGA, S., GONDA, Y., INAGAKI, M., IKAI, A. & HIROKAWA, N. 1990. Effects of phosphorylation of the neurofilament L protein on filamentous structures. *Cell Regul,* 1**,** 237-48.

HOFSLI, E., THOMMESEN, L., YADETIE, F., LANGAAS, M., KUSNIERCZYK, W., FALKMER, U., SANDVIK, A. K. & LAEGREID, A. 2005. Identification of novel growth factor-responsive genes in neuroendocrine gastrointestinal tumour cells. *Br J Cancer,* 92**,** 1506-16.

HORWITZ, J. 1992. Alpha-crystallin can function as a molecular chaperone. *Proc Natl Acad Sci U S A,* 89**,** 10449-53.

HUGHES, B. W., KUSNER, L. L. & KAMINSKI, H. J. 2006. Molecular architecture of the neuromuscular junction. *Muscle Nerve,* 33**,** 445-61.

IKENAKA, K., KATSUNO, M., KAWAI, K., ISHIGAKI, S., TANAKA, F. & SOBUE, G. 2012. Disruption of axonal transport in motor neuron diseases. *Int J Mol Sci,* 13**,** 1225-38.

JENKINS, D., SEELOW, D., JEHEE, F. S., PERLYN, C. A., ALONSO, L. G., BUENO, D. F., DONNAI, D., JOSIFOVA, D., MATHIJSSEN, I. M., MORTON, J. E., ORSTAVIK, K. H., SWEENEY, E., WALL, S. A., MARSH, J. L., NURNBERG, P., PASSOS-BUENO, M. R. & WILKIE, A. O. 2007. RAB23 mutations in Carpenter syndrome imply an unexpected role for hedgehog signaling in cranial-suture development and obesity. *Am J Hum Genet,* 80**,** 1162-70.

JONES, S., NEWMAN, C., LIU, F. & SEGEV, N. 2000. The TRAPP complex is a nucleotide exchanger for Ypt1 and Ypt31/32. *Mol Biol Cell,* 11**,** 4403-11.

JORDANOVA, A., DE JONGHE, P., BOERKOEL, C. F., TAKASHIMA, H., DE VRIENDT, E., CEUTERICK, C., MARTIN, J. J., BUTLER, I. J., MANCIAS, P., PAPASOZOMENOS, S., TERESPOLSKY, D., POTOCKI, L., BROWN, C. W., SHY, M., RITA, D. A., TOURNEV, I., KREMENSKY, I., LUPSKI, J. R. & TIMMERMAN, V. 2003. Mutations in the neurofilament light chain gene (NEFL) cause early onset severe Charcot-Marie-Tooth disease. *Brain,* 126**,** 590-7.

JULIEN, J. P., COTE, F. & COLLARD, J. F. 1995. Mice overexpressing the human neurofilament heavy gene as a model of ALS. *Neurobiol Aging,* 16**,** 487-90; discussion 490-2.

JUNG, C., YABE, J. T., LEE, S. & SHEA, T. B. 2000. Hypophosphorylated neurofilament subunits undergo axonal transport more rapidly than more extensively phosphorylated subunits in situ. *Cell Motil Cytoskeleton,* 47**,** 120-9.

KALININA, T., GUNGOR, C., THIELTGES, S., MOLLER-KRULL, M., PENAS, E. M., WICKLEIN, D., STREICHERT, T., SCHUMACHER, U., KALININ, V., SIMON, R., OTTO, B., DIERLAMM, J., SCHWARZENBACH, H., EFFENBERGER, K. E., BOCKHORN, M., IZBICKI, J. R. & YEKEBAS, E. F. 2010. Establishment and characterization of a new human pancreatic adenocarcinoma cell line with high metastatic potential to the lung. *BMC Cancer,* 10**,** 295.

KARLE, K. N., MOCKEL, D., REID, E. & SCHOLS, L. 2012. Axonal transport deficit in a KIF5A(-/-) mouse model. *Neurogenetics,* 13**,** 169-79.

KASHER, P. R., DE VOS, K. J., WHARTON, S. B., MANSER, C., BENNETT, E. J., BINGLEY, M., WOOD, J. D., MILNER, R., MCDERMOTT, C. J., MILLER, C. C., SHAW, P. J. & GRIERSON, A. J. 2009. Direct evidence for axonal transport defects in a novel mouse model of mutant spastin-induced hereditary spastic paraplegia (HSP) and human HSP patients. *J Neurochem,* 110**,** 34-44.

KAWABE, H., SAKISAKA, T., YASUMI, M., SHINGAI, T., IZUMI, G., NAGANO, F., DEGUCHI-TAWARADA, M., TAKEUCHI, M., NAKANISHI, H. & TAKAI, Y. 2003. A novel rabconnectin-3-binding protein that directly binds a GDP/GTP exchange protein for Rab3A small G protein implicated in Ca(2+)-dependent exocytosis of neurotransmitter. *Genes Cells,* 8**,** 537-46.

KINSELLA, B. T. & MALTESE, W. A. 1992. rab GTP-binding proteins with three different carboxyl-terminal cysteine motifs are modified in vivo by 20-carbon isoprenoids. *J Biol Chem,* 267**,** 3940-5.

KLEMM, R. W., NORTON, J. P., COLE, R. A., LI, C. S., PARK, S. H., CRANE, M. M., LI, L., JIN, D., BOYE-DOE, A., LIU, T. Y., SHIBATA, Y., LU, H., RAPOPORT, T. A., FARESE, R. V., JR., BLACKSTONE, C., GUO, Y. & MAK, H. Y. 2013. A conserved role for atlastin GTPases in regulating lipid droplet size. *Cell Rep,* 3**,** 1465-75.

LALONDE, R. & STRAZIELLE, C. 2011. Brain regions and genes affecting limb-clasping responses. *Brain Res Rev,* 67**,** 252-9.

LEE, M. T., MISHRA, A. & LAMBRIGHT, D. G. 2009. Structural mechanisms for regulation of membrane traffic by rab GTPases. *Traffic,* 10**,** 1377-89.

LEUNG, K. F., BARON, R., ALI, B. R., MAGEE, A. I. & SEABRA, M. C. 2007. Rab GTPases containing a CAAX motif are processed post-geranylgeranylation by proteolysis and methylation. *J Biol Chem,* 282**,** 1487-97.

LI, C., TAKEI, K., GEPPERT, M., DANIELL, L., STENIUS, K., CHAPMAN, E. R., JAHN, R., DE CAMILLI, P. & SUDHOF, T. C. 1994. Synaptic targeting of rabphilin-3A, a synaptic vesicle Ca2+/phospholipid-binding protein, depends on rab3A/3C. *Neuron,* 13**,** 885-98.

LIU, P., BARTZ, R., ZEHMER, J. K., YING, Y. S., ZHU, M., SERRERO, G. & ANDERSON, R. G. 2007. Rab-regulated interaction of early endosomes with lipid droplets. *Biochim Biophys Acta,* 1773**,** 784-93.

LIU, S. & STORRIE, B. 2012. Are Rab proteins the link between Golgi organization and membrane trafficking? *Cell Mol Life Sci,* 69**,** 4093-106.

LO, W. K., WEN, X. J. & ZHOU, C. J. 2003. Microtubule configuration and membranous vesicle transport in elongating fiber cells of the rat lens. *Exp Eye Res,* 77**,** 615-26.

LOFTUS, S. K., LARSON, D. M., BAXTER, L. L., ANTONELLIS, A., CHEN, Y., WU, X., JIANG, Y., BITTNER, M., HAMMER, J. A., 3RD & PAVAN, W. J. 2002. Mutation of melanosome protein RAB38 in chocolate mice. *Proc Natl Acad Sci U S A,* 99**,** 4471-6.

LOVICU, F. J., ANG, S., CHORAZYCZEWSKA, M. & MCAVOY, J. W. 2004. Deregulation of lens epithelial cell proliferation and differentiation during the development of TGFbeta-induced anterior subcapsular cataract. *Dev Neurosci,* 26**,** 446-55.

LUTCKE, A., PARTON, R. G., MURPHY, C., OLKKONEN, V. M., DUPREE, P., VALENCIA, A., SIMONS, K. & ZERIAL, M. 1994. Cloning and subcellular localization of novel rab proteins reveals polarized and cell type-specific expression. *J Cell Sci,* 107 (Pt 12)**,** 3437-48.

MADDALA, R., SKIBA, N. P., LALANE, R., 3RD, SHERMAN, D. L., BROPHY, P. J. & RAO, P. V. 2011. Periaxin is required for hexagonal geometry and membrane organization of mature lens fibers. *Dev Biol,* 357**,** 179-90.

MARINKOVIC, P., REUTER, M. S., BRILL, M. S., GODINHO, L., KERSCHENSTEINER, M. & MISGELD, T. 2012. Axonal transport deficits and degeneration can evolve independently in mouse models of amyotrophic lateral sclerosis. *Proc Natl Acad Sci U S A,* 109**,** 4296-301.

MARTIN, S., DRIESSEN, K., NIXON, S. J., ZERIAL, M. & PARTON, R. G. 2005. Regulated localization of Rab18 to lipid droplets: effects of lipolytic stimulation and inhibition of lipid droplet catabolism. *J Biol Chem,* 280**,** 42325-35.

MARTIN, S. & PARTON, R. G. 2006. Lipid droplets: a unified view of a dynamic organelle. *Nat Rev Mol Cell Biol,* 7**,** 373-8.

MARTSOLF, J. T., HUNTER, A. G. & HAWORTH, J. C. 1978. Severe mental retardation, cataracts, short stature, and primary hypogonadism in two brothers. *Am J Med Genet,* 1**,** 291-9.

MATESIC, L. E., YIP, R., REUSS, A. E., SWING, D. A., O'SULLIVAN, T. N., FLETCHER, C. F., COPELAND, N. G. & JENKINS, N. A. 2001. Mutations in Mlph, encoding a member of the Rab effector family, cause the melanosome transport defects observed in leaden mice. *Proc Natl Acad Sci U S A,* 98**,** 10238-43.

MEGARBANE, A., CHOUEIRI, R., BLEIK, J., MEZZINA, M. & CAILLAUD, C. 1999. Microcephaly, microphthalmia, congenital cataract, optic atrophy, short stature, hypotonia, severe psychomotor retardation, and cerebral malformations: a second family with micro syndrome or a new syndrome? *J Med Genet,* 36**,** 637-40.

MENASCHE, G., PASTURAL, E., FELDMANN, J., CERTAIN, S., ERSOY, F., DUPUIS, S., WULFFRAAT, N., BIANCHI, D., FISCHER, A., LE DEIST, F. & DE SAINT BASILE, G. 2000. Mutations in RAB27A cause Griscelli syndrome associated with haemophagocytic syndrome. *Nat Genet,* 25**,** 173-6.

MERCER, J. A., SEPERACK, P. K., STROBEL, M. C., COPELAND, N. G. & JENKINS, N. A. 1991. Novel myosin heavy chain encoded by murine dilute coat colour locus. *Nature,* 349**,** 709-13.

METUZALS, J., FISHMAN, H. M. & ROBB, I. A. 1995. The neurofilamentous network-smooth endoplasmic reticulum complex in transected squid giant axon. *Biol Bull,* 189**,** 216-8.

MICHAEL, R. & BRON, A. J. 2011. The ageing lens and cataract: a model of normal and pathological ageing. *Philos Trans R Soc Lond B Biol Sci,* 366**,** 1278-92.

MIKI, T., KIYONAKA, S., URIU, Y., DE WAARD, M., WAKAMORI, M., BEEDLE, A. M., CAMPBELL, K. P. & MORI, Y. 2007. Mutation associated with an autosomal dominant cone-rod dystrophy CORD7 modifies RIM1-mediated modulation of voltage-dependent Ca2+ channels. *Channels (Austin),* 1**,** 144-7.

MILLECAMPS, S., GOWING, G., CORTI, O., MALLET, J. & JULIEN, J. P. 2007. Conditional NF-L transgene expression in mice for in vivo analysis of turnover and transport rate of neurofilaments. *J Neurosci,* 27**,** 4947-56.

MILLECAMPS, S. & JULIEN, J. P. 2013. Axonal transport deficits and neurodegenerative diseases. *Nat Rev Neurosci,* 14**,** 161-76.

MONANI, U. R. 2005. Spinal muscular atrophy: a deficiency in a ubiquitous protein; a motor neuron-specific disease. *Neuron,* 48**,** 885-96.

MONTEIRO, M. J., HOFFMAN, P. N., GEARHART, J. D. & CLEVELAND, D. W. 1990. Expression of NF-L in both neuronal and nonneuronal cells of transgenic mice: increased neurofilament density in axons without affecting caliber. *J Cell Biol,* 111**,** 1543-57.

MONTENEGRO, G., REBELO, A. P., CONNELL, J., ALLISON, R., BABALINI, C., D'ALOIA, M., MONTIERI, P., SCHULE, R., ISHIURA, H., PRICE, J., STRICKLAND, A., GONZALEZ, M. A., BAUMBACH-REARDON, L., DECONINCK, T., HUANG, J., BERNARDI, G., VANCE, J. M., ROGERS, M. T., TSUJI, S., DE JONGHE, P., PERICAK-VANCE, M. A., SCHOLS, L., ORLACCHIO, A., REID, E. & ZUCHNER, S. 2012. Mutations in the ER-shaping protein reticulon 2 cause the axon-degenerative disorder hereditary spastic paraplegia type 12. *J Clin Invest,* 122**,** 538-44.

MOROZOVA, N., LIANG, Y., TOKAREV, A. A., CHEN, S. H., COX, R., ANDREJIC, J., LIPATOVA, Z., SCIORRA, V. A., EMR, S. D. & SEGEV, N. 2006. TRAPPII subunits are required for the specificity switch of a Ypt-Rab GEF. *Nat Cell Biol,* 8**,** 1263-9.

MORRIS-ROSENDAHL, D. J., SEGEL, R., BORN, A. P., CONRAD, C., LOEYS, B., BROOKS, S. S., MULLER, L., ZESCHNIGK, C., BOTTI, C., RABINOWITZ, R., UYANIK, G., CROCQ, M. A., KRAUS, U., DEGEN, I. & FAES, F. 2010. New RAB3GAP1 mutations in patients with Warburg Micro Syndrome from different ethnic backgrounds and a possible founder effect in the Danish. *Eur J Hum Genet,* 18**,** 1100-6.

MULLER, M., PYM, E. C., TONG, A. & DAVIS, G. W. 2011. Rab3-GAP controls the progression of synaptic homeostasis at a late stage of vesicle release. *Neuron,* 69**,** 749-62.

MURAKAMI, T., NAGANO, I., HAYASHI, T., MANABE, Y., SHOJI, M., SETOGUCHI, Y. & ABE, K. 2001. Impaired retrograde axonal transport of adenovirus-mediated E. coli LacZ gene in the mice carrying mutant SOD1 gene. *Neurosci Lett,* 308**,** 149-52.

MURRAY, L. M., COMLEY, L. H., THOMSON, D., PARKINSON, N., TALBOT, K. & GILLINGWATER, T. H. 2008. Selective vulnerability of motor neurons and dissociation of pre- and post-synaptic pathology at the neuromuscular junction in mouse models of spinal muscular atrophy. *Hum Mol Genet,* 17**,** 949-62.

NAGANO, F., KAWABE, H., NAKANISHI, H., SHINOHARA, M., DEGUCHI-TAWARADA, M., TAKEUCHI, M., SASAKI, T. & TAKAI, Y. 2002. Rabconnectin-3, a novel protein that binds both GDP/GTP exchange protein and GTPase-activating protein for Rab3 small G protein family. *J Biol Chem,* 277**,** 9629-32.

NAGANO, F., SASAKI, T., FUKUI, K., ASAKURA, T., IMAZUMI, K. & TAKAI, Y. 1998. Molecular cloning and characterization of the noncatalytic subunit of the Rab3 subfamily-specific GTPase-activating protein. *J Biol Chem,* 273**,** 24781-5.

NEVO-YASSAF, I., YAFFE, Y., ASHER, M., RAVID, O., EIZENBERG, S., HENIS, Y. I., NAHMIAS, Y., HIRSCHBERG, K. & SKLAN, E. H. 2012. Role for TBC1D20 and Rab1 in hepatitis C virus replication via interaction with lipid droplet-bound nonstructural protein 5A. *J Virol,* 86**,** 6491-502.

NIWA, S., TANAKA, Y. & HIROKAWA, N. 2008. KIF1Bbeta- and KIF1A-mediated axonal transport of presynaptic regulator Rab3 occurs in a GTP-dependent manner through DENN/MADD. *Nat Cell Biol,* 10**,** 1269-79.

O'SULLIVAN, N. C., JAHN, T. R., REID, E. & O'KANE, C. J. 2012. Reticulon-like-1, the Drosophila orthologue of the hereditary spastic paraplegia gene reticulon 2, is required for organization of endoplasmic reticulum and of distal motor axons. *Hum Mol Genet,* 21**,** 3356-65.

OSTERMEIER, C. & BRUNGER, A. T. 1999. Structural basis of Rab effector specificity: crystal structure of the small G protein Rab3A complexed with the effector domain of rabphilin-3A. *Cell,* 96**,** 363-74.

OZEKI, S., CHENG, J., TAUCHI-SATO, K., HATANO, N., TANIGUCHI, H. & FUJIMOTO, T. 2005. Rab18 localizes to lipid droplets and induces their close apposition to the endoplasmic reticulum-derived membrane. *J Cell Sci,* 118**,** 2601-11.

PEREIRA-LEAL, J. B., HUME, A. N. & SEABRA, M. C. 2001. Prenylation of Rab GTPases: molecular mechanisms and involvement in genetic disease. *FEBS Lett,* 498**,** 197-200.

PEREIRA-LEAL, J. B. & SEABRA, M. C. 2000. The mammalian Rab family of small GTPases: definition of family and subfamily sequence motifs suggests a mechanism for functional specificity in the Ras superfamily. *J Mol Biol,* 301**,** 1077-87.

PEREIRA-LEAL, J. B. & SEABRA, M. C. 2001. Evolution of the Rab family of small GTP-binding proteins. *J Mol Biol,* 313**,** 889-901.

PERNAS-ALONSO, R., PERRONE-CAPANO, C., VOLPICELLI, F. & DI PORZIO, U. 2001. Regionalized neurofilament accumulation and motoneuron degeneration are linked phenotypes in wobbler neuromuscular disease. *Neurobiol Dis,* 8**,** 581-9.

PERROT, R. & EYER, J. 2009. Neuronal intermediate filaments and neurodegenerative disorders. *Brain Res Bull,* 80**,** 282-95.

PFEFFER, S. & AIVAZIAN, D. 2004. Targeting Rab GTPases to distinct membrane compartments. *Nat Rev Mol Cell Biol,* 5**,** 886-96.

PULIDO, M. R., DIAZ-RUIZ, A., JIMENEZ-GOMEZ, Y., GARCIA-NAVARRO, S., GRACIA-NAVARRO, F., TINAHONES, F., LOPEZ-MIRANDA, J., FRUHBECK, G., VAZQUEZ-MARTINEZ, R. & MALAGON, M. M. 2011. Rab18 dynamics in adipocytes in relation to lipogenesis, lipolysis and obesity. *PLoS One,* 6**,** e22931.

RAO, P. V., ROBISON, W. G., JR., BETTELHEIM, F., LIN, L. R., REDDY, V. N. & ZIGLER, J. S., JR. 1997a. Role of small GTP-binding proteins in lovastatin-induced cataracts. *Invest Ophthalmol Vis Sci,* 38**,** 2313-21.

RAO, P. V., ZIGLER, J. S., JR. & GARLAND, D. 1997b. Analysis of small GTP-binding proteins of the lens by GTP overlay assay reveals the presence of unique GTP-binding proteins associated with fiber cells. *Exp Eye Res,* 64**,** 219-27.

REID, E., KLOOS, M., ASHLEY-KOCH, A., HUGHES, L., BEVAN, S., SVENSON, I. K., GRAHAM, F. L., GASKELL, P. C., DEARLOVE, A., PERICAK-VANCE, M. A., RUBINSZTEIN, D. C. & MARCHUK, D. A. 2002. A kinesin heavy chain (KIF5A) mutation in hereditary spastic paraplegia (SPG10). *Am J Hum Genet,* 71**,** 1189-94.

RENVOISE, B. & BLACKSTONE, C. 2010. Emerging themes of ER organization in the development and maintenance of axons. *Curr Opin Neurobiol,* 20**,** 531-7.

RIBCHESTER, R. R. 2009. Mammalian neuromuscular junctions: modern tools to monitor synaptic form and function. *Curr Opin Pharmacol,* 9**,** 297-305.

RIBCHESTER, R. R., THOMSON, D., WOOD, N. I., HINKS, T., GILLINGWATER, T. H., WISHART, T. M., COURT, F. A. & MORTON, A. J. 2004. Progressive abnormalities in skeletal muscle and neuromuscular junctions of transgenic mice expressing the Huntington's disease mutation. *Eur J Neurosci,* 20**,** 3092-114.

RINK, J., GHIGO, E., KALAIDZIDIS, Y. & ZERIAL, M. 2005. Rab conversion as a mechanism of progression from early to late endosomes. *Cell,* 122**,** 735-49.

ROSENTHAL, N. & BROWN, S. 2007. The mouse ascending: perspectives for human-disease models. *Nat Cell Biol,* 9**,** 993-9.

SAKANE, A., MANABE, S., ISHIZAKI, H., TANAKA-OKAMOTO, M., KIYOKAGE, E., TOIDA, K., YOSHIDA, T., MIYOSHI, J., KAMIYA, H., TAKAI, Y. & SASAKI, T. 2006. Rab3 GTPase-activating protein regulates synaptic transmission and plasticity through the inactivation of Rab3. *Proc Natl Acad Sci U S A,* 103**,** 10029-34.

SALLOUM, S., WANG, H., FERGUSON, C., PARTON, R. G. & TAI, A. W. 2013. Rab18 Binds to Hepatitis C Virus NS5A and Promotes Interaction between Sites of Viral Replication and Lipid Droplets. *PLoS Pathog,* 9**,** e1003513.

SALMINEN, A. & NOVICK, P. J. 1987. A ras-like protein is required for a post-Golgi event in yeast secretion. *Cell,* 49**,** 527-38.

SANCHEZ, J. M., BARREIRO, C. & FREILIJ, H. 1985. Two brothers with Martsolf's syndrome. *J Med Genet,* 22**,** 308-10.

SANES, J. R. & LICHTMAN, J. W. 1999. Development of the vertebrate neuromuscular junction. *Annu Rev Neurosci,* 22**,** 389-442.

SASAKI, T., KIKUCHI, A., ARAKI, S., HATA, Y., ISOMURA, M., KURODA, S. & TAKAI, Y. 1990. Purification and characterization from bovine brain cytosol of a protein that inhibits the dissociation of GDP from and the subsequent binding of GTP to smg p25A, a ras p21-like GTP-binding protein. *J Biol Chem,* 265**,** 2333-7.

SCHLUTER, O. M., BASU, J., SUDHOF, T. C. & ROSENMUND, C. 2006. Rab3 superprimes synaptic vesicles for release: implications for short-term synaptic plasticity. *J Neurosci,* 26**,** 1239-46.

SCHLUTER, O. M., KHVOTCHEV, M., JAHN, R. & SUDHOF, T. C. 2002. Localization versus function of Rab3 proteins. Evidence for a common regulatory role in controlling fusion. *J Biol Chem,* 277**,** 40919-29.

SCHLUTER, O. M., SCHMITZ, F., JAHN, R., ROSENMUND, C. & SUDHOF, T. C. 2004. A complete genetic analysis of neuronal Rab3 function. *J Neurosci,* 24**,** 6629-37.

SCHLUTER, O. M., SCHNELL, E., VERHAGE, M., TZONOPOULOS, T., NICOLL, R. A., JANZ, R., MALENKA, R. C., GEPPERT, M. & SUDHOF, T. C. 1999. Rabphilin knock-out mice reveal that rabphilin is not required for rab3 function in regulating neurotransmitter release. *J Neurosci,* 19**,** 5834-46.

SCHNUTGEN, F., DE-ZOLT, S., VAN SLOUN, P., HOLLATZ, M., FLOSS, T., HANSEN, J., ALTSCHMIED, J., SEISENBERGER, C., GHYSELINCK, N. B., RUIZ, P., CHAMBON, P., WURST, W. & VON MELCHNER, H. 2005. Genomewide production of multipurpose alleles for the functional analysis of the mouse genome. *Proc Natl Acad Sci U S A,* 102**,** 7221-6.

SHABO, G., SCHEFFER, H., CRUYSBERG, J. R., LAMMENS, M., PASMAN, J. W., SPRUIT, M. & WILLEMSEN, M. A. 2005. Congenital cataract facial dysmorphism neuropathy syndrome: a clinically recognizable entity. *Pediatr Neurol,* 33**,** 277-9.

SHARPE, J., AHLGREN, U., PERRY, P., HILL, B., ROSS, A., HECKSHER-SORENSEN, J., BALDOCK, R. & DAVIDSON, D. 2002. Optical projection tomography as a tool for 3D microscopy and gene expression studies. *Science,* 296**,** 541-5.

SHEN, H., BARRY, D. M., DALE, J. M., GARCIA, V. B., CALCUTT, N. A. & GARCIA, M. L. 2011. Muscle pathology without severe nerve pathology in a new mouse model of Charcot-Marie-Tooth disease type 2E. *Hum Mol Genet,* 20**,** 2535-48.

SOTOMAYOR, R. E. & HANDEL, M. A. 1986. Failure of acrosome assembly in a male sterile mouse mutant. *Biol Reprod,* 34**,** 171-82.

SPECTOR, D. L. & GOLDMAN, R. D. 2010. Transfection of mammalian cells with fluorescent protein fusions. *Cold Spring Harb Protoc,* 2010**,** pdb prot5517.

STENMARK, H. 2009. Rab GTPases as coordinators of vesicle traffic. *Nat Rev Mol Cell Biol,* 10**,** 513-25.

STENMARK, H. & OLKKONEN, V. M. 2001. The Rab GTPase family. *Genome Biol,* 2**,** REVIEWS3007.

STORRIE, B., WHITE, J., ROTTGER, S., STELZER, E. H., SUGANUMA, T. & NILSSON, T. 1998. Recycling of golgi-resident glycosyltransferases through the ER reveals a novel pathway and provides an explanation for nocodazole-induced Golgi scattering. *J Cell Biol,* 143**,** 1505-21.

SUDHOF, T. C. 2004. The synaptic vesicle cycle. *Annu Rev Neurosci,* 27**,** 509-47.

SZARO, B. G. & STRONG, M. J. 2009. Post-transcriptional control of neurofilaments: New roles in development, regeneration and neurodegenerative disease. *Trends Neurosci,* 33**,** 27-37.

TANAKA, M., MIYOSHI, J., ISHIZAKI, H., TOGAWA, A., OHNISHI, K., ENDO, K., MATSUBARA, K., MIZOGUCHI, A., NAGANO, T., SATO, M., SASAKI, T. & TAKAI, Y. 2001. Role of Rab3 GDP/GTP exchange protein in synaptic vesicle trafficking at the mouse neuromuscular junction. *Mol Biol Cell,* 12**,** 1421-30.

TASAKA, K., MASUMOTO, N., MIZUKI, J., IKEBUCHI, Y., OHMICHI, M., KURACHI, H., MIYAKE, A. & MURATA, Y. 1998. Rab3B is essential for GnRH-induced gonadotrophin release from anterior pituitary cells. *J Endocrinol,* 157**,** 267-74.

THINGHOLM, T. E., JORGENSEN, T. J., JENSEN, O. N. & LARSEN, M. R. 2006. Highly selective enrichment of phosphorylated peptides using titanium dioxide. *Nature protocols,* 1**,** 1929-35.

TOLMACHOVA, T., ANDERS, R., STINCHCOMBE, J., BOSSI, G., GRIFFITHS, G. M., HUXLEY, C. & SEABRA, M. C. 2004. A general role for Rab27a in secretory cells. *Mol Biol Cell,* 15**,** 332-44.

TRUE, L., COLEMAN, I., HAWLEY, S., HUANG, C. Y., GIFFORD, D., COLEMAN, R., BEER, T. M., GELMANN, E., DATTA, M., MOSTAGHEL, E., KNUDSEN, B., LANGE, P., VESSELLA, R., LIN, D., HOOD, L. & NELSON, P. S. 2006. A molecular correlate to the Gleason grading system for prostate adenocarcinoma. *Proc Natl Acad Sci U S A,* 103**,** 10991-6.

TU, P. H., RAJU, P., ROBINSON, K. A., GURNEY, M. E., TROJANOWSKI, J. Q. & LEE, V. M. 1996. Transgenic mice carrying a human mutant superoxide dismutase transgene develop neuronal cytoskeletal pathology resembling human amyotrophic lateral sclerosis lesions. *Proc Natl Acad Sci U S A,* 93**,** 3155-60.

ULLRICH, O., STENMARK, H., ALEXANDROV, K., HUBER, L. A., KAIBUCHI, K., SASAKI, T., TAKAI, Y. & ZERIAL, M. 1993. Rab GDP dissociation inhibitor as a general regulator for the membrane association of rab proteins. *J Biol Chem,* 268**,** 18143-50.

VARNUM, D. S. 1983. Blind-sterile: a new mutation on chromosome 2 of the house mouse. *J Hered,* 74**,** 206-7.

VAVLITOU, N., SARGIANNIDOU, I., MARKOULLIS, K., KYRIACOU, K., SCHERER, S. S. & KLEOPA, K. A. 2010. Axonal pathology precedes demyelination in a mouse model of X-linked demyelinating/type I Charcot-Marie Tooth neuropathy. *J Neuropathol Exp Neurol,* 69**,** 945-58.

VAZQUEZ-MARTINEZ, R., CRUZ-GARCIA, D., DURAN-PRADO, M., PEINADO, J. R., CASTANO, J. P. & MALAGON, M. M. 2007. Rab18 inhibits secretory activity in neuroendocrine cells by interacting with secretory granules. *Traffic,* 8**,** 867-82.

VAZQUEZ-MARTINEZ, R., MARTINEZ-FUENTES, A. J., PULIDO, M. R., JIMENEZ-REINA, L., QUINTERO, A., LEAL-CERRO, A., SOTO, A., WEBB, S. M., SUCUNZA, N., BARTUMEUS, F., BENITO-LOPEZ, P., GALVEZ-MORENO, M. A., CASTANO, J. P. & MALAGON, M. M. 2008. Rab18 is reduced in pituitary tumors causing acromegaly and its overexpression reverts growth hormone hypersecretion. *J Clin Endocrinol Metab,* 93**,** 2269-76.

VERHOEVEN, K., DE JONGHE, P., COEN, K., VERPOORTEN, N., AUER-GRUMBACH, M., KWON, J. M., FITZPATRICK, D., SCHMEDDING, E., DE VRIENDT, E., JACOBS, A., VAN GERWEN, V., WAGNER, K., HARTUNG, H. P. & TIMMERMAN, V. 2003. Mutations in the small GTP-ase late endosomal protein RAB7 cause Charcot-Marie-Tooth type 2B neuropathy. *Am J Hum Genet,* 72**,** 722-7.

WAGNER, O. I., ASCANO, J., TOKITO, M., LETERRIER, J. F., JANMEY, P. A. & HOLZBAUR, E. L. 2004. The interaction of neurofilaments with the microtubule motor cytoplasmic dynein. *Mol Biol Cell,* 15**,** 5092-100.

WANG, L. & BROWN, A. 2002. Rapid movement of microtubules in axons. *Curr Biol,* 12**,** 1496-1501.

WANG, L. & BROWN, A. 2010. A hereditary spastic paraplegia mutation in kinesin-1A/KIF5A disrupts neurofilament transport. *Mol Neurodegener,* 5**,** 52.

WANG, Y., OKAMOTO, M., SCHMITZ, F., HOFMANN, K. & SUDHOF, T. C. 1997. Rim is a putative Rab3 effector in regulating synaptic-vesicle fusion. *Nature,* 388**,** 593-8.

WARBURG, M., SJO, O., FLEDELIUS, H. C. & PEDERSEN, S. A. 1993. Autosomal recessive microcephaly, microcornea, congenital cataract, mental retardation, optic atrophy, and hypogenitalism. Micro syndrome. *Am J Dis Child,* 147**,** 1309-12.

WILSON, S. M., YIP, R., SWING, D. A., O'SULLIVAN, T. N., ZHANG, Y., NOVAK, E. K., SWANK, R. T., RUSSELL, L. B., COPELAND, N. G. & JENKINS, N. A. 2000. A mutation in Rab27a causes the vesicle transport defects observed in ashen mice. *Proc Natl Acad Sci U S A,* 97**,** 7933-8.

WISHART, T. M., HUANG, J. P., MURRAY, L. M., LAMONT, D. J., MUTSAERS, C. A., ROSS, J., GELDSETZER, P., ANSORGE, O., TALBOT, K., PARSON, S. H. & GILLINGWATER, T. H. 2010. SMN deficiency disrupts brain development in a mouse model of severe spinal muscular atrophy. *Hum Mol Genet,* 19**,** 4216-28.

WISHART, T. M., PATERSON, J. M., SHORT, D. M., MEREDITH, S., ROBERTSON, K. A., SUTHERLAND, C., COUSIN, M. A., DUTIA, M. B. & GILLINGWATER, T. H. 2007. Differential proteomics analysis of synaptic proteins identifies potential cellular targets and protein mediators of synaptic neuroprotection conferred by the slow Wallerian degeneration (Wlds) gene. *Molecular & cellular proteomics : MCP,* 6**,** 1318-30.

WISHART, T. M., ROONEY, T. M., LAMONT, D. J., WRIGHT, A. K., MORTON, A. J., JACKSON, M., FREEMAN, M. R. & GILLINGWATER, T. H. 2012. Combining comparative proteomics and molecular genetics uncovers regulators of synaptic and axonal stability and degeneration in vivo. *PLoS Genet,* 8**,** e1002936.

XIA, C. H., ROBERTS, E. A., HER, L. S., LIU, X., WILLIAMS, D. S., CLEVELAND, D. W. & GOLDSTEIN, L. S. 2003. Abnormal neurofilament transport caused by targeted disruption of neuronal kinesin heavy chain KIF5A. *J Cell Biol,* 161**,** 55-66.

YABE, J. T., PIMENTA, A. & SHEA, T. B. 1999. Kinesin-mediated transport of neurofilament protein oligomers in growing axons. *J Cell Sci,* 112 (Pt 21)**,** 3799-814.

YILDIRIM, M. S., ZAMANI, A. G. & BOZKURT, B. 2012. Warburg micro syndrome in two children from a highly inbred Turkish family. *Genet Couns,* 23**,** 169-74.

YOUSSEF, G., GERNER, L., NAEEM, A. S., RALPH, O., ONO, M., O'NEILL, C. A. & O'SHAUGHNESSY, R. F. 2013. Rab3Gap1 mediates exocytosis of Claudin-1 and tight junction formation during epidermal barrier acquisition. *Dev Biol,* 380**,** 274-85.

YU, H., LEAF, D. S. & MOORE, H. P. 1993. Gene cloning and characterization of a GTP-binding Rab protein from mouse pituitary AtT-20 cells. *Gene,* 132**,** 273-8.

YUAN, A., RAO, M. V., VEERANNA & NIXON, R. A. 2012. Neurofilaments at a glance. *J Cell Sci,* 125**,** 3257-63.

YUAN, A., SASAKI, T., RAO, M. V., KUMAR, A., KANUMURI, V., DUNLOP, D. S., LIEM, R. K. & NIXON, R. A. 2009. Neurofilaments form a highly stable stationary cytoskeleton after reaching a critical level in axons. *J Neurosci,* 29**,** 11316-29.

YUKSEL, A., YESIL, G., ARAS, C. & SEVEN, M. 2007. Warburg Micro syndrome in a Turkish boy. *Clin Dysmorphol,* 16**,** 89-93.

ZERIAL, M. & MCBRIDE, H. 2001. Rab proteins as membrane organizers. *Nat Rev Mol Cell Biol,* 2**,** 107-17.

Appendix 1: Movie legends

Movie 1: Optical projection tomography on adult wild-type albino eyes
Optical projection tomography on adult wild-type albino eyes showing normal lens.

Movie 2: Optical projection tomography on adult *Rab18*$^{-/-}$ albino eyes
Optical projection tomography on adult *Rab18*$^{-/-}$ albino eyes showing dense nuclear cataracts in the centre of the lens.

Movie 3: GFP-Rab18 undergoes dynamic movement in mouse primary hippocampal neurons.
Time-lapse movie (2 minute intervals for 16 hours, 10fps) showing wild type mouse hippocampal neurons from E17.5 embryos transfected with GFP-RAB18 at 12-14 DIV. GFP-RAB18 is localised throughout neurons and present in puncta in neuronal processes that are mobile.

Appendix 2: Necropsy report

David Brownstein
Room W3.16
Queen's Medical Research Institute
47 Little France Crescent
Edinburgh EH16 4TJ
Tel:+44-131-242-6730
e-mail: d.brownstein@ed.ac.uk

NECROPSY REPORT

Investigator: Ian Jackson
Date of necropsy: 2/12/10
Path#: DB55-58/10
Subject: KO mouse model which is looking very interesting. Has cataracts and an apparent neuromuscular problem which results in hindlimb weakness progressing to paralysis. These are 106 day-old littermates, agouti, chinchilla?) and black. Two homozygotes are thin with barbered fur over thorax. Both are unsteady on hind legs.
DB55/10-homozygote
DB56/10-heterozygote
DB57/10-wt
DB58/10- homozygote
Gravimetrics:

Path #	Bwt (g)	Heart (mg)	Heart/bwt	Kidneys (mg)	Kidney/bwt	Liver (mg)	Liver/bwt	Spleen (mg)	Thymus (mg)
DB55/10	**27.05**	134	5.0	391	14.5	1355	50.1	77	45
DB56/10	30.4	205	6.7	433	14.2	1272	41.8	86	44
DB57/10	33.41	191	5.7	443	13.3	1230	36.8	85	42
DB58/10	**27.35**	140	5.1	424	15.5	1310	47.9	66	47

Testis (mg): DB55 =118g , DB56 = 198, DB57=234, DB58=170
Gross: homozygotes smaller than heterozygote or wt.

Histopathology. The following tissues were examined and found not to differ significantly between the two homozygous and the heterozygous and wt animals.
A. heart-
B. lung-
C. thyroid, adrenals,
D. testis or uterus-
E. stomach, small intestine (3 levels)-
F. caecum, colon, mesentery-
G. liver, skin, abdominal mammary -
H. brain (3 coronal levels)-
I. pituitary-.
J. lower urinary-

K. kidneys, interscapular brown fat -
L. spleen, pancreas, thymus, lymphosalivary -
M. head (inc. eyes and mid/inner ears) -
N. long bones with knee joint -
O. lumbar spine/spinal cord/aorta-
P. thoracic spine/spinal cord/aorta
Q. cervical spine/spinal cord
R. cross section of thigh muscles

Appendix 3 iTRAQ identification of proteins >20% upregulated in *Rab18*$^{-/-}$ compared to heterozygote nerves with 2 or more unique peptides

Symbol	Protein name	Accession number	# Unique peptides	Ratio Rab18/het
MYH4	myosin, heavy chain 4, skeletal muscle	IPI00404837.3	32	4.278
KRT1	keratin 1	IPI00625729.2	2	3.145
KRT5	keratin 5	IPI00470126.4	4	2.842
KRT10	keratin 10	IPI01008564.1	4	2.696
COL1A2	collagen, type I, alpha 2	IPI00988109.1	12	2.556
APOD	apolipoprotein D	IPI00314309.3	5	2.366
KRT13	keratin 13	IPI00136056.1	2	2.355
COL1A1	collagen, type I, alpha 1	IPI00329872.1	9	2.180
KRT14	keratin 14	IPI00227140.1	5	1.928
KRT2	keratin 2	IPI00622240.4	3	1.886
LGALS3	lectin, galactoside-binding, soluble, 3	IPI00989544.2	2	1.871
Ighg	Immunoglobulin heavy chain (gamma polypeptide)	IPI00109910.4	8	1.851
Ighg2a	immunoglobulin heavy constant gamma 2A	IPI00954663.1	2	1.846
ACTC1	actin, alpha, cardiac muscle 1	IPI00114593.1	8	1.731
COL28A1	collagen, type XXVIII, alpha 1	IPI00357842.7	8	1.663
HIST1H1C	histone cluster 1, H1c	IPI00223713.5	4	1.657
IGHM	immunoglobulin heavy constant mu	IPI00468055.3	4	1.653
RPL6	ribosomal protein L6	IPI00313222.5	11	1.645
JUP	junction plakoglobin	IPI00229475.1	2	1.626
HNRNPA2B1	heterogeneous nuclear ribonucleoprotein A2/B1	IPI00405058.6	4	1.549
IGKC	immunoglobulin kappa constant	IPI00850020.1	2	1.545
Pzp	pregnancy zone protein	IPI00624663.3	12	1.543
PCOLCE	procollagen C-endopeptidase enhancer	IPI00120176.1	2	1.533

HNRNPC	heterogeneous nuclear ribonucleoprotein C (C1/C2)	IPI00759870.1	2	1.508
FGA	fibrinogen alpha chain	IPI00115522.3	8	1.493
RPL18A	ribosomal protein L18a	IPI00162790.1	3	1.484
COL6A3	collagen, type VI, alpha 3	IPI00988390.1	2	1.482
COL4A1	collagen, type IV, alpha 1	IPI00109588.4	5	1.466
FGG	fibrinogen gamma chain	IPI00990997.1	12	1.464
RPL15	ribosomal protein L15	IPI00273803.4	2	1.459
FGB	fibrinogen beta chain	IPI00279079.1	8	1.457
RPL13A	ribosomal protein L13a	IPI00223217.6	3	1.414
RPL24	ribosomal protein L24	IPI00880689.1	3	1.409
RPL14	ribosomal protein L14	IPI00133185.3	3	1.408
BCAP31	B-cell receptor-associated protein 31	IPI00230422.6	2	1.408
COL4A2	collagen, type IV, alpha 2	IPI00338452.3	10	1.401
THY1	Thy-1 cell surface antigen	IPI00109727.1	4	1.399
STEAP3	STEAP family member 3, metalloreductase	IPI00830824.1	3	1.371
RPS11	ribosomal protein S11	IPI00762542.2	5	1.362
CAV1	caveolin 1, caveolae protein, 22kDa	IPI00117829.1	3	1.348
TM9SF2	transmembrane 9 superfamily member 2	IPI00988824.1	2	1.343
Rpl10	ribosomal protein L10	IPI00775915.1	5	1.337
LMNA	lamin A/C	IPI00400300.1	32	1.334
NDUFB6	NADH dehydrogenase (ubiquinone) 1 beta subcomplex, 6, 17kDa	IPI00648743.1	2	1.327
Rrbp1	ribosome binding protein 1	IPI00755120.2	3	1.324
LOC638399	60S ribosomal protein L31-like	IPI00677102.1	2	1.323
COPA	coatomer protein complex, subunit alpha	IPI00989407.1	4	1.322
PABPC1	poly(A) binding protein, cytoplasmic 1	IPI00124287.2	2	1.322
RPL7	ribosomal protein L7	IPI00311236.1	10	1.321
MTCH1	mitochondrial carrier 1	IPI00742287.1	2	1.316
Gm5453	predicted gene 5453	IPI00461641.2	3	1.306
RPL18	ribosomal protein L18	IPI00555113.2	5	1.304
HIST1H1B	histone cluster 1, H1b	IPI00230133.5	6	1.304
SEC23A	Sec23 homolog A (S. cerevisiae)	IPI00985577.1	3	1.293
ENTPD2	ectonucleoside triphosphate diphosphohydrolase 2	IPI00115089.2	9	1.293

POSTN	periostin, osteoblast specific factor	IPI00409326.1	10	1.290
GNG12	guanine nucleotide binding protein (G protein), gamma 12	IPI00227838.4	3	1.290
HNRNPL	heterogeneous nuclear ribonucleoprotein L	IPI00985815.1	4	1.289
RPS4X	ribosomal protein S4, X-linked	IPI00990327.1	10	1.281
PICALM	phosphatidylinositol binding clathrin assembly protein	IPI00404434.1	2	1.279
GNB2L1	guanine nucleotide binding protein (G protein), beta polypeptide 2-like 1	IPI00317740.5	2	1.279
APOA1	apolipoprotein A-I	IPI00877236.1	13	1.276
NDUFA9	NADH dehydrogenase (ubiquinone) 1 alpha subcomplex, 9, 39kDa	IPI00120212.2	3	1.272
NSDHL	NAD(P) dependent steroid dehydrogenase-like	IPI00128692.1	5	1.271
CFH	complement factor H	IPI00856390.1	3	1.270
RPS2	ribosomal protein S2	IPI00318492.11	10	1.267
RPS3	ribosomal protein S3	IPI00134599.1	8	1.264
KARS	lysyl-tRNA synthetase	IPI00620145.1	2	1.263
Gm7429	predicted pseudogene 7429	IPI00463886.1	6	1.257
DAD1	defender against cell death 1	IPI00109082.3	2	1.256
MCAM	melanoma cell adhesion molecule	IPI00667748.1	4	1.252
RPL10A	ribosomal protein L10a	IPI00849927.1	5	1.250
DYNC1I1	dynein, cytoplasmic 1, intermediate chain 1	IPI00990353.1	2	1.250
ANXA1	annexin A1	IPI00230395.5	9	1.249
HNRNPU	heterogeneous nuclear ribonucleoprotein U (scaffold attachment factor A)	IPI00970121.1	10	1.247
DDX5	DEAD (Asp-Glu-Ala-Asp) box helicase 5	IPI00420363.3	4	1.246
MGLL	monoglyceride lipase	IPI00953761.1	3	1.245
C3	complement component 3	IPI00323624.4	30	1.244
SYNCRIP	synaptotagmin binding, cytoplasmic RNA interacting protein	IPI01027389.1	2	1.243
LAMB2	laminin, beta 2 (laminin S)	IPI00119065.2	47	1.242
RPS15A	ribosomal protein S15a	IPI00857457.1	2	1.239
KDELR3	KDEL (Lys-Asp-Glu-Leu) endoplasmic reticulum protein retention receptor 3	IPI00320629.3	2	1.238
RPN1	ribophorin I	IPI00309035.2	11	1.238
MT-CO2	cytochrome c oxidase subunit II	IPI00131176.1	3	1.237
RPL8	ribosomal protein L8	IPI00137787.3	6	1.236
TNXB	tenascin XB	IPI00130794.1	14	1.235

DHCR7	7-dehydrocholesterol reductase	IPI00130988.1	3	1.232
ATP2B1	ATPase, Ca++ transporting, plasma membrane 1	IPI00556827.1	3	1.228
P4HB	prolyl 4-hydroxylase, beta polypeptide	IPI00133522.2	8	1.225
RTN1	reticulon 1	IPI00459442.1	3	1.222
RPL9	ribosomal protein L9	IPI00881026.1	3	1.220
CRIP2	cysteine-rich protein 2	IPI00121319.1	3	1.220
EIF4H	eukaryotic translation initiation factor 4H	IPI00222560.7	2	1.219
RPS9	ribosomal protein S9	IPI00420726.3	6	1.218
COPG1	coatomer protein complex, subunit gamma 1	IPI00223437.5	2	1.217
CYB5R3	cytochrome b5 reductase 3	IPI00759904.1	9	1.216
ATP1A2	ATPase, Na+/K+ transporting, alpha 2 polypeptide	IPI00762871.2	14	1.215
MIF	macrophage migration inhibitory factor (glycosylation-inhibiting factor)	IPI00230427.5	2	1.213
CTSD	cathepsin D	IPI00927957.1	5	1.211
RPS16	ribosomal protein S16	IPI00469918.4	4	1.210
PLP1	proteolipid protein 1	IPI00263013.4	8	1.208
RPL29	ribosomal protein L29	IPI00874437.1	2	1.208
MARC2	mitochondrial amidoxime reducing component 2	IPI00123276.1	3	1.207
ITIH2	inter-alpha-trypsin inhibitor heavy chain 2	IPI00970608.1	2	1.202
RUVBL2	RuvB-like 2 (E. coli)	IPI00856697.1	2	1.202

Appendix 4 iTRAQ identification of proteins >20% downregulated in *Rab18*$^{-/-}$ compared to heterozygote nerves with 2 or more unique peptides

Symbol	Protein name	Accession #	# Unique peptides	Ratio Rab18/het
ALDH1A1	aldehyde dehydrogenase 1 family, member A1	IPI00626662.3	5	0.503
SERPINA1	serpin peptidase inhibitor, clade A (alpha-1 antiproteinase, antitrypsin), member 1	IPI00123927.1	5	0.539
SDPR	serum deprivation response	IPI00135660.5	3	0.579
VAT1L	vesicle amine transport protein 1 homolog (T. californica)-like	IPI00222759.3	16	0.594
MYL6	myosin, light chain 6, alkali, smooth muscle and non-muscle	IPI00354819.5	2	0.594
AKR1B1	aldo-keto reductase family 1, member B1 (aldose reductase)	IPI00223757.4	13	0.604
PMP2	peripheral myelin protein 2	IPI00553439.2	13	0.605
PRX	periaxin	IPI00762284.1	64	0.616
OGN	osteoglycin	IPI00120848.1	13	0.625
ASPA	aspartoacylase	IPI00881964.1	4	0.626
NEFH	neurofilament, heavy polypeptide	IPI00675855.3	35	0.636
SVIP	small VCP/p97-interacting protein	IPI00460224.3	2	0.639
CNTF	ciliary neurotrophic factor	IPI00125017.1	6	0.641
APOA4	apolipoprotein A-IV	IPI00377351.3	2	0.654
NEFM	neurofilament, medium polypeptide	IPI00323800.6	40	0.657
TCEB2	transcription elongation factor B (SIII), polypeptide 2 (18kDa, elongin B)	IPI00131224.1	2	0.664
FBXO2	F-box protein 2	IPI00153176.2	2	0.664
Serpina3k	serine (or cysteine) peptidase inhibitor, clade A, member 3K	IPI00131830.1	4	0.666
SERPINA1	serpin peptidase inhibitor, clade A (alpha-1 antiproteinase, antitrypsin), member 1	IPI00406302.2	4	0.671
DYNC1LI1	dynein, cytoplasmic 1, light intermediate chain 1	IPI00153421.1	2	0.673
NEFL	neurofilament, light polypeptide	IPI00554928.3	32	0.679
TUBA4A	tubulin, alpha 4a	IPI00117350.1	6	0.680

ANXA5	annexin A5	IPI00317309.5	18	0.683
TFG	TRK-fused gene	IPI00130013.4	7	0.683
HDHD2	haloacid dehalogenase-like hydrolase domain containing 2	IPI00111166.7	2	0.684
DDAH1	dimethylarginine dimethylaminohydrolase 1	IPI00109482.3	11	0.688
PLEKHB1	pleckstrin homology domain containing, family B (evectins) member 1	IPI00858298.1	2	0.690
ANXA6	annexin A6	IPI00554894.3	38	0.693
UBE2K	ubiquitin-conjugating enzyme E2K	IPI00880781.1	2	0.693
COL15A1	collagen, type XV, alpha 1	IPI00648224.1	15	0.702
DCN	decorin	IPI00123196.1	15	0.707
BCAS1	breast carcinoma amplified sequence 1	IPI00330860.3	13	0.708
AARS	alanyl-tRNA synthetase	IPI00321308.4	3	0.708
CKB	creatine kinase, brain	IPI00136703.1	13	0.708
LUM	lumican	IPI00313900.1	13	0.709
LDHB	lactate dehydrogenase B	IPI00229510.5	14	0.710
EPB41L2	erythrocyte membrane protein band 4.1-like 2	IPI00330289.4	32	0.713
TUBA1A	tubulin, alpha 1a	IPI00110753.1	6	0.716
PRKCDBP	protein kinase C, delta binding protein	IPI00126939.1	8	0.716
PTRF	polymerase I and transcript release factor	IPI00117689.1	15	0.721
GLO1	glyoxalase I	IPI00321734.7	6	0.724
MDH1	malate dehydrogenase 1, NAD (soluble)	IPI00336324.11	13	0.727
HSP90AA1	heat shock protein 90kDa alpha (cytosolic), class A member 1	IPI00330804.4	15	0.728
PRKCA	protein kinase C, alpha	IPI00321446.4	2	0.731
NAPA	N-ethylmaleimide-sensitive factor attachment protein, alpha	IPI00118930.1	3	0.732
PRDX6	peroxiredoxin 6	IPI00754071.1	5	0.735
PRELP	proline/arginine-rich end leucine-rich repeat protein	IPI00122293.3	15	0.739
NME1	NME/NM23 nucleoside diphosphate kinase 1	IPI00990246.1	9	0.740
GMFB	glia maturation factor, beta	IPI00467495.4	3	0.741
VSNL1	visinin-like 1	IPI00230418.5	3	0.743
DYNLL1	dynein, light chain, LC8-type 1	IPI00121623.1	2	0.744
STXBP6	syntaxin binding protein 6 (amisyn)	IPI00720103.1	6	0.745
CYB5A	cytochrome b5 type A (microsomal)	IPI00918942.1	3	0.746
TUBB	tubulin, beta class I	IPI00117352.1	4	0.748

HSPA1A/HSPA1B	heat shock 70kDa protein 1A	IPI00798482.20	5	0.748
Ube2n	ubiquitin-conjugating enzyme E2N	IPI00165854.3	4	0.750
TUBB3	tubulin, beta 3 class III	IPI00112251.1	6	0.751
BGN	biglycan	IPI00123194.1	9	0.757
GDI1	GDP dissociation inhibitor 1	IPI00323179.3	10	0.759
MAPRE3	microtubule-associated protein, RP/EB family, member 3	IPI00830432.1	3	0.763
Atp5h	ATP synthase, H+ transporting, mitochondrial F0 complex, subunit d	IPI00881799.1	4	0.764
CACYBP	calcyclin binding protein	IPI00115650.4	2	0.770
USP5	ubiquitin specific peptidase 5 (isopeptidase T)	IPI00881918.1	7	0.771
CTNND1	catenin (cadherin-associated protein), delta 1	IPI00752631.1	3	0.772
RUFY3	RUN and FYVE domain containing 3	IPI00622482.2	10	0.772
YWHAH	tyrosine 3-monooxygenase/tryptophan 5-monooxygenase activation protein, eta polypeptide	IPI00227392.5	5	0.773
SERPINA1	serpin peptidase inhibitor, clade A (alpha-1 antiproteinase, antitrypsin), member 1	IPI00129755.2	3	0.774
Ckmt1	creatine kinase, mitochondrial 1, ubiquitous	IPI00128296.1	7	0.777
PGK1	phosphoglycerate kinase 1	IPI00555069.3	17	0.777
DRP2	dystrophin related protein 2	IPI00830746.1	14	0.779
WBP2	WW domain binding protein 2	IPI00648905.1	3	0.780
ANXA3	annexin A3	IPI00132722.9	6	0.782
HSPA4L	heat shock 70kDa protein 4-like	IPI00317711.1	8	0.786
HSPA8	heat shock 70kDa protein 8	IPI00323357.3	25	0.786
YWHAZ	tyrosine 3-monooxygenase/tryptophan 5-monooxygenase activation protein, zeta polypeptide	IPI00116498.1	11	0.786
SNX6	sorting nexin 6	IPI00111827.5	2	0.789
DAG1	dystroglycan 1 (dystrophin-associated glycoprotein 1)	IPI00122273.1	7	0.790
ANXA2	annexin A2	IPI00468203.3	25	0.790
GSTM3	glutathione S-transferase mu 3 (brain)	IPI00990550.1	3	0.791
IDH1	isocitrate dehydrogenase 1 (NADP+), soluble	IPI00762452.2	11	0.791
RAP2A	RAP2A, member of RAS oncogene family	IPI00396701.3	2	0.795
IDH3A	isocitrate dehydrogenase 3 (NAD+) alpha	IPI00608078.1	3	0.796
MARCKS	myristoylated alanine-rich protein kinase C substrate	IPI00229534.5	4	0.798
RAP1GDS1	RAP1, GTP-GDP dissociation stimulator 1	IPI00653794.2	21	0.798

PPP1R7	protein phosphatase 1, regulatory subunit 7	IPI00129319.3	2	0.799
CAPNS1	calpain, small subunit 1	IPI00830335.1	3	0.799
FSCN1	fascin homolog 1, actin-bundling protein (Strongylocentrotus purpuratus)	IPI00353563.4	16	0.799
PYGB	phosphorylase, glycogen; brain	IPI00229796.3	20	0.799
ALDH2	aldehyde dehydrogenase 2 family (mitochondrial)	IPI00111218.1	13	0.799